ABSTRACT

Title of Document: Development of a mN level meso-scale thruster

Vivek Shirsat, 2012

Directed By: Dr. Ashwani Gupta, Distinguished Professor, Department of Mechanical Engineering

This dissertation focuses on the practical application of heat recirculating combustors as thrust chambers for micro-spacecraft systems, including: design, development, stability and operational characteristics of the thruster in both the steady state and pulsed configurations. Stable combustion was realized with partially premixed methanol/steam/oxygen, non-premixed methanol/steam/oxygen, and non-premixed kerosene/steam/oxygen. The steam oxygen mixture is a surrogate for the decomposition products of hydrogen peroxide. The effect of channel geometry on the stability and thermal performance has also been conducted in addition to qualitative and quantitative comparisons of fuel/oxidizer injection configurations. In general it was found that non-premixed combustion is favorable in terms of both thermal performance and flame stability due to the predictable extinction characteristics at low flow rates and the absence of lean blow off at high flow rates. A quantitative extinction criterion was developed to predict extinction at the rich extinction limit. Additionally, nozzle discharge characteristics at low Reynolds number were studied

and a correlation developed to predict the discharge coefficient from the Reynolds number for both cold and hot flow scenarios. It was found the discharge coefficient decays more rapidly for high temperature flows than low temperature flows due to the effects of temperature and viscosity on the boundary layer displacement thickness. Additionally, a milli-Newton level thrust stand was developed to indirectly measure the thrust level without allowing the thruster to translate, the thrust stand resolution was found to be <1mN. Using this device a study of the thrust characteristics was carried out in both the steady state and pulsed modes. Measurements of the specific impulse efficiency indicate that the conversion efficiency is high and any loss in thermal efficiency from the adiabatic scenario is due to wall heat losses and not incomplete combustion. Experiments conducted with hydrogen peroxide decomposed in the inlet channel of the combustor were used to validate the results taken with the steam/oxygen as the oxidizer and demonstrated that heat recirculation from the products to the exhaust is sufficient to promote efficient decomposition of the hydrogen peroxide.

DEVELOPMENT OF A mN LEVEL MESO-SCALE THRUSTER

By

Vivek Kiran Shirsat

Dissertation submitted to the Faculty of the Graduate School of the
University of Maryland, College Park, in partial fulfillment
of the requirements for the degree of
Doctor of Philosophy
2012

Advisory Committee:

Professor Ashwani K. Gupta, Advisor/Chair

Professor Ahsan Choudhuri

Professor Jungho Kim

Professor Bao Yang

Professor Kenneth Yu, Dean's Representative

Dedication

This dissertation is dedicated to my family, without their support and encouragement none of this would be possible.

Acknowledgements

I would like to begin by thanking my advisor, Dr. Ashwani Gupta, for his guidance, encouragement, and support throughout the graduate process and for emphasizing the value of hard work and perseverance.

Additionally, I would like to thank my committee, Dr. Sunderland, Dr, Yu, Dr. Yang, and Dr. Choudhuri for their support. In particular, I cannot emphasize enough the guidance Dr. Choudhuri has provided, beginning with the pursuit of my Masters under his at the University of Texas at El Paso through the completion on my PhD his unflinching support has helped to remove many barriers along the road to success and make possible the completion of this work.

The role my family has played in supporting and encouraging me throughout my life is without question the motivating force that gives me both the confidence and the strength to continue pursuing those things which are important to me.

Without question the members of the combustion lab, from the summer of 2008 until now, have contributed greatly to the quality and direction of the work performed during my graduate studies, in particular I would like to acknowledge Dr. Vineeth Vijayan who's fundamental studies laid the groundwork for my research. Most importantly the camaraderie and the friendships developed in the lab over the past four years I will keep with me for the rest of my life.

Finally, I would like to thank the support of our sponsors, Missile Defense Agency for supporting this research through to its completion; thanks in particular are due to Mr. Richard Schwartz for his help, support, and many useful suggestions.

Table of Contents

List of Tables

List of Figures

Chapter 1: Introduction

Section 1 Practical Relevance

Green Propulsion

The history of rocket propulsion and the development of propellants have been driven largely by the need to achieve the maximum amount of impulse while expending the minimum amount of mass. Many launch boosters have essentially evolved from the German V2 rocket, utilizing liquid oxygen and kerosene as propellants. Over time some systems have replaced the kerosene with liquid hydrogen, delivering a specific impulse so high that the complicated cryogenic storage systems and safety issues present themselves as a marginal tradeoff. During the cold war, the development of "storable" liquid oxidizers became a major concern for intercontinental ballistic missiles (ICBM) that could potentially sit in missile silos for indefinite periods of time. Requiring room-temperature liquid oxidizers some utilized highly toxic propellants or hypergolic combinations such as nitrogen tetra oxide and hydrazine. Some, namely the Titan class of launch vehicle, have evolved into heavily utilized civilian satellite launch systems. For space propulsion, the success of hydrazine as a mono-propellant and hypergolic bi-propellant have led to its almost exclusive use in high performance upper stages and RCS engines. However, recent trends toward environmentally conscious propulsion system design have been sparked by lowering the cost of spacecraft through *simple* miniature systems. Recognizing the need for miniature green propulsion systems, hydrogen

peroxide, having environmentally benign decomposition products, presents a viable solution to the problems surrounding toxic space propellants.

Micro-Spacecraft

In general, the trend for satellite design is towards smaller less expensive vehicles with overall mission functionality distributed over a number of spacecraft[1]. The cornerstone of these low-cost and design-to-cost missions is the use of small-satellites to mitigate, among other things, the burdensome cost of launch (i.e launching small satellites as secondary payloads and maneuvering into the final orbit). With this in mind, mission designers have expressed interest in using distributed micro-spacecraft architectures (constellations and clusters) to meet requirements that are currently satisfied by single, expensive, multi-role satellites[2]. In order for these spacecraft to be effective, they will require propulsion systems for launcher injection error, drag compensation, constellation phasing, and proximity maneuvering and rendezvous[3]. Owing to their low inertia, these maneuvers will require extremely low thrust (mN and μN) and low impulse bit. Contemporary satellites requiring low thrust for primary propulsion and vernier control can have a number of different propulsion options, including: cold gas, chemical monopropellant, chemical bi-propellant, vaporizing liquid, solid propellant, and a number of electric propulsion schemes. In general, experimental research in meso and micro scale propulsion has involved the scaling down of these devices. Table 1[2] below outlines the current developments in micro-propulsion including thruster type, thrust level, specific impulse and developing agency.

Table 1.1 Current Meso and Microscale Thruster Programs[2]

Thruster Type	Specific Impulse[s]	Thrust[μN]	Developing Agency
H_2O_2-Monopropellant	160	1-1000	NASA GSFC
Cold Gas	40-80	500-50000	MIT,NASA JPL
Digital Solid	200	10-100000	NASA GRC,TRW,CNES
Vaporizing Liquid	75-125	1-100	NASA JPL
Ion Engine	1400-2000	.1-10	NASA JPL
FEEP*	17000	10-200	University of Pisa

*Field Emission Electric Propulsion (FEEP)

With these future missions in mind, the rapid miniaturization of electronics and the emergence of MEMS manufacturing technology has allowed for the conceptualization of batch manufactured low-cost miniature spacecraft with the potential to drive down mission costs without substantially compromising on performance.

Section 2 Historical Perspective

The use of Hydrogen Peroxide for propulsion and power is not new, it was heavily utilized in the infancy of rocket research. The pioneering work was performed by Dr. Helmut Walter while at the Germania shipbuilding yard in Kiel, Germany in the early 1930's. There he recognized the unique problem to submarine propulsion, namely that the air supply had to be compromised between propulsion and breathable air for the crew.[4] Furthermore, the underwater cruising speeds of submarines could potentially be increased by the use of gas turbines; however the extravagant air requirements made them impractical. To overcome this issue research was initiated into the use of liquid oxidizers for gas turbine based submarines. Weighing the complexity of liquid oxygen storage against the toxicity of nitric acid Walter concentrated on the use of hydrogen peroxide decomposition products as a potential oxidizer source. He recognized that the tremendous increase in volume upon decomposition and high temperatures could be

utilized to drive steam turbines in both the “cold” (monopropellant) mode and the “hot” (bi-propellant) mode. The “hot” engine utilizes combustion of fuel with the hot oxygen in the decomposition products to further raise the temperature of the superheated steam. In autumn of 1940 the experimental submarine V80 reached an underwater speed of 28 knots, compared to 8 knots for its diesel-electric counterparts.

With the onset of World War II the German Army Ordinance Department expressed interest in the development of liquid fueled rockets and rocket propelled aircraft. The first monopropellant hydrogen peroxide rocket was tested in 1936. The thrust chamber was lined with a permanganate paste catalysts into which the concentrated hydrogen peroxide was injected. These tests evolved into the development of RATO units that were deployed on the Henkel 176 fed by 80% hydrogen peroxide. 1941 saw the most famous application of hydrogen peroxide with the maiden flight of the Messerschmidt 163 rocket powered aircraft. The aircraft would eventually reach speeds of up to 1000km/hr, 300km/hr more than its jet powered counterparts. The aircraft engine was fed with hydrogen peroxide, and a blend of hydrazine, methanol, water, and calcium permanganate as a catalyst for the peroxide. The two liquids (the peroxide and the mixture) were injected simultaneously in a bi-propellant derivative.

The use of peroxide in a launch vehicle as a main engine propellant has seen only one application. Between 1958-1965 the UK Black Knight and Black Arrow research rockets completed 22 successful sub-orbital flights with a flight to LEO in 1971. The “Gamma” series engines relied on hydrogen peroxide and kerosene as propellants, with the peroxide decomposed over silver screen catalyst packs immediately upstream of the combustion chamber.

With the onset of the cold war the design trade space shifted to favor performance over safety, reliability, and cost. This combined with the development of the UHP hydrazine and the Shell 405 catalyst led to the almost absolute displacement of hydrogen peroxide by hydrazine in monopropellant RCS systems, and by hydrazine/NTO in bi propellant systems. The only current application of hydrogen peroxide is in the RCS thrusters of the Russian Soyuz.

As mentioned above the use of HTP is making a comeback, largely due to the end of the cold war and the paradigm shift towards low cost environmentally benign design. The various historical applications of hydrogen peroxide are shown in Tables 1.2, 1.3, and 1.4, below.

Table 1.2. Mono-Propellant

RCS Thrusters
X-1
Centaur RCS
Centaur propellant settling
X-15
Mercury
Scout Roll Control
Little Joe II
Burner II
SATAR
122Y
Astronaut Maneuvering Unit
SYNCOM
COMSAT
HS 303A
ATS

Table 1.3. Gas Generator Applications

Description	Device Type
Type 18-X submarine, Germany WWII	300 ton class H2O2-kersosene turbine drive
V-2 turbo-pump gas	Liquid injection of catalyst
V-1 catapult	Liquid injection of catalyst
X-1 turbo-pump gas	Mono-propellant gas generator
Redstone turbo-pump gas	Pellet bed mono-propellant gas
Jupiter turbo-pump gas	Pellet bed mono-propellant gas
Centaur boost pump gas	Mono-propellant gas generator
Viking turbo-pump gas gen.	Mono-propellant gas generator
X-15 turbo-pump gas gen.	Mono-propellant gas generator
Mk 16 torpedo	70% H2O2
X-1 mini submarine	Mono-propellant gas generator
GE hybrid	H2O2-PE hybrid
GE plug nozzle	Mono-propellant thrusters
Hyprox system	Mono-propellant gas generator for

Table 1.4. Bi-Propellant Applications

Description	Device Type
Me 163 Komet Rocket Plane	Bi-propellant rocket engine with hydrazine hydrate and methanol
Gamma 201 rocket engine	Closed loop pump fed regen. Cooled rocket engine, UK
Gamma 301 rocket engine	Closed loop pump fed regen. Cooled rocket engine, UK
AR family of rocket engine	Gas Generator, pump fed regen. Cooled rocket engines, RD
LR-40 rocket engine	Closed loop pump fed regn. Cooled rocket engine, RMI
PR 37 rocket engine	Derivative of Gamma 201 engine
BS 605	Derivative of Gamma 201 engine

Section 3 Fundamentals of Meso-Scale Hydrogen Peroxide Propulsion

Introduction

The following section will outline the fundamental principles behind hydrogen peroxide propulsion, and the challenges associated with its operation at the meso-scale. Generally, the basic operation of an H_2O_2 based engine has not changed since the inception of the first Walter steam turbines in the 1930's. Hydrogen Peroxide is pressure fed (either by pump or pressurant) across a fuel injector which distributes the peroxide

over a catalyst bed.[4] The resultant oxygen rich superheated steam mixture is fed either through a nozzle, in a monopropellant configuration, or into a combustion chamber to react with fuel, in a bi-propellant configuration. In the early phases of hydrogen peroxide rocket development both the solid catalyst salt solution and hydrogen peroxide were injected under pressure into the combustion chamber. This was the principle behind the RI203 and RI209 Rocket Assisted Takeoff (RATO) units deployed by the Germans in WWII. [4] A later evolution of the RATO units would include mixing the catalyst with fuel doped with hydrazine hydrate. This combination is hypergolic with hydrogen peroxide and would yield much higher specific impulse than hydrogen peroxide alone. This research would lead to the development of the Me163 rocket interceptor, the only piloted aircraft powered by hydrogen peroxide. Although successful, the long term stability of fuels blended with catalysts is questionable and such systems have not been widely used.[5] Another methodology is injecting the hydrogen peroxide and fuel directly into the combustion chamber and initiating combustion using a pilot flame.[6] However, in such systems it is difficult to ensure ignition and stable combustion. [5] The above techniques can be summarized in the following way:

- Mono-Propellant
    - *Injection of hydrogen peroxide over a catalyst bed (heterogeneous catalysis).* This configuration is more complex than direct injection of catalyst into the combustion chamber, and comes with generally larger pressure drops. However, the decomposition products are clean since there is no solid material flowing with the superheated steam and oxygen. This configuration was utilized in the Walter steam turbine driven submarines.

- *Simultaneous injection of hydrogen peroxide and catalyst (homogenous catalysis).* `This configuration was widely used by the Germans in WWII for rocket propulsion and catapult work due to its simplicity. However, the catalyst salt precipitates out of solution during the catalytic reaction. The solid material flowing with the decomposition product could potentially clog small orifices and injectors leading to failure. [5]

- Bi-Propellant
  - *Decomposition over a catalyst pack with subsequent combustion with fuel (heterogeneous catalysis).* Such a configuration has been successfully utilized in the black knight and black arrow research rockets however have not been utilized in a launch system since.
  - *Catalytic/Hypergolic reaction between hydrogen peroxide and fuel (homogenous catalysis).* This involves blending the fuel with hydrogen peroxide catalysts/hypergolics. Although successfully deployed, the long term stability of the fuel blends is not well understood, and the use of hypergolics (inorganic amines such as hydrazine) does not eliminate the reliance on toxic propellants.

The selection of the appropriate decomposition technique requires consideration of the unique requirements of meso-scale thrusters. Meso propulsion systems *must* be simple in design and operation since complicated systems only increase cost. A system that involves the injection of a liquid catalyst increases the overall system mass but circumvents the catalyst degradation problems associated with heterogeneous catalysis. Inevitably this leads to decomposition efficiencies that are constant over the system lifespan. [5] On the other hand, the catalyst salt precipitates out of solution potentially clogging small flow pathways and injectors.[5] For micro satellite systems with limited mission duration the development of catalytic micro-reactors in series with mono and bi-

propellant thrust chambers presents the most practical option for a hydrogen peroxide based micro propulsion system. The following sections will focus on the challenges associated with heterogeneous catalysis of hydrogen peroxide, and those associated with a complementary meso-scale thruster.

Homogenous and Heterogeneous Catalysis of Hydrogen Peroxide

When hydrogen peroxide comes into contact with a catalyst surface it decomposes into oxygen rich superheated steam. The decomposition temperature increases monotonically with hydrogen peroxide concentration due to the presence of excess water in the initial liquid phase solution. The adiabatic decomposition temperature versus weight percent hydrogen peroxide is shown in Figure 1.1, below. [7]

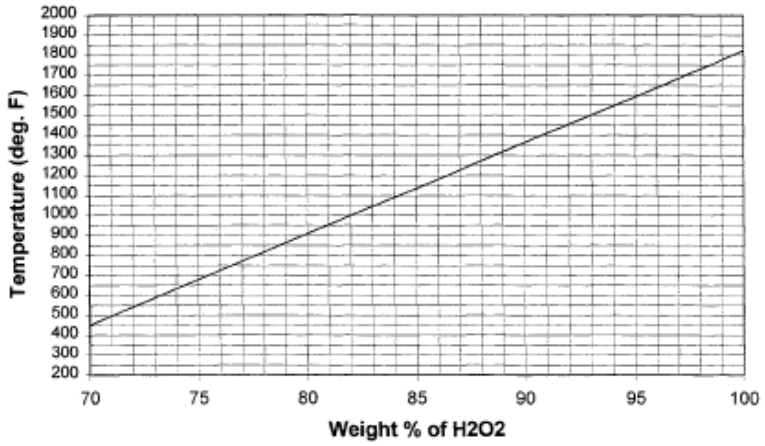

Figure 1.1 Adiabatic decomposition temperature of hydrogen peroxide solution versus weight percent of hydrogen peroxide

The final temperature also depends on the effectiveness of decomposition on the catalyst bed. The effectiveness is a function of the nature of the active catalyst material's distribution on the catalyst bed and its available reaction surface. This is dependent on the geometry of the bed (its surface area and length) and the catalyst activity. Due to the heat sinking effect of water, peroxide solutions of less than 68% hydrogen peroxide do not

possess the chemical energy necessary to vaporize all of the water in solution and thus will not yield steam.[8] For pure hydrogen peroxide the global decomposition can be represented by the following net reaction [8]:

$$2H_2O_2(l) \rightarrow 2H_2O(g) + O_2(g)\left[\Delta HR \approx \frac{96kJ}{mol}\right] \qquad \text{Eq.1.1}$$

In order to determine the nature of decomposition numerical studies performed in a single channel have allowed the segregation of the catalyst bed into five distinct regions. [9] The five regions are shown in Figure 1.2, below.

I. The heat of reaction raises the mixture temperature to the boiling point of water in the initial solution

II. Isothermal boiling of water

III. The solution temperature is increased up to the hydrogen peroxide boiling point

IV. Isothermal boiling of hydrogen peroxide

V. Vapor phase/Thermal decomposition of hydrogen peroxide up to the final gas temperature

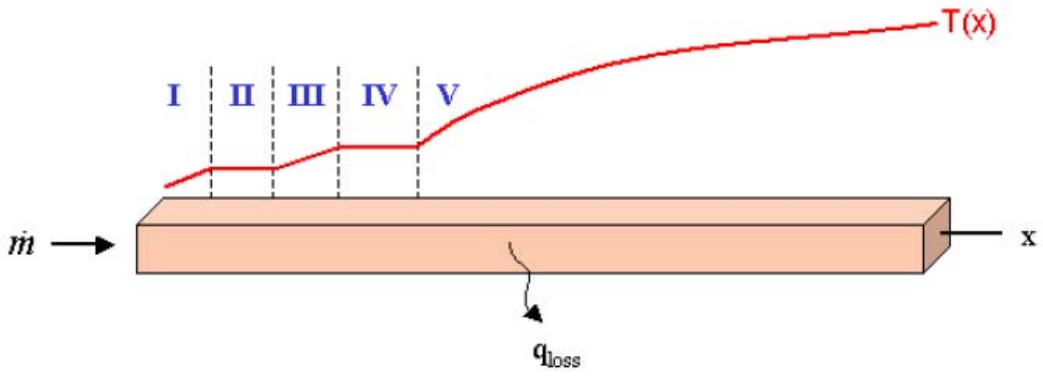

Figure 1.2. Five regions of decomposition, note that the length of the regions is for illustrative purposes only and not indicative of realistic behavior [9]

The first four regions involve the liquid phase decomposition of hydrogen peroxide with catalyst, the critical length of which is determined by the time required to boil off the liquid constituents in the initial solution. The decomposition mechanism in the liquid phase is not entirely understood, and formulating the reaction kinetics in an Arrhenius form requires consideration of variables which are largely unpredictable, such as the impurities in the initial solution and both catalysis and inhibition of catalysis by the experimental apparatus (fuel lines, fuel injector, etc.) these amount to irreproducibility in the system. [10] However, the general scheme involves the disassociation hydrogen peroxide at the surface of the catalyst; the products of disassociation (two OH radicals) are held at the surface and react with the molecules impinging from the surrounding fluid, allowing the reaction to propagate. [10] The propagation is considered to be homogenous. It is important to note that this net initial step is common to most hydrogen peroxide disassociation mechanisms because between the two bond types present in hydrogen peroxide (O-O and O-H) rupturing the O-O bond requires less energy and is more probable. Numerical results indicate that the critical length for decomposition, that is the length required to reach the product gas temperature, is dominated by Regions I-IV due to the latent heat of vaporization of both the water and hydrogen peroxide.[10] This length can be minimized by increasing the catalyst activity in these regions, increasing the surface area, and decreasing the heat loss. The first two directly relate to the rate of disassociation at the catalyst surface and the availability of active sites for disassociation, and the latter to the rate of temperature increase in the reactor.

Region V represents decomposition in the vapor phase; the decomposition mechanism is presented below. As in the liquid phase the reaction is initiated by disassociation of peroxide into its constituent hydroxyl radicals. [10]

$$H_2O_2 \rightarrow OH + OH$$
$$OH + H_2O_2 \rightarrow HO_2 + H_2O \qquad (1.2, 1.3, 1.4)$$
$$HO_2 + H_2O_2 \rightarrow OH + H_2O + O_2$$

The reactions are terminated by one of the following mechanisms:

$$2OH \rightarrow H_2O_2 + M$$
$$2HO_2 + M \rightarrow H_2O_2 + O_2 + M \qquad (1.5)$$
$$OH + HO_2 + M \rightarrow H_2O + O_2 + M$$

There are three important factors concerning the vapor phase decomposition mechanism. The first is that chain branching reactions are not thermodynamically favorable, so the overall reaction rate is dictated by the chain initiation step, Reaction 1.2. [10] The above mechanism applies to both homogenous and heterogeneous vapor phase decomposition; when the vapor is passed over a catalyst it provides a reaction pathway with lower activation energy, allowing the reaction to proceed at lower temperature. [10] However, at above roughly 425°C [10] the heat of reaction is sufficient to disassociate hydrogen peroxide into its constituent OH radicals; the result is a change from a heterogeneous to homogenous reaction that is thermal in nature. The practical result is that after the initial liquid is vaporized the decrease in total heat capacity results in an abrupt temperature increase, leading to homogenous decomposition. Additionally, in the vapor phase the reaction rate is higher than the diffusion rate of hydrogen peroxide to the catalyst surface, meaning that the choice of catalyst for Region V is independent of the catalyst activity; this is unlike the behavior in Regions I-IV where catalysis of high

activity inevitably lead to shorter bed lengths. These factors lead to the following conclusions for catalyst design, the major goal being to maximize the bed load while minimizing the total reactor volume (reducing the mass). The bed load is defined as the ratio of the reactant mass flow rate to the nominal cross sectional area of the catalyst bed:

- High catalyst activity in the Regions I-IV where liquid phase reaction occurs
- Minimal heat loss from the reactor or preheating of the reactor. This will lead to higher evaporation rates in Regions I-IV and quicker progression to homogenous reaction in Region V reducing the reactors critical length.[9] Approximating adiabatic conditions will also lead to higher product gas temperatures and heightened performance
- High surface area to promote catalyst activity

The above considerations apply to any miniature hydrogen peroxide steam generator while some mechanical considerations are particular to propulsion systems:

- High resistance to thermal and mechanical shock
- Low catalyst degradation
- High resistance to fouling by hydrogen peroxide stabilizing agents: The use of stabilizers will promote the long term stability of fuel stored for extended periods
- Minimal weight and pressure drop across the bed: minimizing the pressure drop will reduce the ancillary equipment necessary to deliver the required upstream pressure for a desired chamber pressure

Hydrogen peroxide is unique in that it can be catalyzed by a number of inorganic materials. Of historical interest is the use of manganese in the form of permanganate [4], this was heavily used in the developmental phase of hydrogen peroxide propulsion. The

manganese was present in the form of calcium permanganate, which readily dissolves in water. Calcium permanganate (as opposed to other permanganate salts such as potassium permanganate) was chosen because of its higher solubility in water at low temperature. This requirement was borne out of the necessity for storable propellants to survive the harsh German winters during World War II. Modern catalysts arrangements focus on the use of either silver, platinum/platinum black, or permanganate solutions in any one of basically four configurations: liquid-liquid, pellet bed, packed screen beds, and monoliths. All four configurations have their benefits and setbacks. As stated earlier, liquid-liquid homogenous decomposition requires both storage and pressurization, either by pressurant or pump, of both hydrogen peroxide and liquid catalyst. These extra requirements increase the overall system mass; however, liquid-liquid systems do not suffer from catalyst fouling and deliver consistent performance over the lifespan of the system. Pellet beds have the benefit of having a high surface area to volume ratio, however packed pellet beds suffer from large pressure requirements and damage from thermal shock. Metallic screens have similar benefits and limitations as pellet beds however do not suffer from attrition due to pellet motion, since the screens are kept stationary. [5] Silver based metallic screens also tend towards low structural stability, since the silver melting temperature is close to the decomposition temperature of highly concentrated hydrogen peroxide; platinum screens could be used to increase the working temperature but at prohibitive cost.[5] For miniature systems, monolithic beds are attractive due to their low pressure drops (two to three orders of magnitude less than packed beds), controllable surface area, simple flow geometries, and high structural stability.[5] Monolithic catalyst beds can be divided into three distinct regions: the support material

that defines the monolith geometry, a wash-coat that increases the surface area, and the active catalyst metal. [5] It is beneficial to fabricate the support material from a porous refractory ceramic in order to maximize surface area and thermal resistance. Some potential monolithic catalyst arrangements are shown in Figure 1.3.

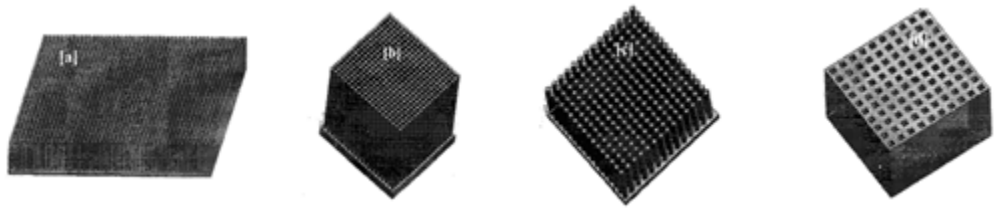

Figure 1.3. Potential catalyst bed arrangements: a) multiple stage rectangular channel. b) Circular post. c) Diamond post. d)monolithic cellular ceramic

The next section will discuss the nature or combustion as the meso-scale, the problems associated with combustor scaling and the basic requirements for a successful combustor/thrust chamber.

Meso-Scale Combustion

Meso- and micro scale combustors are those who's limiting dimension is between 1.0 cm. and 1.0 mm and less than 1 mm., respectively. Although this size definition does not characterize the size of the combustor or combustion system as a whole, the limiting dimension creates a thermo-physical environment that is different from combustors at the macro-scale. This section will discuss in detail the differences between meso- and micro-scale combustion and their macro-scale counterparts. It is important to note that the whole combustor or combustion system may be of the macro scale.

In an early review of small scale combustion research *Fernandez-Pello* [11] provided a detailed analysis of the problems and challenges associated with combustion at the meso- and micro-scale. The following is adapted from that reference to reflect the

concepts that are relevant to results presented in this report. In order to stabilize a flame in a finite volume (in a combustor) a number of basic conditions must be satisfied, these conditions are listed below:

- At a minimum the rate of heat generated by the flame must balance the rate of heat lost through the walls of the combustor
- The residence time of the mixture in the combustion chamber must be equal to or greater than the time required for the fuel and oxidizer to react
- For non-premixed reactants the characteristic mixing time must be larger than the residence time for complete mixing to occur, for liquid fuels this includes the time required to evaporate the fuel (or oxidizer)

As stated above with regards to heat loss the heat liberated by chemical reaction must approximately balance the heat lost through the walls of the combustor in order to stabilize the flame. As the length scale of a combustor is reduced the surface area available for heat loss becomes large relative to the volume available for the reaction to take place. When the combustor is made sufficiently small the rate of heat loss will increase to the point where the reaction will quench. The "quenching distance" is defined as the diameter of a tube (a cold tube) through which a flame cannot propagate due to the adverse effects of heat lost through the walls. This effect is commonly used as a safety measure to ensure that premixed flames do not back up into the fuel/air supply lines. In order to understand the requirements for stabilization of a flame in an environment of adverse heat loss an analogue can be drawn to the requirements for ignition of a steadily propagating spherical flame.[12] Considering a large (infinite) volume of premixed fuel and air in which a spark is initiated, provided the spark has enough

energy a spherical flame will originate from the spark location. When the flame is small its surface area to volume ratio is huge and the rate of heat loss from the flame will be much larger than the rate of heat liberated by the chemical reaction of the small volume of gas on the periphery of the flame where the reaction takes place. In order for the flame to propagate the enthalpy of the burned gas contained within the sphere must be large enough to provide the heat required to promote the reaction and balance the heat lost from the flame surface. Eventually, the flame radius will grow large enough to where the volume of gas contained within has enough energy to support the reaction; this is known as the critical flame radius, or the radius below which a self-propagating flame cannot exist. However, in order for a flame to get to reach the critical radius the spark must raise the enthalpy of the gas so high that the added energy allows the burned gas temperature to remain above the adiabatic flame temperature as the subcritical flame cools and grows to the diameter of a steadily propagating spherical flame. This excess enthalpy is a component of the required ignition energy. When the flame is confined in a sub-critical volume this excess enthalpy requirement is never relaxed and with the exception of an adiabatic wall heat in excess of the minimum required to ignite the mixture must be provided to the reactants in order to stabilize the flame.

In this regard, different small scale-combustion schemes are often characterized by the technique employed to overcome thermal quenching. Wu et al. [12] utilized asymmetric ‘‘whirl’’ whereby recirculating flow act as a source of enthalpy and radical species to stabilize flames in geometries close to the quenching distance. Developed as a precursor to a mesoscale thruster the H2/air ‘‘whirl’’ combustor demonstrates relatively high characteristic velocity (C*) efficiency ratios, which is defined as the ratio of hot

flow C* efficiency to cold flow C* efficiency, indicating high combustion efficiency. Characteristic velocity represents the exhaust velocity of a converging nozzle with a thrust coefficient of one, and is hence related to the enthalpy of the exhaust gas. Additionally, the lack of heat exchangers for heat transfer between products and reactants makes for small overall geometries; however, the combustor characteristic length is larger than the quenching distance at standard conditions. Ahn et al. [13] used Pt catalysts to provide a reaction pathway with decreased activation energy, which increased the amount of heat loss the system could tolerate prior to thermal quenching. The use of catalysts is shown to broaden the extinction regime in the low Reynolds number (low heat load) direction and with low chamber temperatures. Sher et al. [14] computationally explored the limits of Homogenous Charge Compression Ignition (HCCI) as a means to miniaturize micro-internal combustion engines. HCCI involves the homogenous reaction of a charge when it is compressed and is not subject to the limitations of normal flame propagation. In these devices the limitations are imposed by frictional losses, charge leakage through the piston cylinder gap, and timing problems. Several researchers have used structural conduction as a means to preheat the incoming reactants without dilution, thus enabling combustion in ‘‘sub-quenching’’ dimensions.[13,15,16] Sub-quenching is defined as any space where the smallest dimension is less than the quenching distance with the reactants and wall held at ambient conditions. The predominant example is the heat recirculating or ‘‘swiss-roll’’ combustor, which utilizes a spiral countercurrent heat exchanger to preheat the incoming reactants; the spiral is situated such that the reactants are always outside the products. The concept is a meso-scale adaptation of the large-scale heat recirculating combustors studied by Jones et al. [19] who used this device to burn fuels of low energy

content and extend the lean flammability limits of conventional fuels. The cause for this extension of the extinction regime is discussed below.

As stated above, with regards to critical times scales within the combustion chamber the time required for chemical reaction must be equal to or greater than the amount of time the mixture stays in the combustion chamber. If the residence time is smaller than the chemical time the flame will get pushed out of the combustion chamber, if the residence time is larger than the reaction time the flame may propagate upstream of the combustion chamber and quench in the inlet region. In the case of small scale combustors, low velocity extinction limit is often due to the onset of thermal quenching of the reaction, or blow off of the flame when heat loss from the reaction zone cools the reactor to the point where the characteristic reaction time to fall below the residence time. Due to the small combustor dimensions the Reynolds number will be low (laminar to transitional) and the residence times small and hence the flame will not benefit from the added reaction rate gained from turbulent combustion. High reaction rates (low chemical times) can be achieved by ensuring high combustion temperatures, reducing heat loss from the combustion chamber, preventing radical depletion at the wall, increasing the reactant temperature, using near stoichiometry mixtures, and using highly energetic fuels. [11]

Since the Reynolds numbers are low mixing of non-premixed reactants will be largely via molecular diffusion, and although the small dimensions of meso- and micro-combustors aids in reducing the mixing time the low residence times may be insufficient for complete mixing. For example, a gaseous fuel air mixture flowing through a .5mm channel will have a diffusion time will be on the order of 0.2 sec. Whereas if the flow

velocity is on the order of 1m/s, 25mm of channel is required to ensure complete mixing. [11] Enhanced mixing may be achieved through dynamic approaches such as flow instabilities, ultrasound, etc. although fabrication complexities make these options difficult. If the fuel is a liquid there is an additional requirement that the fuel be vaporized in addition to mixed with the oxidizer. The time required for mixing may be large compared to residence time, especially if spray atomization is used; this complexity is in addition to the small droplet sizes required to ensure vaporization as per the d^2 relationship for droplet vaporization. Alternatives to spray combustion include both pre vaporization using porous media and liquid film combustion. In the former, the liquid fuel is passed through a porous heat recuperator which receives heat either directly from the flame or through structural conduction with the combustor. In the latter, a liquid fuel film is formed on the combustor walls, this aids in two ways. First the wall temperature does not exceed the volatilization temperature of the fuel, since any energy added to the wall goes into vaporizing more fuel. Second, since the fuel vaporizes from the wall surface there is a substantial standoff distance between the flame and the wall, since the fuel must vaporize and mix prior to burning. This inhibits the reaction quenching effects of the wall via both active species loss and heat.

Section 5 Research Goals

The following lists the research goals providing the foundation for the material presented in this thesis: based on the motivation, background, and practical needs presented above:

- Develop a mesoscale thrust chamber capable of producing mN levels of thrust at moderate Isp (~150s), assembly volume should be on the order of a few cm3
- Utilize the heat recirculating "Swiss-Roll" geometry as the basis for the thrust chamber
- Adapt the geometry for use with Hydrogen peroxide decomposition products as an oxidizer source (Steam +oxygen) where the fuel and oxidizer are injected separately
- Integrate the thrust chamber with a catalytic hydrogen peroxide driven gas generator for bi-propellant operation

Section 6 References

[1]Wertz, J. *Reducing Space Mission Cost*. Boston: Kluwer Academic Publishers, 1996.

[2]Bonafacio, S. "Analysis and Design of a Multi-phase Catalytic Reactor for the Decomposition of Hydrogen Peroxide in Space Propulsive Systems". PhD Dissertation, Universita degli Studi di Napoli "Federico II"..Web. 2006

[3]Baker, A., Curiel, A., Schaffner, J., and Sweeting, M.""You can get there from here": Advanced Low Cost Propulsion Concepts for Small Satellites beyond LEO." *ACTA ASTRONAUTICA*. 57. (2005): 288-301.

[4]Stokes, P.R. "Hydrogen Peroxide for Propulsion and Power." Science Museum of London. London, Jan 14, 1998. Address.

[5]. Scharlemann. C., Schiebel., M, Marhold, K., Tajmar, M., Miotti, P., Kappenstain, C., Batonneau, Y., Brahmi, R., "Development and Test of a Miniature Hydrogen Peroxide Monopropellant Thruster". 42 AIAA/ASME/ASEE Joint Propulsion Conference and Exhibit. Sacramento California. July 2006.

[6]. Musker, A. Roberts, G., Ford, S., Reakes, E., Westbury, T. "Auto-Ignition of Fuels Using Highly Stabilized Hydrogen Peroxide." AIAA Paper 2005-4454, 19 Oct. 2007.

[7]. Ventura, M.C. “Advancements in High Concentration Hydrogen Peroxide Catalyst Beds.” AIAA Paper 01-3250, July 2001

[8]. An, S., Lim, H. and Kwon, S., “Hydrogen Peroxide Thruster Module for Microsatellites with Platinum Supported by Alumina as Catalyst”.

[9]. Zhou, X. Hitt, D.L. “One Dimensional Modeling of Catalyzed H2O2 Decomposition in Micro-Channel Flows”.

[10]. Schumb, Walter. “Hydrogen Peroxide”Reinhold Publishing Company New York, New York. 1955

[11]. Fernandez-Pello, A.C, “Micro-Power Generation using Combustion: issues and approaches” 29th Int. Symposium on Combustion, The Combustion Institute, Pittsburgh, PA, 2002, pp. 1–45

[12] Wu, M., Wang, Y., Yang, V., and Yetter, R.A., “Combustion in Meso-Scale Vortex Chambers,” *Proceedings of the Combustion Institute,* Vol. 31, Issue 2, Jan. 2007, pp.3235-3242.

[13] Ahn, J., Eastwood, C., Sitzki, L., and Ronney, P.D., “Gas Phase and Catalytic Combustion in Heat Recirculating Burners,” *Proceedings of the Combustion Institute,* Vol. 29, Issue 7, 2002, pp.957-963.

[14] Sher, I., Levinson-Sher, D., and Sher, E., “Miniaturization Limitations of HCCI Internal Combustion Engines,” *Applied Thermal Engineering*, Vol. 29, Issues 2-3, Feb. 2009, pp. 400-411.

[15] Vijayan, V. and Gupta, A.K., "Combustion and Heat Transfer at Meso Scale with Thermal Energy Recirculation," *47 AIAA Aerospace Sciences Meeting, January 5-8, 2009*.

[16] Kim, N., Aizumi, S., Yokomari, T., Kato., S., Fujimori, T. and Maruta, K., “Development and Scale Effects of Small Swiss Roll Combustors,” *Proceedings of the Combustion Institute*, Vol. 31, 2007, pp. 3243-3250.

[17] Jones, A.R., Lloyd, S.A., and Weinberg, F.J., “Combustion in Heat Exchangers,” *Proceedings of the Royal Society of London. Series A, Mathematical and Physical Sciences,* Vol. 60, 1978, pp.97-115.

Chapter 2: Literature Review

Micro and mesoscale combustion has gained much interest largely because of the rapid development of MEMS technology and the need to provide power to microscale systems.[1] This is further compounded with the desire to replace batteries with hydrocarbon based fuels due to their higher energy density and to provide portable power. Even at 10% energy conversion efficiency hydrocarbon fuels can provide 10 times the energy density of the most advanced batteries.[2] Note that this argument is made by considering only the specific energy of the fuel consumed as opposed to the mass of the entire combustion system (i.e., tankage, lines, flow control, combustor). Power systems in development include the miniaturization of Brayton and Rankine cycle engines and the development of both thermoelectric and thermophotovoltaic generators utilizing gas phase and catalytic combustion as a heat source. The promise lies in overall power densities that are substantially larger than their marcoscale counterparts.[1] Potential applications include: future electronics, remote sensors, aerial vehicles, portable battlefield power, and Divert and Attitude Control Systems (DACS) for small satellites.

With regards to scale, combustion length scales can generally be broken into three categories macro, meso, and micro-scale. Macro-scale covers systems where the characteristic geometry is larger than 1.0 cm., meso-scale covers systems where the characteristic dimensions are between 1.0cm. and 1.0mm., and micro-scale covers systems where the characteristic dimension is less than 1.0mm. It is important to note that the association of a particular scale to a system depends on the minimum length scale that substantially affects the dynamics of the flame and not the overall size of the device.

As will be seen later a meso-scale combustion system is typically larger than meso-scale in overall size.

Regardless of the application, developing a combustor capable of burning fuels/propellant at the meso-scale requires careful attention to scaling problems associated with combustion. The principle challenge is overcoming the adverse effects of heat loss due to large surface area to volume ratios (heat loss to heat generation). When the latter is approximately one or greater the combustion reaction cannot propagate. In this regard, different small scale-combustion schemes are characterized by the technique employed to overcome thermal quenching. Some successful schemes include the recirculation of active species and heat through asymmetric whirl[3], reduction of the activation energy through the use of catalysts[4], Homogenous Charge Compression Ignition (HCCI)[5], and heat recirculation[6]. The use of heat recirculation for sub-quenching flames is a meso-scale adaptation of the large-scale heat recirculating combustors studied by *Jones, Lloyd, and Weinberg*[6] . The focus of their studies was to burn fuels with low energy content and extend the lean flammability limits of conventional fuels. This enhancement in flammability limits provide heat recirculating combustors with the flexibility to be used as either for power generation or thrust production depending on the conditions of operation and geometry. This review is primarily focused on experimental work that has been conducted on heat-recirculating "Swiss-Roll" combustors as well as the impact of geometry, materials, catalysts, and scale on the thermal performance, extinction criteria/regimes, and flame dynamics. Additionally, an overview of meso-scale power systems is provided covering both propulsion and electric power generation.

Section 1 Thermal Performance, Flame Extinction, and Flame Dynamics

Experiments carried out to determine the thermal performance and extinction criteria of meso-scale heat recirculating combustors have largely been focused on the effects of the following combustor characteristics: the effect of scale both in terms of heat exchanger geometry (channel width, number of turns, and the wall thickness) and combustion volume, the effect of catalyst on the heat loss induced extinction criteria, and the effect of material and its contribution to overall wall conductance. The following sections will discuss some experimental efforts to qualify and quantify these effects; however, they will be preceded by a general discussion of extinction phenomenon and global thermal performance characteristic of heat recirculating meso-combustors.

Extinction regimes for heat recirculating combustors typically exhibit dual branched characteristics with extinction occurring at both high and low Reynolds numbers for a given fuel flow rate. Extinction regimes for "Swiss-roll" type meso-combustors are shown below, in Figure 2.1, as reported by both *Vijayan and Gupta*[7], similar results have been presented by *Oh, Huh, Ahn, and Ronney*[8] for a similar geometrical configuration.

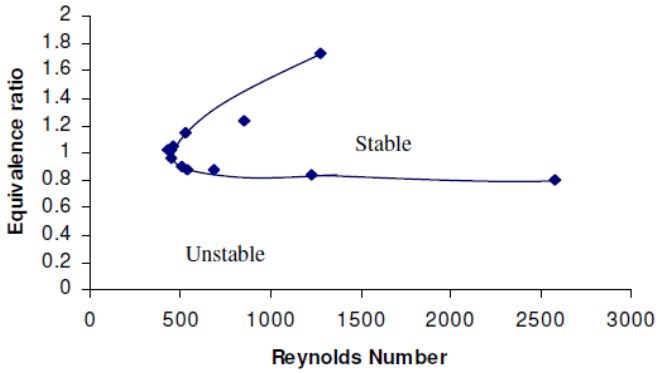

Figure 2.1. Extinction regime for premixed propane/air in a zirconium phosphate meso-combustor

The high Reynolds number (Re), high mass flow rate, limit is a flame "blow off" limit where the velocity of the incoming reactants is larger than the flame propagation velocity and the flame is pushed out of the combustion volume. This is a characteristic of premixed combustion systems and is not unique to the meso-scale. The influence of flame propagation at the meso-scale becomes more apparent at the low Reynolds number extinction limit where small rates of heat release are coupled with high heat losses to induce extinction. The heat loss driven limit may occur as a consequence of thermal quenching, whereby the rate of heat lost from the combustion volume approximately balances the rate of heat liberation by chemical reaction[9], alternately a second "blow-off" limit is possible at low Re whereby the combustion volume cools to the point where the flame velocity is lower than the incoming flow velocity. The second mode of low Re extinction is especially important for premixed meso-combustors where the small geometries render high flow velocities even at low Re and hot combustor walls inhibit thermal quenching. It is important to note that the heat lost from the combustion chamber is only weakly dependent on Re, since heat losses are driven by temperature gradients, however it is highly dependent on equivalence ratio. Conversely, the rate of heat release is dependent on both Re and equivalence ratio, since it is proportional to the mass of fuel consumed. For this reason if the low Re extinction mode is by thermal quenching than the extinction limit should be dependent on both Re and equivalence ratio (ratio of heat liberated to heat lost), however if the extinction is a result of low Re blow off then the extinction limit should be roughly independent of Re and dependent on equivalence ratio. It is important to note that in some cases the combination of high preheat temperatures and premixed reactants lead to the flame flashing-back to the burner inlet.[8]

Vijayan and Gupta[10,11] conducted several studies on the global thermal performance of ceramic heat recirculating burners burning both propane/air and methanol/air by a semi-empirical method by using thermocouples to measure the exhaust temperature and equilibrium exhaust gas properties to determine the global ratios of heat output/heat input, heat output/heat load, heat loss/heat input and heat loss/heat load. Figure 2.2 shows exhaust and pre-heat temperatures for several fuel flow rates (heat loads).[10] Note that the heat load is calculated based on complete consumption of the limiting reactant.

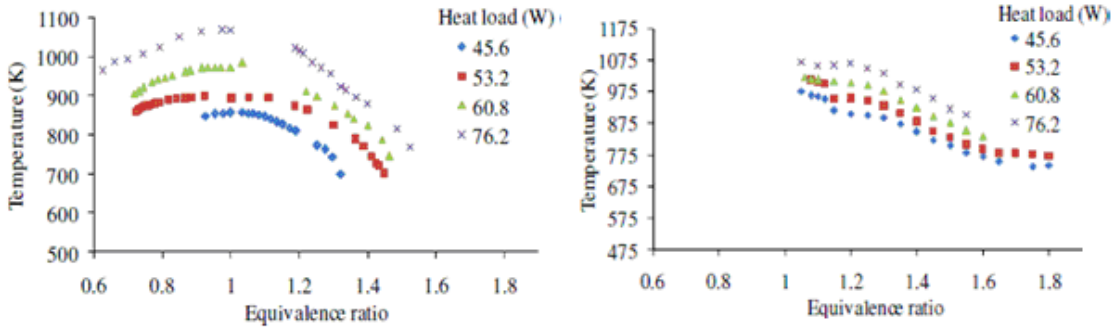

Figure 2.2..Exhaust and preheat temperatures for heat recirculating "Swiss-roll" combustors burning propane/air. 10

Figure 2.2 (left) shows the variation in preheat temperature with equivalence ratio at constant fuel flow rate (heat load). The preheat temperature increases with decrease in equivalence ratio since the amount of fuel consumed and hence the heat released increases with decrease in equivalence ratio. As the mixture is made fuel lean the preheat temperatures decreases since the fixed heat release is made to heat up a larger amount of air. Exhaust temperatures (right) increase monotonically with decrease in equivalence ratio. This is contrary to the flame temperature which decreases on both sides of stoichiometric condition. If the objective is to utilize the enthalpy of the exhaust to do

work than the global effect of this behavior is to provide the highest efficiency close to the lean stability limit. However, if the objective is to utilize the heat lost through the reactor walls than the most efficient mode of operation is close to the rich stability limit. Figure 2.3, shows both the enthalpy of the exhaust/heat load for varying heat loads.[10]

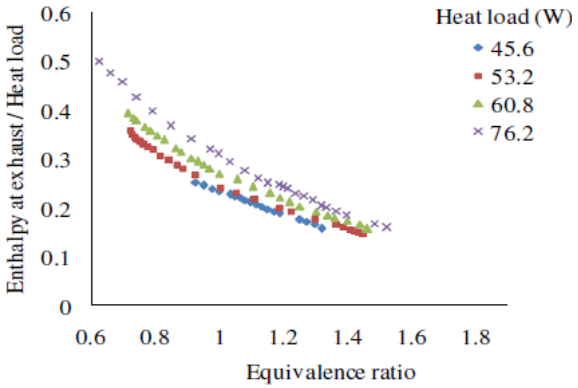

Figure 2.3. Normalized output power (thermal efficiency) vs. equivalence ratio at various heat loads (with propane fuel) [10]

Section 2 Geometry and Scale Effects

Geometry and scale effects on the performance of both "Swiss-Roll" and "Flat-type" countercurrent combustor geometries have been studied by *Oh, Huh, Ahn, and Ronney*[12], *Lee, Cho, Choi, and Kim*[13], and *Lee and Kim*[14] , *Vijayan and Gupta*[15], and *Kim, Kato, kataoka, Yokomiru, Maruyama, Fujimori, and Maruta*[16]. Ronney et. al[12] studied the effect of scale on both the gas phase and catalytic combustion of propane/air in combustors of the "Swiss-roll" configuration having 3.5 turns and fabricated from titanium-811 alloy sheets wrapped into a rectangular spiral. Three combustors with the same channel width and constant varying wall thickness (0.25mm, 0.5mm, and 1.0mm) were fabricated to

asses the impact of wall conductance on extinction, and a fourth combustor with a wall thickness of 0.25mm and at half the scale was constructed to asses the applicability of Damkholer number as opposed to Reynolds number as the appropriate criterion for extinction. Catalysis is provided by a Pt foil catalyst placed along the walls of the central combustion volume. The top and bottom of the reactors were sealed with approximately 6 mm of fibrous ceramic blanket, backed by 6 mm aluminum plates and secured with ceramic adhesive. Figure 2.4 shows schematics of both the "full-scale" and "half-scale" combustors.[12]

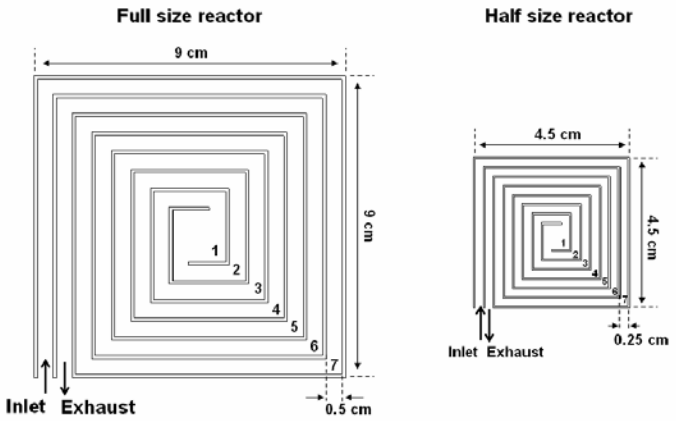

Figure 2.4. Full-scale and half-scale "Swiss-roll" combustors the numbers 1-7 represent thermocouple locations within the combustor

Figure 2.5 shows the extinction regimes of both the "full-scale" and "half-scale" combustors both with and without catalyst.[12] As cited by the authors the extinction regimes were determined by starting from a steady burning state and decreasing or increasing the fuel concentration (holding Re fixed) or increasing or decreasing Re (holding the fuel concentration fixed) until steady-state operation ceased and burner temperatures decayed to ambient. These limits were found to be independent of the path

in mixture – Reynolds number space used to reach the limit, thus no hysteresis was found.

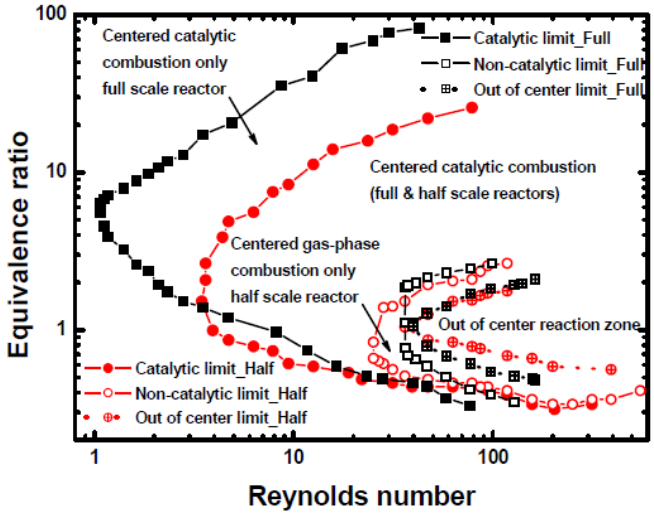

Figure 2.5.Extinction regimes for gas phase and catalytic combustion of propane and air for both the full and half scale combustors, note that the full-scale combustor has a wall thickness of .5mm while the half-scale combustor has a wall thickness of .25mm.[12]

Analysis of scale effects was carried out by considering the minimum Reynolds number that could support combustion, both in the gas phase and with catalysis. The minimum Re that could support combustion in the full-scale reactor with and without catalysis was 0.9 and 36 respectively. Likewise for the half scale reactor the minimum Re to support combustion were 3.5 and 25 for catalytic and gas phase combustion, respectively. For combustion with catalysis the extinction regime for the half-scale reactor shifted towards higher Reynolds numbers as mentioned above, however for gas phase combustion the smaller reactor was able to support a flame at lower Re than its larger counterpart, due to its smaller size. The authors note that the difference between the minimum stable Re for catalytic and gas phase combustion decreases as the reactor size decreases indicating that at sufficiently small size the marginal benefit of catalysis

may become negligible. Although not related to scale effects it is notable that that the reaction does not always occur inside the combustion space, this is labeled as "out of center reaction zone" in the figure, since the mixture is pre-mixed flame propagation upstream of the reaction zone is possible given the appropriate conditions.

Differences in the thermal performance of the half scale and full scale reactors were also addressed by measuring the maximum temperature measured inside the combustion chamber using thermocouple. Figure 2.6 shows the maximum temperatures at the lean extinction limit for both gas phase and catalytic combustion for both the half scale and full scale reactors.[12]

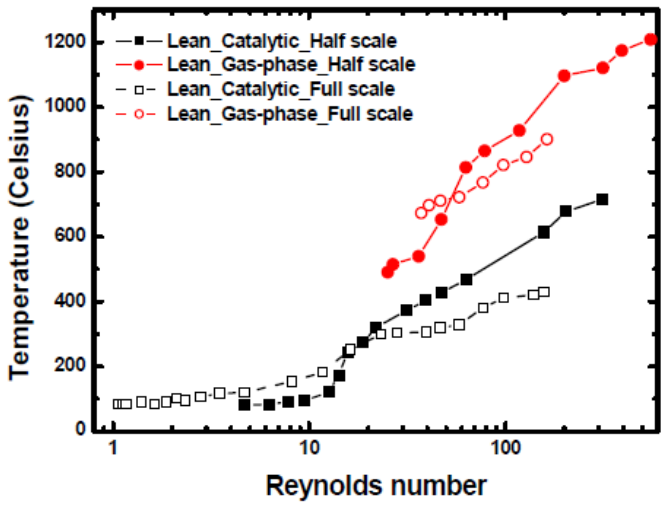

Figure 2.6. Maximum temperatures at the lean extinction limit for both gas phase and catalytic combustion for both the half scale and full scale reactors. [10]

Although not related to a discussion of scale the authors note that the minimum temperature measured in the reactor was 55°C at a Re of 0.9 for the full-scale reactor. Overall gas phase combustion yielded substantially higher temperatures than heterogeneous catalytic combustion. With both geometries at higher Reynolds numbers

the half-scale reactor demonstrated higher temperatures for both catalytic and gas phase combustion while the opposite trend was observed at lower Re.

As mentioned previously the effect of wall thickness was also addressed in three full scale reactors with varying wall thickness. Figure 2.7 shows the effect of wall thickness on the extinction regimes for both gas phase and catalytic combustion.[12] The results show that reducing the wall thickness allows for the combustion of weaker mixtures (for catalytic combustion); this is in agreement with theoretical analysis which showed that reducing the wall thermal conductance should increase the performance at low Re.[17] It should also be noted that for gas phase combustion varying the wall thickness has no appreciable effect on the minimum Re, however it does have an effect on the equivalence ratio at the minimum Re. This can be explained by considering that the reaction rate and hence Damkohler number (Da) are effected by the maximum temperature achieved in the chamber which is only weakly dependent on Re. Hence the heat loss from the combustion zone is not strongly dependent on Re, however it is dependent on both geometry and equivalence ratio (temperature). This is why the extinction criteria for gas phase combustion is independent of Re but dependent on equivalence ratio.

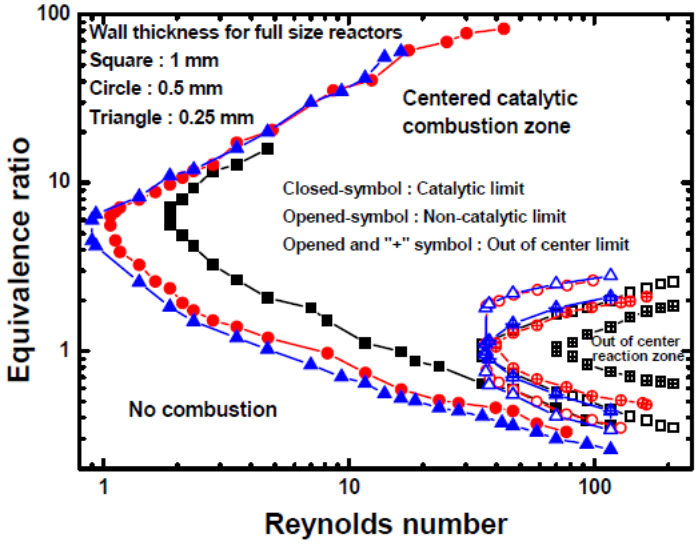

Figure 2.7. Extinction regimes for reactors with varying wall thickness[12]

Kim et. al.[13] studied the effects of wall thickness combustion space size and scale on heat recirculating combustors of the countercurrent type burning methane/air. However they avoided the use of spirals because they are difficult to fabricate and difficult to treat analytically. Alternately, a "flat-type" or "one-dimensional" heat recirculating combustor was designed to study the effects of design parameters on flame stabilization, and the effects of scale down on stabilization and performance through measurements of the surface temperatures and exhaust gas composition. A schematic of the combustor along with a photo showing the relevant dimensions is shown in Figure 2.8[13]. In Figure 2.8, u is the upstream channel gap, d is the downstream channel gap, w is the wall thickness and h is the combustion space height.

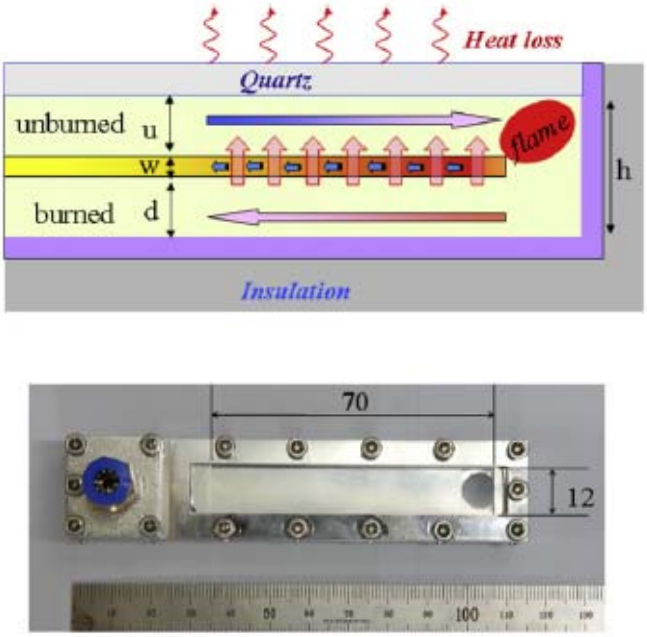

Figure 2.8.Configuration parameters and a direct photo of the baseline combustor[13]

This combustor demonstrated a number of flame modes, some of which involve flame propagation in both the upstream and downstream channels. In order to determine the effect of wall thickness the up steam and downstream channel widths were maintained at 1.1mm., which is less than half of the ordinary quenching distance for methane and air. Figure 2.9[13] shows the stability margins for four combustors, the naming conventions for the combustors are as follows: 'BSw05u11d11' is a base scale stainless steel combustor with a wall thickness of 0.5mm an upstream channel width of 1.1mm and a downstream channel width of 1.1mm.

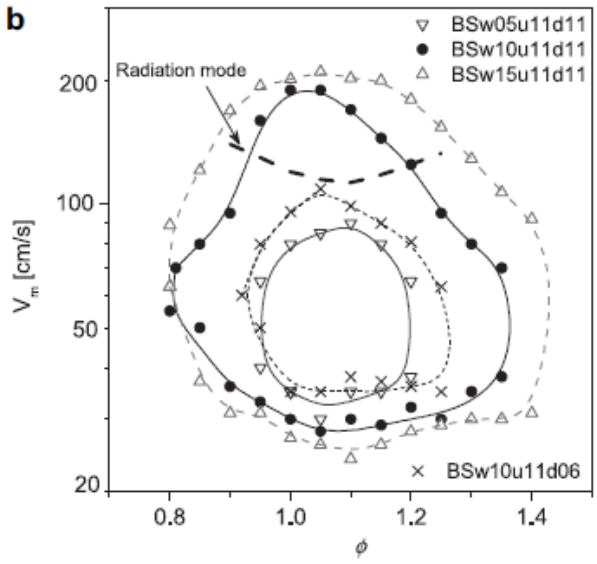

Figure 2.9.Effect of wall thickness on flame stabilization in the combustion space[13]

Considering the cases of 'BSw05u11d11', 'BSw10u11d11', and 'BSw15u11d11' reducing the wall thickness from 1.5-0.05mm resulted in narrowing of the flame stability margins. This is counterintuitive since heat transfer between two channels with a finite temperature difference is inversely proportional to the thickness of the middle wall. An explanation for this behavior is provided by the flame dynamics of the 'BSw10u11d11', and 'BSw15u11d11' combustors, that is, the combustors with larger wall thickness. It was observed that the middle wall glows due to heat feedback from the flame, this radiation helped to heat the incoming reactants thereby increasing the net heat recirculation. It is important to note that the flame anchoring characteristics that allow the flame to sit close to the wall, thereby heating it, come from both the thermal and hydrodynamic characteristics of the combustor. CFD results obtained using FLUENT for non-reacting flow were used to qualitatively asses the impact of wall thickness on flame stabilization. Results showed that as the wall thickness was increased a recirculation

zone formed at the tip of the wall which may contribute to flame holding at this location. The CFD results are shown in Figure 2.10[13].

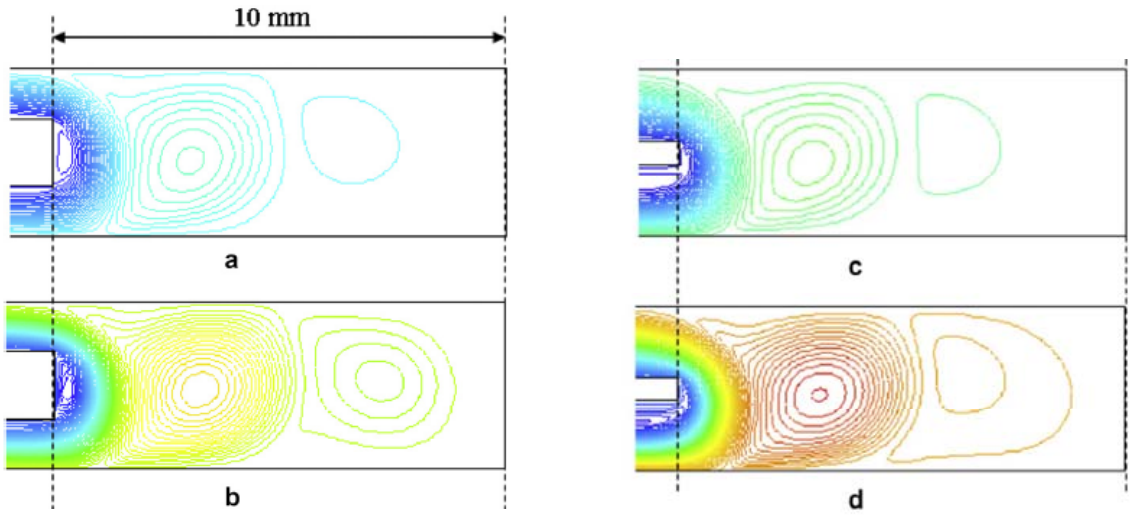

Figure 2.10.Schematics of the cold flow field at a mean temperature of 900 K:'BSw15u11d11': (a) Vm ¼ 100 cm/s, (b) Vm ¼ 300 cm/s, 'BSw05u16d16': (c) Vm ¼ 100 cm/s, (d) Vm ¼ 300 cm/s.[13]

Vijayan and Gupta[15] examined the effects of scale on the heat exchanger geometry of "Swiss-Roll" combustors burning propane/air and having heat exchangers of different lengths. Three combustors were fabricated from zirconium phosphate my means of standard machine tools on a CNC vertical mill. Zirconium phosphate (having thermal conductivity of 0.8 W/m-K) was chosen in order to minimize back plane (normal) heat losses. The combustor geometries considered are shown in Figure 2.11 along with the heat exchanger lengths normalized by the channel width.[15]

Combustor	Length of inlet channel	Length of outlet channel	Total length
A	19.3	8.1	27.4
B	36	19.2	55.2
C	70.4	45.2	115.6

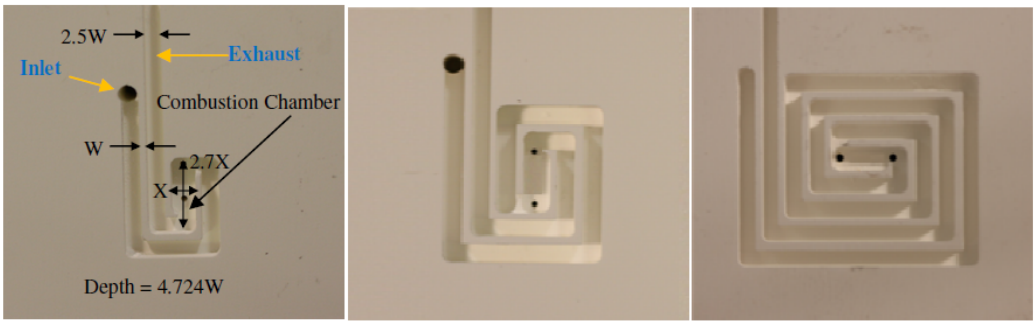

Figure 2.11.Combustor geometries investigated for (a) Combustor A, (b) Combustor B, and (c) Combustor C[15]

It is important to note that the width of the spiral channels was smaller than the quenching distance for a propane/air premixed flame at normal state conditions. A quartz window was used to provide optical access to the combustor. Figure 2.12 shows the flammability regimes for combustors A, B and C, respectively.[15]

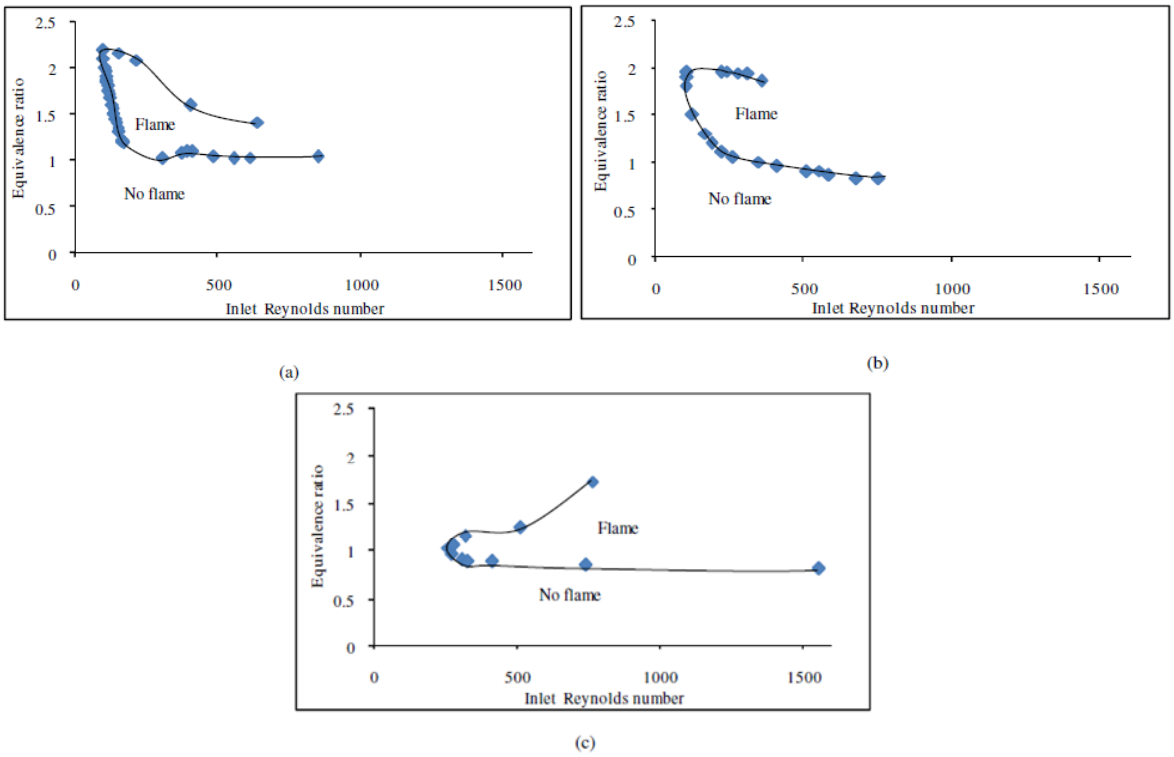

Figure 2.12. Flammability map of the combustors for (a) Combustor A, (b) Combustor B, and (c) Combustor C. Here the Reynolds number is calculated at the inlet using inlet hydraulic diameter[15]

The effect on channel length on the flammability limits of the combustor is apparent in both the lean and rich flammability limits. Combustor A (shortest channel length) was not able to support combustion at lean equivalence ratios (and hence the lean limit is rich of stoichiometric condition), this is because the amount of preheating is not sufficient to overcome heat losses at the lean conditions. This was not the case with combustors B and C which were able to support fuel lean combustion, due to the higher degrees of preheating. Additionally, decrease in the channel length allowed for the combustion to occur at lower inlet Reynolds numbers (which were calculated based on the inlet hydraulic diameter). This is because the lower amounts of preheating renders lower inlet temperatures to the combustion volume and supports flames with lower burning velocity.

For this reason combustors A and B were able to support flames at much lower inlet velocity than combustor C (0.66m/s and 0.68m/s as compared to 1.78m/s, respectively). Additionally, it was observed that the flammability regime for combustor C narrows dramatically at low Reynolds numbers while that for combustors A, and B the flammability regimes at low Reynolds numbers are relatively broad.

The thermal performance was evaluated by determining the exhaust enthalpy flow rate and normalizing based on the heat load. The former is based on the measured exhaust temperature and isobaric equilibrium combustion products and the latter is based on the Lower Heating Value (LHV) of the fuel assuming complete consumption of the limiting reactant. Figure 2.13 shows the enthalpy at the exit/heat load for the three combustors.[15]

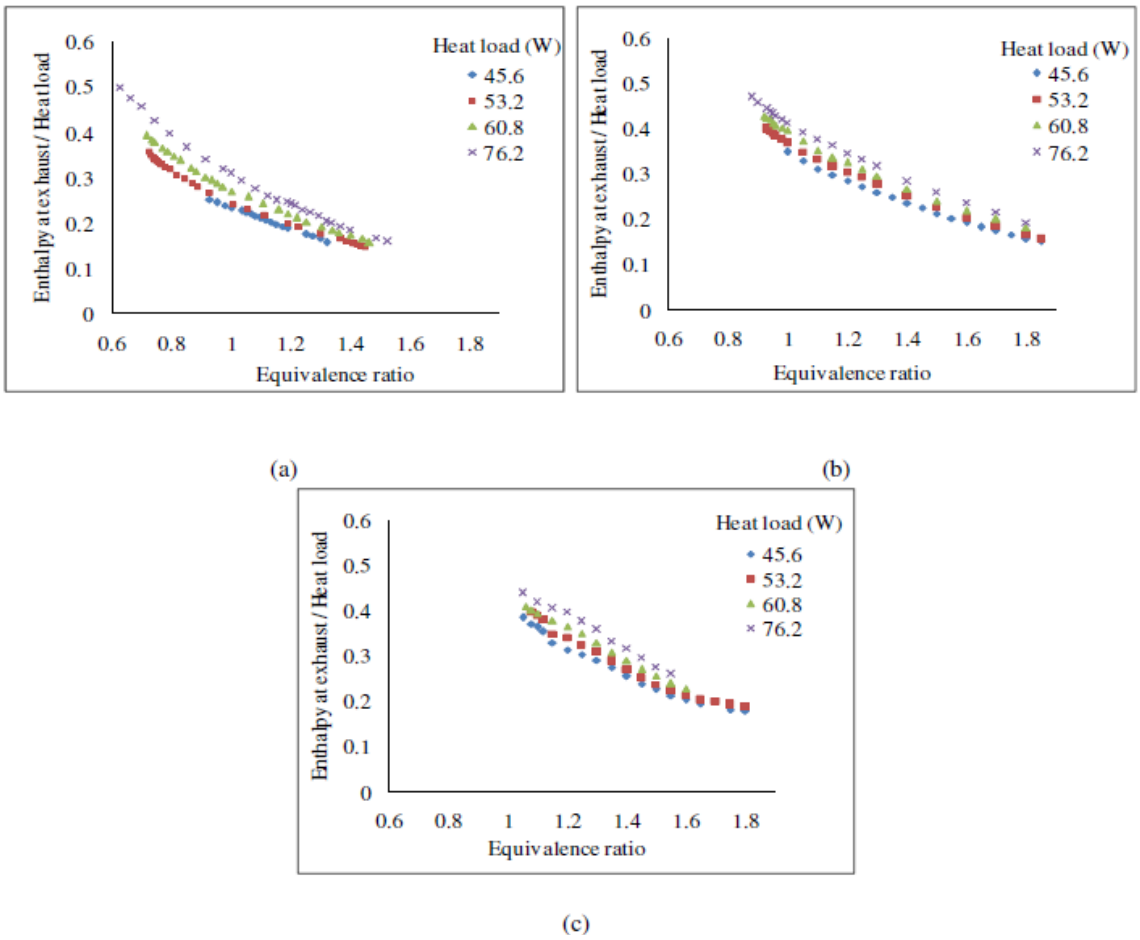

Figure 2.13.Normalized output power (thermal efficiency) vs. equivalence ratio at various heat loads (propane flow rates) for (a) Combustor A, (b) Combustor B, and (c) Combustor C[15]

Figure 2.13 shows that the thermal efficiencies were higher for higher heat loads at a given equivalence ratio and in general varied between 15% and 50%.[15] Considering only the range of equivalence ratios that could support stable combustion in combustor A, combustor A demonstrated the highest efficiencies. This is because the exhaust temperatures are higher for combustors with shorter inlet channels since they have the lowest outer wall surface area for available for heat loss. However, since combustor C could support fuel lean flames the thermal efficiency is higher than that of combustors A

and B in the lean regime. This is because the exhaust temperature increases monotonically in the fuel lean direction.

It is also notable that the high preheat temperatures measured in combustor C lead to flame instabilities that do not present themselves in combustors A and B. High preheat temperatures (>1000K) lead to pre-ignition of the mixture upstream of the combustion volume leading to oscillation of the flame between the combustion chamber and upstream location and significant acoustic emission.[18] No such instabilities are observed in combustors A and B due to the lower preheat temperatures (<800K and <900K, respectively).

Maruta et. al[16] studied the performance variations of Swiss-Roll combustors of various sizes and found that the mean velocities and flammable limits of the combustor varied based on the size and shape. However, the mean temperatures in the combustors were similar and were dependent largely on equivalence ratio alone. Exhaust gas analysis also showed that NO_x emissions decreased with combustor size, however CO emissions increased. The emissions of CO were mitigated by the use of catalysts as the exhaust mixture was allowed to pass through a channel filled with ceramic balls coated with Pt catalyst.

Section 3 The Effect of Catalyst

The large surface area to volume ratios of meso-combustors coupled with the high heat losses lend itself to catalytic combustion, which is an area rather than volume limited process. Additionally, the use of catalytic combustion enables the combustion of fuel at very low temperatures (~55 ^{o}C observed minimum temperature[12]) and this allows for very low level power production without waste. For example at the observed minimum

presented above, Ronney et. al.[12] demonstrated 3W of thermal energy release with near complete consumption of the fuel (propane), such a low heat release flame would be difficult to achieve with gas phase combustion. Furthermore, low temperatures allow for the use of plastics and other polymers as combustor materials from which arbitrarily complicated geometries can be manufactured from a large variety of techniques (eg. rapid prototyping, injection molding, and CNC machining to name a few). The effects of catalysis on the extinction criteria of heat recirculating burners have been reported by *Ahn, Eastwood, Stizki, and Ronney*[19], and *Lee and Kim*[14]. *Ronney et. al* [19] . They all studied the extinction criteria, temperature distributions, and exhaust gas characteristics of a 3.5 turn square spiral counter-flow "Swiss-roll" combustor burning propane/air. The burner was constructed by bending sheets of 0.5mm thick inconel-718 alloy into a 7cm by 7cm by 5cm tall burner, with each inlet and exhaust channel being 3.5mm wide. For catalysis, strips of bare Pt foil were placed along the wall of the central section of the burner and a Kanthal wire was used as a glow plug for ignition source. Figure 2.14 shows the burner configuration with thermocouple locations 1-7 with 'i' and 'e' representing inlet and exhaust, respectively.[19]

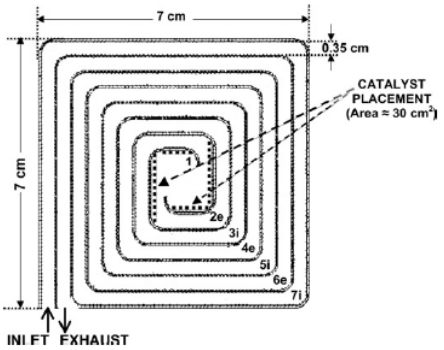

Figure 2.14. Schematic of the Swiss roll burner, Platinum catalysts are placed as shown [19]

The extinction regimes in terms of inlet Re, calculated based on the channel width and ambient conditions, are shown in Figure 2.15 along with a comparison with gas phase combustion of propane/air in the same combustor.[19]

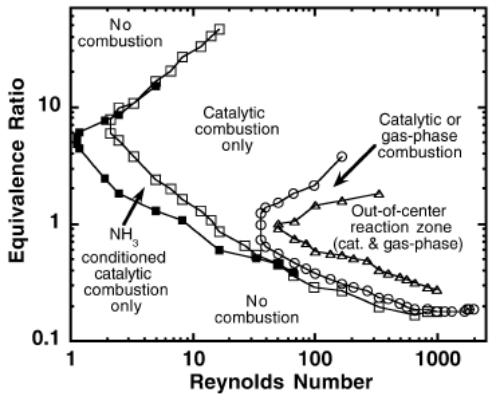

Figure 2.15. Extinction limit map for catalytic and gas phase combustion in the inconel Swiss-roll [19]

Figure 2.15 shows that both the gas phase and catalytic combustion exhibit the dual branched behavior discussed previously, however the influence of catalysis is to increase the fuel rich extinction limit dramatically and the fuel lean extinction limit only slightly. Additionally, the black symbols represent catalyst that has been treated by burning the propane/air mixture with 5% of the propane replaced by ammonia, as a reducing agent, which is beneficial at conditions with low residence time and high heat losses (low Re). At high Re (lean combustion) the extinction regimes for gas phase and catalytic combustion converge, the explanation for this is that since laminar flow prevails throughout the combustor, mass transfer to the catalyst is largely by diffusion and does not increase with Re, so that at high Re only a small fraction of the fuel can be burned catalytically. Thermal performance results show that at the lean extinction limit the maximum temperatures achieved in the burner are slightly lower for catalytic combustion

as opposed to gas phase combustion for the same inlet conditions, indicating that the use of catalysis is only applicable for conditions where gas phase combustion cannot be achieved, or conditions where extremely low power output is desirable. *Kim et. al.*[14] present work with methane and air regarding the effect of Pt wire catalysts on the extinction limits of flat-type countercurrent combustors and arrive at largely the same conclusions, with the application of catalyst affecting the rich extinction regime dramatically and the lean regime only slightly. Additionally, it was found that the use of Pt catalysts placed in an upstream channel had no effect on the extinction limits from the viewpoint of catalysis. However, the wires did contribute positively to the net heat recirculated to the reactants. This was verified by experiments conducted with Iron and Copper wires placed at the same location with the same inlet conditions and yielding the same results as Pt. It is possible however that the use of catalytic wires upstream of the combustion volume could have a beneficial effect if the gas temperature were high enough to achieve thermal pyrolysis of the fuel (>530 ^{o}C for methane). Although this temperature was never achieved in the configuration presented by the authors, other configurations readily achieve this preheat temperature, see Figure 2, and could benefit from the placement of catalyst upstream.[10]

Section 4 The Effect of Material Thermal Conductivity

Since heat losses play a dominant role in the performance of meso-scale combustors the material thermal conductivity is of critical importance in combustor design. *Vijayan and Gupta*[20,21] performed simulations to highlight the importance of material thermal conductivity and determined the range of thermal conductivities over which combustion could be supported. The results showed that heat loss from the combustion chamber was

lower for lower thermal conductivity materials with the overall heat loss being roughly independent of thermal conductivity. However, it is heat lost from the combustion chamber that promotes thermal quenching and not the overall heat loss. Lower thermal conductivity materials also have higher rates of heat recirculation to the reactants. In general, it was found that high thermal conductivity materials (>15W/mK) have roughly uniform surface temperature at steady state, indicating that they behave like a lumped body where the rate of conduction within the material is faster than the heat transfer between the material and the gas. On the other hand, low thermal conductivity materials (<15W/mK) are able to sustain huge temperature gradients across the channel walls, minimizing the heat lost from the combustion chamber and maximizing the heat recirculated to the reactants. Figure 2.16 shows the effects of thermal conductivity on heat transfer rates.[21] Note that the total heat recirculated and heat recirculated through the channel wall increases substantially at roughly 15W/mK, while the heat lost from the combustion chamber decreases substantially at 15W/mK; indicating this value as the upper limit on thermal conductivity, and limiting the range of applicable combustor materials to ceramics. Note also that this analysis applies only to monolithic combustors machined from solid blocks of material, where a high thermal conductivity pathway exists around the channel; combustors fabricated from folding sheets of metal and then sealing the top and bottom with refractory ceramics, (i.e, *Ronney et. al.*[19]), would be subject to different limiting conditions since the thermal resistance around the channel is higher.

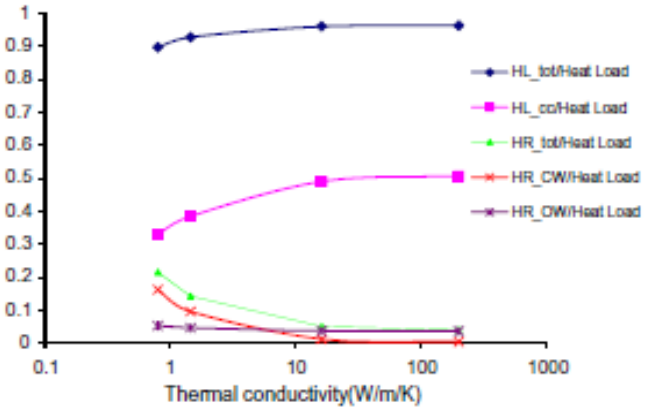

Figure 2.16. Effect of thermal conductivity on heat transfer rates for a heat load of 29W (HL_cc = rate of heat loss in the combustion chamber, HL_tot = rate of total heat loss from the combustor, HR_CW = rate of heat recirculation to the reactants throug h the channel walls, HR_OW = rate of heat recirculation to the reactants through the outer walls and HR_tot = total rate of heat recirculation to the reactants).[21]

In order to experimentally determine the effects of thermal conductivity, Vijayan and Gupta fabricated two combustor.[21] One from Macor glass ceramic (thermal conductivity of 1.46W/mK) and one from zirconium phosphate (thermal conductivity of 0.8W/mK). Extinction regimes showed that the Macor combustor was able to support flames at lower inlet Reynolds numbers, i.e, lower total mass flow rate and lower velocity, than the Zirconium Phosphate combustor. As mentioned previously decreasing the thermal conductivity increased the amount of reactant preheating, and higher preheat temperatures translated into higher flame velocities in the chamber. Since the lower thermal conductivity material delivers mixtures with higher flame velocity it was not possible to support flames at low channel velocities. Figure 2.17 shows the extinction regimes for the Macor and Zirconium phosphate combustors for propane and air.[21]

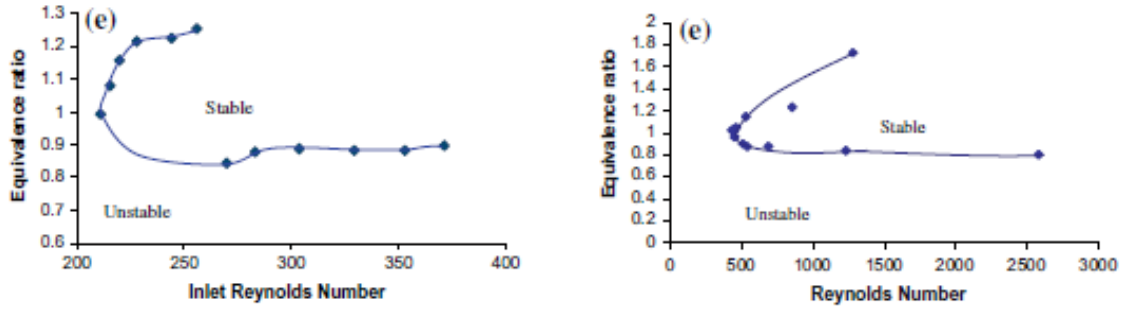

Figure 2.17.Extinction regimes for the Macor and Zirconium Phosphate combustors. Left: Macor combustor Right : Zirconium Phosphate combustor.[21]

Kim et. al.[13] experimentally tested flat-type countercurrent combustors with different materials to examine the effects on both extinction limits and flame dynamics. When comparing combustors fabricated from stainless steel and quartz it was found that the quartz combustor could support flames at slightly lower chamber velocities because the low thermal conductivity enables the temperature near the flame to remain high. The difference in low Re behavior between the flat type and spiral combustor could be attributed to differences in pre-heat temperature. Preheat temperatures in the spiral combustor were between 775-1075K whereas the preheat temperatures in the flat-type combustor were in the range of ~523-773K, which limited the effects of flame speed enhancement on extinction.

Maruta et. al.[16] studied the performance of different Swiss Roll combustor designs under various heat transfer conditions created by applying various degrees of insulation to a stainless-steel combustor (insulating all sides versus all but the top side) and changing the material that seals the combustor top surface (stainless steel or quartz). It was found that as the heat loss increased the flammable region became narrower, and higher mean velocities were required to stabilize the flame. Higher mean velocities tend

to imply higher heat release rates, which would reduce the ratio of heat loss to heat generation, although this is not explicitly stated by the authors.

Section 5 Flame Dynamics and Instability

Vijayan and Gupta[22] examined the flame dynamics and instabilities in premixed propane/air countercurrent burners through an array of diagnostic methods including temperature, high-speed imaging, chemiluminecence, and acoustic measurements. Since the combustion occurred in a confined space and was aerodynamically held by flow recirculation the flames were accompanied by significant acoustic emission. Measurements of the sound frequency distribution indicated that the natural frequencies of the reactant and product gasses in the channel were excited by fluctuations in the heat release, since only unsteady heat addition can excite standing waves. The correlation between acoustic signature and combustor geometry was made by assuming the combustor to be a square channel open on both ends with homogenous mixture composition. The composition was assumed to be of the equilibrium combustion products of propane/air, and a length weighted average temperature was used based on the inlet, preheat, chamber, and exhaust temperatures and the length of channel between those locations. These were compared to measured values of the noise accompanying the flame with reasonable agreement. It is important to note that the transient phenomenon in the combustion chamber were those exhibiting limit cycle behavior in the sense that they were self sustaining once initiated and did not lead to extinction. However, they did often lead to mechanical failure of the combustor through resonance with the combustor material. Additionally, unstable behavior was observed at conditions where the preheat

temperatures were high (>1000K), the high temperature leads to repetitive pre-ignition and quenching of the mixture in an upstream channel, leading to a pulsating flame mode.

Section 6 Summary of Fundamental Research

Experimental work in thermal performance, extinction behavior, and flame dynamics can be summarized as follows:

- Reduction in the wall thickness and in total wall conductance allows for the combustion of weaker mixtures. However, this effect can be mediated or even reversed through appropriate hydrodynamic stabilization. This means that the extinction behavior is highly dependent on both the thermal and aerodynamic characteristics of the combustion chamber
- Increase in the heat exchanger length allows for the combustion of leaner mixtures because of higher preheat temperatures but results in higher overall heat losses, since more material is in contact with the gas. Shorter heat exchanger lengths have higher exhaust temperatures and support combustion at lower Re, however, could only support combustion in rich regimes
- Catalysis extends the rich (low Re heat-loss-driven) extinction limit dramatically and the lean extinction limit only slightly. Due to the lower thermal performance of catalytic combustors compared to gas phase combustion in the same geometry they are only applicable when gas phase combustion cannot be achieved, or when low temperatures are required (for example when using thermoelectric elements or polymer combustors)
- Simulations showed that for monolithic Swiss-Roll combustors the maximum thermal conductivity that can support combustion without dramatic degradation

of thermal performance was 15W/mK. This is due to the higher rates of reactant preheating below 15W/mK and the lower rates of heat loss from the combustion chamber. This limits the applicable materials to ceramics. Note that this only applies to monolithic combustors having a high thermal conductivity pathway around the channel

- A combination of geometry and pre-heat effects lead to significant flame acoustics and flame dynamics under the right conditions, however do not lead to extinction. When the acoustic emissions from such flames resonate with the natural frequency of the combustor catastrophic mechanical failure (cracking) does occur.

Section 7 Micro-Power Generation

In order for micro and meso-scale combustion systems to become viable it is necessary to convert the thermal output from the combustor into to useful electrical or kinetic energy. This undoubtedly requires some downstream energy conversion scheme. A schematic layout of the various elements of a generalized micro combustor package is shown in Figure 2.18[23].

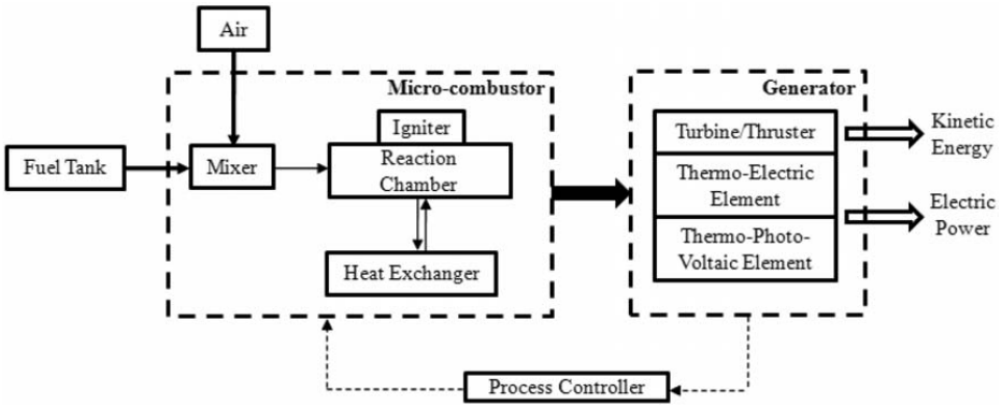

Figure 2.18.Flow diagram of a generic micro-power generation system[23]

In the following overview devices pertaining to the use of a micro-combustor for power or thrust generation will be discussed categorically in terms of those pertaining to propulsion and those pertaining to electricity generation.

Micro Propulsion

Currently, micro-air and space vehicles rely largely on battery power for providing propulsive force. However, a number of patents have recently been awarded for propulsion devices utilizing micro-combustors. *Epstein, Senturia, Waitz, Lang, Jacobson, Ehrich, Schmidt, Ananthasuresh, Spearing, Breuer and Nagle*[24] patented an invention relating to the generation of combined electrical and shaft power from a micro-turbine and micro-combustor in a Brayton cycle type arrangement. A schematic diagram along with a photograph of the micro-machined turbine and stator blades is shown in Figure 2.19. The centrifugal compressor and radial turbine rotor had diameters of 8 mm and 6 mm, respectively. The compressor discharge air wraps around the outside of the combustor to cool the combustor walls, capturing the waste heat and thus increasing the combustor efficiency while reducing the external package temperature. The rotor was supported on a journal bearing on the periphery of the compressor and/or turbine and by thrust bearings on the rotor centerline. All the components were fabricated using MEMS manufacturing techniques and represent the state of the art in micro fabrication. This is represent one of the major contributions of the development along with demonstration of long term operation of a Silicon based micro-combustor burning hydrogen and air[25] and hydrocarbon mixtures and the operation of the turbine at over 1.3 million RPM's on air bearings[26].

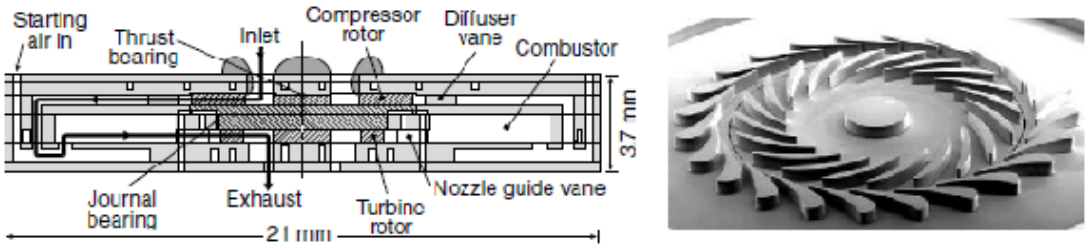

Figure 2.19.MIT micro-turbine schematic and SEM Image.[26]

Youngner[27] patented an invention by which thrust was produced from the combustion of solid propellants in a micro-machined enclosure and the high temperature high pressure gas was expelled through a micro-nozzle. A schematic and photograph of the device are shown in Figure 2.20[28], below. The novel approach eliminates the need for external propellant storage and management, namely tanks and valves. However, the consequence was a single shot thruster incapable of reuse. Several fabrication techniques have been used to assemble the thruster assemblies which were comprised of three individual components and no moving parts. The top layer consists of a silicon nitride burst diaphragm and nozzle which was fabricated by anisotropic KOH wet etching of a silicon wafer. The second layer was the combustion chamber formed from through-holes HF etched into FOTURAN photosensitive glass; the chambers were loaded with lead styphnate propellant based on the required impulse bit. The bottom layer consists of a matching array of polysilicon micro resistors which acted as igniters.[28] When power was applied to the polysilicon resistors the lead styphnate propellant was heated to its auto ignition temperature (543°K[23]). The combustion increased the pressure until the burst diaphragm ruptured and the gas was expelled through the nozzle.

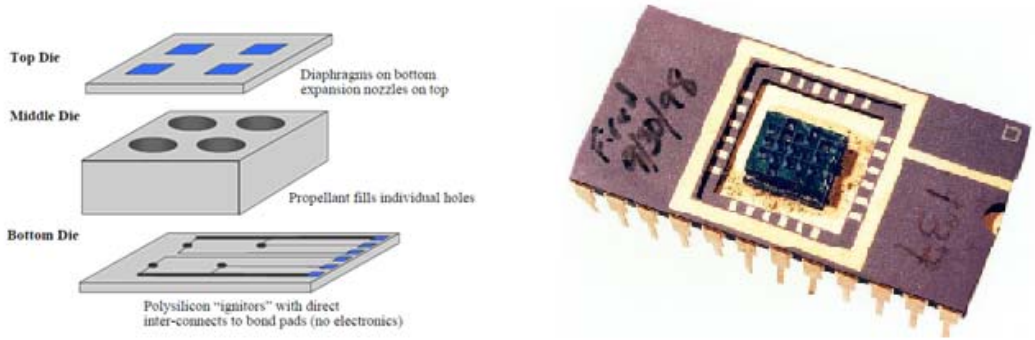

Figure 2.20.Digital micro-thruster schematic and photograph[28]

The small size allowed for up to a million thrusters, which can be fired individually or in clusters, to be fabricated on a single wafer. Each thruster was capable of a minimum impulse bit of 10^{-4} N-s, using lead styphnate as propellant.[28]

Masel and Shannon[29] developed a micro-combustor fabricated from stacked silicone wafers utilizing catalytic ignition to initiate combustion in a long serpentine two-stage channel. The combustor is schematically shown in Figure 2.21.[29] The unique combustor utilizes a Y shaped passive mixer at the inlet, immediately downstream is an electrically heated Pt strip used for ignition, followed by two serpentine reaction sections. The first reaction section is a catalytic channel that allows for the catalytic combustion of fuel and oxygen, and the second is a gas phase combustion section where the combustor walls are specially treated to inhibit radical quenching. Radical quenching occurs when reactive species are removed from the reaction by the material forming the combustion chamber walls through the process of chemisorbtion. For radical quenching to be avoided the combustor walls must have a low well depth, which is defined as the heat of absorption of radicals on the surfaces. The heat of absorption being further defined as the energy required by molecules to adhere to other materials, so that as the well depth approaches

zero the probability of a radical being trapped decreases.[29] The use of Silicon Carbide due to its low well depth and favorable high temperature properties is unique to this combustor. Thermal management through the use of low thermal conductivity materials and thermal isolation cavities helps prevent overall heat loss and enables the combustor to maintain high wall temperatures thus inhibiting thermal quenching.

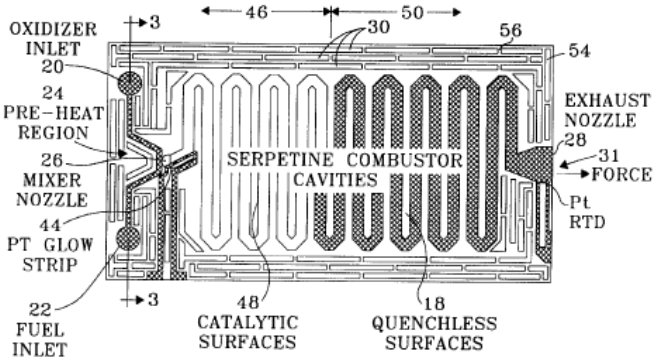

Figure 2.21.Catalytic SiC micro-combustor[29]

In a more conventional geometry *London, Ayon, Epstien, Spearing, Harrison, Peles and Kerrebrock*[30] developed a micro fabricated silicon thruster designed for high pressure combustion (chamber pressures of 125 atm.) with liquid oxygen and ethanol. The thruster was fabricated from a six wafer silicon stack that includes fuel and oxidizer injection orifices and cooling passages for the combustion chamber, throat, and nozzle. The fabrication was achieved using the Deep Reactive Ion Etching (DRIE) technique which allowed for the fabrication of high aspect ratio features with high precision.[30] The thruster has been tested with gaseous oxygen and methane using ethanol as a coolant at a chamber pressure of 12atm and this produced thrust levels as high as 1N. The thruster is shown in Figure 2.22[30].

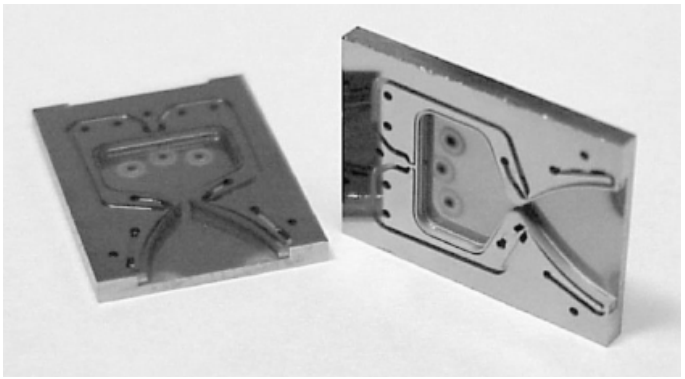

Figure 2.22.Two halves of a micro-rocket thrust chamber, the die size is 18mm x 13.5mm x 3mm.[30]

Wu, Wang, Yang, and Yetter[31] utilized asymmetric "whirl" whereby flow recirculation acts as a source of enthalpy and radical species to stabilize flames in geometries close to the quenching distance. Developed as a precursor to a meso-scale thruster the H_2/Air "whirl' combustor demonstrated relatively high C* efficiency ratios, defined as the ratio of hot flow C* efficiency to cold flow C* efficiency, indicating high combustion efficiency. Additionally, the lack of heat exchangers for heat transfer between products and reactants makes for small overall geometries; however, the combustor characteristic length was larger than the quenching distance at standard conditions. The same geometry was also used to test the high pressure decomposition of nitro-methane in monopropellant mode. The configuration along with flow streaklines are shown in Figure 2.23.[31] Additionally, the fabrication of meso- and micro-scale, 3-dimensional, uni-body combustion chambers and nozzles from ceramics using stereolithography was demonstrated.[31]

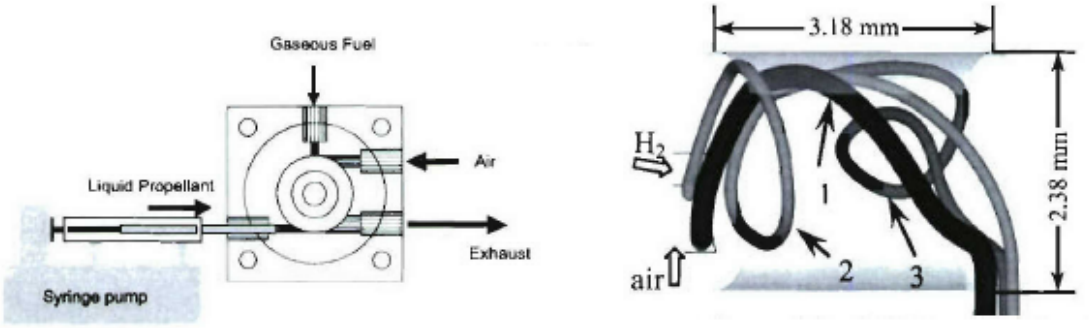

Figure 2.23.Asymmetric whirl combustor configuration with flow streaklines.[31]

Herrault, Crittenden, Torish, Birdsell, Glezer, and Allen[32] developed a self resonant MEMS-fabricated air-breathing engine, or valveless pulsejet where the pulsing exhaust can be used to either generate thrust or converted into vibrational energy for electric power generation. The combustor was fabricated from laser machined ceramic cross sections which are laminated and sintered to form the cylindrical combustor body. Figures 2.24[32], and 2.25[32] show the combustor and power generation cycle, respectively.

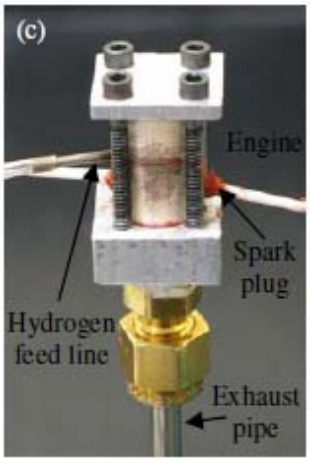

Figure 2.24.Valveless pulse jet assembly[32]

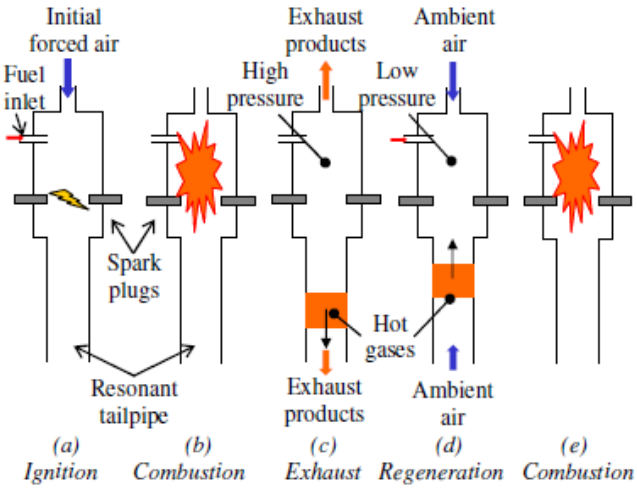

Figure 2.25.Valveless pulsejet cycle[32]

In the power generation cycle the initial charge comprised of forced air and fuel that was ignited by spark. The high pressure combustion products then exit through both the air inlet and resonant tailpipe. During this evacuation process the pressure in the chamber drops to sub-atmospheric levels and fresh air was sucked into the combustion chamber. Additionally, some of the hot exhaust products and active chemical species were sucked up from the resonant tailpipe allowing for re-ignition providing fresh fuel is supplied. With hydrogen and air the engine resonates in the frequency range of 0.9-1.6kHz with pressure differentials in the chamber of up to 10kPa.

Electricity Generation

The development of electricity through micro-and mesoscale combustion represents largely two scenarios: the first is the conversion of shaft power from microscale heat engines into electricity via dynamo, and the second is the direct conversion of thermal energy lost through the combustor walls into electrical energy via the Seebeck and Peltier effects and through thermo-photo voltaic conversion (TPV).

Early attempts at developing microscale heat engines were focused on the miniaturization of their existing macro-scale counterparts utilizing both the Brayton and Otto power cycles. *Fernandez-Pello*[33] focused on power generation using small rotary or "Wankel" engines, chosen because the planar configuration lends itself to microfabrication. Figure 2.26 shows both the meso-scale and micro-scale engine.[33] The mesoscale engine was fabricated from stainless steel by wire EDM and was successfully operated with hydrogen and air with a rotor speed of 9300rmp generating 4W at the output shaft.[1] However the overall efficiency was low (~.2%) largely due to low compression ratio arising from leakage between the rotor tip seals and the housing. The micro-scale version was fabricated from silicon using MEMS manufacturing; the rotor included integrated apex seals and a silicon carbide coating to add oxidation resistance, wear resistance, and to prevent leakage. The proposed device will include an integrated magnetic-electric generator.[1] It is important to note that MEMS manufacturing technology has enabled the integration of high temperature materials with electromechanical hardware allowing for a wide variety of designs that would otherwise be extremely difficult or impossible to fabricate.

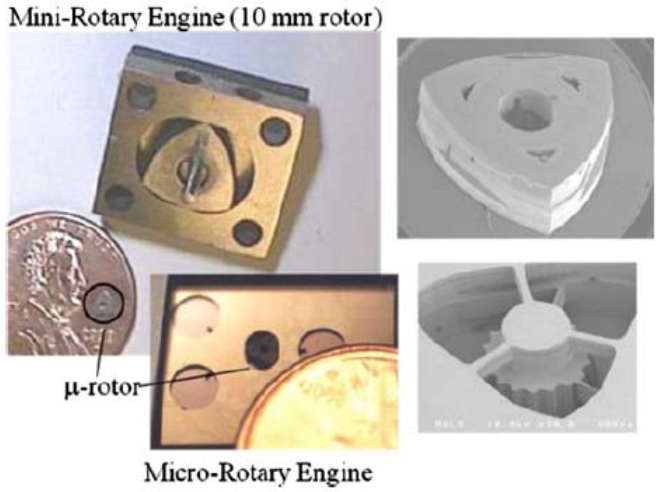

Figure 2.26.Rotary engine prototypes under development[33]

Aichlmayr, Kittelson, and Zachariah[34] designed a Homogenous Charge Compression Ignition (HCCI) free piston micro-engine with a power production capability of 10W. In HCCI engines the premixed air-fuel mixture is compressed until ignition occurs spontaneously and as a result do not require an external ignition source. Additionally, variations in charge composition and temperature cause ignition to occur in reaction centers distributed throughout the combustion chamber, hence it is not subjected to the limitations of conventional flame propagation, such as quenching distance. Power was generated by the motion of the free piston in the magnetic field induced by the permanent magnet generator.[34] Normal Heptane (n/heptane) and air mixture at equivalence ratio of 0.69 and 0.25 were successfully ignited in the single shot HCCI engine with a stroke of 57mm.[34] A schematic and photograph of the experimental engine are shown in Figure 2.27.[34]

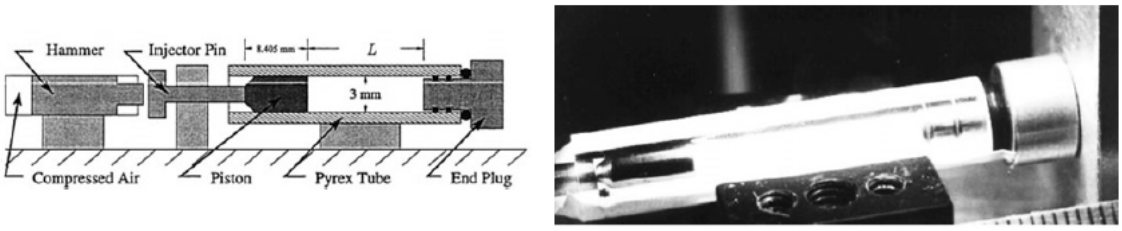

Figure 2.27.Schematic and photograph of the HCCI free piston micro-engine.[35]

Dahm, Ni, Mijit, Mayor, Qiao, Benjamin, Gu, Lei, and Papke[35] developed a micro internal combustion swing engine (MICSE) for the 20W power range operating on butane fuel. A swing engine is a rotationally oscillating free-piston engine in which combustion occurs in four chambers separated by a single rotating swing arm, the swing arm being virtually the only moving part. The rotational oscillatory motion was more readily converted to electrical energy than the linear motion of a free piston.

Energy conversion without utilizing shaft work from a heat engine is generally carried out through thermoelectric and thermo photovoltaic systems. Thermoelectric systems consist of four major components: a micro combustor, a thermal spreader, a thermoelectric device and a heat sink. In general the heat generated from the micro combustor is conducted through the heat spreaders to the thermoelectric device, which is connected to a heat sink. The thermoelectric device operates based on the Seebeck effect where two different thermoelectric materials, with different Seebeck coefficients, are placed in thermal contact with each other. For energy production (as opposed to temperature measurement) the thermoelectric materials are typically p and n type semiconductors. When subjected to a temperature gradient electrons move from the n-type semiconductor to the cooler region, the holes in the p-type semiconductor will flow in the direction of the current, which is used to power a load.[26] Bismuth telluride compounds, such as, Bi_2Te_3 and Bi_2-$XSbXTe_3$ are commonly employed n-type and p-type

materials, respectively. A schematic of a microcombustor-thermoelectric generator assembly is shown in Figure 2.28.[26]

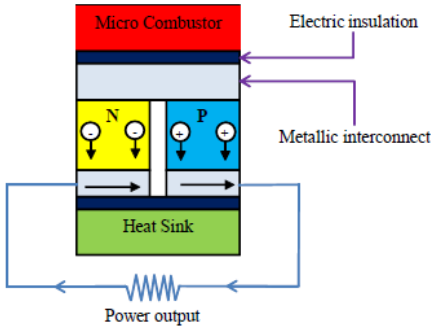

Figure 2.28.Typical meso-combustor thermoelectric generator lay up.[26]

It is important to note that although the power output from the thermoelectric generator is proportional to the square of the temperature gradient the maximum working temperature of the thermoelectric materials is on the order of 300 ^{o}C, limiting their application to combustors that operate catalytically at low temperature or having sophisticated thermal management.[26]

Vlachos, Wetzel, Voit, Bruggemann, Norton, and Federici[36] developed a catalytic micro combustor with integrated thermoelectric elements for portable power production. The combustor was formed by a microchannel (300 micron width) between two catalytic surfaces. The catalyst was formed by depositing platinum on an alumina substrate. Alumina was chosen due to its extreme porosity, yielding 1500m^2 of alumina for every geometric meter of coverage. A thermoelectric sandwich was formed by placing a thin aluminum nitride insulating sheet in between commercially available thermoelectric elements. Copper heat spreaders were placed between the thermoelectric material and the combustor in order to take heat from the reaction zone and spread it uniformly over the device. The study focused on the effects of fuel flow rate and heat removal from the

cold side on power generation. As expected power generation was found to increase with fuel-air flow rate. Forced convective cooling of the cold side of the thermoelectric device was found to greatly increase power generation by establishing larger temperature gradients. Maximum power generated was 0.65W at 1.1% efficiency with methanol/air. A schematic of the facility is shown in Figure 2.29.[36]

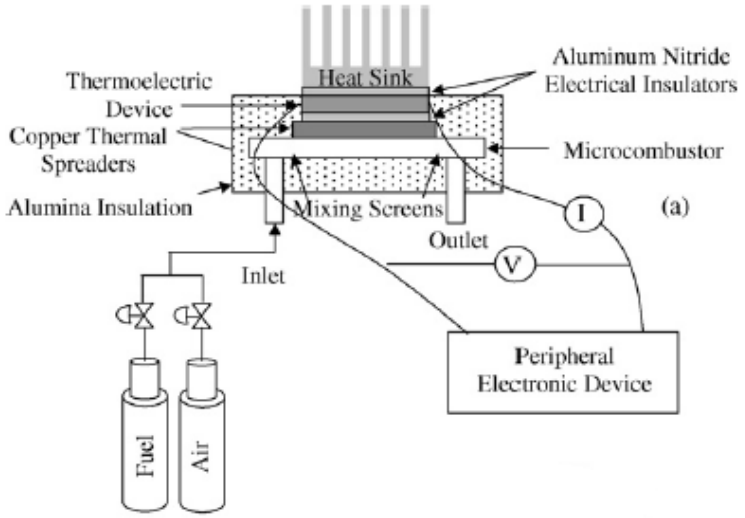

Figure 2.29.Schematic view of the micro combustor and thermoelectric device[36]

Cohen, Ronney, Frodis, Sitzki, Melburg and Wussow[37] patented a device based on a swiss-roll countercurrent combustor that has a toroidal design formed by circularly extruding a 2-D swiss roll combustor in order to avoid out of plane heat losses. The thermoelectric elements were integrated into the walls of the combustor's heat exchanger channels. The design suggests that the complex geometry should be fabricated by electrodeposition in layers that include the combustor body, thermoelectric materials, and heat spreaders integrated into the walls of the combustor. The toroidal microcombustor and combustion-based thermoelectric microgenerator are shown in Figure 2.30.[37]

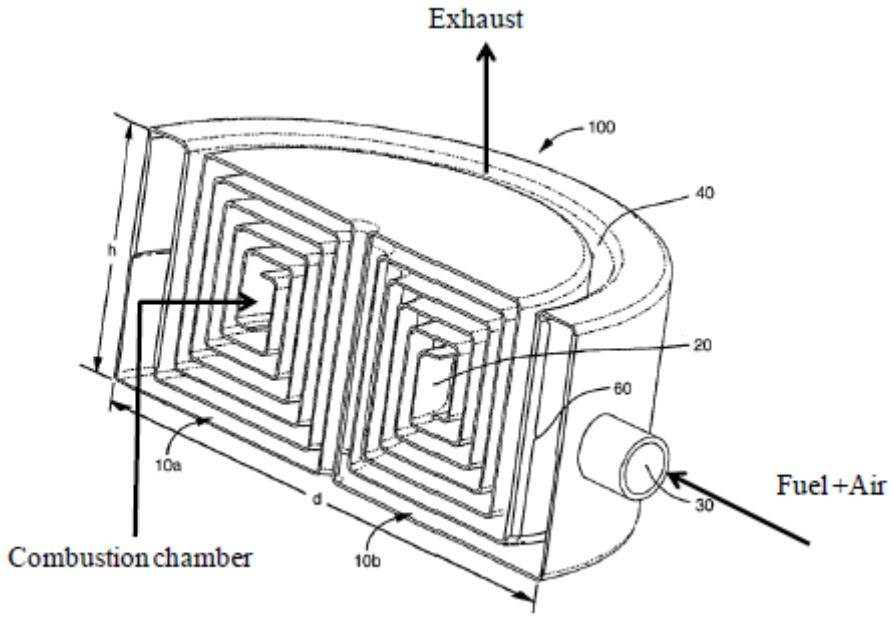

Figure 2.30.Toroidal microcombustor and combustion based thermoelectric microgenerator.[37]

Thermophotovoltaic (TPV) systems generally operate by using the heat released from combustion to heat a material which radiates thermal energy (the material could be either the combustor body or some other secondary material). The radiated energy is converted to electricity through the use of photo-voltaic cells. This means of energy generation favors gas phase combustion because, unlike thermoelectric materials, the emitter materials can be raised to very high temperatures without degrading. Thermophotovoltaic cells operate in much the same way as common photovoltaic (PV) "solar" cells in that they absorb optical energy and use it to generate and separate charge carriers that result in the flow of current. The functional difference between TPV and PV cells is the optical wavelength over which they are most efficient. In order for a photovoltaic system to work the wavelength of the absorbed optical energy must be equal to or greater than the band-gap of the TPV material, energy above and below the band-gap will result in undesirable heating.[26] In order to fully utilize the emitted radiation

from the combustor, selectively emitting materials and optical filters are often used to ensure that all the photons reaching the TPV material are of the appropriate wavelength. Selective emitters are materials that emit thermal radiation over a narrow bandwidth, the choice of material matches this bandwidth with the band gap of the TPV cell. Selective emitters matching the bandgap of Gallium Arsenide (GaAs) TPV cells include oxides of Erbium, Samarium, Neodynium, and Ytterbium.[38]

Xue, Yang, Chou, Shu, and Li[39] utilized a cylindrical microcombustor with a backwards facing step to create heat recirculation behind the step to enhance the fuel oxidizer mixing process. The combustor was fabricated from SiC which exhibited broad-band emission and utilized cobalt/nickel-doped magnesium oxide as the selectively emitting material in conjunction with Gallium Antimonide TPV cells. The combustor demonstrated uniform wall temperatures of up to 1000K and produced electric power ranging from 0.7-0.74 watts burning hydrogen/air.

Lee and Kwon[40] utilized a cylindrical heat recirculating combustor as a micro-emitter for a 1-10W power generating TPV system. Heat recirculation was used to achieve stable combustion in a micro-scale environment, and provide high and uniform wall temperatures, so that the TPV cells are subject to uniform radiation over their entire area. Calculations show that the system could potentially deliver up to 3.6W at 3.2% efficiency with a one percent increase in efficiency available by changing the combustor material to SiC. A schematic of the TPV system is shown in Figure 2.31.[40]

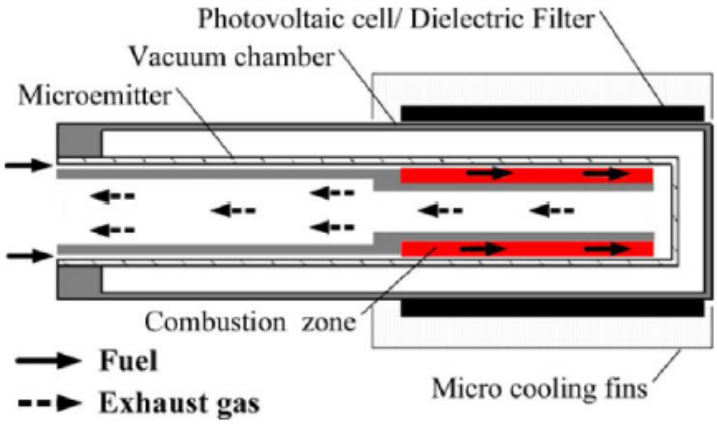

Figure 2.31.Conceptual design of a Micro-TPV system.[40]

Patents issued for TPV technology generally consist of the same design architecture, including a micro-combustor, selectively emitting material/optical filters, TPV cells, and TPV cooling.[41] Differences in design are generally limited to which combustion scheme is used to stabilize the flame (dependent largely on extinction regime and wall temperature/uniformity), and how to best remove all thermal energy from product gasses prior to exhausting into the atmosphere.

Section 8. References

[1]Jacobson, S., and Epstien A. "An Informal Survey of Power MEMS." *International Symposium on Micro-Mechanical Engineering*. Tsuchiura and Tsukuba, Japan, December 1-3, 2003.

[2] Ahmed, Mahabub., "Flame Dynamics of a Mesoscale Combustor,". PhD Dissertation, University of Texas at El Paso. 2008.

[3] Wu, M-H., Wang, Y., Yang, V., and Yetter, R. A., "Combustion in Meso-Scale Vortex Chambers," *Proceedings of the Combustion Institute,* Vol. 31, Issue 2, Jan. 2007, pp.3235-3242.

[4] Sitzki, L.,Borer, K., Schuster, E. and Ronney, P. "Combustion in Microscale Heat-Recirculating Burners" *Third Asia Pacific Conference on Combustion*. Seoul, Korea, June 24-27, 2001.

[5] Sher, I., Levinson-Sher, D., and Sher, E., "Miniaturization limitations of HCCI Internal Combustion Engines," *Applied Thermal Engineering*, Vol. 29, Issues 2-3, Feb. 2009, pp. 400-411.

[6] Jones, A.R., Lloyd, S.A., and Weinberg, F.J., "Combustion in Heat Exchangers," *Proceedings of the Royal Society of London. Series A, Mathematical and Physical Sciences,* Vol. 60, 1978, pp.97-115.

[7]Vijayan, V., Gupta, A.K., "Combustion and Heat Transfer at Meso-scale with Thermal Energy Recirculation" *6th International Energy Conversion Engineering Conference (IECEC)*. Cleveland, OH. July. 28-30, 2008.

[8] Cho, J-H., Chien, S. L., Richards, C., D., Richards, R. F., Ahn, J., and Ronney, P, D., "Demonstration of an External Combustion Micro-Heat Engine," *Proceedings of the Combustion Institute,* Vol. 32, 2009, pp.3099-3105.

[9] Turns, S., *An Introduction to Combustion*. 2nd ed., McGraw Hill, Boston, 2006.

[10] Vijayan, V., Gupta, A.K., "Experimental Investigation of a High Power Density Ceramic Meso-scale Combustor " *47th AIAA Aerospace Sciences Meeting including The New Horizons Forum and Aerospace Exhibition*. Orlando, FL. Jan. 5-8, 2009.

[11] Vijayan, V. and Gupta, A.K., "Experimental Investigation of a Meso-scale Liquid Fueled Combustor " *45th AIAA/ASME/SAE/ASEE Joint Propulsion Conference and Exhibit*. Denver, CO. Aug. 2-5, 2009.

[12] Oh, H., Huh, H., Ahn, J. and Ronney, Paul. "Effect of Scale on the Performance of Heat-Recirculating Reactors". *4th International Energy Conversion Engineering Conference and Exhibit*. San Diego, CA. June. 28-29, 2006.

[13] Lee, M., Cho, S., Choi, B. and Kim N. "Scale and Material Effects on Flame Characteristics in Small Heat Recirculation Combustors of a Counter-Current Channel Type" *Applied Thermal Engineering,* Vol. 30, 2010, pp. 2227-2235.

[14] Lee, M. and Kim N. "Experiment on the Effect of Pt-Catalyst on the Characteristics of a Small Heat-Regenerative CH_4-air Premixed Combustor" *Applied Energy,* Vol. 87, 2010, pp. 3409-3416.

[15] Vijayan, V. and Gupta, A.K., "Effect of Channel Length on a Meso-Scale Spiral Combustor Performance" *46th AIAA/ASME/SAE/ASEE Joint Propulsion Conference and Exhibit*. Nashville, TN. July. 25-28, 2010, Paper No. AIAA-2010-7065.

[16] Kim, N., Kato, S., Kataoka, T., Yokomori, T., Maruyama, S., Fujimori, T., and Maruta, K. "Flame Stabilization and Emission of Small Swiss-roll Combustors as Heaters" *Combustion and Flame,* Vol. 141, 2005, pp.229-240.

[17] Spadaccini, C.M., Zhang, X., Cadou, C. P., Miki, N., and Waitz, I. A. "Development of a Catalytic Silicon Micro-Combustor for Hydrocarbon-Fueled Power MEMS", MEMS 2001, Las Vegas NV, Jan 2002

[18] Vijayan, V., and Gupta, A.K., "Flame Dynamics of a Meso-scale Heat Recirculating Combustor" *7th International Energy Conversion Engineering Conference*. Denver, CO. Aug. 2-5, 2009, Paper No. AIAA 2009-4604.

[19]Ahn, J., Eastwood, C., Sitzki, L., and Ronney, P. D., "Gas Phase and Catalytic Combustion in Heat Recirculating Burners," *Proceedings of the Combustion Institute,* Vol. 29, Issue 7, 2002, pp.957-963.

[20]Vijayan, V., and Gupta, A.K., "Thermal Performance of a Meso-scale Heat Regenerating Combustor" *7th International Energy Conversion Engineering Conference*. Denver, CO. Aug. 2-5, 2009.

[21] Vijayan, V., and Gupta, A.K. "Thermal Performance of a Meso-scale Liquid Fueled Combustor" *Applied Energy,* 2011.

[22] Vijayan, V., and Gupta, A.K. "Flame Dynamics of a Meso-scale Heat Recirculating Combustor" *Applied Energy,* Vol. 87, 2010, pp.3718-3728.

[23] Jejurkar, S., and Mishra, D. "A Review of Recent Patents on Micro-Combustion and Applications" *Recent Patents in Engineering,* Vol. 3, 2009, pp.194-209.

[24] Epstein, A.H., Senturia, S.D., Waitz, I.A., Lang, J.H., Jaconson, S.A., Ehrich, F.F., Schmidt, M.A., Ananthasuresh, G.K., Spearing M.S., Breuer, K.S., Nagle, S.F.: US Patent US20026392313B1, 2002.

[25] Mehra, A., and Waitz, I. A, "Development of a Hydrogen Combustor for a Microfabricated Gas Turbine Engine", Solid *State Sensor and Actuator Workshop*, Hilton Head, GA, 1998.

[26] Vijayan, V., "Combustion and Heat Transfer in Meso-Scale Heat Recirculating Combustors,". PhD Dissertation, University of Maryland at College Park, 2010.

[27] Youngner, D. W.: US patent US20026378292B1 (2002).

[28]Lewis, David., Janson, Siegfried., Cohen, Ronald., Antonsson, Erik. "Digital MicroPropulsion" *Sensors and Actuators A,* Vol. 80, 2000, pp.143-154.

[29] Masel, R.I., and Shannon, M.A.: US patent US20016193501B1, 2001.

[30] London, A.P., Ayon, A.A, Epstien, A.H., Spearing, S.M., Harrison, T., Peles, Y., and Kerrebrock, J.L.. "Microfabrication of a High Pressure Bipropellant Rocket Engine" *Sensors and Actuators A,* Vol. 92, 2001, pp. 351-357.

[31] Yetter, R.A, Yang, V., Aksay, I.A and Dryer, F.L. *Meso and Micro Scale Propulsion Concepts for Small Spacecraft*. Arlington VA. AFOSR. 2004. AFRL-SR-AR-TR-05-0016,FA9260-01-1-0376.

[32] Herrault, F., Crittenden, T., Yorish, S., Birdsell, E., Glezer, A., and Allen, M. G. "A self-resonant MEMS-fabricated, Air-breathing engine" *Solid-State Sensors, Actuators, and Microsystems Workshop*, Hilton Head Island, South Carolina, June 1-5 2008.

[33] Fu, K., A.J. Knobloch, F.C. Martinez, D.C. Walter, C. Fernandez-Pello, A.P. Pisano, D. Liepmann, K. Miyasaka, and K. Maruta. "Design and Experimental Results of Small-scale Rotary Engines." *Proceedings of 2001 ASME International Mechanical Engineering Congress and Exposition*. New York, NY, ASME, 41, pp. 295-302.

[34]Aichlmayr, H. T., Kittelson, D. B. and Zachariah, M. R. "Miniature Free-piston Homogeneous Charge Compression Ignition Engine-compressor Concept- Part I: Performance Estimation and Design Considerations Unique to Small Dimensions",*Chemical Engineering Science*, vol. 57, 2002, pp. 4161-4171.

[35] Dahm, W. J. A., Ni, J., Mijit, K., Mayor, J. R., Qiao, G., Dyer, S. W., Benjamin, A. G. , Gu, Y., Lei, Y., and Papke, M.L., "Micro Internal Combustion Swing Engine (MICSE) for Portable Power Generation Systems". AIAA Paper 2002-0722, AIAA, Reno, NV. 2002.

[36] Federici, J. A., Norton, D. G., Bruggemann, T., Voit, K. W., Wetzel, E. D., and Vlachos, D. G. "Catalytic Microcombustors With Integrated Thermoelectric Elements for Portable Power Production" *Journal of Power Sources* ,Vol.161, 2006, pp.1469–1478.

[37] Cohen, A L., Ronney, P., Frodis, U., Sitzki, L.; Meiburg, E., and Wussow S.: US patent 6,613,972 B2, 2003.

[38]Guazzoni, "High Temperature Spectral Emittance of Oxides of Erbium, Samarium, Neodynium, and Ytterbium", *Applied Spectroscopy*, Vol. 26, 1972, pp. 60-65.

[39]Xue, H., Yang, W. M., Chou, S. K., Shu, C. and Li, Z. W. "Microthermophotovoltaics power system for portable mems devices", *Microscale Thermophysical Engineering*, 9 2005, pp.85-97

[40] Lee, K. H., and Kwon, O. C. "Studies on a Heat-recirculating Microemitter for a Micro thermophotovoltaic System". *Combustion & Flame*, 153, 2008, pp. 161-172

[41]Nelson, R.: US patent 4,584,426, 1986.

Chapter 3: Experimental Facilities and Procedures

Section 1 Combustors

Combustor Geometries

A number of combustor geometries and configurations were used during the course of the experimental program, some geometrical modifications were made to alleviate functional problems that arose during experimentation, and others were made in order to parametrically study the effects of geometry on performance. The different geometries used will be discussed below. The baseline combustor is a 2.5 turn design adopted from the work of *Vijayan and Gupta*[1] the channel cross section is 0.0625 in. x 0.11811 in. and the combustor was initially fabricated from Zirconium phosphate. This material was chosen because of it low thermal conductivity (0.8W/mK) and its resistance to thermal shock. Initially the liquid fuel was introduced partially premixed; the fuel was injected through a porous heat recuperator placed 0.75 turns upstream of the combustor volume. The heat recuperator was used because fuel evaporation and mixing times can be significant when compared to the gaseous premixed residence time, because liquid evaporation and mixing at low Reynolds numbers is generally poor. Space constraints related to feeding ignition wires, plumbing, and diagnostics through the back of the combustor dictate the exact location of the porous fuel injector. Compressed double aught steel wool was used as the recuperating material. Figure 3.1, below shows the combustor with heat recuperator. The exact dimensions of the combustor can be found in the appendix.

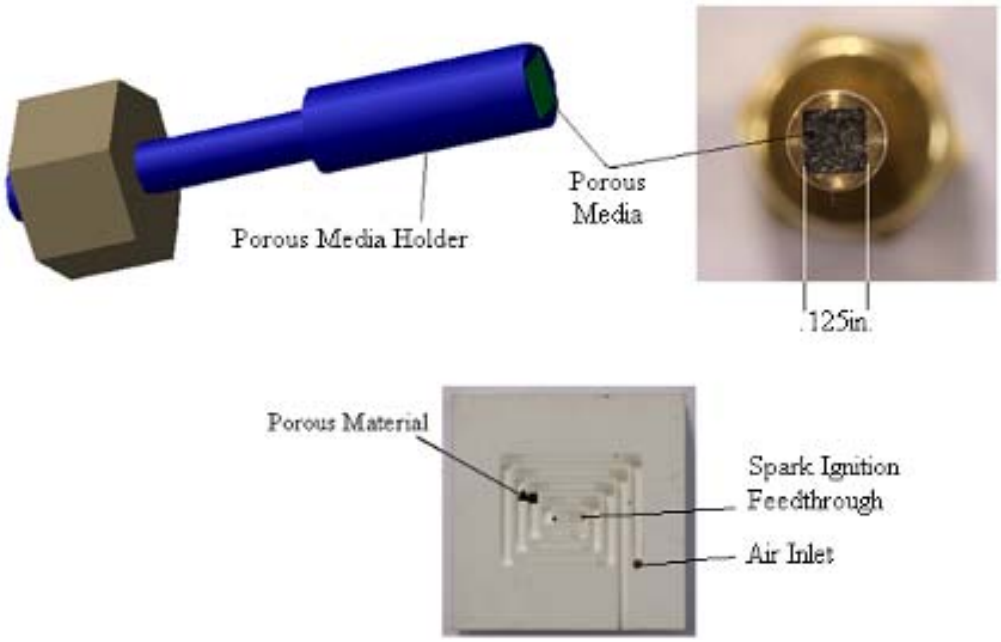

Figure 3.1. 2.5 Turn zirconium Phosphate Heat Recirculating Combustor

Subsequent combustors were shortened in size from 2.5 turns to 1.0 turn while maintaining the same channel cross section and combustion chamber geometry. This was done because increasing the heat exchanger length leads to higher reactant temperatures, the ability to support lean flames, and broader stability regimes. However, large heat exchanger lengths naturally translate to higher surface areas for heat loss, leading to lower exhaust enthalpy. Additionally, shortening the heat exchanger length lowers the preheat temperature and as a consequence the flame velocity, enabling the combustor to operate at low heat loads (low thrust). Hence the change in geometry is driven entirely by application, for propulsion the channel length is minimized to maximize the exhaust enthalpy, however for power generation a long channel length is preferable since heat loss through the walls is the mechanism by which power is generated (for example in TPV and TE systems). This change in combustor geometry also came with a change in material. Alumina Silicate was used in favor of Zirconium Phosphate; this was done

because alumina silicate is substantially less porous than zirconium phosphate, this prevents the material from absorbing liquid fuels that are injected into the combustor. The downside of the lower porosity is higher thermal conductivity; alumina silicate has a thermal conductivity of roughly 1.98W/mK relative to 0.8W/mK for zirconium phosphate. The single turn combustor is shown in Figure 3.2, below.

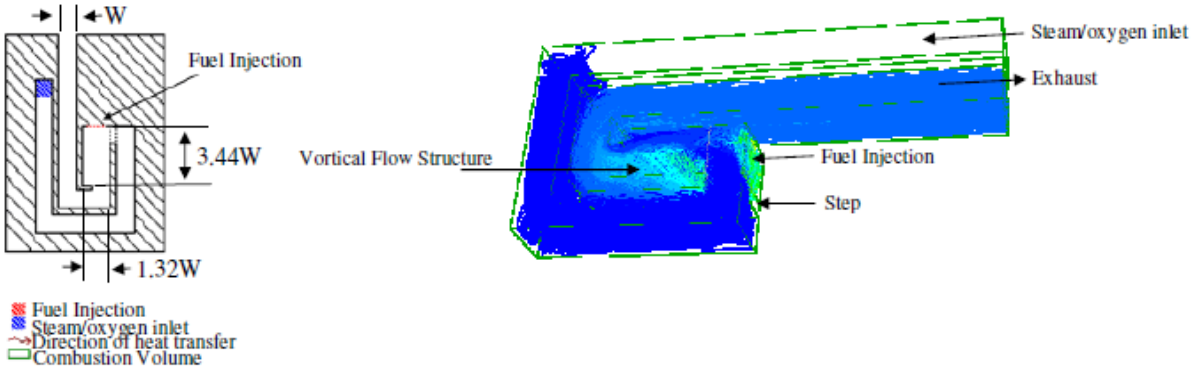

Figure 3.2. Single Turn Combustor. The non-premixed configuration is shown, two mixing strategies were examined.

Iterations on the single turn geometry were made to study the effect of channel geometry on the extinction limits of the combustor. Three variations were fabricated; the channel aspect ratios (width/depth) were varied from 0.5 to 0.3 in increments of 0.1 with constant hydraulic diameter. The hydraulic diameter was kept constant so that the cold flow Reynolds numbers would be constant between combustor for the same inlet conditions. Note that since the whole combustor is at constant depth changing the depth of the channel changes the depth of the combustion chamber as well, and hence a combustor with lower aspect ratio channels has a combustion chamber with larger volume.

Typically, in a bi-propellant hydrogen peroxide thruster, hydrogen peroxide is decomposed in a gas generator using an appropriate catalyst into superheated steam and

oxygen. This happens upstream of the combustion chamber. The global decomposition reaction proceeds according to Equation 3.1.

$$2H_2O_2 \rightarrow 2H_2O + O_2 \qquad \text{Eq. 3.1}$$

The decomposition products are passed to the combustion chamber and burnt with fuel. For the experimental combustor the superheated steam/oxygen mixture is generated using a lean burning hydrogen oxygen flame (Φ=0.5) upstream of the combustor, the stoichiometry of which is shown in Equation 3.2. This was done in order to study the flame dynamics of the experimental combustor while decoupling it from the complexity of developing a meso-scale hydrogen peroxide gas generator.

$$2H_2 + 2O_2 \rightarrow 2H_2O + O_2 \qquad \text{Eq. 3.2}$$

For fabrication simplicity the hydrogen oxygen burner and heat recirculating combustor are fabricated into a single unit, with the exhaust from the hydrogen oxygen burner ported into the inlet channel of the heat recirculating combustor. Since the heat release rate from a hydrogen-oxygen flame is larger than the heat release rate from hydrogen peroxide decomposition, a thermal isolation cavity is machined in between the steam generator and the heat recirculating combustor. Note that due to the large heat release intimate thermal contact between the hydrogen/oxygen burner and the heat recirculating combustor could unduly influence the results.

Because the product gas temperature of a hydrogen/oxygen flame can easily surpass the adiabatic decomposition temperature of hydrogen peroxide, the experimental conditions that can be realistically tested are limited to those where the steam/oxygen temperature is less than or equal to the hydrogen peroxide adiabatic decomposition

temperature. Hence there is an upper limit on the amount of H_2/O_2 that can be burnt before the temperature limit is reached. All the experimental results presented are below this limit. The combustor/steam generator system was calibrated with the steam generator only in order to determine this limit.

As mentioned previously, the combustor was fabricated from alumina-silicate. Initial experiments were conducted with the combustor material in its green state. However, stresses possibly arising from differential thermal expansion of the material and its housing led to cracking at high heat loads, thus limiting the regime over which the combustor could operate. A heat treatment of 45 minutes at 1050°C with a ramp rate of 2°C per minute was used to increase both the hardness and strength of the material with promising results. Additionally, the steam generator was lined with a refractory zirconia blanket to protect the alumina silicate from the hydrogen/oxygen flame, the blanket was both rigidized and surface hardened to prevent deterioration. Figure 3.3 shows the combustor/steam generator used in the experiments.

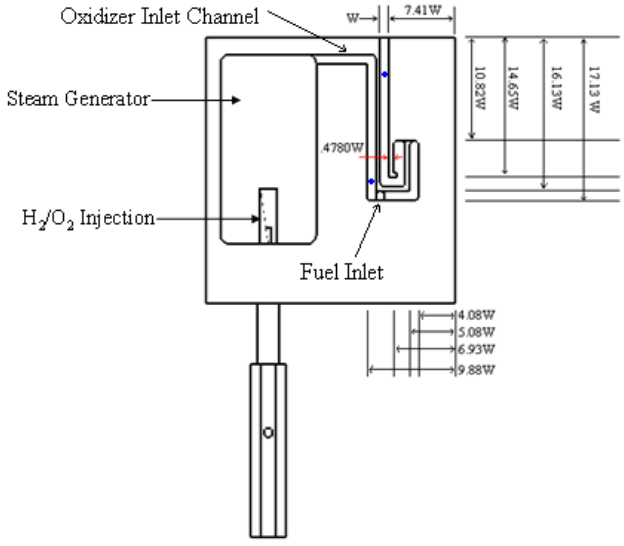

Figure 3.3. Combustor/Steam Generator

A second fuel injection configuration was tested whereby fuel is injected through an alumina/zirconia porous ceramic heat recuperator placed directly in the combustion chamber, wherein the recuperator receives heat directly from the flame. This configuration was chosen based on a combination of empirical experience and numerical simluations. The exact location was selected such that the interplay between the aerodynamics of the combustion volume and the injected fuel lead to both rapid mixing and flame stabilization. Aerodynamic flame holding is achieved via a step entrance to the combustion chamber, which provides a vortical flow structure and a local recirculation zone, thus recirculating both heat and active species from the products to the reactants. The fuel is injected into the center of the vortex. Figure 3.4 shows the fuel and oxidizer injection configuration indicating the steam/oxygen inlets, the combustion zone, and the fuel injection location. Additionally, flow pathlines through the combustion chamber are shown to illustrate the flow structure in the chamber and the direction of fuel injection relative to the vortical flow structure in the chamber.

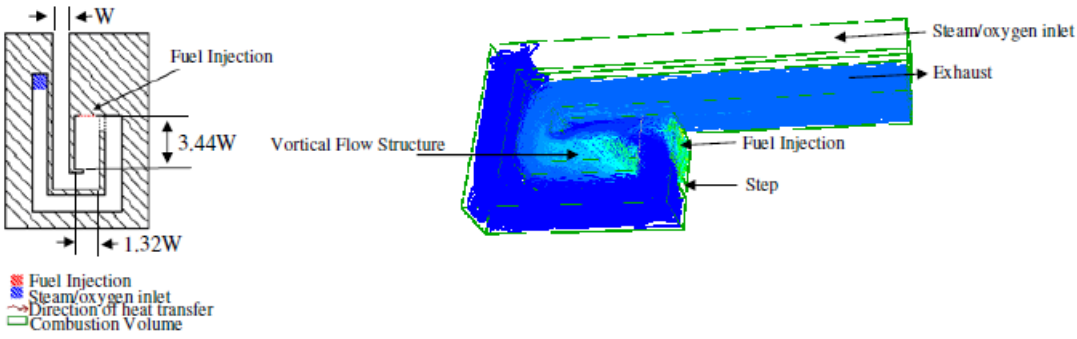

Figure 3.4. Non-premixed combustor

In order to pressurize the thrust chamber a converging nozzle was fabricated into the exhaust. The relative geometry of the nozzle is shown in Figure 3.5, below, along with pressure tap and thermocouple locations. The nozzle has a rectangular cross section

and three sides of the nozzle are converged in two stages. The initial convergence begins at the hatched region of Figure 3.5, just downstream of the chamber pressure tap. In this region the depth of the channel is reduced by 58%. This was done for fabrication reasons since fabricating the throat section of the nozzle at full channel depth on a CNC would require a long slender tool that would lack the rigidity to make an accurate cut. In the second converging stage the channel width is reduced 75% from the full channel width to the throat width. This leads to a nozzle contraction ratio 9.52, the contraction ratio being defined as the ratio of the inlet area of the nozzle to the throat area of the nozzle.

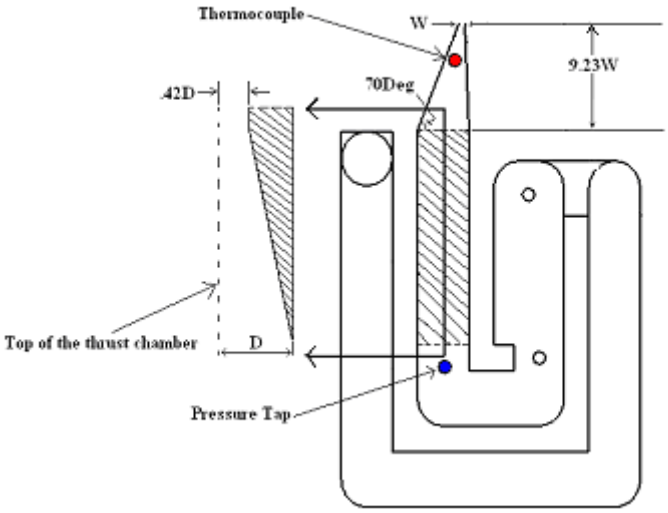

Figure 3.5. Combustor with Nozzle

In order to determine discharge characteristics the throat area was determined by flowing high flow rates of oxygen through the thrust chamber and measuring the chamber pressure and mass flow rate discharged through the nozzle. This calibration was performed at high Re so that the discharge coefficient can be assumed to be 1.0. The throat area was then calculated based on the measured pressure ratio and flow rate. This was done for two reasons. First, as mentioned previously, the thrust chamber is machined in its green state and then heat treated to increase its strength and temperature resistance.

However, the heat treatment also results in an ~2% dilation in the material volume, which causes channel widths to decrease from the as-machined state. Additionally, the thrust chamber is fabricated from a porous ceramic material, as such all plumbing is bonded and sealed to the back of the combustor using refractory alumina bonding and sealing cement. Since the cement is composed of fine particles it has some porosity which limits its capacity to seal against pressure. Since multiple thrust chambers are used during the course of an experimental program, each one is calibrated for effective throat area prior to data analysis.

For steady state performance the hot steam and oxygen mixture is allowed to come to thermal equilibrium in the thrust chamber prior to introducing the fuel, hence the heat recuperator is hot and readily vaporizes the fuel. However, this situation does not arise when pulsing from a cold start. In order to provide the initial heat necessary to vaporize the fuel a miniature resistive heating element is fabricated into the porous heat recuperator, the element consumes 6W and brings the recuperator to roughly 160°C. Figure 3.6 shows the combustor with resistive heating element installed along with a thermocouple for measuring the recuperator temperature.

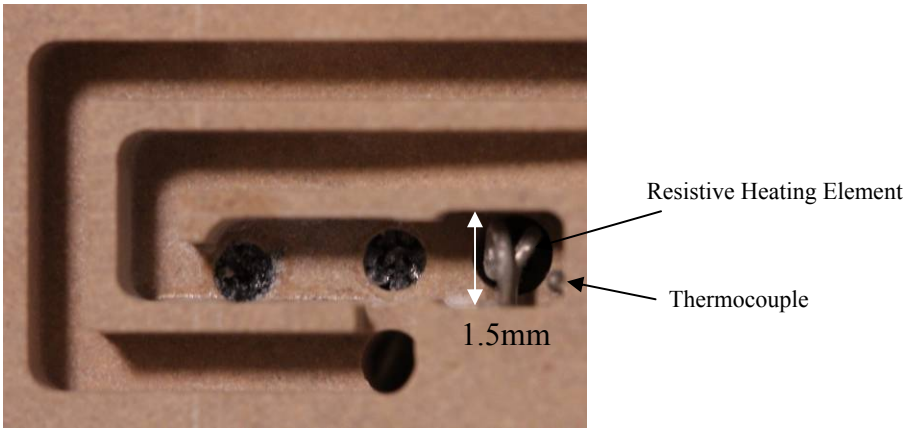

Figure 3.6.Combustor with heating element and thermocouple fabricated into the heat recuperator

Note that the exact dimensions of the combustors along with the NC codes used to machine them are provided in the appendix.

Ignition

In all of the presented experimental results ignition is achieved via spark. Achieving successful spark ignition in a meso-scale chamber is complicated both by the underlying physics of heat recirculating combustors and the engineering challenges that come with providing high voltage in confined spaces while avoiding undesired arcing. With regard to the former, since a high preheat temperature is required to stabilize the flame the ignition source must remain on until the flame heats both the incoming reactants and the combustor walls enough to stabilize itself. During this process the flame is in a periodic cycle of ignition and extinction where the spark acts as the excess enthalpy source required for stabilization. If the spark frequency is too low then the thermal energy added during an ignition event to both the walls of the combustor and the reactants will be lost during an extinction event before the arrival of the next spark, and in this scenario the flame could never stabilize.

A purpose built igniter was developed based on an Echlin E6-B 6Volt automotive ignition coil. The coil was driven via a square wave generator that provided short square pulses with both variable frequency and duty cycle, in order to tailor the spark frequency required to stabilize the flame at the required the inlet total mass flow rate and equivalence ratio. Because the ignition coil discharges the spark when the circuit providing power to the coil is opened, the width of the pulse or "high time" is not as significant as the pulse frequency, since the spark occurs only on the falling edge of the pulse. Note that because the square wave generator cannot provide the power required to

drive the ignition coil the generator was used to drive a relay, the relay rapidly connected and disconnected the ignition coil ground to provide the spark. Power to the coil and pulse generator was provided via a 400 Watt modified ATX power supply. Power for other facility equipment was provided largely from the same unit. The circuit diagram for the ignition system is shown in Figure 3.7. Element values are shown in Table 3.1.

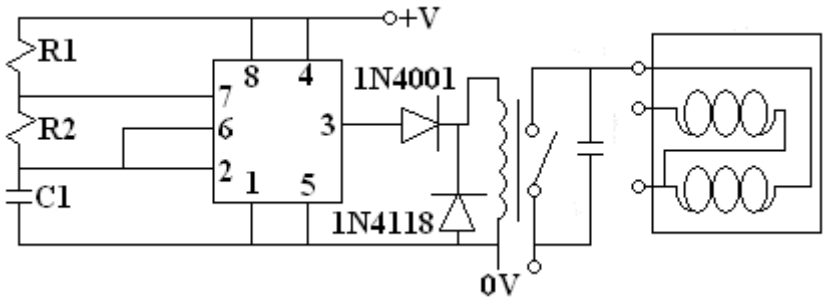

Figure 3.7. Ignition circuit the values used for the circuit elements are shown in the accompanying table. The circuit is based on the a-stable 555 timer oscillator.

Table 3.1 Ignition Circuit Element Values

Element Name	Value
R1	1kΩ
R2	0-10 kΩ
C1	.1μF
Rectifying Diode	1N4001
Signal Diode	1N4148

Fabrication

The methodology for feeding ignition lines into the combustor has evolved as a consequence of both experimental and fabrication experience. Initially bare Kanthal resistance wires (1/64 in. diameter) were fed through the back of the combustor, the feed-throughs being sealed with refractory alumina cement. An air gap was maintained between the alumina seals for each of the Kanthal wires in-order to provide sufficiency electrical insulation. A sketch of this configuration is shown in Figure 3.8, below.

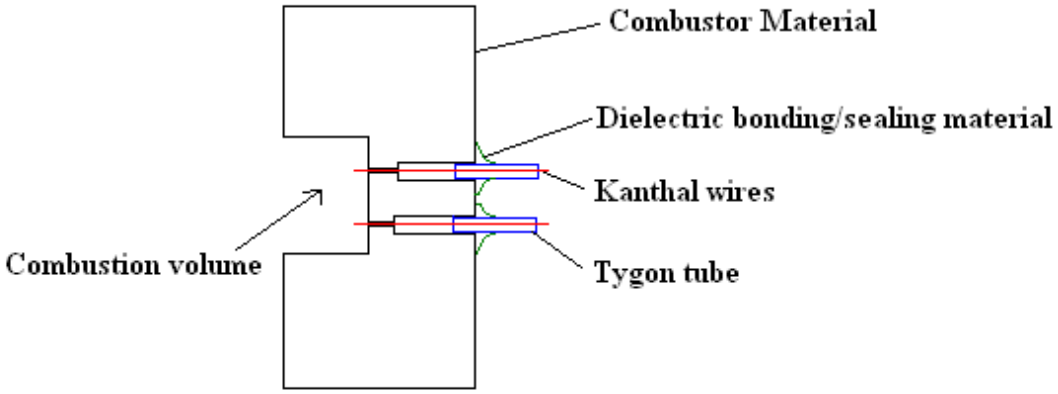

Figure 3.8. Combustor with Kanthal wire igniters

During experimentation it was found that the Kanthal wires suffer substantial corrosion as a result of exposure to the flame. This corrosion products lead to changes in the geometry of the wire and deterioration of the wire performance. In order to extend the life of the ignition electrodes and provide a combustion volume that is free from protrusions (note that the Kanthal wires although 1/64in. in diameter are nearly 25% of the width of the combustor) flush mounted silicon carbide ignition electrodes were integrated into the combustor body. The combustor with electrodes is shown in Figure 3.9.

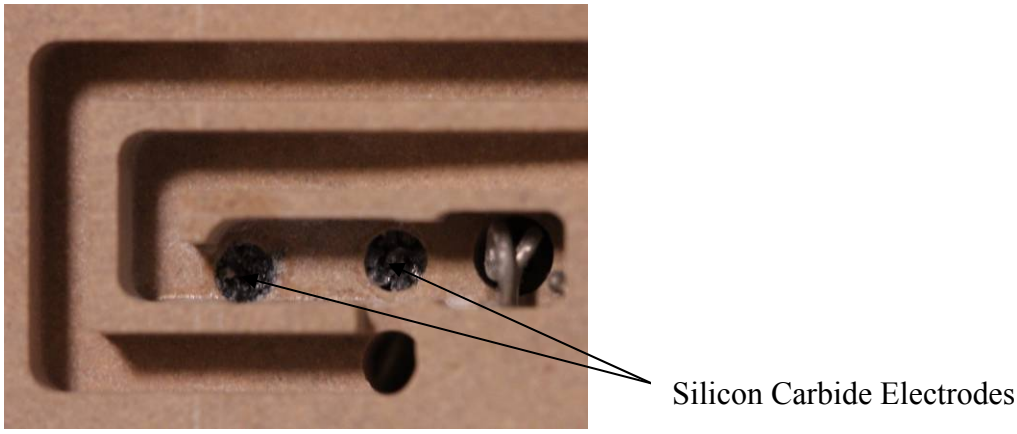

Figure 3.9. Silicon carbide ignition electrodes

The electrodes were connected to custom machined brass banana-jack terminals via copper wires fed through the sides of the combustor. The terminals were mounted at the sides of the combustor in order to provide maximum separation and avoid undesired arcing. A sketch of the combustor with both igniters and side mounted ignition terminals is shown in Figure 3.10.

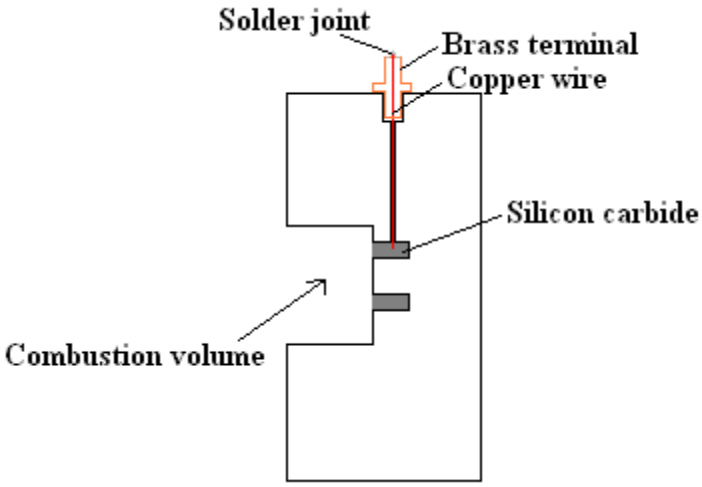

Figure 3.10. Combustor with silicon carbide igniters

Section 2 Flow Control

Steady State Measurement of Extinction and Thermal Performance

The experimental facility was designed to provide the necessary controls and diagnostics for determining stability regimes and thermal performance of the combustor, in addition to measuring the chamber total pressure, chamber dynamic pressure, and pressure and temperature startup transients. Omega FMA 5500 Thermal conductivity mass flow controllers were used to control the flow rates of hydrogen and oxygen. The accuracy of each flow controller is ±1.5% of full scale, a number of controllers were used during the course of the experiment to minimize the experimental errors. The maximum

error was 7.5mL/min and the maximum error in flow rate is 75mL/min. A Harvard Apparatus PHD2000 infusion syringe pump was used to control the methanol and kerosene fuel flow rates. A K-Type thermocouple (Nickel-chromium vs. Nickel-Aluminum) was used to measure the temperature of the product gas just prior to entering the throat section of the nozzle. A National Instruments NI9211 cold junction compensated thermocouple data acquisition module recorded the temperature through a personal computer at a sample rate of 4Hz with an accuracy of 2.2°C. The thermocouples were unsheathed and the exposed beads yield a blockage ratio of approximately 2.8%; careful installation insured that the thermocouple beads did not make any contact with the combustor material. Chamber pressure was measured using a SETRA model 204 digital pressure transducer with an accuracy of 0.11% of full scale, the measurements were acquired through a data acquisition module sampling at 100Hz and recorded through a personal computer. Dynamic pressure was measured using an excited piezoelectric dynamic pressure sensor with a sensitivity of 50mV/psi, the data was acquired through a data acquisition module sampling at 2000Hz and recorded on a personal computer. A schematic diagram of the steady state facility is shown in Figure 3.11, below.

The experimental error has been determined based on the above values. Results provided without error bars are provided as such because the experimental error is too small to be interpretable in the figure (i.e in temperature measurements where the fixed 2.2°C is small compared to measured temperatures which may by on the order of 1000°C).

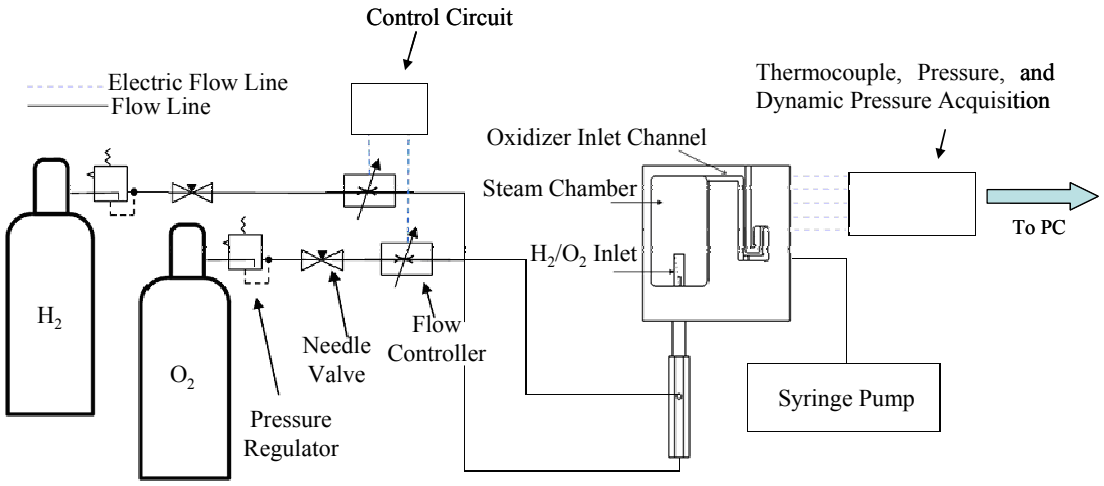

Figure 3.11. Schematic of the experimental facility

Pulsing

A pulsing and thrust measurement facility was fabricated to allow for pulsing of the thruster at high pressure ratios and rapid response times. Fuel was provided via a pressure fed fuel tank with regulated tank pressure. Oxidizer was provided via high pressure industrial oxygen cylinder. Oxidizer and fuel delivery to the combustor was controlled via miniature solenoid valves placed upstream of the combustor. Clippard EV-2-06 and E210A-1W012 miniature solenoid valves were used because of their low power consumption and voltage requirements along with high pressure tolerance. Custom valve manifolds were fabricated from free machining brass for the E210A-1W012 valves. The facility measures the chamber pressure, differential pressure across the valve, the trigger pulses, and the thrust. The data is acquired through National Instruments NI USB 6008 and NI USB 9215 high speed data acquisition cards sampling at 100Hz. The pulsing facility is shown in Figure 3.12, below; the facility is mounted to a sled carrying the valves, thruster, and valve electronics. A Light Emitting Diode (LED) is wired into the

power line for the fuel valve and acts as a synchronization lamp for the high-speed camera.

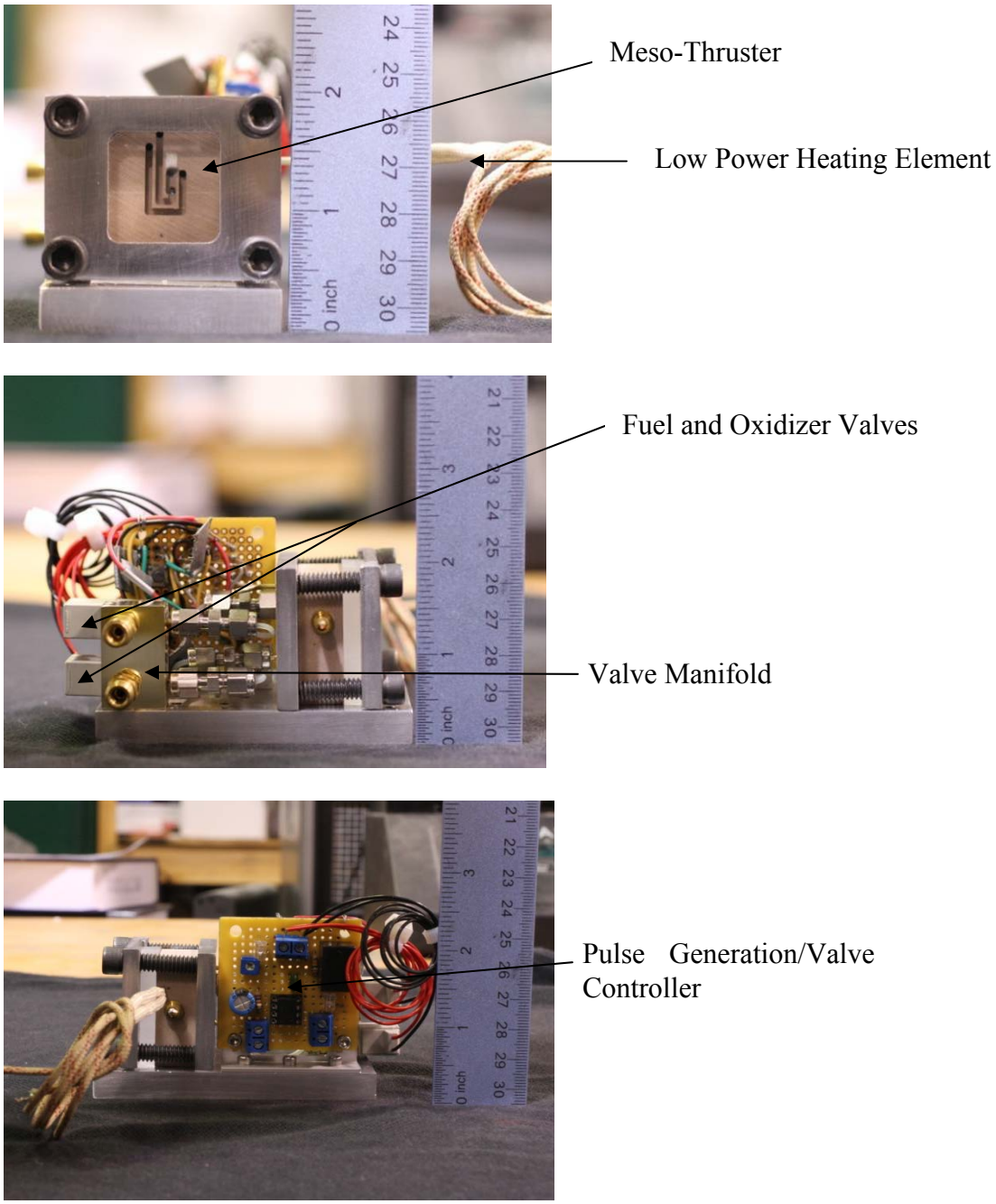

Figure 3.12.Pulsing facility including valves, valve electronics, and thruster

The valve controller is based on the mono-stable 555 timing circuit, similar to the one used to provide ignition pulses. The circuit diagram is provided in Figure 3.13, below along with a table of circuit element values. The controller provides a single on demand square pulse, a potentiometer in series with R1 allows for varying of the pulse width. The controller shown above provides for variable pulse widths from 0.1-1.1 seconds.

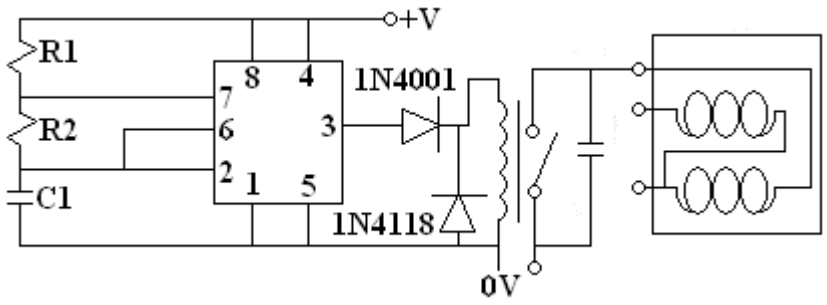

Figure 3.13. Valve control circuit

Table 3.2. Single Pulse Generation Circuit

Element Name	Value
R1	1kΩ
R2	0-10 kΩ
C1	.1μF
Rectifying Diode	1N4001
Signal Diode	1N4148

The thrust stand (discussed later), flow controllers and pressure transducers are shown in Figure 3.14.

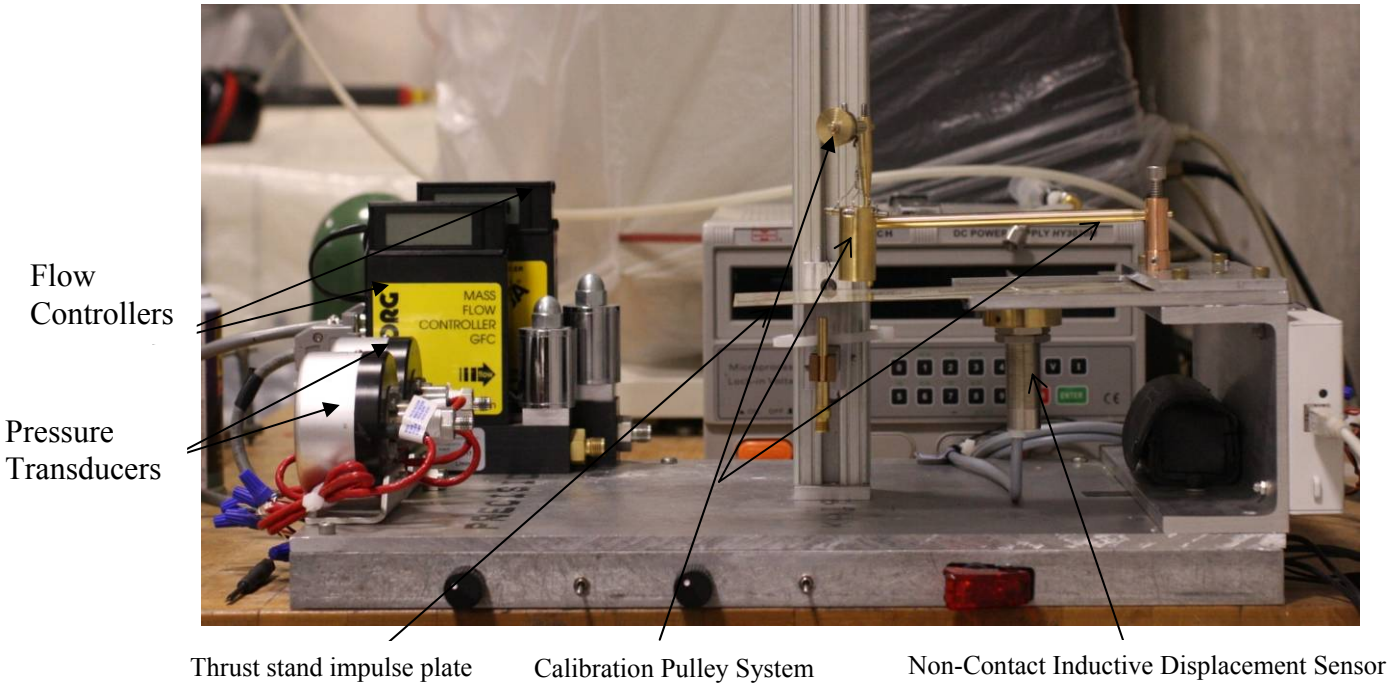

Figure 3.14. Relative locations of the mass flow controllers, pressure transducers, and thrust stand used in pulsing experiments

Since the maximum pulse width used was 1.1 seconds the flow rate delivered by the system during that pulse could not be measured in real time because the response times of the mass flow controllers is too slow. In order to estimate the global equivalence ratio and the total amount of mass consumed during the pulse the flow rate of fuel was calibrated a priori. The fuel flow rate was determined by discharging the fuel for one second at a particular pressure ratio into a catch tank, the mass of fuel discharged into the catch tank was measured on a scale and it is assumed that the fuel was discharged at a constant flow rate for the width of the one second pulse. Figure 3.15 shows a sample calibration curve for methanol.

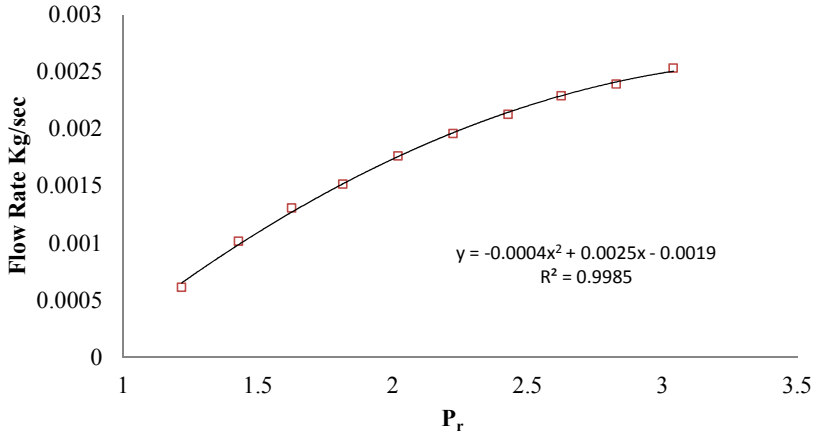

Figure 3.15. Calibration curve for methanol in terms of total mass flow rate versus pressure ratio (upstream/chamber)

The oxygen flow rate was determined in a similar fashion whereby the value set by the thermal mass flow controller was correlated to the pressure drop across the oxygen injection apparatus. The calibration curve for oxygen is shown in Figure 3.16, below.

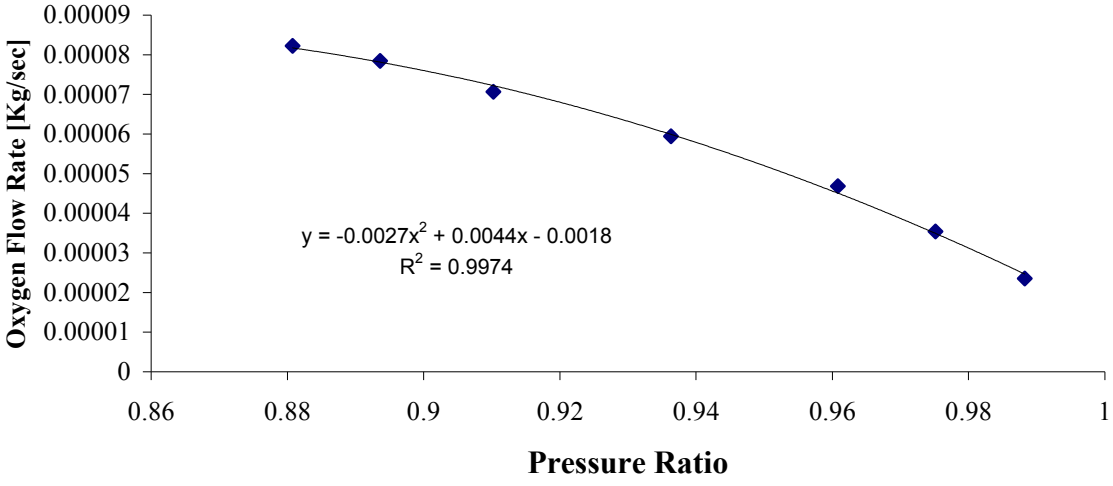

Figure 3.16. Oxygen flow rate versus pressure ratio across the injector

Additionally, preliminary experiments injected the fuel directly into the porous heat recuperator using a 1/16in. OD tube with 1/32" ID. This provided for flow rates that were substantially larger than what the combustor could tolerate, ultimately leading to flooding. A small micro-orifice fuel injector was developed prevent combustor flooding. The fuel injector is shown in Figure 3.17, below. The diameter of the orifice is .003 in.

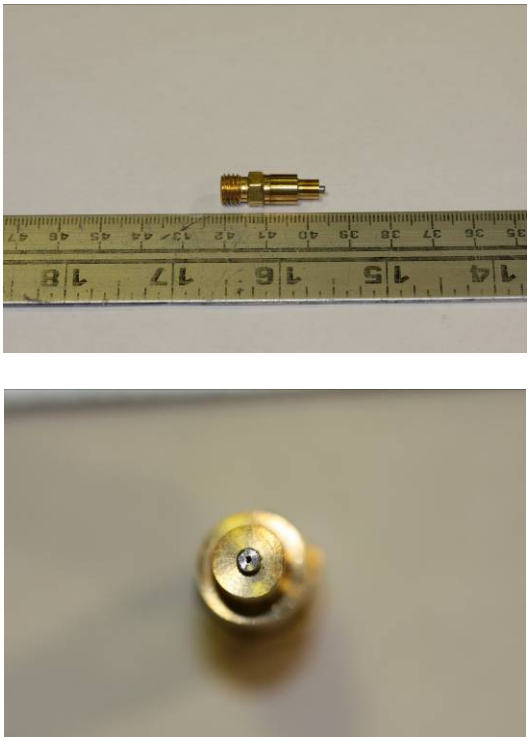

Figure 3.17. Fuel injector

Section 3 Optical Diagnostics

High Speed Video

High speed vide was used extensively to evaluate the presence of instabilities and study the evolutionary nature of the flame during a thrust pulse. An IDT Red-Lake Y4M high speed black and white video camera with a maximum frame rate or 4000fps was used in the experiments. For steady state experiments the high speed video was used to

track the flame dynamics and instability behavior. Each frame was analyzed using MatLab by tacking certain pixels or regions of interest and tabulating the intensity values for those regions versus time. Post processing techniques such as the Fast Fourier Transform were used to analyze the results. A copy of the MatLab code used to acquire the data is provided in the Appendix. For pulsing experiments the high speed camera was synchronized to the data acquisition module via a synchronization lamp wired into the fuel valve power line. The lamp was on upon initiation of the valve trigger. The video data was used to determine the chamber L* along with the ignition delay times versus chamber conditions. The images of the plume along with its phenomenology were also acquired using the high speed video, however no post-processing of the data was performed.

Section 4 Thrust Measurement

Impulse Balance Thrust Stand

In order to determine the overall performance of the thrust chamber a mN level thrust stand has been developed based on the indirect measurement principle, whereby the impulse of the exhaust jet on a plate placed downstream of the jet is measured. The control volume for the thruster-impulse plate system is shown in Figure 3.19, below. [2] This measurement technique has been used by a number of researchers [2,3] for determining the thrust from micro-thrusters, and is used in systems where allowing the thruster to translate is inconvenient because the thrust levels produced are too small to overcome the stiffness of propellant lines and diagnostics fed to the thruster. The basic principle can be expressed by applying the conservation of momentum theorem to the control volume shown in Figure 3.19 [2].

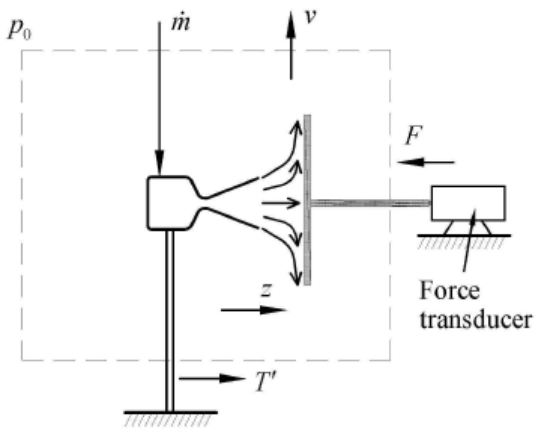

Figure 3.19. Control volume for indirect thrust measurement [adapted from Wu et al., Ref. 2]

In Figure 3.19 the boundaries of the control volume are placed far enough from the thruster and thrust plate that the pressure at the boundary equals the environmental pressure and the inlet mass flow is entering orthogonal to the direction of the thrust force. In this scenario the force experienced by the force transducer attached to the plate, *F*, is equal to the reaction force exerted by the sting on the thruster ,*T*'. Detailed analysis of the aerodynamics of indirect thrust measurement show that this simplified scenario is accurate as long as the thrust plate is large enough that the exhaust gases leave the control volume perpendicular to the thrust force and the plate is far enough away from the thruster exit plane that the impinging exhaust gasses do not interfere with the jet. [2]

The thrust stand is comprised of a cantilevered brass beam with a cross section of 4in. x 0.01in. and a length of 7.0 in. supported at the root by a heavy base clamp. Note that the thrust stand total plate area is 17,920 times larger than the exit plane area of the thruster. The thrust force is related to the displacement of the beam through calibration. The calibration is performed by suspending weights from a pulley mounted to a fixture above the thrust stand, the tension in the line in coincident with the thrust force. The displacement is measured close to the root via an inductive non-contact displacement

sensor. As mentioned previously calibration was performed by applying a load coincident with the thrust force through calibration pulley and dead weights. The relative locations of the thrust stand, displacement sensor, and calibration pulley are shown in Figure 3.20. In the Figure a calibration jet is positioned below the thrust stand.

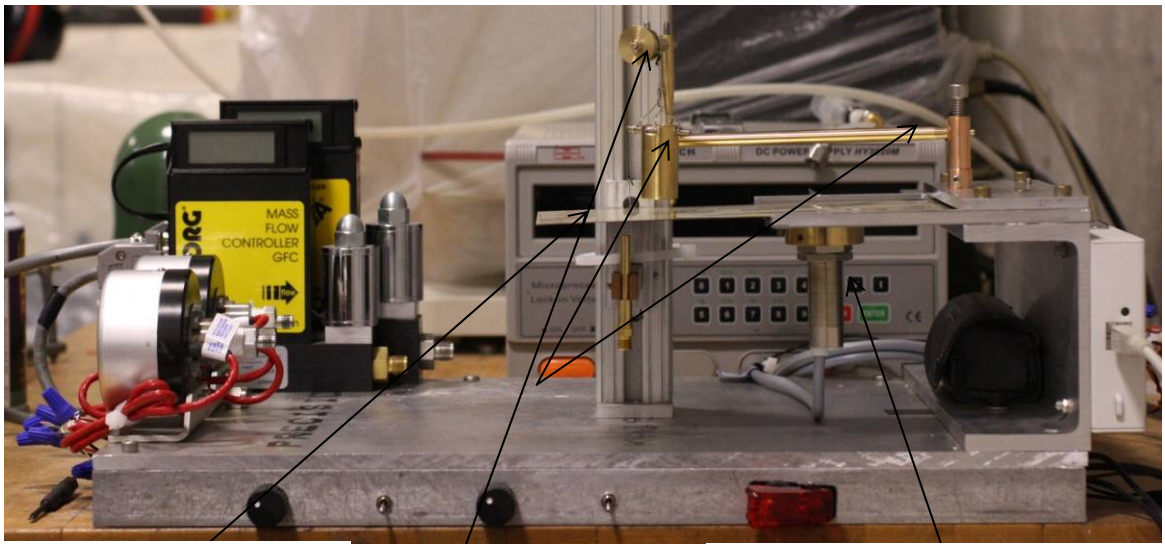

Figure 3.20. Thrust stand with calibration jet indicating the locations of the impulse plate, calibration system, and non-contact displacement sensor

Potential sources of errors associated with the measurement technique are discussed below. Note that these are in addition to those intrinsic to the sensor used to measure either the force on the plate or its displacement.

i. Loss of momentum due to the flow leaving the control volume with residual momentum in the direction of the thrust vector.

ii. Interaction between the exhaust plume and the flow impinging on the plate.

iii. Because the thrust stand is cantilevered, force added to the tip causes a change in the angle of the plate relative to the jet exit plane. This can

cause potential errors due in part to both axial momentum loss and a decrease in the thrust force due to the component of the shear force on the plate in the direction of the thrust vector. There effects are described schematically in Figure 3.21, below

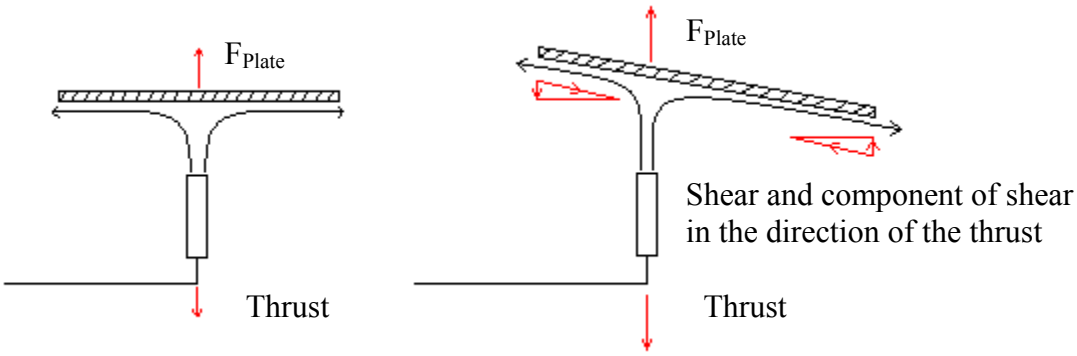

Figure 3.21. Potential sources of error due to the use of a cantilevered beam; the schematic on the right shows the ideal impulse plate force balance, whereas the schematic on the right shows the cantilevered force balance

Experimental analysis has been performed to address these issues and answer the following related questions;

i. How large should the plate be relative to the jet to accurately capture the thrust?

ii. How far from the plate should the jet exit plane be to accurately capture the thrust?

iii. Is deflection angle a concern, and if so what deflection angle is tolerable?

The issue of momentum loss due to flow leaving the control volume in a direction not orthogonal to the thrust vector was not addressed experimentally as this would involve the fabrication of a number of thrust stands of varying size. Alternately the plate

area was sized substantially larger than the jet exit area (17920 times larger) to avoid this problem.

Experiments were performed to determine the appropriate separation distance between the thruster and thrust stand. A facility was developed utilizing a moving calibration jet to simultaneously measure the distance between the thrust stand and the jet exit plane and the thrust. The facility is shown in Figure 3.22, below.

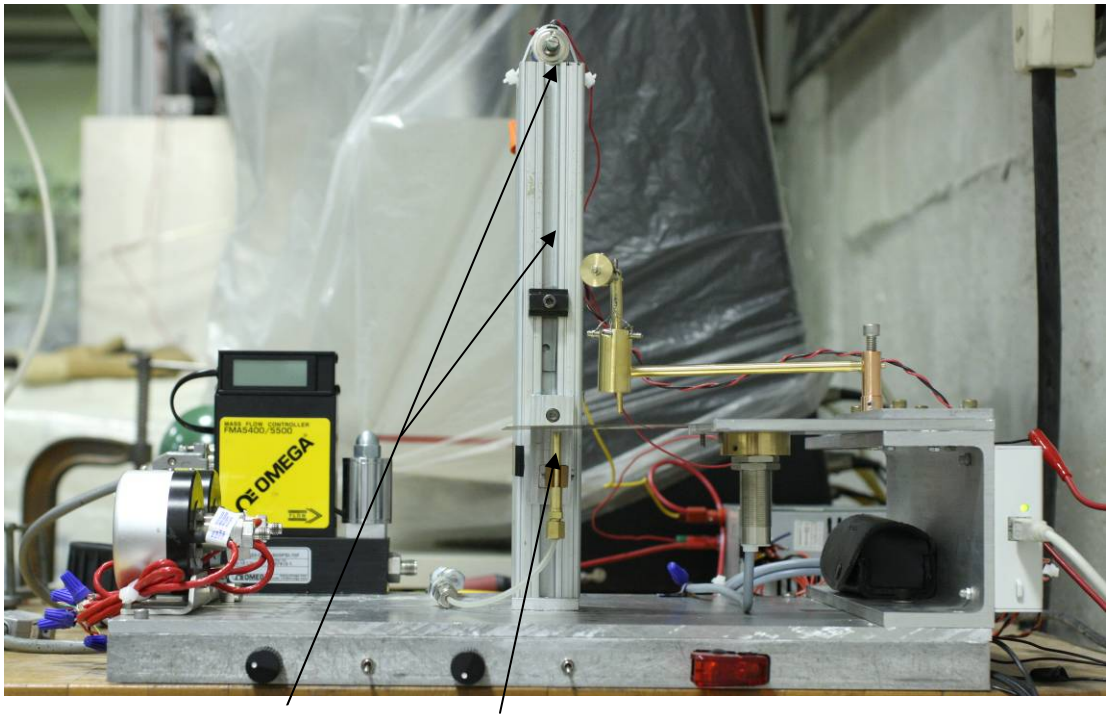

Figure 3.22. Calibration jet (#55), position indicating potentiometer, and thrust stand

The calibration jet [diameter = .0445in. (#55)] is mounted on a carriage and rail assembly and held in place by a set screw. A linear taper potentiometer is attached to the top of the rail and attached to a lug on the back of the carriage via pulley and thread; as the carriage moves the output is from the potentiometer changes, forming an ad-hoc traversing mechanism. In order to acquire the data the thrust stand is zeroed, and the calibration jet is brought as close to the thrust stand as possible. Flow through the

calibration jet is started and the carriage set screw is released, as the carriage falls away from the thrust stand the potentiometer resistance changes and the displacement is calculated via Equation 3.3.

$$y = \frac{D_f - D_o}{V_f - V_o}V - \frac{D_f - D_o}{V_f - V_o}V_o \qquad \text{Eq. 3.3}$$

Figures 3.23, 3.24, and 3.25 show the results of the separation distance experiments at supple pressures of 60psig, 80psig, and 100psig. The pressures correspond to volumetric flow rates of 6.40SCFH, 8.12SCFH, and 9.81SCFH as determined via calibrated orifice (diameter=.010in.).

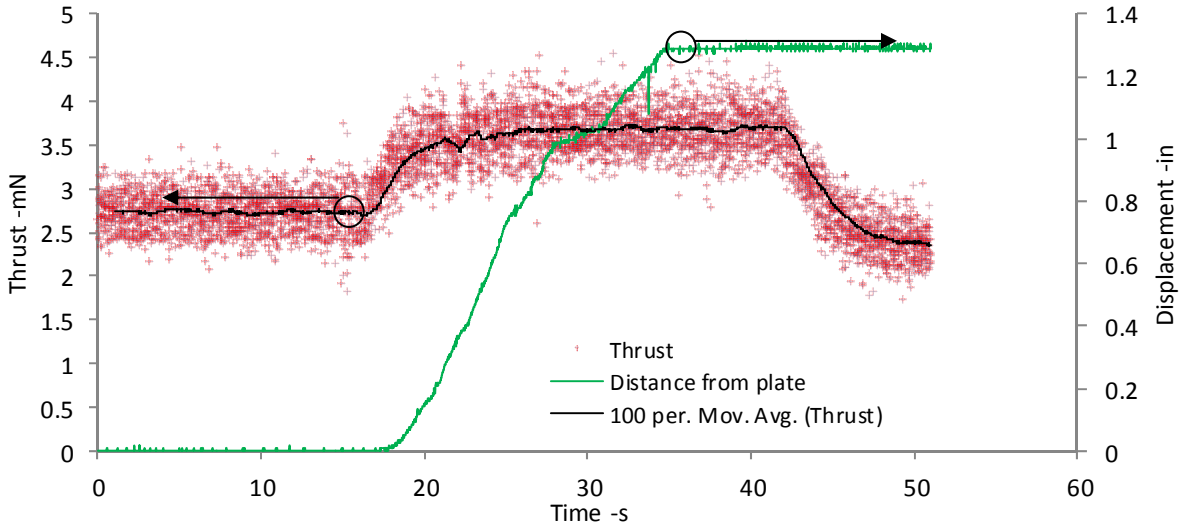

Figure 3.23. Thrust versus distance at 6.40SCFH oxygen flow rate. The green line represents the displacement whereas the black line represents a moving average of the thrust taken in 100 sample increments (at the sampling frequency). The red markers are the raw data, the spread in the raw data is due to zero mean random noise which has been shown, via FFT, to have no discrete frequency components.

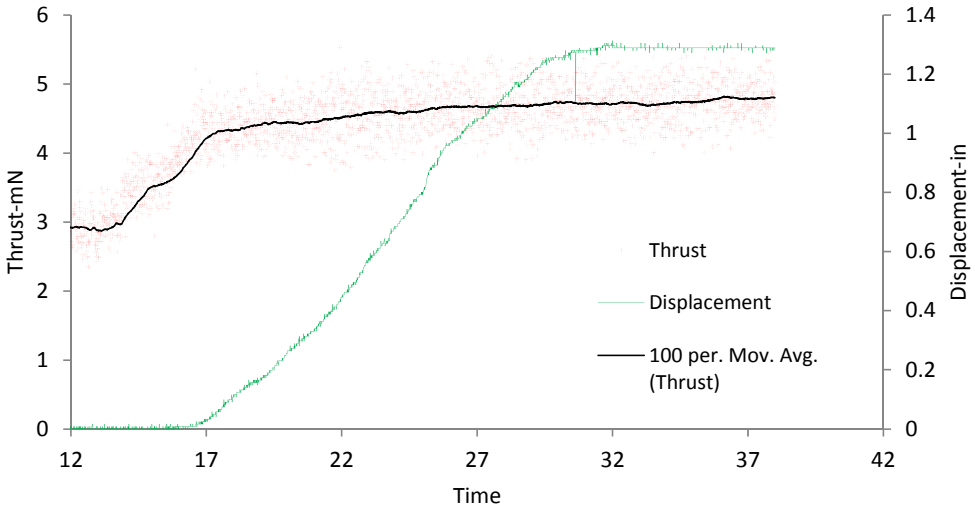

Figure 3.24. Thrust versus distance at 8.12SCFH oxygen flow rate. The green line represents the displacement whereas the black line represents a moving average of the thrust taken in 100 sample increments (at the sampling frequency). The red markers are the raw data, the spread in the raw data is due to zero mean random noise which has been shown, via FFT, to have no discrete frequency components.

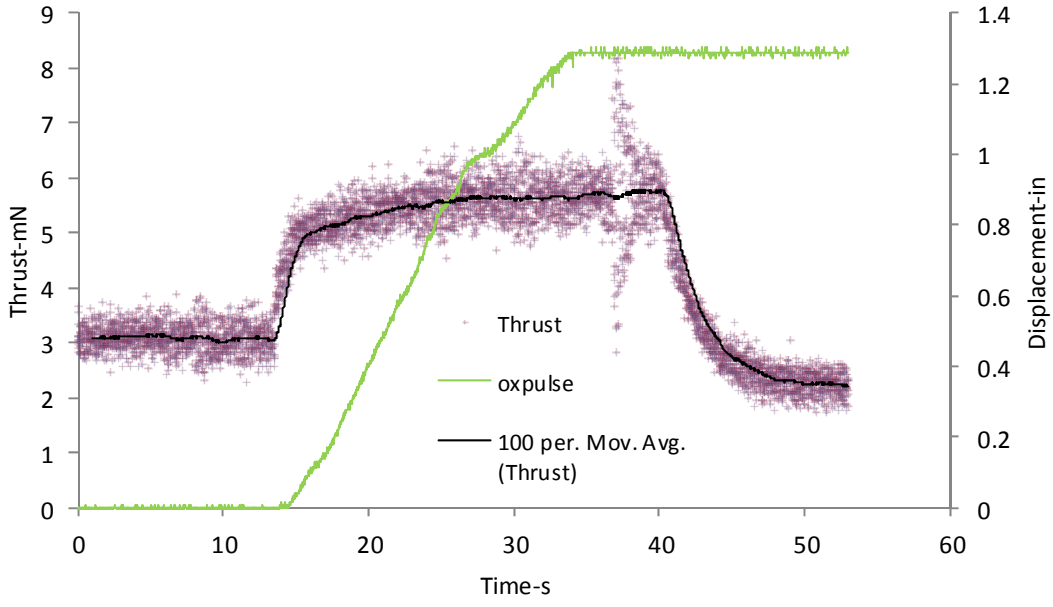

Figure 3.25. Thrust versus distance at 8.12SCFH oxygen flow rate. The green line represents the displacement whereas the black line represents a moving average of the thrust taken in 100 sample increments (at the sampling frequency). The red markers are the raw data, the spread in the raw

data is due to zero mean random noise which has been shown, via FFT, to have no discrete frequency components.

In Figures 3.23, 3.24, and 3.25 the right hand side 'y' axis represents the displacement from the plate in inches. The zero displacement level, where the calibration jet is almost touching the thrust stand, corresponds to the minimum thrust level on the left. As the jet is moved away from the thrust stand the thrust increases, and above a certain distance no measurable increase in thrust can be observed. For the three examples shown above this distance is approximately .9in away from the thrust stand, however 90% of the mean thrust us realized once the calibration jet has cleared .4in from the thrust stand or approximately 10 jet diameters. The measured thrust decreases sharply below this point.

In order to determine the effect of plate angle on the measured thrust an experiment was conceived whereby the plate would be displaced by a measured pre-load. Digital images were used to determine the tip deflection angle. The images and corresponding beam deflection angles are shown in Figure 3.26, below.

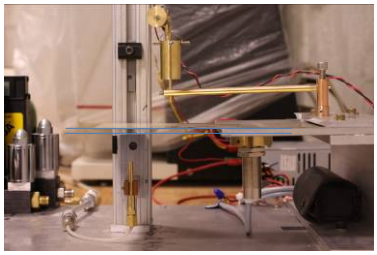

~0 Deg

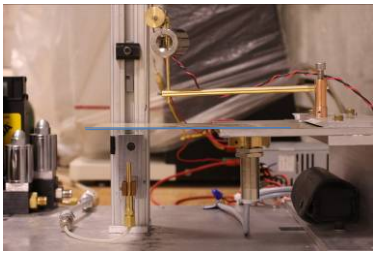

1 Deg

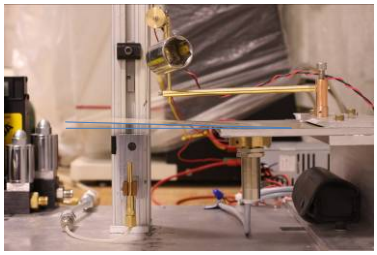

3 Deg

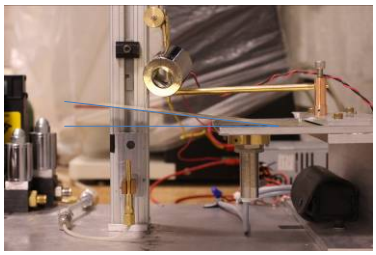

6.5 Deg

Figure 3.26. Four measurements of beam deflection by a pre load to a specific angle. The lines used to calculate the angular deflection and the deflection angles are shown in the figure.

The preload was not used to calculate the angle based on beam bending theory because the beam deflects under its own weight, and a certain amount of preload is required to maintain a level surface. Once the deflection angle has been established and the beam has stabilized the calibration jet is used to apply a force of fixed flow rate (9.81SCFM or 7.48mN as calculated from continuity) and the output from the displacement sensor recorded. The variation in displacement in response to the jet as a function of the beam deflection angle is shown in Figure 3.27, below.

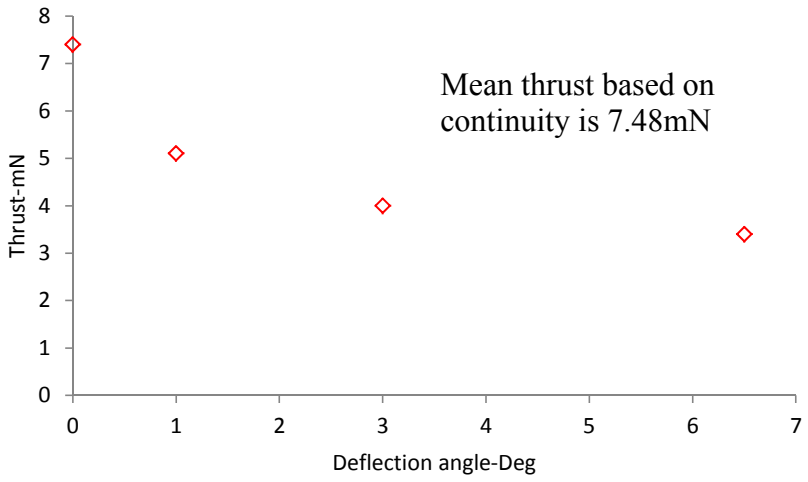

Figure 3.27. Deflection angle versus measured thrust for a 9.81SCFM calibration jet; note that the measured thrust decays rapidly with any increase in deflection angle, and tends to level off at large (~7 Deg.) deflection angles.

The results shown in Figure 3.27 indicate that even small deflections in the beam angle can result in significant variation in the thrust measurement. As second experiment was conducted to determine the effect of beam deflection angle on a variable thrust force and determine a correction factor that relates the measured thrust and the actual thrust.

Figure 3.28 shows the variation in thrust calculated at the exit plane of the calibration jet (shown in Figure 3.27) based on continuity versus the thrust force measured at the thrust stand. Additionally the ratio of the measured thrust to actual thrust is also shown (T/T_0).

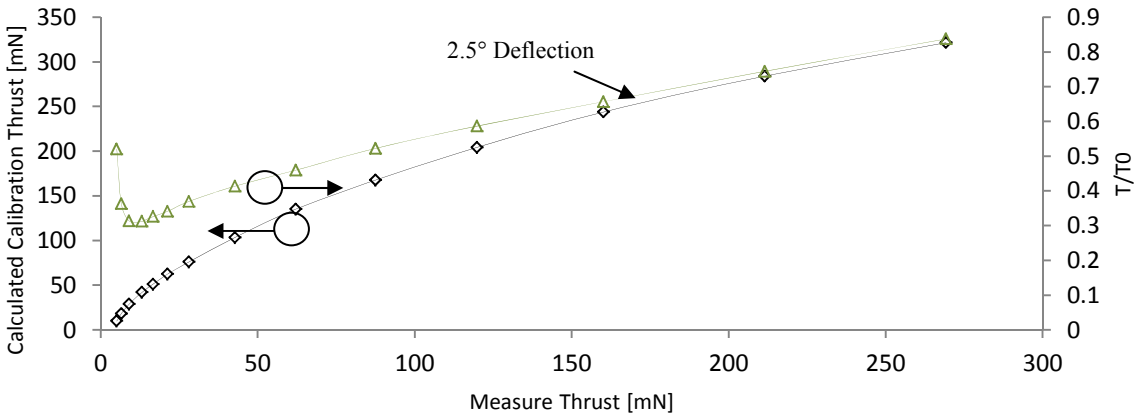

Figure 3.28. Variation in thrust calculated at the exit plane of the thruster versus the measured thrust along with the ratio of the measured thrust to the calibration thrust

Figure 3.28 shows that the effect of deflection angle is dramatic at low to moderate thrust levels however the T/T_0 ratio grows as the thrust force increases. This can be seen in Figure 3.27 as well where the measured thrust decreases sharply with deflection angle up to a deflection angle of ~2.5° at which point any increase in the deflection angle produces a negligible change in the error. Since a wide variety of beams are available in the 4in. width required for the thrust stand assembly in the course of experimentation beam bending theory was used to determine the beam thickness required that would result in the minimum displacement for the expected thrust level.

Additional sources of error may arise from the following sources (non-inclusive): twisting of the beam due to a non-centered application of the load and effects of the beam surface not being parallel with the sensor plane. Both of these effects can be minimized by careful experimentation and calibration, respectively.

The composite result of seven calibrations from 0-100mN is shown in Figure 3.29; the results are presented in terms of voltage output from the sensor along with the theoretical results for beam displacement versus load. The composite result shows a

linear relationship between the applied load and the voltage output from the displacement sensor which is consistent with both the linear response of the sensor, and the linear relationship between load and displacement provided by beam bending theory. Note that in measuring the thrust the thrust stand is recalibrated immediately prior to each experiment and the calibration obtained is used to determine the thrust.

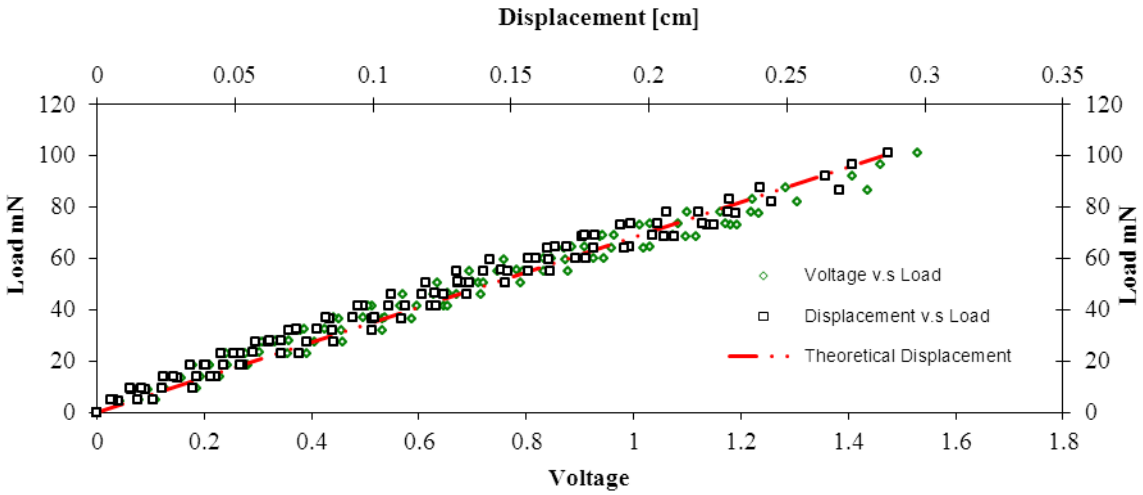

Figure 3.29. Composite calibration curves for the cantilever beam versus both voltage and displacement

Figure 3.30 shows the calibration curve extended to 366mN, above ~100mN the calibration is no longer linear and a quadratic fit is used to obtain the thrust measurements. Measurements at high loads (large beam displacements) are more prone to error due to inclination angles between the thrust stand and sensor face, and the thrust stand and nozzle exit plane as discussed above.

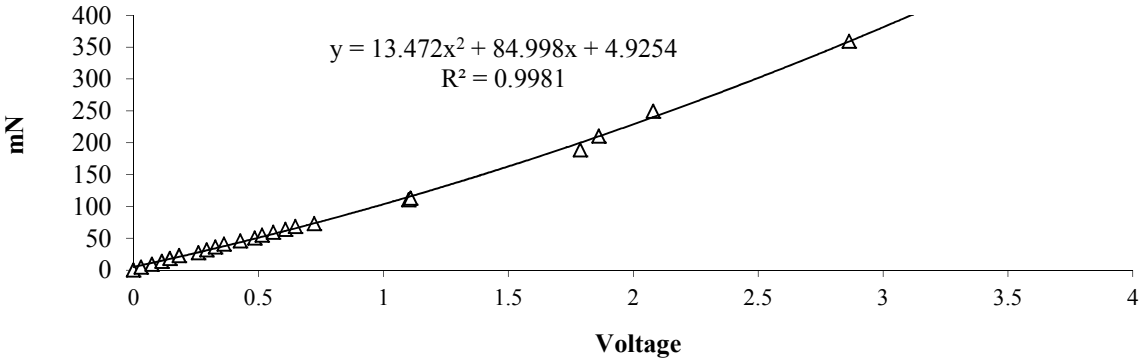

Figure 3.30. Calibration curve extended to 366mN, note that above 100mN the calibration is non-linear. The quadratic curve fit to the calibration data is shown as well

The sensitivity of the thrust stand was measured by incrementally increasing the load until the output from the sensor could be differentiated from the noise; the sensitivity was determined to be 1.2mN. A histogram of the output voltage measured at the step calibration load (3mN) over 300 measurements was used to determine the precision error in the measurement, the mean and standard deviation (scaled by the calibration curve) was found to be 3.006mN and .1026mN respectively. Figure 3.31 shows both the sensitivity and precision error measurements.

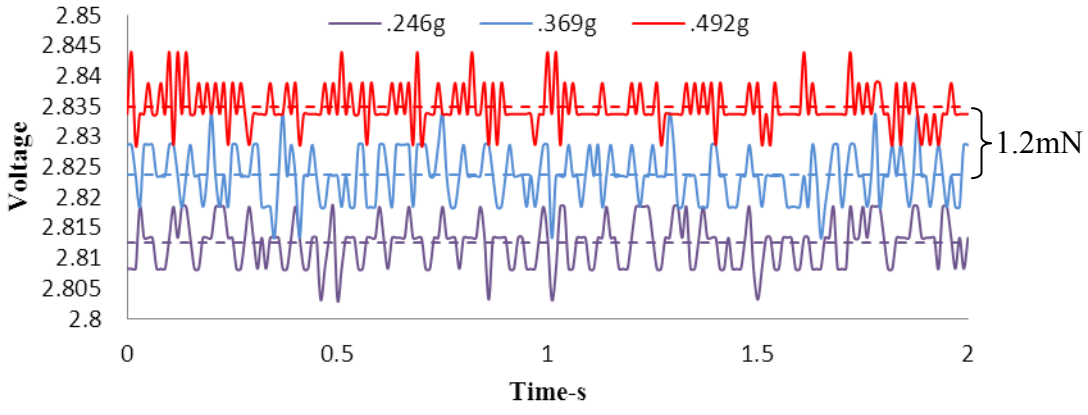

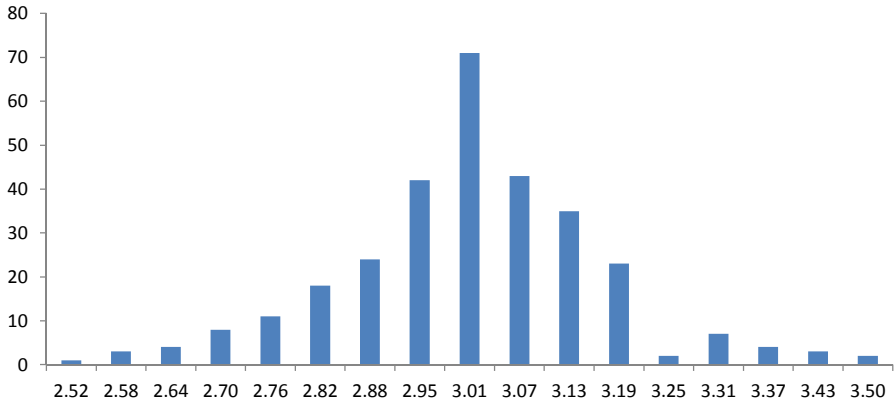

Figure 3.31. Sensitivity and precision error measurement

From Figure 3.31 (bottom) a .602mN standard error reflects a 95% confidence interval around the mean value and will be used as the standard error in thrust measurement for the remainder of this report.

Since the exhaust jet from the thruster is hot the response of the beam to a change in beam temperature was determined in order to correct for any variations in the measurement that might occur due to changes in the beam geometry via thermal expansion. In order to evaluate the behavior, the beam was held at a constant load of 59.61mN and the underside of the beam was heated by a candle flame. The beam temperature was measured by thermocouple and the change in displacement was recorded over a long period of time. Figure 3.32 shows the thermal stability results, indicating that fluctuations in the beam response to change in temperature are within the .602mN standard limits of error described above for a beam within 25-150°C. Based on these results no correction for beam temperature will be made.

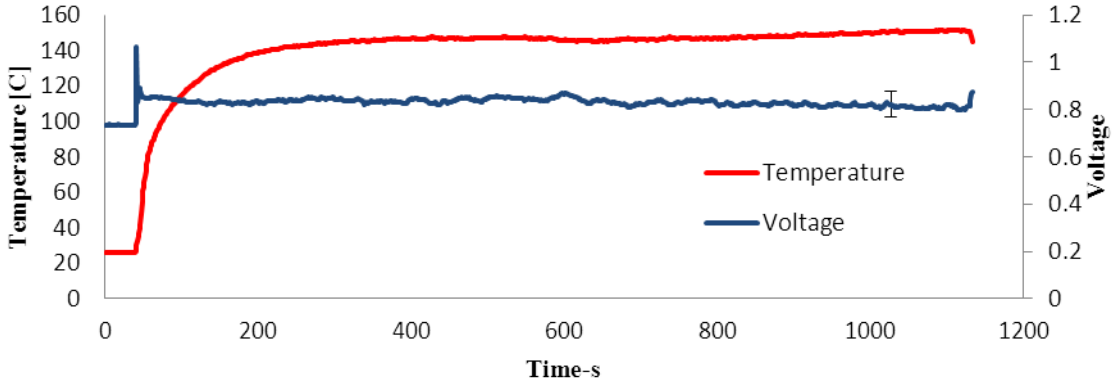

Figure 3.32. Temperature stability over time, representative error is shown by the error bar on the right

Using both the calibration and error estimation presented in Figures 3.29 and 3.31 the thrust stand was tested by measuring the thrust force exerted by a 1.0mm diameter circular jet on the plate and comparing it to the calculated thrust force at the exit plane of the jet. The force was calculated as the product of the mass flow rate and the velocity, where the velocity was calculated through continuity, the flow was assumed to be both uniform and incompressible at the jet exit plane. Figure 3.33 shows the thrust force versus oxygen volumetric flow rate for the circular jet test where the discrete points are the experimental data and the dashed red line is the calculated theoretical result.

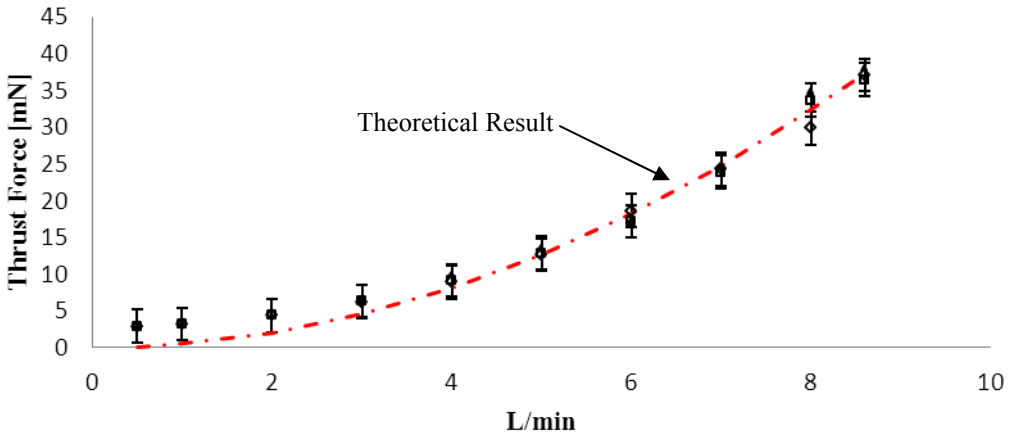

Figure 3.33. Thrust force exerted by a circular jet on the thrust stand versus the theoretical result

Figure 3.33 shows reasonable agreement between the measured thrust force and the calculated results. The measured values deviate from the theoretical result at low flow rates (low thrust) because the calibration curve does not pass through the origin, whereas the theoretical result does.

Since the thrust stand behaves like an under damped mass-spring-damper system the damped natural frequency, spring constant, and damping ratio were determined experimentally in order to analyze the temporal variations in the thrust force at steady state. Figure 3.34 shows the time decay in displacement for the thrust stand resulting from an arbitrary initial displacement. The experimentally determined values yielded a damping ratio of 0.0885, damped natural frequencies of 3.55Hz, 15.1Hz, and 34.71Hz, and a spring constant of 382.49mN/cm.

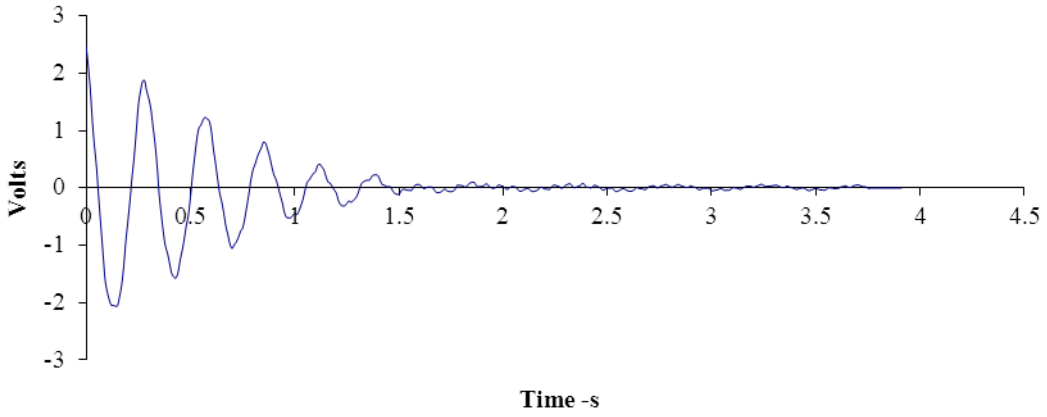

Figure 3.34. Time history in displacement (in volts) for the thrust stand in free vibration

The natural frequencies of the thrust stand were filtered out of the final result using a digital stop band filter integrated into the National Instruments Lab-View virtual instrument used to gather and process that data.

Section 5 Procedures

Experimental procedures will be discussed in the results section, this is done to allow for the discussion of the effects of procedure on both the results and the performance of the thruster.

Section 6 References

[1] Vijayan, V., "Combustion and Heat Transfer in Meso-Scale Heat Recirculating Combustors,". PhD Dissertation, University of Maryland at College Park, 2010.

[2] Wu, C.K.,Wang, H.X., Meng, X., Chen, X. Pan, W.X. "Aerodynamics of indirect thrust measurement by the impulse method", *Acta Mechanica Sinica,* Vol.27, 2011, pp. 152-163.

[3] Lun, J. "Development of a vacuum arc thruster for nanosatellite propulsion". Masters Thesis. Stellenbosch University.2008

Chapter 4: Results

Section 1 Organization of the experimental results

The experimental results will be organized in way that highlights the developmental progress of the meso-scale thruster while capturing the technical lessons learned along the way. Experimental results will be compared to those found in the literature to explain the physical significance of the results and attempt to shed light on the phenomenology. The results are presented by first discussing the nature of flame extinction in meso-scale thrust chambers and the effects of fuel/oxidizer inlet conditions, fuel injection strategy, and geometry on the flame extinction limits. The effects of fuel, geometry, and fuel injection strategy on the thermal performance of the combustion will then be addressed. Third the effects of Reynolds number on the thruster nozzle discharge coefficient and steady state thrust production will be discussed and compared to the thermal performance results presented prior. The results section will conclude with a discussion of the pulsing performance of the thruster.

Section 2 Extinction Behavior

Partially Premixed Combustion

Micro and meso-scale combustor in the literature largely focus on the combustion of premixed gaseous reactants. This is done because mixing and burning in small volumes with very limited residence times adds an additional challenge to the meso-combustion problem. Although the gaseous premixed configuration is valuable in addressing the basic characteristics of the combustor, moving toward a non-premixed

liquid fuelled configuration is necessary in order to apply the combustor to any practical device. As such the initial configuration used here is a partially-premixed with the fuel being injected through a porous heat recuperator placed upstream of the combustion volume. The combustor is shown in Figure 4.1 below.

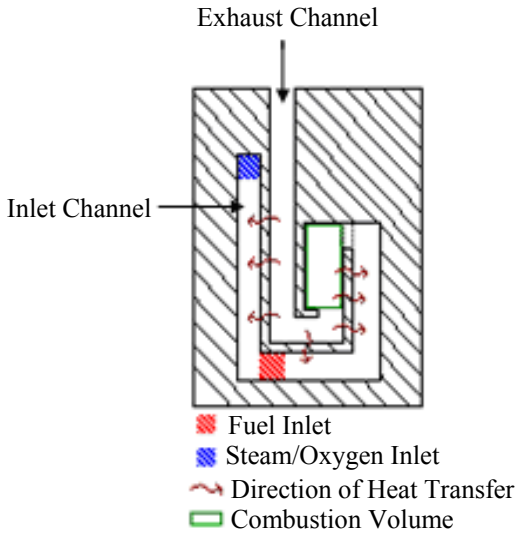

Figure 4.1. Single turn partially-premixed combustor

In the analytical study of non-adiabatic heat recirculating combustors *Ronney* [1] identifies two distinct extinction limits; a high mass flow rate or "blow off" limit where fresh mixture is delivered to the reaction zone faster than it can be consumed, and a low mass flow rate heat-loss driven limit where the fraction of heat release lost to the ambient increases with decreasing mass flow rate leading to thermal quenching of the flame. This dual limit behavior is consistent with the findings of other researchers. [2,3] However, the analytical model is limited by the fact that the reaction zone is assumed to remain in the same location regardless of the inlet conditions.

Figure 4.2 shows the extinction regime for the partially-premixed combustor with aspect ratio of 0.5 utilizing steam and oxygen as an oxidizer and methanol as fuel. The

extinction regime demonstrates the dual branched behavior that is typical of this type of combustor. The fuel lean limit represents flame blow-off which was observed through the window of the combustor. The rich combustion limit represents a flashback limit where high fuel concentrations and high oxidizer inlet temperatures (between 500-550°C prior to mixing with fuel) combine with low channel velocities allowing the flame to propagate upstream of the combustion chamber, and stabilize at the fuel injection location. [Note that auto ignition temperature of methanol is 470°C]. This is analogous to the "out-of-center" reaction zone reported by *Ronney et. al.*[4] (see Figure 2.5 Section 2.1), however, in the context of this study the flame is considered "extinct" at the flash-back limit.

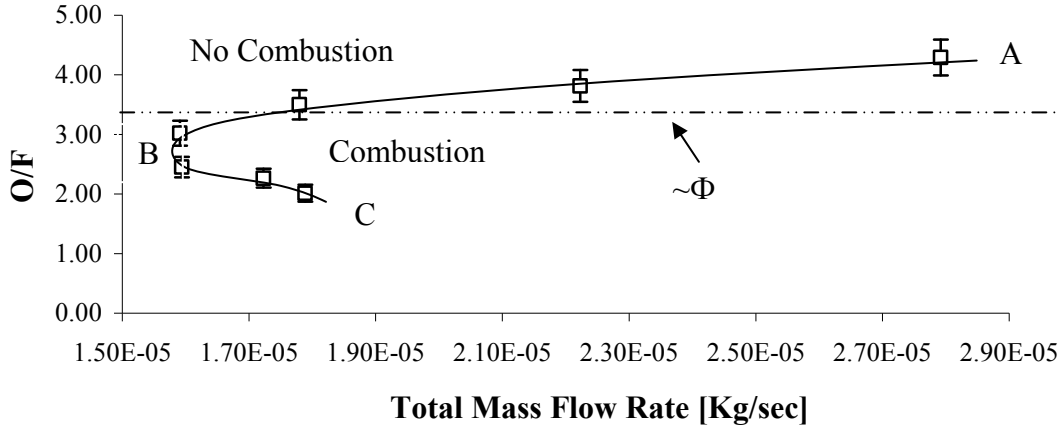

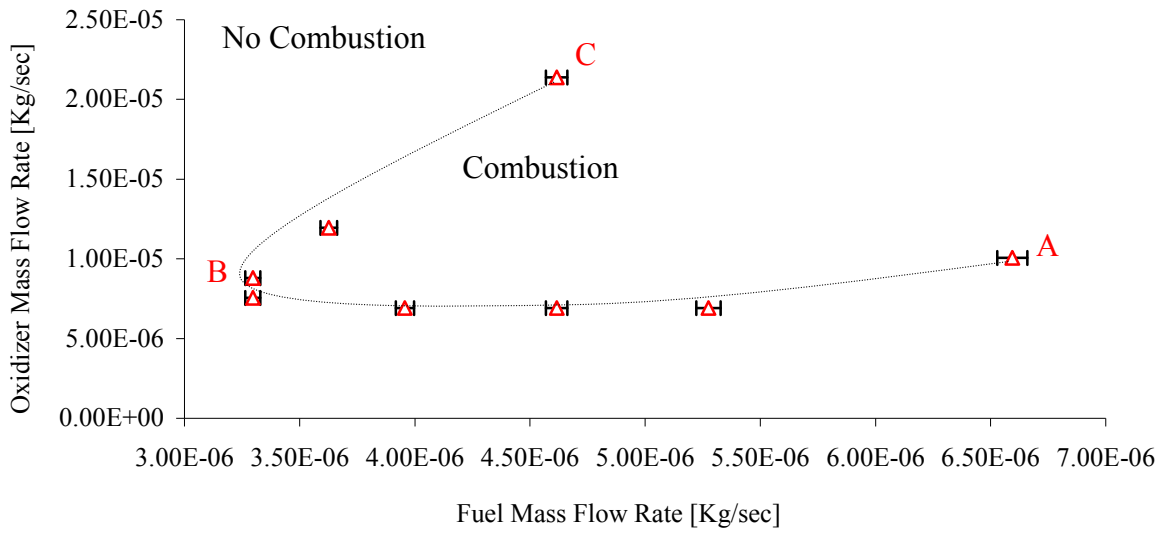

Figure 4.2. Extinction limits for the partially-premixed combustor burning methanol-steam-oxygen

In Figure 4.2, top, the top line representing the lean blow off limit is nearly horizontal with only a slight increase in slope with increase in total mass flow rate towards high O/F ratios (lower Φ). This is because the inlet velocity to the combustion volume is largely dependent on the oxidizer flow rate and independent of the fuel flow rate. Because of this, the combustor blows off at almost the same oxidizer flow rate for all conditions, the slight increase in the equivalence ratio being due to the addition of slightly more fuel. Note that in order to determine the upper performance limit a flame is stabilized at an equivalence ratio close to unity and the hydrogen and oxygen flow rates are incrementally decreased at constant equivalence ratio until a flame is no longer supported. The lower limit is found through an analogous procedure. At each increment the combustor is allowed to reach steady state, this was determined by thermocouple measurements taken in the exhaust.

The ‘C’ shape is essentially described by three points, as labeled in the figure: point A is a structural limit which is discussed later, point B is the minimum stable Re

(rich extinction limit at the minimum heat input), and point C is the rich extinction limit at the maximum heat input. Experimentally, point A is the point where the combustor fractures due to overheating and occurs at roughly the same point for all the tested configurations and is thus dictated by material properties. The fracture occurs at the junction of the steam generator and the heat recirculating combustor. Points B and C are associated with flame flashback and are thus sensitive to the combustor geometry, since it plays a role in channel velocities and upstream gas temperature which influences flame velocities.

In order to further understand the flashback behavior simulations were performed in Chemkin to determine the laminar flame speeds of mixtures of methanol/steam/oxygen. The flame speeds of mixtures of methanol/superheated steam/ and oxygen are calculated using the C1 mechanism [5,6] for methanol oxidation. However they are not correlated to experimental data due to a lack thereof, for this reason the calculations should be taken only as a qualitative comparison to established experimental data for methanol/air. Flame speeds are calculated using the PREMIX subroutine of the Chemkin software package. Figure 4.3 shows the flame speeds for a mixture of steam/oxygen/methanol at 400K, along with simulation results for methanol/air at 358K and experimental results from *Liao et. al.*[7] and *Saeed and Stone*[8] for methanol/air at 358K. For the following calculations the molar ratio of steam to oxygen is fixed at 2 to 1.

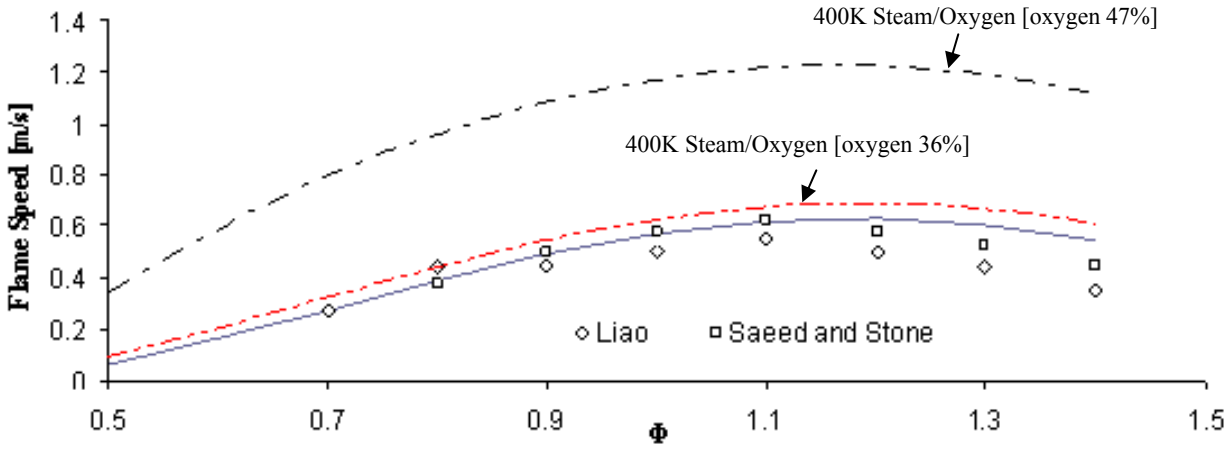

Figure 4.3. Laminar flame speeds for methanol/superheated steam/oxygen and methanol/air as compared to literature values

The 358K methanol/air simulation results correlate well with the experimental data in the lean regime with slight overestimation in the rich regime. Due to the reasonable fit the same model parameters (grid points, gradient and adaptive curvature options) used for the methanol/air simulations were used for the superheated steam/oxygen/methanol simulations. Flame velocities for methanol/superheated steam/oxygen are estimated to lie between 35cm/s and 1.1m/s with a maximum at an equivalence ratio of roughly ~1.1. Additionally, Figure 4.3 shows the flame velocity for decreased oxygen concentration (36% by mass). Figure 4.4, shows the adiabatic flame temperatures for superheated steam/oxygen/methanol and air/methanol. The burned gas temperature is higher for mixtures of steam/oxygen/methanol as compared to mixtures with air for the same unburned gas temperature; this likely drives the higher flame speeds since flame speed has a strong direct dependence on burned gas temperature.[21] Adiabatic flame temperatures are calculated using CEA.

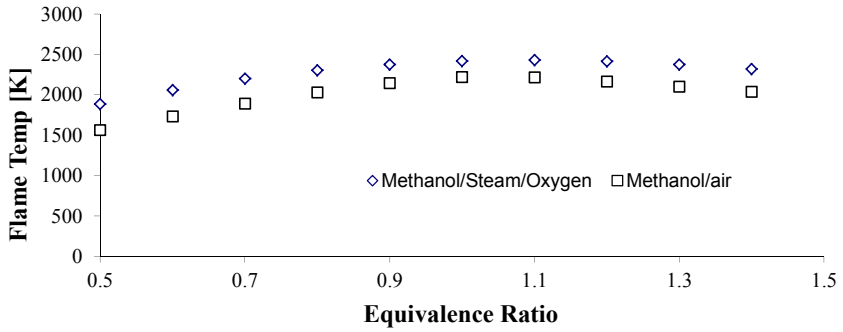

Figure 4.4. Adiabatic flame temperatures for methanol/superheated steam/oxygen and methanol/air

Using the flame speed data shown in Figure 4.3, the quenching distance can be approximated using Equation 4.1 .[9]

$$d = 2\alpha\sqrt{b/S_L} \qquad \text{Eq. 4.1}$$

In Equation 4.1 "d" is the quenching distance, "α" is the thermal diffusivity of the burned gas, "b" is an arbitrary parameter, and "S_L" is the flame speed. It is important to note that Equation 4.1 is derived for a one dimensional laminar flame in a slot formed by two parallel walls, subject to the condition that the rate of heat liberated by chemical reaction is equal to the rate of heat lost from the flame by conduction to the walls. Figure 4.5 shows the schematic diagram used to formulate the model.[9] This approximate solution considers only thermal quenching of the flame and does not consider quenching caused by the diffusion and termination of active species at the wall.[10] Figure 4.6 shows the approximate quenching distance for methanol/steam/oxygen and methanol/air for an un-burnt gas temperatures of 400K. The thermal diffusivities of the equilibrium combustion products are calculated using CEA. The value of "b" has been chosen such

that Equation 4.1 yields 1.8mm for methanol/air at an equivalence ratio of 1 and un-burnt gas temperature of 298K, which is the experimentally determined quenching distance found in the literature.[21]

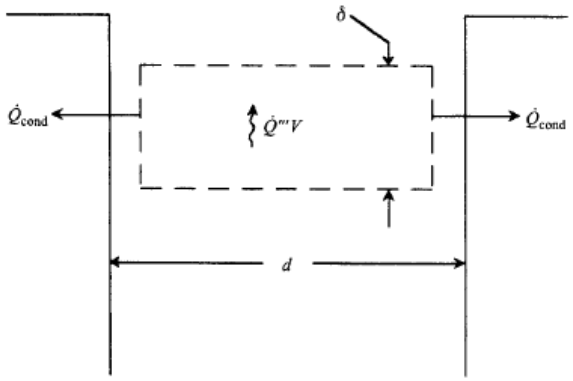

Figure 4.5. Laminar flame in a slot formed by two parallel walls[21]

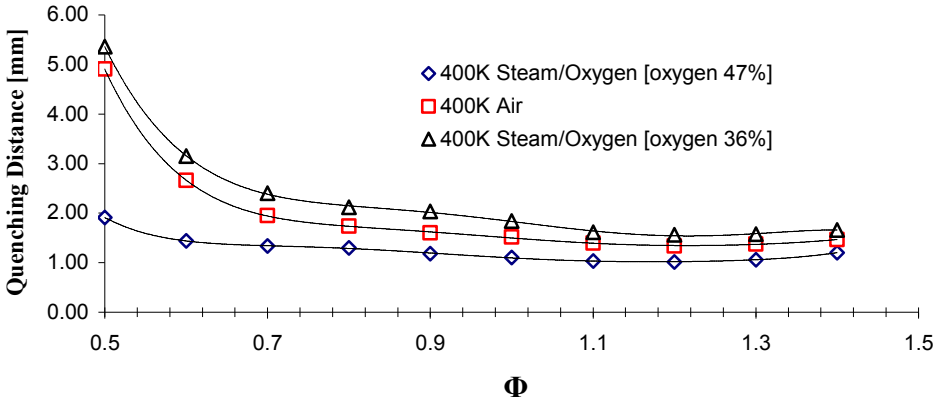

Figure 4.6. Simulation results of the quenching distances for methanol/air and methanol/steam/oxygen

Figure 4.6 shows that the variation in quenching distances between 400K Steam/Oxygen [oxygen 47%] and 400K air is not significant (.31mm or 29% at the minimum), which is unexpected considering the significant difference in flame velocity (.6m/s or 97% at the maximum. This is because the thermal diffusivities of the combustion products of Steam/oxygen are on average 140% larger than the thermal diffusivities of mixtures in air. Within the scope of the model used to derive Equation 4.1 the result of increasing the

thermal diffusivity is an increase in the thickness of the laminar flame, which results in a larger projected area of the flame on the wall and larger rates of heat loss. At lower oxygen concentrations, the quenching distances are larger than those in air due to the same effect, even though the flame velocities are slightly higher.

Since the fuel lean and fuel rich extinction limits are blow-off and flash-back limits respectively they are intrinsically related to the velocities and mixture composition at the inlet to the combustion volume. The latter relates to the flame velocity that can be supported by the inlet mixture. Hence extinction limit control should be possible by varying either the inlet geometry (inlet to the combustion chamber, which is analogous to the channel geometry) or the inlet mixture composition. Varying the inlet mixture composition is done by changing the concentration of oxygen in the oxidizer stream, which is analogous to changing the inlet concentration of hydrogen peroxide. Two additional combustors were fabricated to test the effect of channel width on the combustor extinction limits; the channel aspect ratio was sized such that the Reynolds number, based on hydraulic diameter, was constant between the two combustors for identical inlet conditions. Hence the narrower channel is deeper in order to maintain a constant hydraulic diameter. The result is three combustors with channel aspect ratios of .5, and .4, and .3 respectively. Figure 4.7 shows the extinction regimes for the three combustors. The extinction regimes are written in terms of total mass flow rate and O/F ratio and in terms of cold flow inlet velocity versus O/F ratio. Note that the cold flow channel velocities are calculated for oxygen, steam, and methanol, and the 100C (temperature of saturated steam at 1atm).

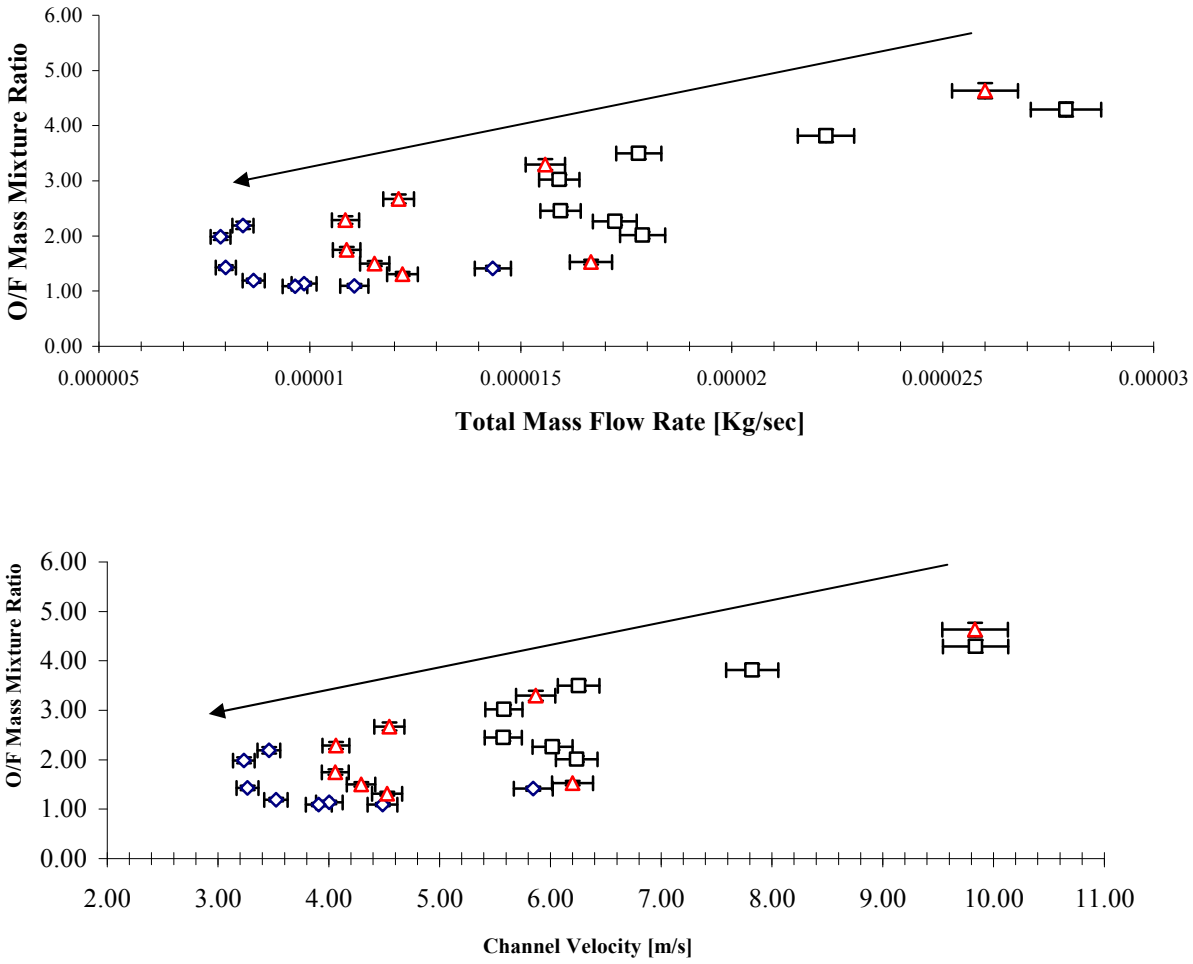

Figure 4.7. Extinction regimes for the partially-premixed combustors with three different aspect ratios, the arrow points in the direction of decreasing channel aspect ratio.

In Figure 4.7, top, the low mass flow rate extinction limits shift to the left with decreasing channel aspect ratio. In each of the three cases the upper branch represents a blow off limit while the lower branch represents a flashback limit. In Figure 4.7, bottom, the lean blow off limits for the three combustors lie along roughly the same line, however the rich limits are biased towards lower channel velocities for lower aspect ratios. Since preheating will cause a substantial increase in the mixture temperature the channel velocities shown in Figure 4.7, bottom, are likely less than what actually occurs. However, it is possible that the enhancement of flame velocity due to preheat offsets the

increase in flow velocity due to temperature, enabling the flame to flashback at the rich limit. The leftward shift of the rich extinction limit at lower aspect ratios could be attributed to a loss of flame speed due to a larger fraction of the heat released being lost to the ambient, preventing flashback at comparatively lower channel velocities. This becomes evident when for identical inlet compositions low aspect ratio combustors demonstrate lower exhaust temperatures than their high aspect ratio counterparts. The larger heat loss occurs because the channel aspect ratio was varied such that the channel Reynolds number is constant for the same inlet conditions; this means that as the channels are made narrower they are also made deeper. This increases the outer wall area which is responsible for transferring heat away from the flame

Additionally, the diffusive mixing in the upstream channel may play a role in initiating the flashback behavior. Note that in comparing the cold flow channel velocities presented in Figure 4.7 to the laminar flame velocities presented in Figure 4.3 the cold flow channel velocities are larger than the predicted laminar flame velocities for the entire extinction regime, especially at O/F ratios. [Cold flow velocities ranging from 4-10 m/s] Hence flashback is more likely to occur near the walls where the velocity field vanishes. [11] Since the combustor operates in a non-premixed mode the flashback propensity for a particular geometry should be related to both the local velocity and the local equivalence ratio in the channel upstream of the combustion volume. Since the Reynolds number in the channel is laminar at best ($100<Re<600$) the mixing upstream of the combustion chamber should predominantly be due to molecular diffusion. Isothermal mixing simulations performed in commercially available CFD software indicate that the mixture immediately upstream of the combustor is only partially premixed, and large

gradients in fuel mass fraction (local equivalence ratio) exist in the channel. Figure 4.8 shows the simulation results for methanol at the rich extinction limit of the AR=.5 combustor for an inlet methanol flow rate of .30mL/min. From left to right: (i) shows the velocity field at the entrance to the combustion chamber, (ii) shows the equivalence ratio field at the entrance to the combustion chamber and (iii) shows regions on the plane where the local flow velocity in the direction of the channel is smaller than the local flame velocity at the same location ($0<V_y/S_L<1$), these are regions where flashback would be more probable.

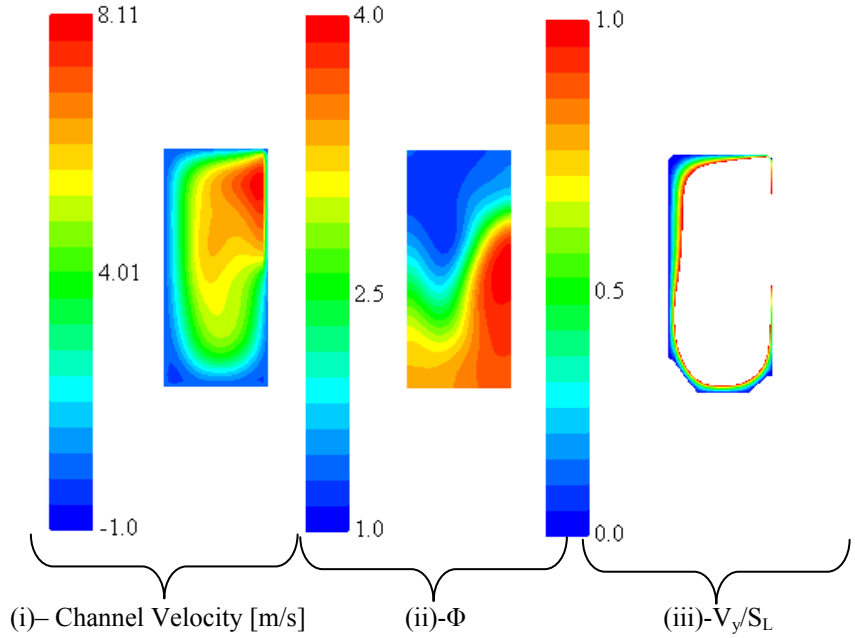

Figure 4.8.Channel Velocity, Equivalence Ratio, and Flashback Propensity on the cutting plane

In Figure 4.8i the velocity field in the direction of the channel indicates low velocity regions on the bottom left and right hand portions of the channel with higher velocities at the top of the channel close to the entrance to the combustion chamber and the high velocity core flow. In Figure 4.8ii the reddish region near the bottom of the image represents the developing fuel mass as it diffuses into the oxidizer rich region

above it; due to the high global equivalence ratio stoichiometric conditions are found near the top left hand portion of the channel with fuel rich regions in the high speed core flow. Figure 4.8iii shows regions where the flashback propensity should be high (regions where $V_y<S_L$), these regions are close to the wall and predominantly at the top left hand corner of the channel, where the local equivalence ratios favor higher flame velocities. The results suggest two conclusions: first, even in the presence of high mean channel velocities the partially premixed combustor can succumb to flame flashback if the local equivalence ratio near the wall can support large flame velocities; and second, the tendency for flashback is a symptom of incomplete mixing. Providing more aggressive mixing upstream of the combustion chamber inlet could alleviate this problem by ensuring that the mixture is closer to the global equivalence ratio, which at the rich extinction limit cannot support high flame velocities.

The rich extinction behavior has also been investigated through thermodynamic analysis of the combustors it approaches the rich extinction limit. This is done semi-empirically by measuring gas temperatures at particular locations in the combustor and using tabulated gas properties to calculate the enthalpy flow rate of the gas at that location. The net rates of heat transfer are calculated using a first law based model. In order to provide a sufficient amount of detail in the analysis, the combustor has been divided into five sections. Section one is the steam generator, section two is the cold side of the heat exchanger, section three is the mixing stage (which is the second leg of the cold side of the heat exchanger and represents the introduction of fuel into the oxidizer stream), section four is the combustion volume, and section five is the exhaust channel or hot side of the heat exchanger. Figure 4.9 shows the model schematic along with the

thermocouple locations labeled 2, 3, 4, 5 and 6 representing the inlet and outlet conditions for sections one through five. Thermocouple location 1 is the ambient lab temperature and represents the inlet to section one.

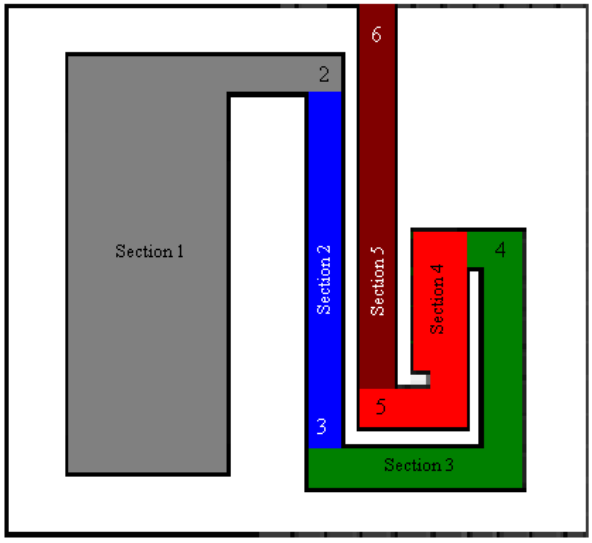

Figure 4.9. First Law Model of the Combustor

In section one the inlet mass fluxes are room temperature hydrogen and oxygen at a fixed equivalence ratio of .5 (Φ=.5). The energy balance on section one is shown in Eq. 4.1 and involves the H_2/O_2 heat of reaction, the heat transferred from section one to two and the heat lost from section one. Note that the specific heat at section two is different from the specific heat at section one due to the reaction and represents a mixture of steam and oxygen with a steam mass fraction of .53. For all sections unless otherwise specified temperature dependent specific heats are used to calculate the enthalpy flux terms. These are found in the NIST online chemistry webbook[16], and are weighted by mass fraction.

$$\dot{m}_1 C_{p,2} T_2 - \dot{m}_1 C_{p,1} T_1 = \dot{Q}_{reaction} - \dot{Q}_{1-2} - \dot{Q}_{loss,1} \qquad \text{Eq.4.1}$$

Section two is the beginning of the cold side of the heat exchanger and the first preheat section, the energy balance on section two is shown in Eq. 4.2 and involves the heat transferred from section one, the heat transferred from section five and the heat lost from section two in addition to the inlet and exit enthalpy flux.

$$\dot{m}_1 C_{p,2} T_3 - \dot{m}_2 C_{p,2} T_2 = \dot{Q}_{1-2} + \dot{Q}_{5-2} - \dot{Q}_{loss,2} \qquad \text{Eq. 4.2}$$

Section three is the mixing section and the inlet corresponds to the injection point for the methanol. The energy balance involves the heat transferred from section four, the heat lost from section three, and the influx of methanol from the heat recuperating fuel injector in addition to the steam oxygen mixture coming from section two. The energy balance is shown in Eq. 4.3.

$$\dot{m}_2 C_{p,3} T_4 - \dot{m}_2 C_{p,3} T_3 = \dot{Q}_{4-3} - \dot{Q}_{loss,3} \qquad \text{Eq. 4.3}$$

Section four is the combustion volume and the first hot section of the combustor. The energy balance involves the heat transferred to the mixing section, the heat transferred to the exhaust channel, and the heat of reaction for methanol/steam/oxygen in addition to the inlet and exit enthalpy fluxes. The specific heat at the exit is calculated through adiabatic isobaric equilibrium simulation performed in CEA. The species and specific heat are frozen at the exhaust of section four and assumed constant for section five. The energy balance for section four is shown in Eq. 4.4.

$$\dot{m}_2 C_{p,4} T_5 - \dot{m}_2 C_{p,3} T_4 = \dot{Q}_{reaction} - \dot{Q}_{4-3} - \dot{Q}_{4-5} - \dot{Q}_{loss,4} \qquad \text{Eq. 4.4}$$

Section five is the exhaust section and the hot side of the heat exchanger. The energy balance involves the heat transferred from section four to section five, the heat transferred from section four to section two and the heat lost from section five, in addition to the inlet and exit enthalpy fluxes. As mentioned previously, because of the complex mixture composition a constant specific heat is assumed between the inlet of section five (which is the exhaust of section four) and the exhaust of section five.

$$\dot{m}_2 C_{p,4} T_6 - \dot{m}_2 C_{p,4} T_5 = \dot{Q}_{4-5} - \dot{Q}_{5-2} - \dot{Q}_{loss,5} \qquad \text{Eq. 4.5}$$

Temperatures two through six are measured with k-type thermocouples and the measurements are left uncorrected, temperature one is assumed to be 298K. The above five equations cannot be solved together for the individual terms involved, however they can be used independently to draw conclusions about the net effect of heat transfer in each section of the combustor. Figure 4.10-4.14 show the enthalpy flow rate (Watts) of the gas at thermocouple locations one through six for a fixed fuel flow rate of .30mL/min and varying equivalence ratio. The enthalpy flow rate is calculated as the product of the heat capacity rate in that section and the temperature at the inlet and exit.

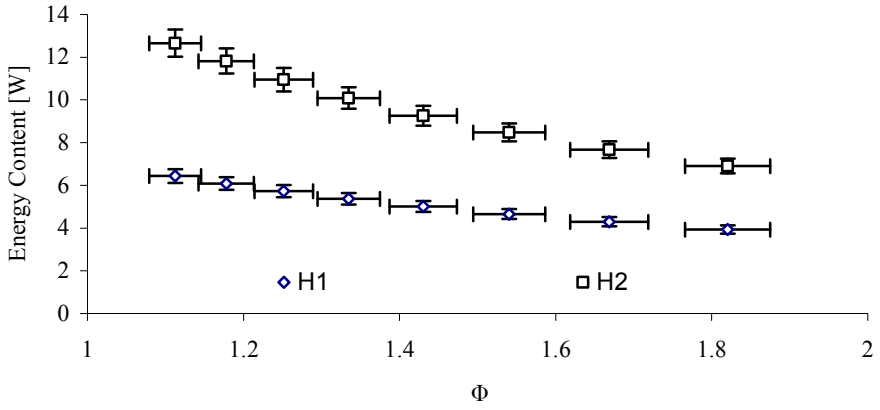

Figure 4.10. Enthalpy flow rate at locations one and two for a methanol flow rate of .3mL/min

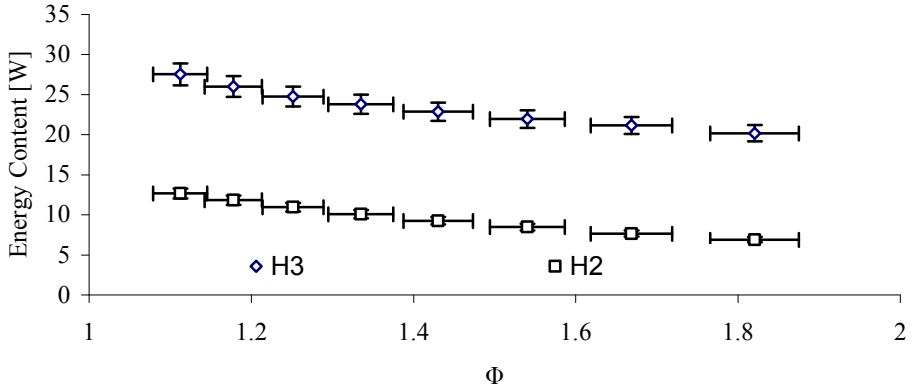

Figure 4.11. Enthalpy flow rate for locations two and three for a methanol flow rate of .3mL/min

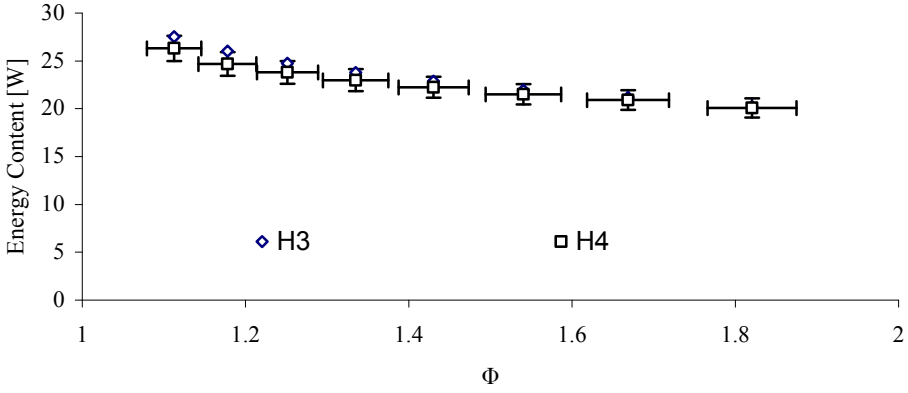

Figure 4.12. Enthalpy flow rate for locations three and four for a methanol flow rate of .3mL/min

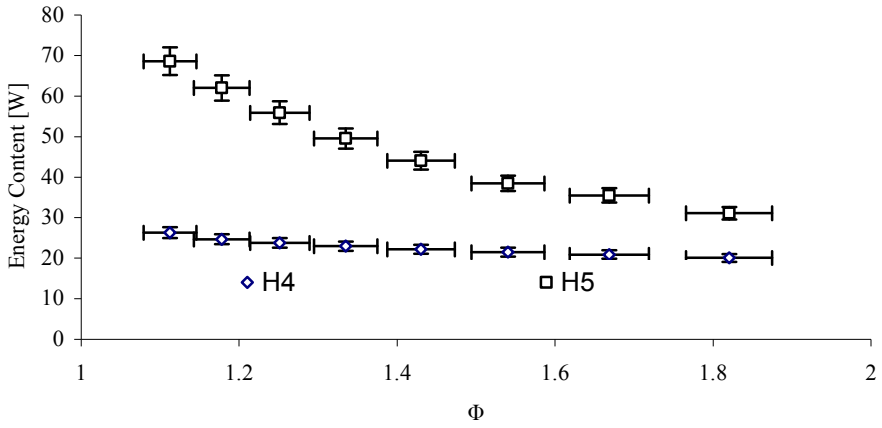

Figure 13.Enthalpy flow rate for locations four and five for a methanol flow rate of .3mL/min

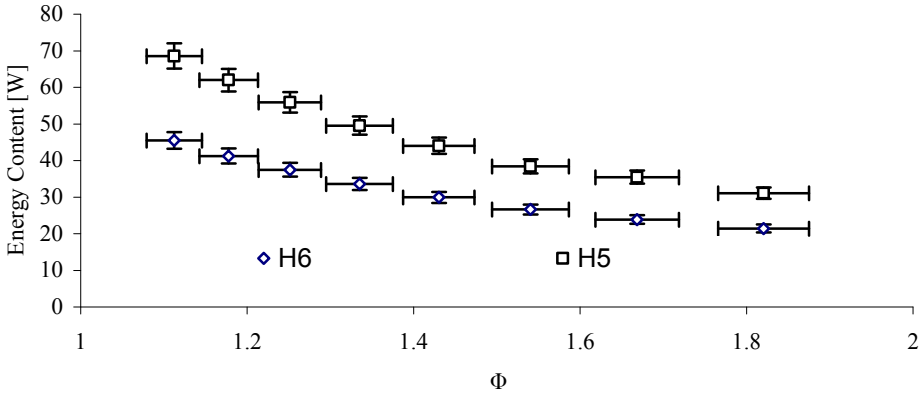

Figure 4.14. Enthalpy flow rate for locations five and six for a methanol flow rate of .3mL/min

In Figure 4.10 the data set labeled H1 represents the oxidizer input power to the combustor and decreases with increasing equivalence ratio at constant fuel flow rate. H2 represents the output power from section one and the difference between H1 and H2 is equal to the sum of the heat of reaction for the steam generator, the heat lost from the steam generator to the ambient and the heat transferred by conduction from the steam generator to the cold side of the heat exchanger. As the mixture is made progressively fuel rich the difference between H1 and H2 becomes smaller indicating that the net heat transfer from section one becomes large compared to the heat released by reaction at low

flow rates. Recall that the reaction in section one is at constant equivalence ratio. In Figure 4.11 the data set labeled H2 represents the input power to the cold side of the heat exchanger and the data set labeled H3 represents the output power to the mixing section. The difference between H2 and H3 is equivalent to the heat transferred from the steam generator, the heat transferred from the exhaust, and the heat lost to the ambient. This difference is relatively insensitive to equivalence ratio, indicating that for a fixed fuel flow rate the net heat input to the cold side of the heat exchanger does not vary significantly with inlet composition. In Figure 4.12, the data set labeled H3 is the input power to the mixing section and the data set labeled H4 is the output power to the combustion volume. The difference between H3 and H4 shows that the heat input from the combustion volume and the heat lost from the mixing section are balanced in the rich regime with a small net heat loss close to the stoichiometry and a small net heat gain close to the rich extinction limit. This indicates that the contribution to preheat from the mixing section is negligible at best. The reason for this is the nearly two-fold increase, on average, of the heat capacity rate compared to section two meaning that the same heat release from the combustion volume must heat up a mixture with nearly twice the thermal mass as section two with the additional introduction of cold reactants.

The combustion zone is the beginning of the hot side of the combustor and in Figure 4.13 the data set labeled H4 is the input power to the combustion zone and the data set labeled H5 is the output power to the exhaust channel. The difference between H4 and H5 is equivalent to the sum of the heat of reaction, the heat transferred to the exhaust, the heat transferred to the mixing region and the heat lost from the combustion zone. Close to stoichiometric conditions, the heat of reaction is significantly larger than

the combined heat transfers away from the combustion zone, however, as the mixture is made rich the difference rapidly decays. The combustor succumbs to flashback before H4 becomes equal to H5, however, this would represent the theoretical thermal quenching limit had flashback not taken place.

In Figure 4.14 H5 represents the output power from the combustion zone and H6 represents the exhaust power. The difference between H5 and H6 is the combination of heat transferred from the combustion zone to the exhaust channel, the heat transferred from the exhaust channel to section two, and the heat lost from the exhaust channel. The exhaust channel experiences a net heat loss which decreases as the mixture is made fuel rich, indicating that the heat gained through conduction from the combustion volume tends to balance the net heat lost through the walls. This is consistent with the predictions shown in Figure 4.15 however a decrease in the net heat loss would be expected in the lean regime.

The net heat recirculated from the exhaust channel back to the reactants (from section five to section two) cannot be calculated directly from Eqs 4.1-4.5 and the experimental data. However, it can be approximated by the difference between the output power from section one and the input power to section three prior to ignition and after stabilization of the flame, shown by the difference between Eq. 4.6 and Eq.4.7. The net heat transfer to the reactants is shown in Figure 4.15 along with the net heat transfer as a fraction of the heat input. The heat transferred to the reactants is roughly constant with equivalence ratio at constant fuel flow rate varying between 6.2 and 7.57 Watts. The ratio of the heat transfer to heat input increases with equivalence ratio due to the concurrent

decrease in input heat. The heat transferred to the reactants is highest at the rich extinction limit at 6.9%.

$$\dot{m}C_{p,2}(T_3 - T_2) = Q_{1-2} + Q_{5-2} - Q_{loss,2} \text{ [With stable flame]} \quad \text{Eq. 4.6}$$

$$\dot{m}C_{p,2}(T_3 - T_2) = Q_{1-2} - Q_{loss,2} \quad \text{[Prior to Ignition]} \quad \text{Eq.4.7}$$

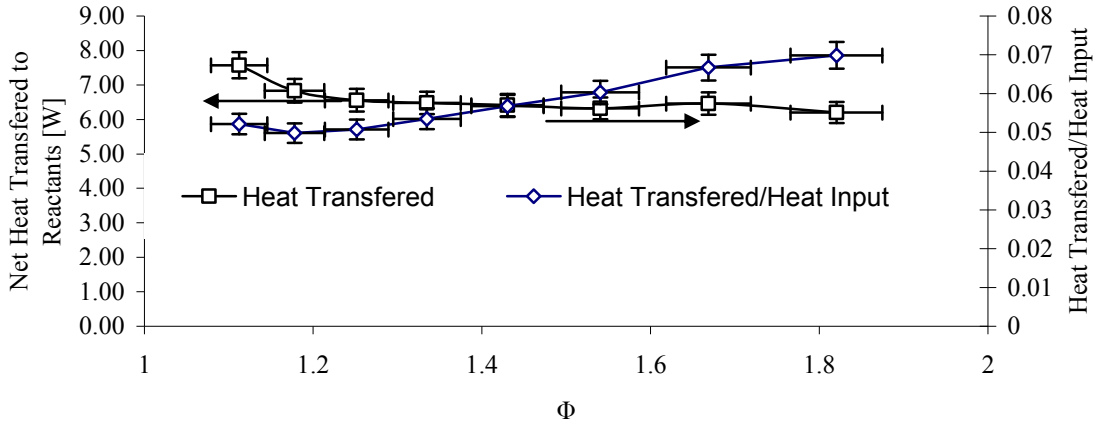

Figure 4.15. Heat transferred to the Reactants, both net and as a fraction of the heat input for a Methanol flow rate of .30mL/min

In brief, the lessons learned from the partially premixed combustion scheme can be summarized by the following:

- The extinction regimes are limited by blow-off at the lean combustion limit and flashback at the rick combustion limit
- Decreasing the channel aspect ratio allows for the stabilization of flames at lower total mass flow rates and richer equivalence ratios due to suppression of flashback. This behavior could be due in part to higher heat losses in smaller aspect ratio channels and incomplete mixing in the upstream channel
- All of the preheating occurs upstream of the fuel injection point downstream of which the temperature variation is minimal, this is

due to the increase in heat capacity rate downstream of the fuel injection point. If the mixing section of the inlet channel were longer then the preheat temperature may increase due to larger amounts of heat transfer from the products; however, this would come at the expense of lower exhaust enthalpy

Non-Premixed Combustion

As mentioned in Section 3.1 a second fuel injection configuration was tested whereby the fuel is injected directly into the combustion chamber. This configuration is shown in Figure 3.4, and was tested with both methanol and kerosene (grade 1K). It is important to note that kerosene combustion was not possible at any condition in the partially premixed configuration. The extinction limits for the methanol flame in non-premixed combustion are shown in Figure 4.16, below.

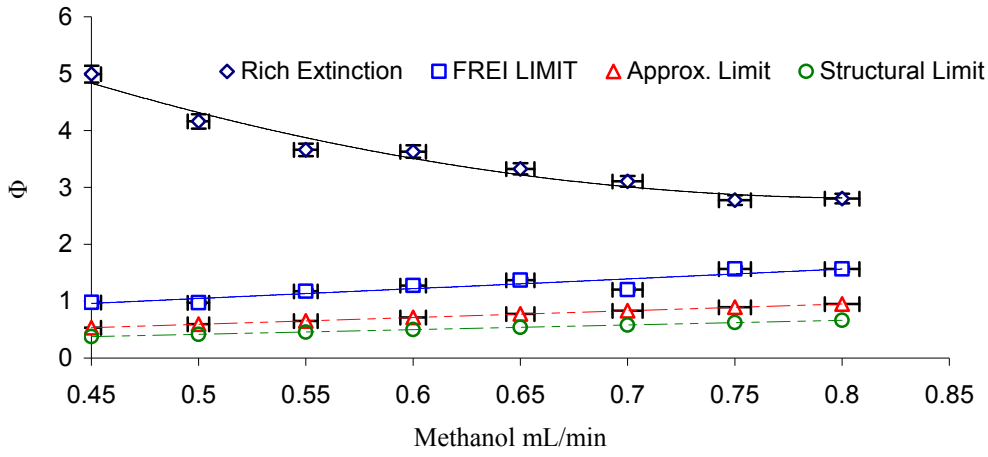

Figure 4.16. Extinction limits for non-premixed combustion of methanol

In Figure 4.16, Φ represents the global equivalence ratio and no absolute lean extinction limit could be found due to limitations with the experimental facility that were

discussed in Section 3.0. The red line labeled Approx. Limit represents the point where the steam/oxygen inlet temperature is larger than the adiabatic decomposition temperature of pure hydrogen peroxide. The green line labeled structural limit is the point where the combustor fractures at the inlet as shown in Figure 2, and the blue line labeled FREI LIMIT are conditions where the flame experiences repetitive extinction and ignition events (named Flame with Repetitive Extinction and Ignition (FREI) in the literature [12]). Temperatures were measured at four locations in this configuration, they are: the inlet steam and oxygen temperature, the preheat temperature (which is the inlet to the combustion chamber), the product gas temperature (which is the exit from the combustion chamber), and the exhaust temperature. The four measured temperatures versus equivalence ratio for a methanol flow rate of 0.45mL/min are shown in Figure 4.17.

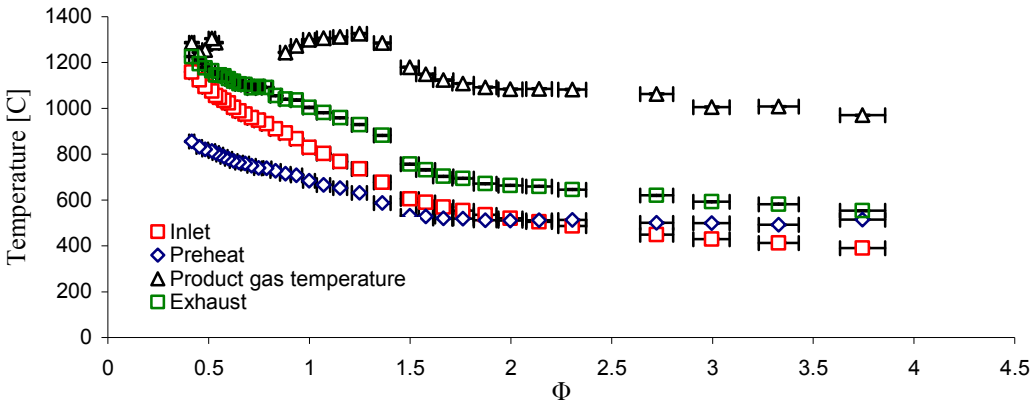

Figure 4.17. Inlet, preheat, product gas, and exhaust temperatures for non-premixed methanol combustion

Figure 4.17 shows similar global behavior as was experienced with partially premixed combustion with exhaust temperatures increase monotonically in the fuel lean

direction, with the rate increasing at around Φ=1.5. It is important to note that the preheat temperatures are always lower than the inlet temperatures unless the combustor is operating in globally rich conditions with Φ>2. This means that the rate of heat loss from the steam/oxygen mixture is larger than the rate of heat recirculation from the products. Additionally, the inlet temperature increases with decrease in equivalence ratio due to the larger amount of hydrogen and oxygen burnt to produce the oxidizer. The discontinuity in the data at Φ~1.4 occurs because the flow controllers were changed at this point in order to provide for a broader measurement range. Figure 4.18 shows the enthalpy flow rates at the inlet, pre-preheat, product gas, and exhaust locations.

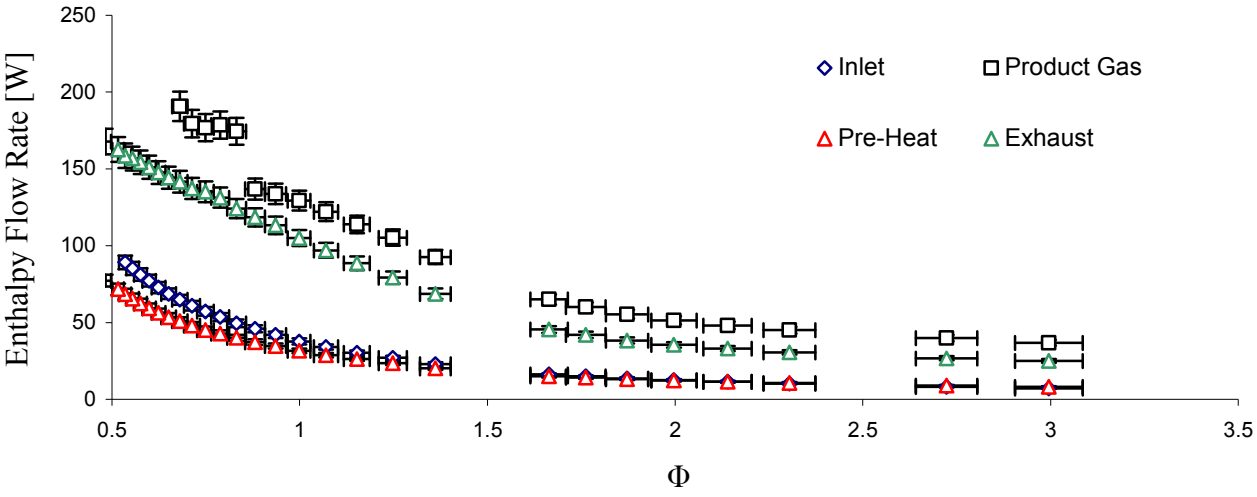

Figure 4.18. Enthalpy flow rates at the inlet, preheat, product gas, and exhaust locations versus equivalence ratio at a methanol flow rate of .45mL/min

Applying the same analysis as was applied to the partially-premixed combustor the difference between the enthalpy flow rates at the product gas location and the preheat location is equal to the difference between the heat gained due to combustion and the heat transferred away from the combustion zone. The gain in product gas enthalpy at

extinction indicates that the rich extinction criteria is not due to thermal quenching but rather some alternative mechanism.

Figure 4.19 shows the steam oxygen enthalpy flow rates at the inlet and preheat locations versus equivalence ratio during methanol combustion (labeled after) and the enthalpy flow rates at the inlet and preheat conditions without the methanol flame (labeled before).

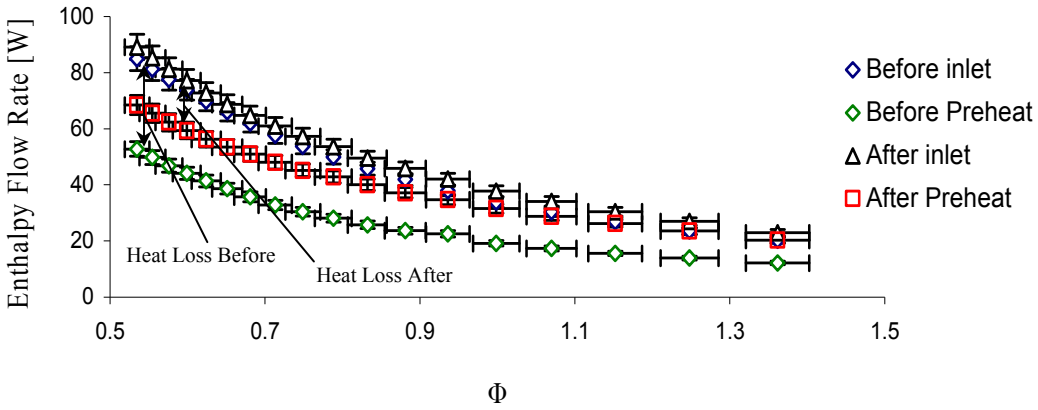

Figure 4.19. Inlet and preheat enthalpy flow rates before and after combustion

As mentioned previously, FREI instability behavior was observed in the lean regime and is present at all conditions between the lines labeled FREI limit and Approx. Limit in Figure 4.16. High speed cinematography was used to investigate the FREI instability behavior in non-premixed methanol/steam/oxygen combustor with Kanthal wire igniters. Figure 4.20 shows the combustor in the stable flame state, extinct state, and at the initiation of a FREI event.

Figure 4.20. High speed images of an FREI event. From left to right: Stable flame, extinct flame, onset of re-ignition

Since the flame surface is not clearly visible the grayscale intensity was tracked at two locations inside the combustion chamber and one location just downstream of the combustion chamber and the intensities used to infer the extinction and re-ignition event. The time trace of the intensities is shown in Figure 4.21; the line labeled "Downstream Location" is the intensity at the product gas thermocouple, the line labeled "In Chamber 1" is the intensity at the downstream ignition wire, and the line labeled "In Chamber 2" is the intensity at the upstream ignition wire.

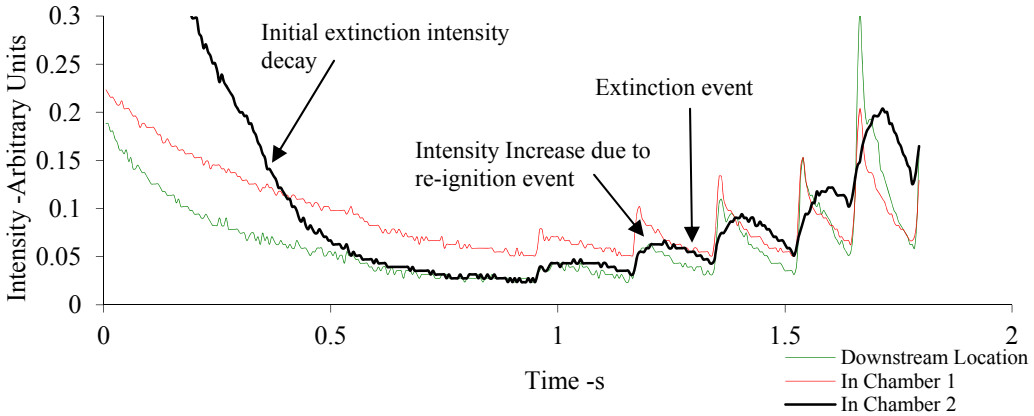

Figure 4.21. Time trace showing the extinction and re-ignition process

From the time history it can be inferred that after the initial intensity decay due to flame extinction, cyclic re-ignition and extinction events occur in pulses roughly separated by 0.175 sec. or 5.7Hz. The peak intensity rises with each subsequent pulse because each prior pulse heats the combustor slightly and the next pulse comes before the heat can be lost. This continues until the flame is re-stabilized inside the combustion chamber. The high speed video shows that the re-ignition occurs in the exhaust and the flame propagates back upstream. A proposed mechanism for re-ignition is shown in Figure 4.22.

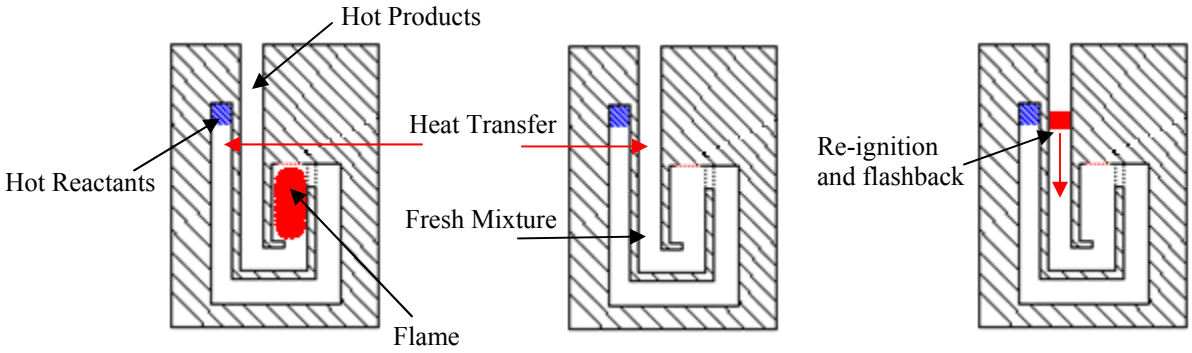

Figure 4.22. FREI mechanism for the heat recirculating combustor

In Figure 4.22, drawing (i) shows a flame stabilized in the combustion chamber with hot steam and oxygen mixture entering through the inlet channel and hot combustion products exiting through the exhaust channel. The direction of heat transfer is from the hot combustion products to the steam oxygen mixture, as can be seen in Figure 4.22. In drawing (ii) the flame is extinct, hot steam and oxygen are still entering through the inlet channel; however, fresh mixture at a lower temperature is exiting through the exhaust channel; here the direction of heat transfer is from the steam oxygen mixture to the exhaust. In drawing (iii) the heat input from the steam oxygen mixture causes re-ignition of the reactant stream flowing out of the exhaust; with no-where to

anchor, the flame flashes back into the combustion chamber and re-stabilizes. Although the proposed mechanism for re-ignition is plausible, the cause for the initial flame extinction is not readily apparent. It will be shown later that the FREI instability behavior can be eliminated by changing the ignition hardware from Kanthal wires protruding into the chamber to flush mounted SiC igniters, suggesting that the extinction is caused by interaction between the flame and ignition wires.

As mentioned previously the non-premixed combustor was tested with kerosene as well. Figure 4.23 shows the extinction regime for kerosene/steam/oxygen combustion; note that this combustor utilized flush mounted SiC igniters due to the heightened performance and more stable operation with methanol. Because of limitations with the experimental facility the lean extinction limit could not be determined and is represented by the approximation and structural limits shown in Figure 4.16. Because the combustor was able to support kerosene flames at very high global equivalence ratios the rich limit was defined as the point where the combustor begins producing noticeable amounts of soot. Soot formation is caused by a competition between soot production and soot oxidation and is an intrinsic property of hydrocarbon diffusion flames. The propensity for soot formation is a strong function of equivalence ratio, flame temperature, and mixing [13]. In the experimental facility the onset of soot production was identified by the deposition of soot on both the channel walls and quartz window and the yellowish white incandescence from the soot producing regions of the flame. Operation at global equivalence ratios larger than the limit for soot production would be undesirable since deposition on the channel walls would alter the characteristics of heat transfer to the

reactants and may clog small passages downstream of the combustor, like a meso-scale nozzle throat, for example.

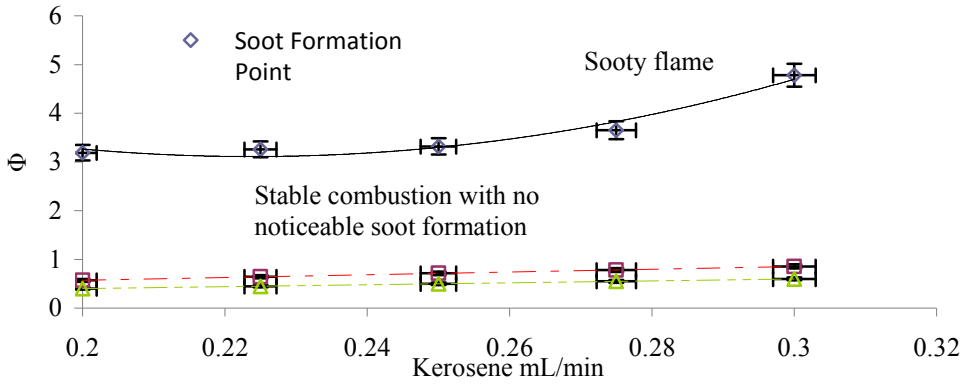

Figure 4.23. Extinction regime for kerosene combustion

Kerosene combustion is possible over a relatively narrow range of fuel flow rates, between 0.2mL/min. and 0.3mL/min. and the global equivalence ratio limit for the formation of soot tends to increase with increase in fuel flow rate. No FREI or other instability mechanisms were observed at any condition. Figure 4.24 shows the flame images and the development of the global flame structure for the kerosene flame from the soot production limit to the approximate limit for a fuel flow rate of 0.2mL/min.

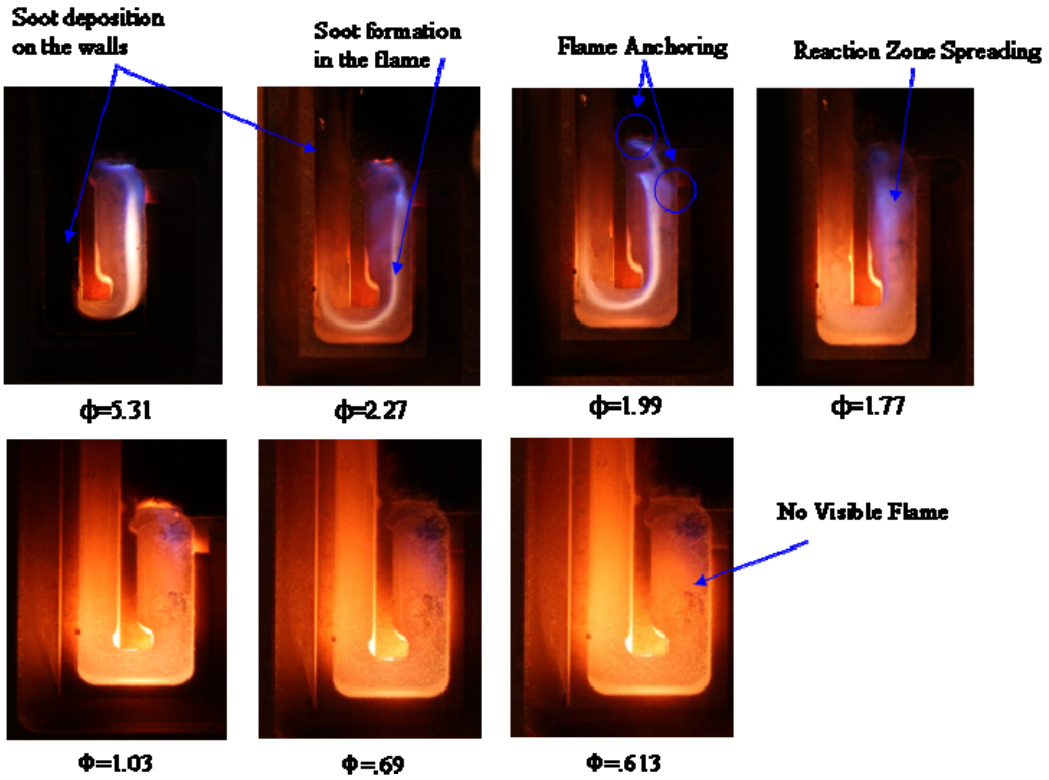

Figure 4.24. Development of the kerosene global flame structure

Figure 4.24 shows the progression of the global flame structure from a diffusion flame with a very discrete reaction zone at very rich conditions to a condition that exhibits no visible flame at very lean conditions. At Φ =2.27 the deposition of soot on the channel walls and quartz window becomes visibly apparent, and at Φ=5.31 the soot deposition on the window is so thick that it obscures the luminosity from the channel entirely. The regions of the flame exhibiting soot nucleation and incandescence become visible at Φ=1.99. In the globally fuel rich regime the flame appears to be anchored at two locations, one anchoring location is at the fuel injector and the other at downstream edge of the step inlet to the combustion chamber. This dual branching behavior is apparent at Φ=2.27 and Φ=1.77 but is most obvious at Φ=1.99. At Φ=1.77 the reaction

zone spreads out, and although the anchoring locations are still apparent the surface of the flame is not as distinct. Close to the lean Approximate Limit the flame loses all visible emission and the combustor operates in the "flameless" mode. This combustion mode has been reported by *Ahn et. al* [14] in mesoscale heat recirculating combustors burning propane and air, and in macro-scale combustors with non-premixed fuel and highly pre-heated air. The reason for reaction zone broadening and "flameless" combustion in mesoscale heat-recirculating burners could be due to the small characteristic geometries and highly-preheated reactants which make it difficult to support the large temperature gradients associated with thin reaction zones. [14]

The extinction regime for the combustor with nozzle shown in Figure 3.5 was also tested with methanol/steam/oxygen to study the effect of both pressure and exhaust channel geometry on flame extinction. Figure 4.25 shows the global stability regime for the thrust chamber; the stability regime for the open channel combustor (chamber pressure of 1 atm.) is also shown for comparison. In the figure, the line representing the thrust chamber stability regime is labeled 'confined' while the line representing the open channel stability regime is labeled 'unconfined'. No absolute lean limit of combustion was determined due to limitations with the experimental facility that were discussed above. The red line labeled "Approx. Limit" represents the point where the steam/oxygen inlet temperature is larger than the adiabatic decomposition temperature of pure hydrogen peroxide.

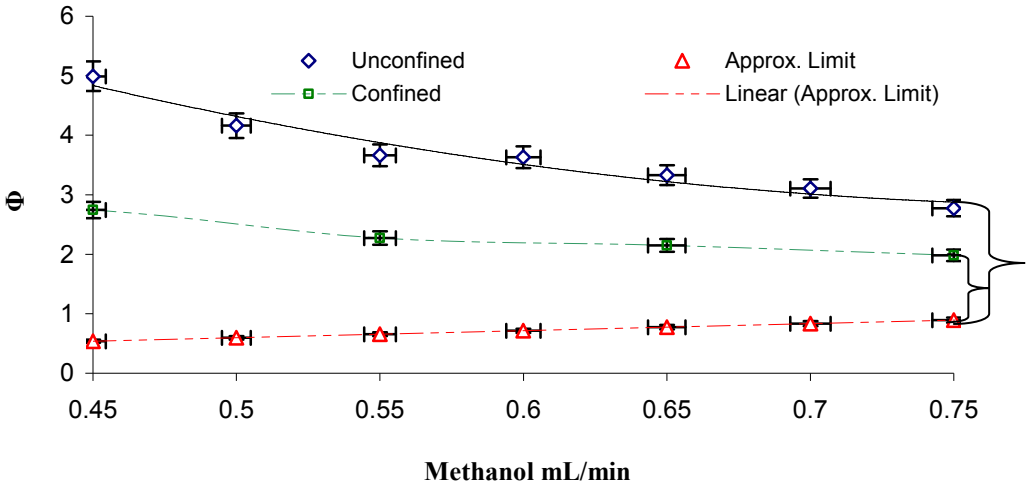

Figure 4.25. Global Flame Stability Regime

From Figure 4.25 it is evident that the global extinction regime for methanol combustion in the confined combustor is substantially narrower than the global extinction regime for the unconfined combustor. However, the trend in flame extinction is similar, with a wider extinction limits at low heat loads, and a narrower extinction limits at high heat loads. The differences in the extinction regimes can be explained through trends in both the exhaust and pre-heat temperatures of both the confined and unconfined combustors. Figures 4.26 shows both the exhaust temperature and pre-heat temperatures for both the confined and unconfined combustors for a methanol flow rate of 0.45mL/min. Note that other than the presence of the nozzle the combustors are identical. Figure 4.27 shows that exhaust temperatures for the confined combustor are higher than for the unconfined combustor over the entire extinction regime, the difference in temperature decreases as the mixture is made fuel rich. Note that Figure 4.26 only shows conditions where the extinction regimes for the confined and unconfined combustors overlap. Recall from Section 3.1 that the nozzle is converged from the nozzle inlet cross

section to the throat cross section in two stages. In the first stage of convergence the depth of the nozzle is reduced form the full channel depth to the throat depth. This ramp decrease in depth reduces the area available for heat transfer away from the exhaust gas due to the gradual decrease in the exhaust channel cross sectional area. This seems beneficial because the stagnation enthalpy is higher, and as mentioned previously, increase in stagnation enthalpy is the prime driver for increases in meso-scale thruster performance. However, the total heat transferred away from the exhaust channel includes contributions from both the heat lost to the environment, and heat transferred from the exhaust gasses to the reactants. It would be expected then that the tapered geometry of the confined combustor would result in lower preheat temperatures as a consequence of the higher exhaust temperatures. This is reflected in Figure 4.27, where the preheat temperatures for the unconfined combustor are larger than the preheat temperatures for the confined combustor, with the difference in temperature increasing as the mixture is made fuel rich.

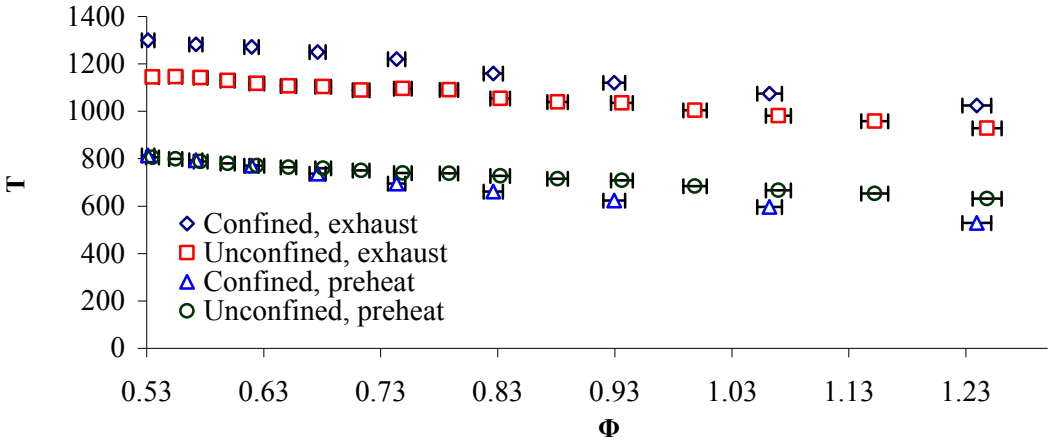

Figure 4.26.Exhaust and Preheat Temperatures for both the confined and unconfined combustors for a fuel flow rate of 0.45mL/min

Figure 4.27 shows the preheat-temperatures for the confined and unconfined combustor; however, the regime is extended to the rich extinction limit for the unconfined combustor.

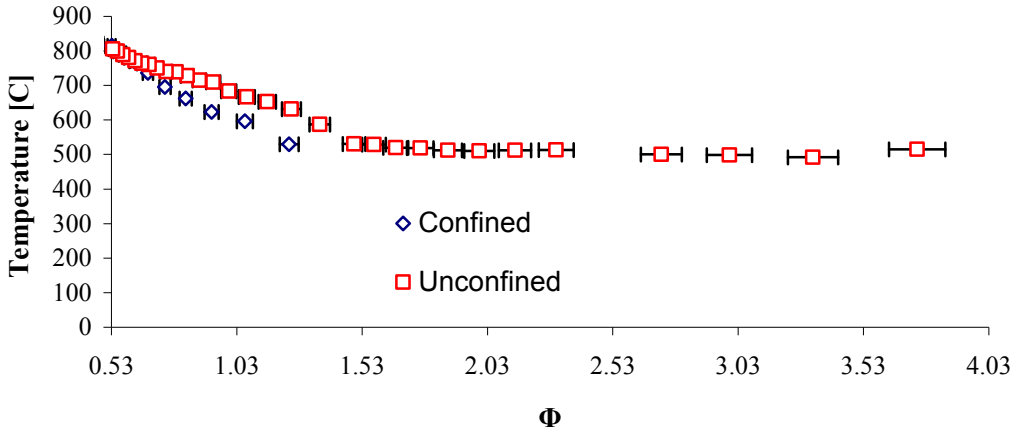

Figure 4.27. Preheat temperatures for the confined and unconfined combustors for a fuel flow rate of 0.45mL/min

Figure 4.27 suggests that the rich extinction criteria can be pinned to certain preheat temperature, which is then independent of the channel geometry. For a fuel flow rate of 0.45mL/min this appears to be ~490°C. Note that the auto ignition temperature for methanol is 470°C. In this case the rich extinction (low Re) limit could be identified by the point where the hot oxidizer is no longer able to auto-ignite the freshly vaporized fuel. Since at higher fuel flow rates more heat is required to raise the fuel temperature to the auto-ignition temperature an extinction criteria (E_{crit}) can be defined by equating the enthalpy flow rate of the oxidizer to the enthalpy flow rate of the fuel. Solving for the fuel temperature and then normalizing by the auto-ignition temperature of the fuel, as per Equation 4.8, if Eq. 4.8 is less than one the flame will become extinct, because the fuel temperature will be less than the auto-ignition temperature.

$$E_{crit} = \frac{\dot{m}_{ox} C_{p,ox} T_p}{\dot{m}_{fuel} C_{p,fuel} T_{AI}} \qquad \text{Eq. 4.8}$$

Figure 16 shows the extinction criteria versus equivalence ratio for five different methanol flow rates of: 0.45mL/min, 0.5mL/min, 0.55mL/min, 0.6mL/min, and 0.65mL/min. In Figure 7 the isobaric temperature dependent specific heats were obtained from the NIST chemistry Web Book. [15] Figure 4.28 shows that for the five flow rates presented extinction occurs within a narrow band around an extinction criteria of one (E_{crit}=1). The points where rich extinction occurs are marked with bold filled symbols.

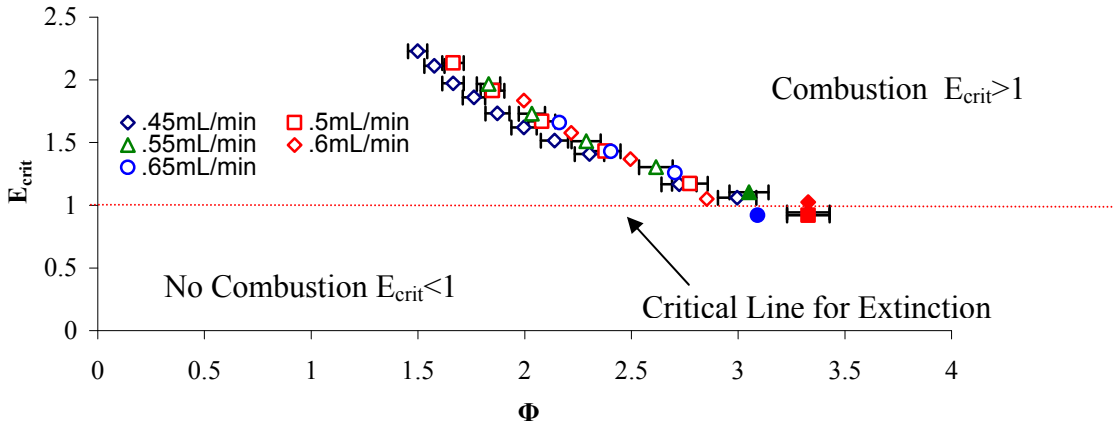

Figure 4.28. Extinction criteria versus equivalence ratio for five methanol fuel flow rates for both the confined and unconfined combustor, the points where rich extinction occurs are marked with bold filled symbols.

Figure 4.28 shows that for the non-premixed configuration described above and for a prescribed set of inlet conditions, namely fuel and oxidizer mass flow rates; the preheat temperature required to avoid extinction can be determined from Eq. 5.

Referring back to Figure 4.16, procedurally the experiment was conducted by igniting a flame close to a global equivalence ratio of one and decreasing the oxidizer

flow rate until the flame became extinct. Figure 4.29 shows a generic extinction regime for a non-premixed, non-soot producing combustor.

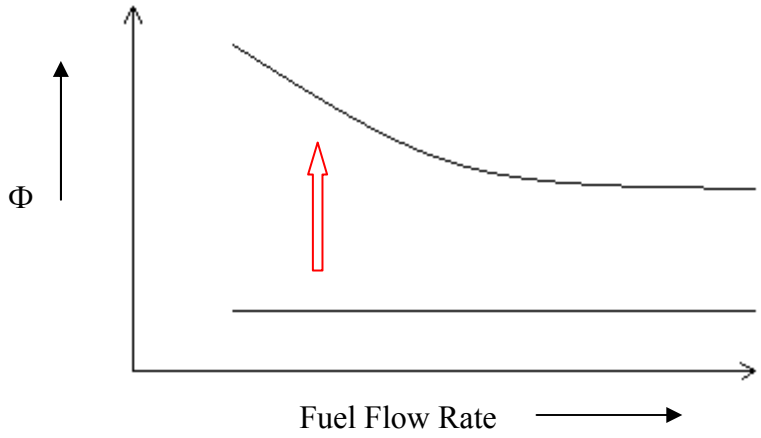

Figure 4.29. Generic extinction regime for a non-premixed, non-sooting combustor. The red arrow is the progress of the experiment from the ignition condition to the rich extinction limit.

From Figure 4.29 as the fuel flow rate is increased the extinction limit tends towards lower global equivalence ratios. This is because a larger oxidizer enthalpy (preheat temperature) is required to ignite the larger amount of fuel. Since the temperature is provided via pre-heating of the oxidizer a higher flame temperature is required to provide an adequate amount of heat transfer to the reactants, and hence the tendency is for the rich extinction limit to decrease toward lower equivalence ratios (closer to one) as the fuel flow rate is increased.

Section 3 Thermal Performance

The thermal performance of the combustor, both in the partially-premixed and non-premixed modes has been determined based on computation of the enthalpy flow rates. The measurements are taken primarily in the exhaust however upstream measurements are taken at times to explain the experimental results. Thermal and

performance efficiencies are determined and act as a base for comparison with the thrust results that will be presented later in this report.

Partially-Premixed Combustion

Figure 4.30 shows the exhaust temperature versus equivalence ratio for three different fuel flow rates .30mL/min, .25mL/min, and .20mL/min. The exhaust temperature increases steadily in the fuel lean direction, this result is counterintuitive since the flame temperature decreases in both the lean and rich directions peaking at close to stoichiometry. This behavior is consistent with premixed heat recirculating combustors discussed in Section 2.0, and can be explained through a first law analysis of the exhaust channel, shown in Eq. 4.9, assuming the exhaust gasses enter the exhaust channel at the flame temperature.

$$CT_{flame} - (\dot{Q}_{h-c} + \dot{Q}_{loss}) = CT_{exhasut} \qquad \text{Eq.4.9}$$

The combined rate of heat transfer from the exhaust channel can be calculated from Eq. 4.9 and is shown versus equivalence ratio for a methanol flow rate of .30mL/min in Figure 4.31, along with the variation in heat capacity rate with equivalence ratio for the same data set. The combined rate of heat transfer is calculated as the sum of both the heat transfer from hot to cold flow and the heat lost from the exhaust channel.

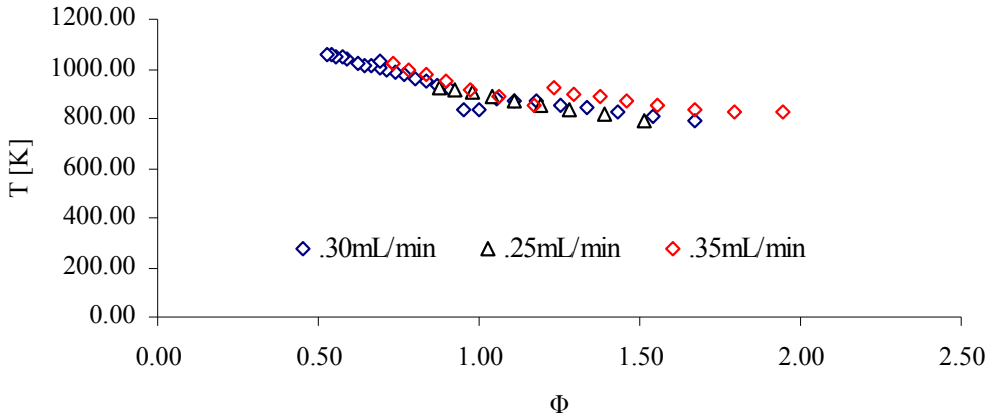

Figure 4.30.Variation of exhaust temperature with equivalence ratio for three methanol flow rates

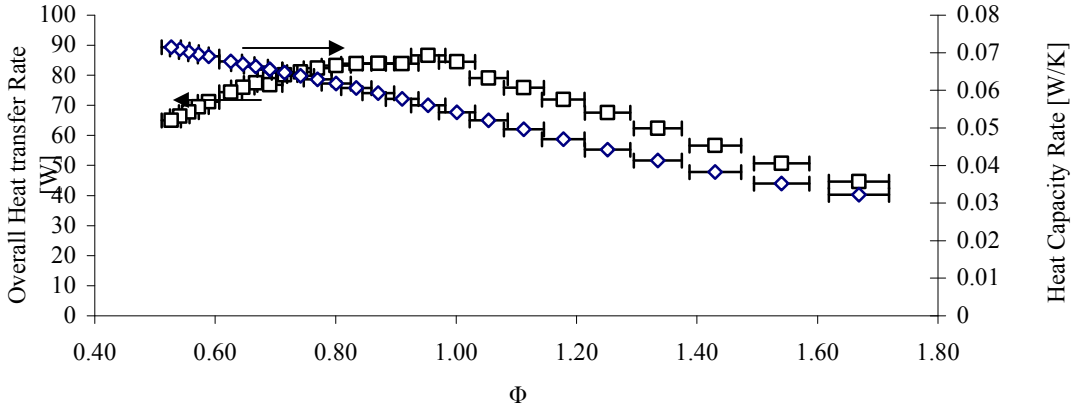

Figure 4.31.Variation in combined heat loss rate and heat capacity rate from the exhaust channel for a methanol flow rate of .3mL/min

In Figure 4.31, as the equivalence ratio is decreased the combined heat transfer rate away from the exhaust gas increases from 44W at the rich extinction limit to a maximum of 86W close to stoichiometry and then decreases as the mixture is made fuel lean. The heat capacity rate increases monotonically over the same regime, and continues increasing in the lean direction. This means that as the equivalence ratio decreases more substantial rates of heat transfer away from the exhaust gasses would be required to induce the same drop in gas temperature that would be experienced at either the rich or stoichiometric conditions. However, the net heat transfer rate away from the channel decreases with

equivalence ratio in the lean direction, causing the temperature drop across the exhaust channel to decrease as well (temperature drop being defined as the difference between the flame temperature and the exhaust temperature). This allows the exhaust temperature to increase as the mixture is made fuel lean even if the flame temperature is decreasing. The exhaust channel temperature drop is shown in Figure 4.32 and is calculated as the ratio of the overall heat transfer rate and the heat capacity rate.

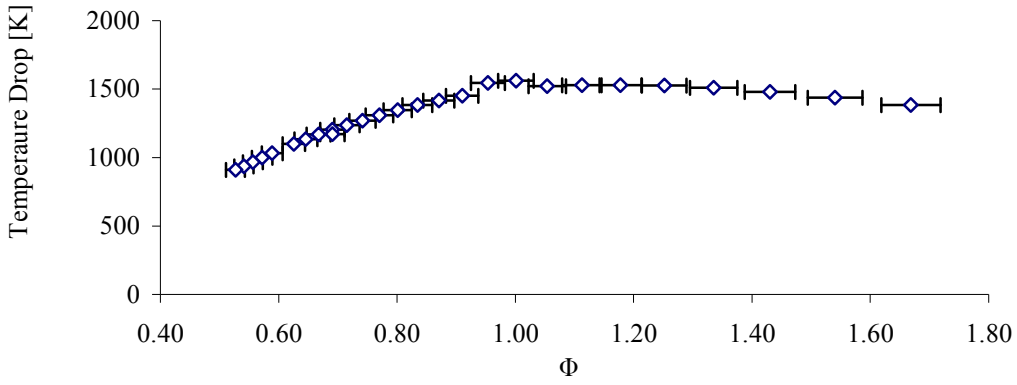

Figure 4.32.Temperature drop across the exhaust channel

The output power, calculated as the product of the heat capacity rate and the exhaust temperature is shown in Figure 4.33 for three different methanol flow rates. The output power increases continuously in the lean direction due to the increase in input heat with decrease in equivalence ratio and relatively constant efficiency with variation in Φ (discussed below). Figure 4.34 shows the overall heat loss, calculated as the difference between the heat input and the heat output with equivalence ratio for the same fuel flow rates. The overall heat loss through the combustor walls also increases with decrease in equivalence ratio. For the same equivalence ratio both the output power and heat loss are larger at higher fuel flow rates.

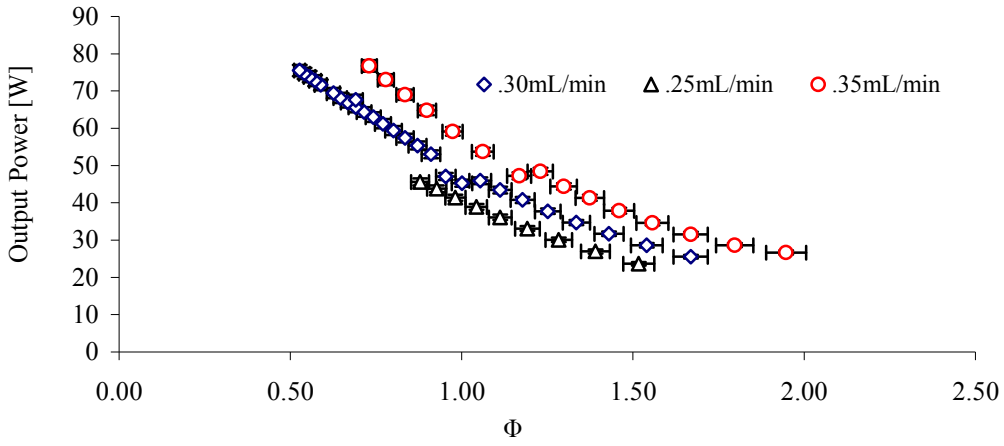

Figure 4.33. Heat output for three different flow rates versus equivalence ratio

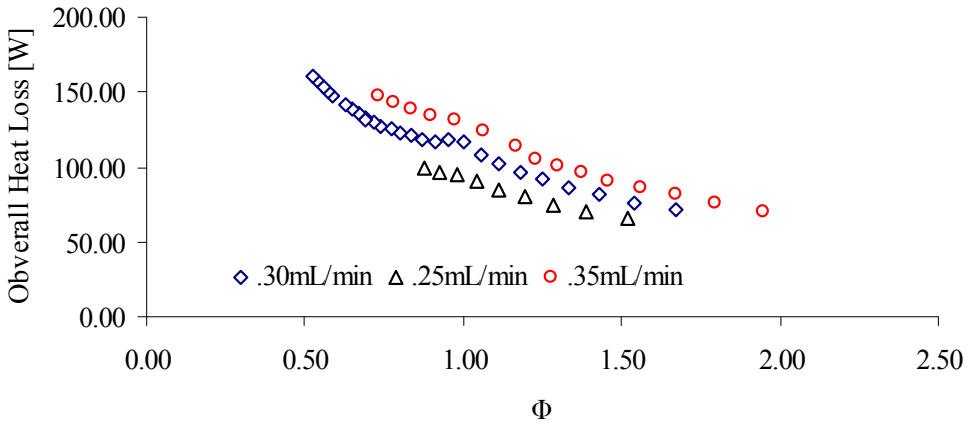

Figure 4.34.Overall heat loss for three different flow rates versus equivalence ratio

Due to the overwhelming effect of the heat capacity rate over the rate of heat loss from the exhaust channel the ratio of the overall heat loss from the combustor to the heat input is minimized at fuel lean conditions and maximized at fuel rich conditions, this is shown in Figure 4.35 for three different fuel flow rates. This behavior is somewhat consistent with the performance of heat recirculating combustors burning mixtures with air.[16] However, the variation in efficiency with equivalence ratio is not as dramatic since the heat input increases with decreasing equivalence ratio because production of the oxidizer (steam + oxygen) releases heat into the system. Consequently, the efficiency

varies only 3% from minimum to maximum compared to over 30% for mixtures with air over similar equivalence ratio regimes. [16]

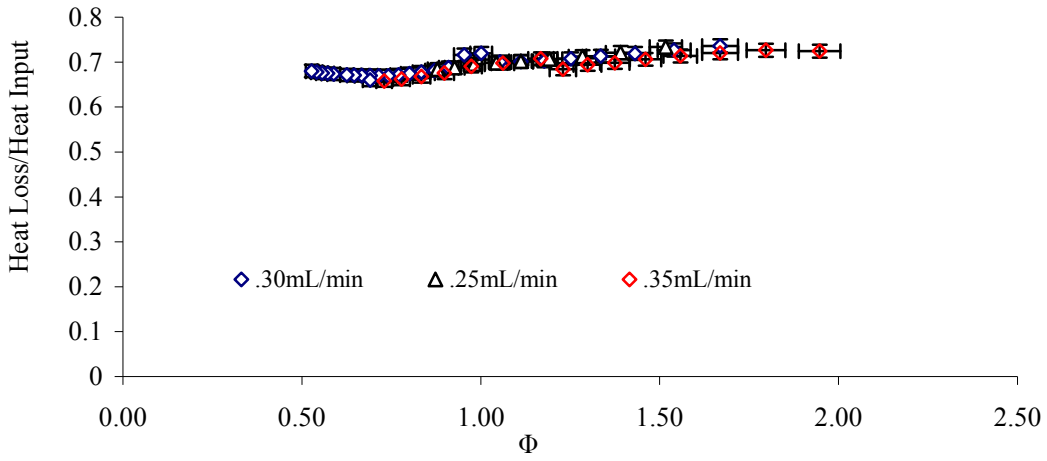

Figure 4.35. Heat loss/Heat input, and overall heat loss from the combustor for three different fuel flow rates

Figure 4.36 shows the overall heat loss along with the fraction of the input heat associated with the oxidizer for a fuel flow rate of .30mL/min.

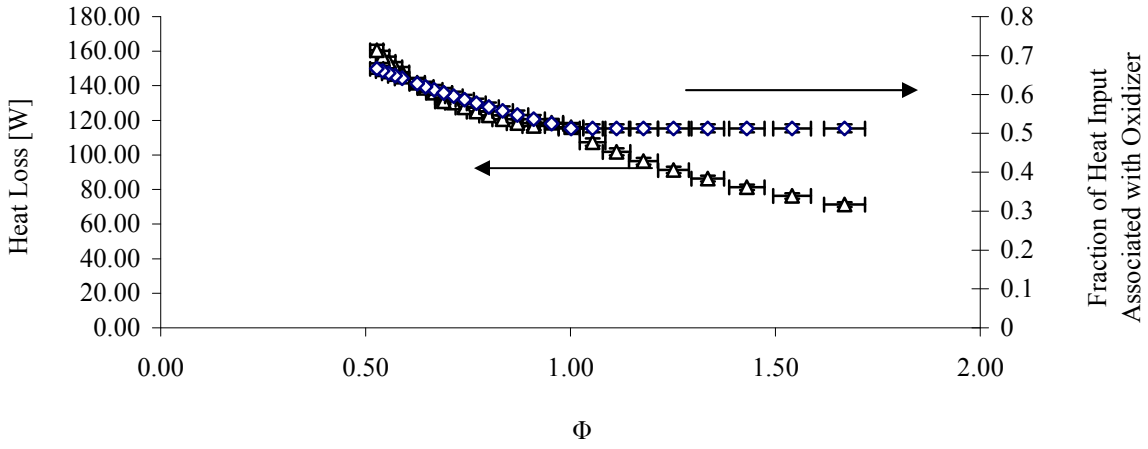

Figure 4.36.Overall heat loss and the fraction of heat input associated with the oxidizer for a fuel flow rate of .3mL/min. Note that the inflection in the heat loss occurs because of a change in the flow controller

Since the input heat is determined based on complete consumption of the limiting reactant the fraction of the heat input associated with the oxidizer is roughly constant in rich conditions since the amount of fuel consumed increases with decreasing equivalence ratio, offsetting the increase in oxidizer heat. In the lean regime the heat contribution from the oxidizer source increases substantially, owing to a fixed heat release rate from the fuel. This offsets the larger overall heat losses to the ambient experienced in the lean regime, causing the ratio of heat loss/heat input to remain relatively constant. The ratio of the output to input power is subject to the same effect and is shown in Figure 4.37 with efficiencies as high as 34% at the lean extinction limit with a variation of 7% over the entire regime tested.

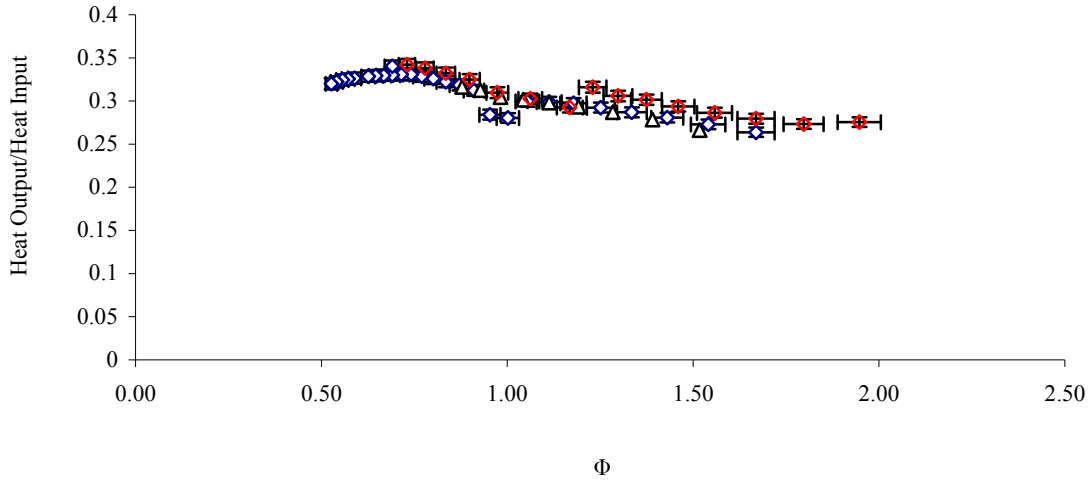

Figure 4.37. Heat output/Heat input for three fuel flow rates

Since this investigation is centered on the use of the heat recirculating combustor in a propulsion device. The thermal performance is measured based on the specific impulse and characteristic velocity efficiency (ηC* and ηIsp, respectively) of the combustor. The efficiencies are defined as the ratio of the calculated value based on the measured exhaust temperature and the adiabatic flame temperature for the same

conditions. The characteristic velocity and specific impulse are related to the enthalpy of the product gas and is therefore dependent on gas properties, such as specific heat. However, since the gas properties used in the calculation of both C* and Isp are based on chemical equilibrium of the product gasses they are the same for both the experimental conditions and the adiabatic conditions. Hence the ratio of experimental C* and Isp and adiabatic C* and Isp is independent of gas properties. Equation 4.10 shows the relationship used to calculate the efficiencies. Both the efficiencies and the exhaust temperature are shown in Figure 4.38, for varying mixture ratio and four different fuel flow rates.

$$\eta C^* = \eta I_{sp} = \sqrt{\frac{T_{\exp}}{T_{ad}}} \qquad \text{Eq.4.10}$$

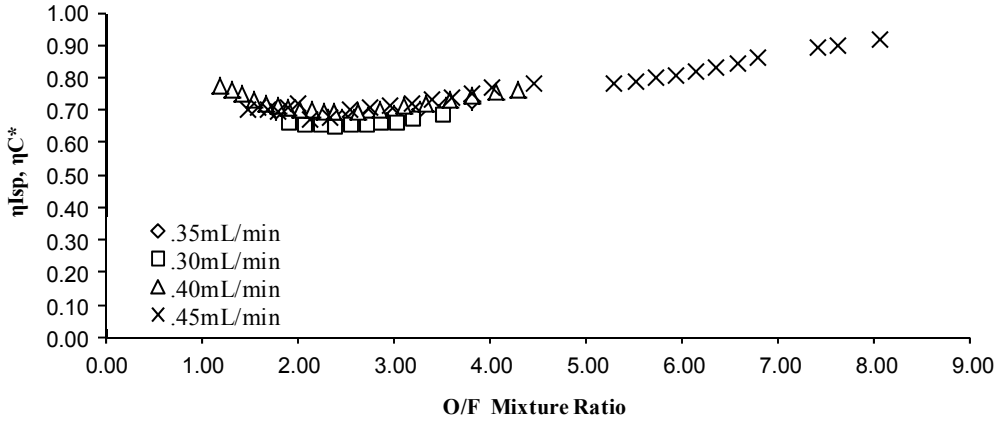

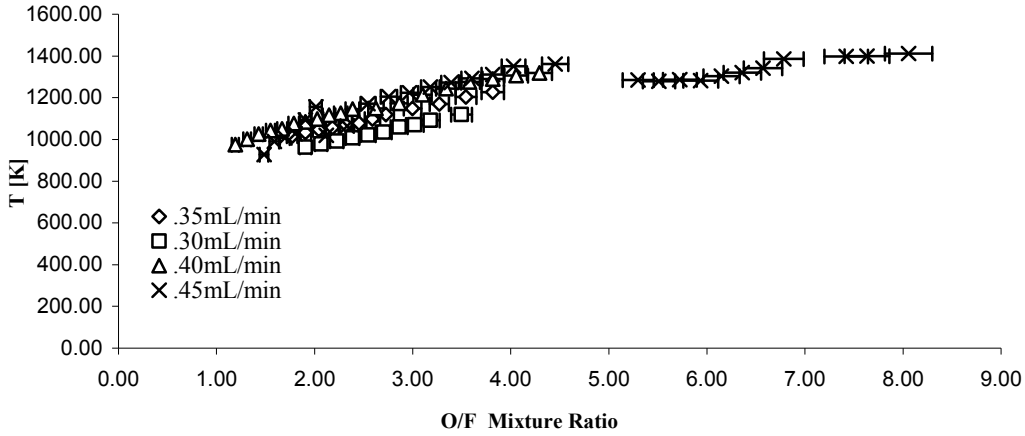

Figure 4.38.Thermal performance of the heat recirculating combustor. Top: C* and Isp efficiencies, Bottom: exhaust temperature.

Figure 4.38 shows that the maximum efficiencies are found at the fuel lean extinction limit for all four fuel flow rates, and the minimum at stoichiometric conditions with the overall range between ~60% and ~90%. Figure 4.38 also shows that the exhaust temperatures increase monotonically as the mixture is made fuel lean. Since the product gasses undergo heat exchange with the reactants and heat loss to the combustor material before exiting the combustor, the exhaust temperature is related to both the rate of heat loss from the product gas, its temperature as it exits the combustion chamber, and its heat capacity rate (the product of the total mass flow rate and the specific heat capacity). The flame temperature decreases as the mixture is made fuel lean while the heat capacity rate increases. Because of the latter the energy content (enthalpy flow rate in watts) is much larger at lean conditions because of the larger mass flow rate, and the heat exchanger cannot provide a means to lose that energy. This allows the temperature to increase as the mixture is made fuel lean despite the drop in flame temperature. For this reason, at a

particular fuel flow rate, the efficiencies are largest at the fuel lean limits, and at the maximum the exhaust temperature is 83% of the adiabatic flame temperature.

The characteristics of the thermal performance: the monotonic increase in temperature with decrease in equivalence ratio and performance regimes that are flat with respect to equivalence ratio are the same for both the partially-premixed combustor and non-premixed combustor. The specific performance results are presented below for the non-premixed combustor burning methanol/steam/oxygen and kerosene/steam/oxygen.

The thermal efficiency of the non-premixed combustor is shown in Figure 4.39. As in Figure 4.38, the efficiencies are reported in terms of Isp and C* efficiency as per Eq. 4.10. The thermal efficiency of the partially premixed combustor for the same fuel flow rate (0.45mL/min) is also shown for comparison.

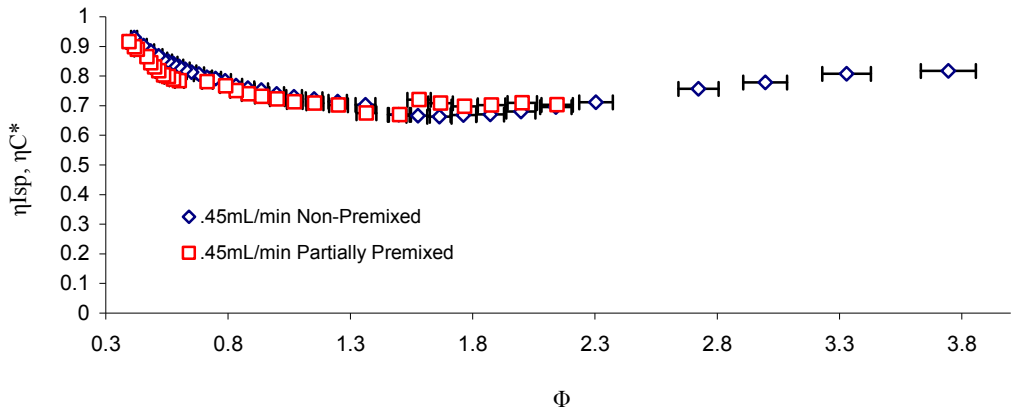

Figure 4.39.Thermal efficiencies of partially premixed and non-premixed combustor

Overall, the partially-premixed and non-premixed combustors demonstrate similar trends in thermal efficiency with minimums in the slightly fuel rich regime and maximums close to the fuel lean limit. The maximum efficiency is found at the lean extinction limit with a 1.4% variation in efficiency between the two combustors. The jump in efficiency in the

partially premixed case at Φ=1.5 is an artifact of the experimental facility since the flow controllers were changed at this point to accommodate higher flow rates. Additionally, Figure 4.39 shows that the combustor is able to support a flame in the combustion chamber over a much broader range of equivalence ratio, since in the non-premixed case the flashback mechanism of flame extinction is irrelevant.

As mentioned previously, changing the ignition hardware from Kanthal wire electrodes that protrude into the chamber to flush mounted SiC igniters has a marked effect on stability, eliminating the FREI instability present in the methanol combustor. It is interesting to note that the change in ignition hardware comes with a change a variation in the thermal performance and global flame structure as well. Global flame images of the partially-premixed and non-premixed combustor also show notable differences in flame location and shape. Figure 4.40 shows flame images of the partially premixed and non-premixed combustors at roughly the same global equivalence ratio (Φ=1.0 and Φ=1.15, respectively), and subsequent images of the non-premixed combustor at equivalence ratios of Φ=0.83 and Φ=0.68. Although the flame surface is not explicitly visible in any of the images the high luminosity from the walls in the partially-premixed combustor just left of center in the combustion chamber suggests a localized reaction zone at that location. The wall luminosity in the non-premixed combustor is more uniform and suggests a broader reaction zone. In the non-premixed combustor as the global equivalence ratio is decreased at constant fuel flow rate the flame appears to be pushed further away from the combustor inlet. This is made apparent by the glowing of the downstream ignition wire and product gas thermocouple.

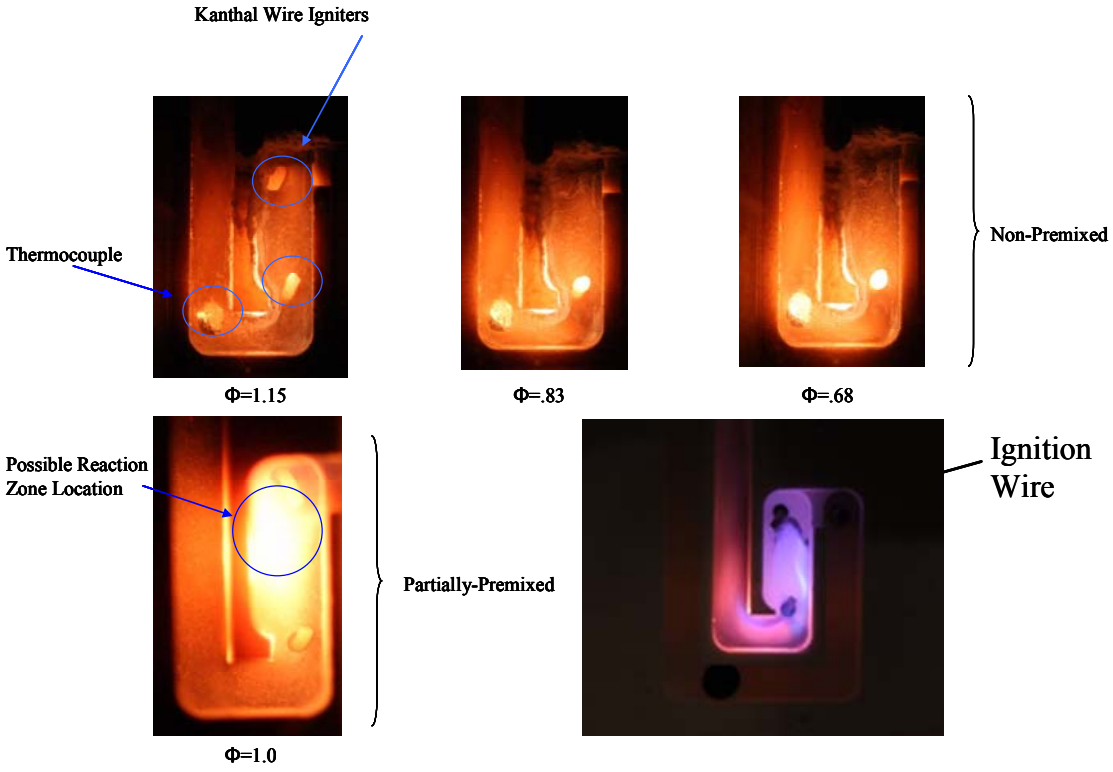

Figure 4.40. Flame images of the partially-premixed and non-premixed combustor. The bottom right-most image shows a partially-premixed propane air flame that appears to be stabilized on the upstream ignition wire.

Note that the size of the Kanthal ignition wires (1/64 in. diameter) is significant compared to width of the combustion chamber, and at Φ=0.83 and Φ=0.68 it appears that the flame may be stabilized on the downstream ignition wire and the product gas thermocouple. In order to test this, a second variation of the non-premixed combustor was fabricated without the product gas thermocouple and with Silicon Carbide (SiC) igniters that are flush mounted with the bottom of the combustor, so that nothing is protruding into the combustion chamber. Figure 4.41 shows the flame images for the non-premixed combustor with flush mounted SiC igniters.

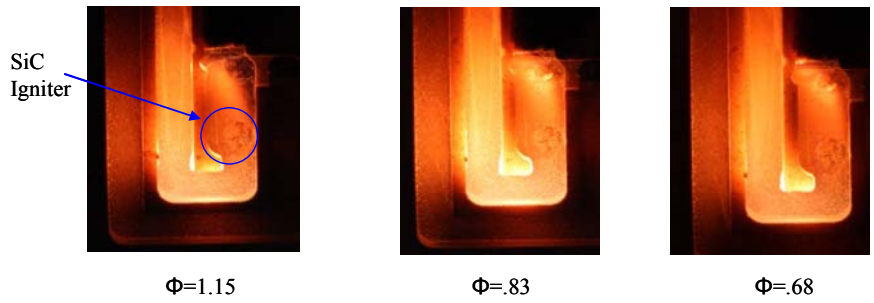

Figure 4.41. Flame images with SiC igniters

Based on the wall luminosity the non-premixed combustor with SiC igniters also shows a broad reaction zone as compared to the partially-premixed case, with regions of higher luminosity close to the exit of the chamber. What is notable is that changing the ignition scheme changes the dynamics of the flame in several ways. First, the reaction front does not move away from the fuel injector as the equivalence ratio is decreased. Second, the combustion with the wire igniters is very loud, with high pitched acoustics over the entire extinction regime which is accompanied by motion of the flame inside the combustion chamber as seen from high speed cinematography (at 200fps). Over the same conditions, the combustor with the flush mounted SiC igniters is silent with no apparent flame motion; this is accompanied by higher exhaust temperatures than the combustor with wire igniters. Finally, the combustor with SiC igniters does not demonstrate any FREI behavior. The exhaust temperatures and thermal efficiencies of the non-premixed wire igniter combustor and non-premixed SiC igniter combustor are shown in Figure 4.42, for a methanol flow rate of 0.45mL/min.

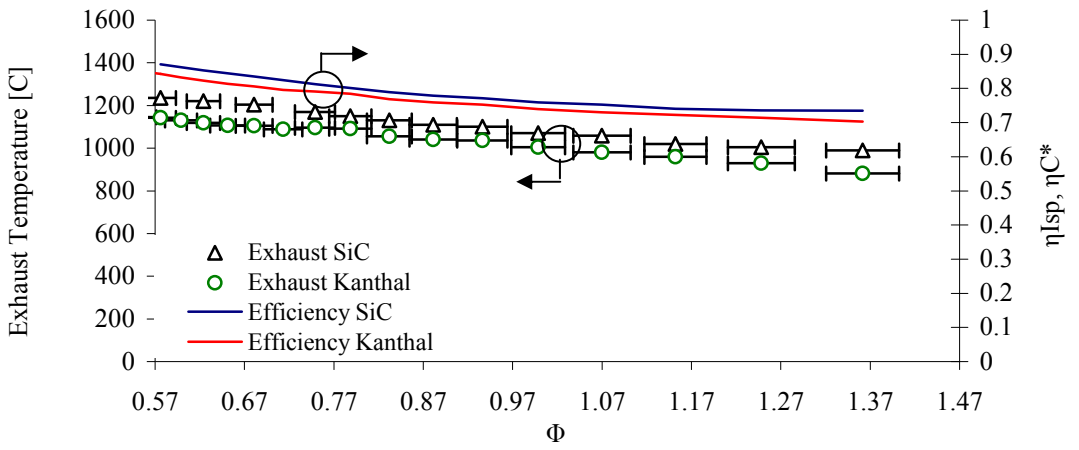

Figure 4.42. Exhaust temperatures and thermal efficiencies for the non-premixed combustor with Kanthal wire igniters and SiC igniters at a methanol flow rate of 0.45mL/min.

The efficiency of the non-premixed combustor with flush mounted SiC igniters is on average 2.3% higher than the non-premixed combustor with Kanthal wire igniters with a maximum efficiency difference of 3.2% at the lean extinction limit and a minimum of 1.6% at Φ=1.37.

Figure 4.43 shows the exhaust temperatures and thermal efficiency for kerosene combustion at a fuel flow rate of 0.2mL/min, along with methanol combustion at 0.45mL/min. The heat inputs, calculated as the product of the lower heating value (LHV) and the fuel flow rate, are similar for the above kerosene and methanol cases at ~120W and ~125W respectively. In order to apply Eq.4.10 to calculate the efficiency for kerosene combustion, kerosene was modeled as C_8H_{18}.

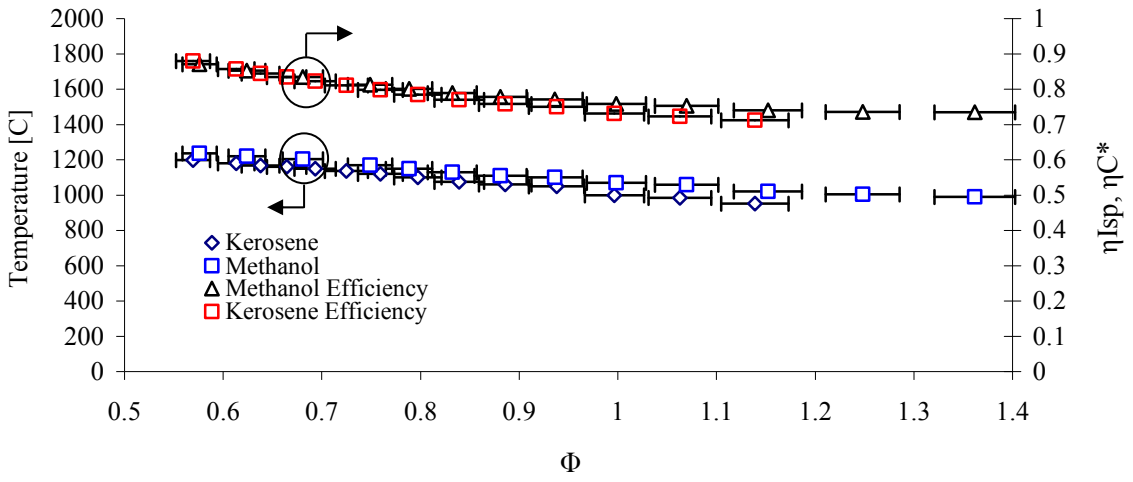

Figure 4.43.Thermal performance of kerosene combustor with methanol for comparison

Figure 4.43 shows that both the exhaust temperatures and combustor thermal efficiency for methanol and kerosene are similar, with maximum thermal efficiency of approximately 88% occurring at the lean limit. It would appear from Figure 4.43 that performance of the combustor at similar heat inputs with kerosene and methanol is nearly identical, and in fact calculated estimates of the specific energy of the exhaust gas (C_pT) show that methanol has a higher specific energy (at the lean limit where the efficiency is highest) than kerosene and is therefore more efficient in terms of mass consumption. However, for small scale devices and micro-satellites in particular, propellant mass is not the limiting factor especially considering that small satellites tend to piggyback on larger satellites in launch fairings that are not stretched for mass (lifting capacity of the launch vehicle) but are severely constrained in volume (available space in the launch fairing). [17] For this reason the volume specific energy (ρC_pT) may be a more applicable measure of performance, this is analogous to the density-impulse or 'ρI_{sp}' sometimes used to characterize rocket propellants and is a measure of how much volume of propellant is

required to produce a certain amount of thrust. Figure 4.44 shows the specific energy and density impulse from experiments for methanol, kerosene, and adiabatic values for hydrazine monopropellant and hydrazine/nitrogen tetroxide bi-propellant found in the literature. The density impulse is calculated based on the exhaust temperature and adiabatic equilibrium gas properties determined using CEA [18] assuming a 1 atm. chamber pressure and expansion to vacuum. Additionally, the density impulse is calculated using the density of the fuel and oxidizer at room temperature assuming the oxidizer originates as 100% hydrogen peroxide.

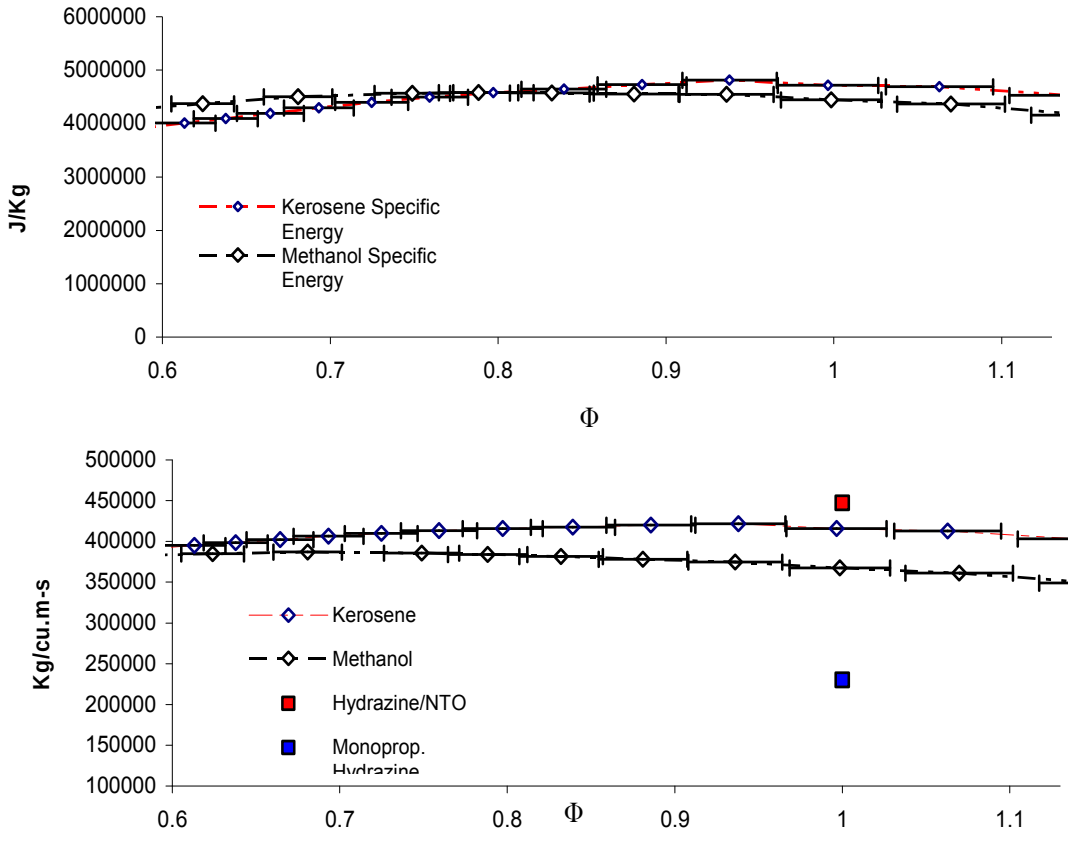

Figure 4.44. Top: Specific energy and Bottom: Density impulse for methanol (.45mL/min) and kerosene (0.20mL/min)

The calculated density impulse of kerosene/steam/oxygen is maximum at slightly fuel lean conditions (Φ =0.93) and 5.6% smaller than the adiabatic density impulse of bi-propellant hydrazine/nitrogen tetroxide. However, heat losses from a meso-scale hydrazine thrust chamber would lower that value considerably and bring it closer to the experimental values reported above. Also, although the specific energies reported above are high, they are applied to mass flow rates in the mg/sec range with maximum output enthalpy flow rates of ~170W. In order to determine the performance characteristics of the thrust chamber as a whole, an understanding of the nature of low Reynolds number discharge through micro-nozzles is necessary. These inherent physical limitations combine with the combustion efficiency to determine the overall efficiency of the thruster.

Section 4 Discharge Through low Reynolds Number Nozzles

It is well known that discharge though small scale nozzles, particularly at low Re, is adversely affected by boundary layer growth within the nozzle. The pioneering work on understanding the structure of low Reynolds number nozzle flows was performed by *Rothe* [19] who used electron beam measurements to study the internal flows of optically accessible graphite nozzles with 2.5 and 5.0mm throat diameters operating at chamber pressures of 0.15psia (55<Re<550) using room temperature nitrogen as the propellant. By determining the temperature and density profiles in the nozzle it was inferred that the ability of the nozzle to expand the flow diminishes with decrease in Reynolds number because some of the kinetic energy of the flow is converted to heat through viscous dissipation, causing the temperature to increase. *Massier* [20] investigated the variation in discharge coefficient (C_d) between Reynolds numbers of 650-350,000 through a

0.5944in. throat diameter circular nozzle using room temperature Ar, N_2, and He as propellants, demonstrating discharge coefficients above 90% in this regime. *Kuluva and Hosack* [21] investigated the discharge coefficients of 1mm. throat diameter circular nozzles and determined that the ability of a nozzle to discharge decays rapidly at a Reynolds number of roughly 500. This behavior was approximated analytically for an axis-symmetric circular nozzle by solving for the discharge coefficient in terms of the Reynolds number by using the concept of boundary layer displacement thickness. Although a reasonable agreement was found between the analytical and experimental data for axis-symmetric circular nozzles, extending the analysis to a two dimensional rectangular nozzle, which is the preferred geometry for a micro-machined thruster, has not been performed. *Bayt et. al* [22] studied the discharge characteristics of rectangular MEMS machined nozzles with throat widths of 19-35μm using room temperature nitrogen as a propellant. Again the coefficient of discharge was observed to decrease substantially at Re<500. In this section the discharge characteristics were determined for a low pressure (14.7psia<P_0<20psia) converging nozzle for high temperature flows resulting from the combustion of both methanol/oxygen, and methanol/steam/oxygen.

Since the nozzle discharges into atmospheric pressure all but the highest Reynolds numbers tested are at subsonic conditions. In this case the calculation of the isentropic mass flow rate involves determination of the flow Mach number. The Mach number was calculated under the assumption of isentropic flow based on the pressure ratio and exhaust gas properties determined through chemical equilibrium of the exhaust products at the measured chamber pressure and temperature. Note that the gas temperature was measured just upstream of the throat. Equation 4.11 shows the pressure ratio as a function

of the Mach number and ratio of specific heats.[23] Equation 4.12 shows the isentropic mass flow rate as a function of the chamber pressure, throat area, Mach number, stagnation temperature and exhaust gas properties. [23]

$$\frac{P}{P_0} = (1 + \frac{k-1}{2} M^2)^{\frac{-k}{k-1}} \qquad \text{Eq.4.11}$$

$$\dot{m} = \frac{A_t P_0}{\sqrt{T_0}} \sqrt{\frac{k}{R}} M (1 + \frac{k-1}{2} M^2)^{-\frac{k+1}{2(k-1)}} \qquad \text{Eq.4.12}$$

The discharge coefficient is calculated based on the ratio of the measured mass flow rate and the mass flow rate calculated as per Eqs. 4.11 and 4.12. The Reynolds number is calculated based on the mass flow rate and the hydraulic diameter based on Equation 4.13.

$$\mathrm{Re} = \frac{4\dot{m}}{P\mu} \qquad \text{Eq.4.13}$$

Note than in Eq. 4.13 the viscosity is calculated based on the equilibrium gas composition using the viscosity of the individual species, the mol fraction of the individual species, and an interaction parameter. The calculation is performed automatically by the NASA-Lewis Chemical Equilibrium with Applications (CEA) software. Initial experiments were conducted with room temperature oxygen, in a similar fashion to experiments found in the literature. This was done to ensure that the thrust chamber was behaving as expected and isolate any leaks. Figure 4.45, shows the discharge coefficient as determined from Equations 4.11 and 4.12 versus Reynolds number for the thrust chamber for mixtures of both oxygen/methanol and steam/oxygen/methanol.

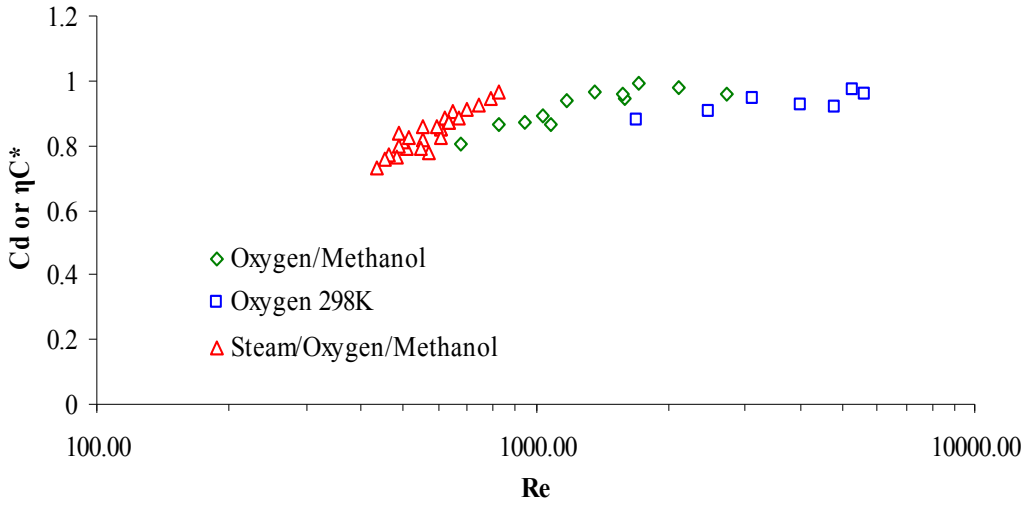

Figure 4.45. Discharge Coefficients versus Reynolds number for: oxygen, oxygen/methanol, and steam/oxygen/methanol. Note that the Re is on a logarithmic scale.

Figure 4.46, shows the discharge coefficient vs Reynolds number for the data presented in Figure 4.45 along with historical data obtained from *Rothe* [19], *Kuluva* et al.[21], *Messier et al.* [20], and *Bayt et al.* [22]. A correlating function, Equation 4.14, is also presented that relates C_d to the Reynolds number. The correlation is valid with the range 40<Re<355000 for cold flows. A summary of the test conditions covered by the data is shown in Table 4.1. The wide range of test conditions accounts for large variability in the throat geometry, chamber pressure, stagnation temperature, ambient conditions, and exhaust gas properties (specific heat ratio, gas viscosity, and exhaust gas molecular weight). Note that in Figure 4.46, reacting flow cases are fit to the red line and cold flow cases are fit to the green line.

Table 4.1: Summary of the Test Condition Covered in Figure 4.39

Author	Throat Characteristic Dimension/X-sect	Gas	Stagnation Temp. [K]	Stagnation Pressure [Psia]
Baryt, R. et al.[21]	19-35μm/rectangular	Nitrogen	300	5-100
Kuluva, G.A et al. [20]	1mm/circular	Argon, Helium	300	-
Rothe, D.E [18]	.5-2.5mm/circular	Nitrogen	300	-
Massier, P [19]	.5944in/circular	Argon, Nitrogen, Helium	300	<14.7
This Study	.0156in/rectangular	Oxygen Cold Gas, Methanol/Oxygen combustion products, Methanol/Steam/oxygen combustion products	298-2383	14.9-19.7

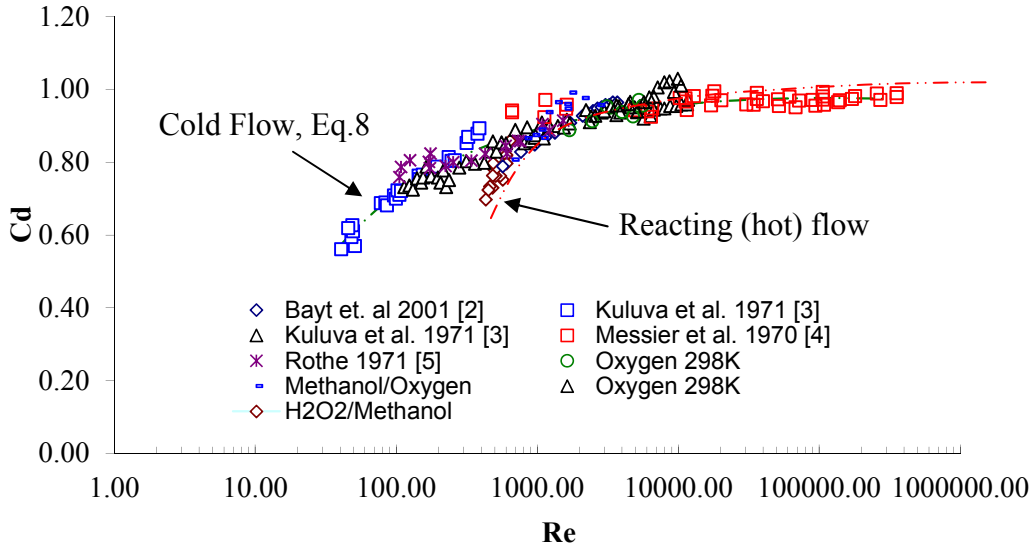

Figure 4.46. Discharge coefficient versus Reynolds number. Note that the x-axis is on a log scale.

$$C_D = 1.33 - 8.75e^{-04} Ln^2(\mathrm{Re}) - \frac{2.78}{Ln(\mathrm{Re})} \quad \text{For} \quad 40<\mathrm{Re}<355000 \qquad \text{Eq.4.14}$$

Note that for the reacting flow cases, indicated by the red line, the discharge coefficient decreases more rapidly as the throat Reynolds number is decreased. Discharge coefficients as low as 0.69 occur at Reynolds numbers as high as 500. Whereas a Reynolds number of ~100 is required to achieve the same discharge coefficient in cold flow conditions. Note that the decay in discharge coefficient with decrease in Reynolds number occurs because the large boundary layers effectively reduces the throat area, thereby reducing the mass flow rate discharged at a particular chamber pressure.[24] Since the boundary layer displacement thickness is a function of the Reynolds number its sensitivity to gas temperature and gas viscosity is different from the sensitivity of Reynolds number to temperature. It would be expected then that increasing the gas temperature would cause the discharge coefficient to remain low, even if the Reynolds number is high. This effect was predicted by *Louisos and Hitt*[25] in a numerical study who found that larger gas temperatures led to thickening of the boundary layer for flows with the same throat Reynolds number, however the effect was not confirmed experimentally. The overall performance of a thruster in terms of impulse is related to the product of the total mass flow rate through the nozzle and the exhaust gas velocity. The former is directly dependent on the discharge coefficient and the latter is directly dependent on the combustion efficiency. A tradeoff occurs at high temperatures and low Reynolds numbers because increasing the combustion efficiency results in higher gas temperatures, however, higher gas temperatures result in lower discharge coefficients. Since the temperature of the gas at the throat section of the nozzle is not known a correlation for the hot flow is not provided.

Section 5 Thrust Measurement

Steady State

Using the thrust stand described in Section 3.4 the thrust was measured for both cold flow and hot flow conditions. The thrust force versus oxygen volumetric flow rate for oxygen cold flow is shown in Figure 4.47 along with the theoretical results (shown in blue). Since both the thrust and chamber pressures are stable in cold flow conditions these measurements were used to re-validate the thrust stands performance and check for leaks. Note that all the measurements presented are subsonic with the jet discharging into the ambient lab conditions (static pressure of 1atm.).

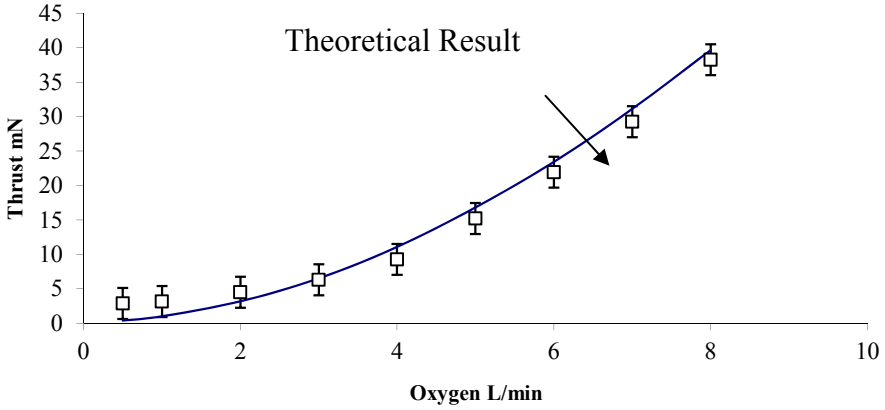

Figure 4.47.Cold flow thrust measurements and theoretical prediction.

As in Figure 3.34 the measured thrust agrees favorably with the predicted values with a slight over-prediction at low thrust levels due to characteristics of the calibration discussed above. Unlike the results presented in Figure 3.34 the predicted thrust is calculated as the product of the exit plane Mach number, the local sound speed, and the measured mass flow rate in order to account for compressibility of the gas.

Unlike the cold flow measurements shown above hot flow measurements taken with methanol/steam/oxygen are subject to combustion instabilities that contribute to temporal variations in the thrust force. Figure 4.48, below shows the time history of the thrust force for a methanol flow rate of 0.85mL/min and an equivalence ratio of 1.28.

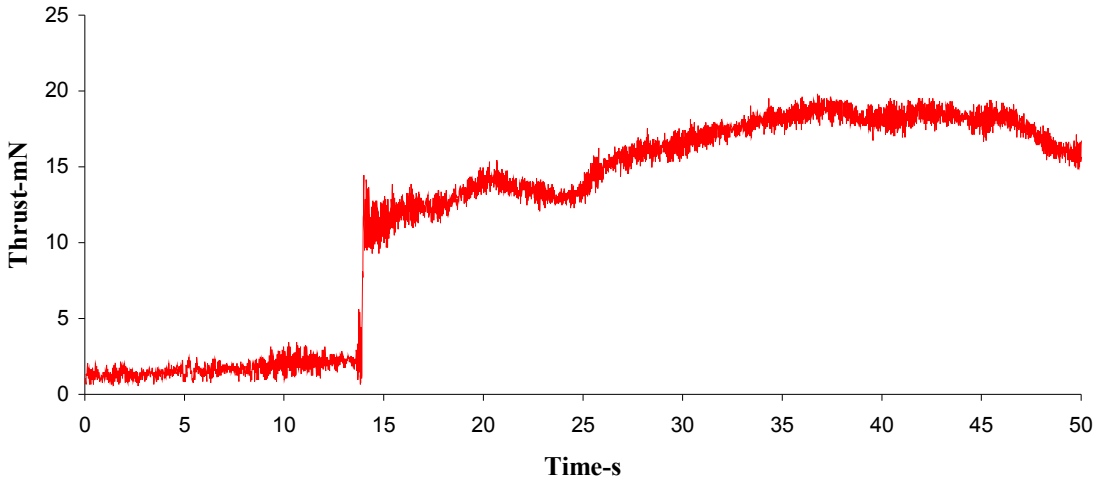

Figure 4.48. Time history of the thrust produced at a methanol flow rate of .85mL/min and an equivalence ratio of 1.28.

Spectral analysis through the Fast Fourier Transform was used to determine the frequency and magnitude of the fluctuations in the thrust around the mean value. Figure 4.49 shows the fluctuating frequency versus the ratio of the fluctuations in the thrust to the mean thrust for a methanol flow rate of 0.85mL/min and equivalence ratios of 2.81, 2.01, and 1.76.

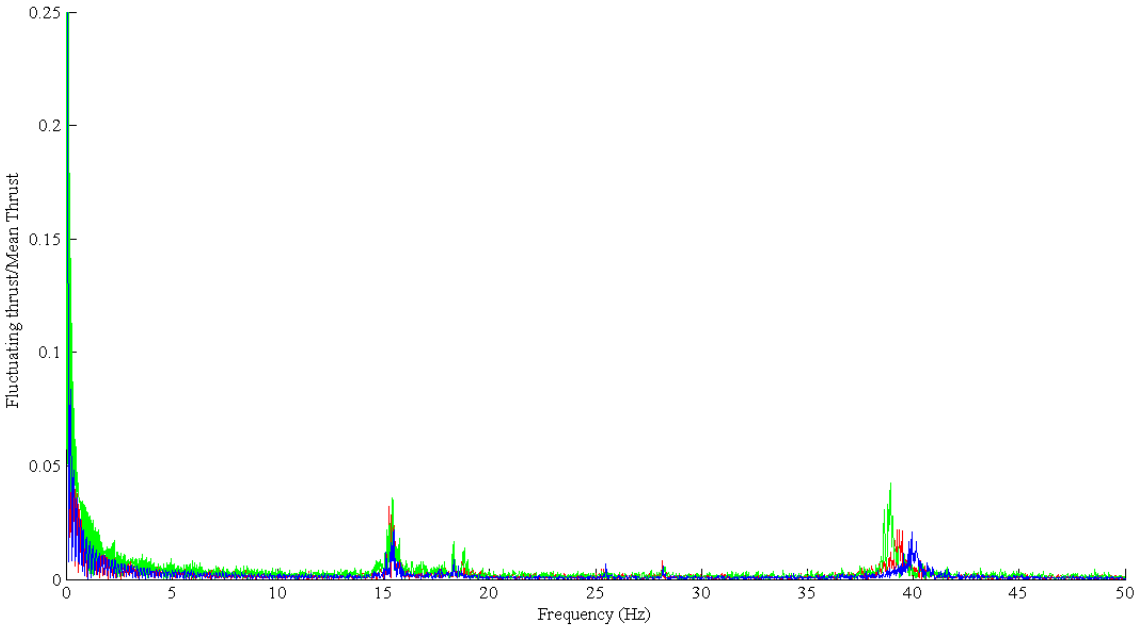

Figure 4.49. Fluctuating thrust/Mean thrust for a methanol flow rate of .85mL/min and equivalence ratios of 2.81,2.01,1.76, at mean thrust levels of 9.24mN, 9.45mN and 13.40mN respectively.

Figure 4.49 shows that fluctuations in the thrust force drive the thrust stand at a number of frequencies. Dominant frequencies include the thrust stand damped natural frequency of approximately 15Hz and a secondary frequency of ~40Hz. As a percentage of the mean thrust the ~40Hz fluctuations decrease from ~4.25% to ~2.10% in magnitude as the mean thrust is increased (with simultaneous decrease in the equivalence ratio), with a shift in the peak towards high frequencies. However, the percentage variation in the thrust is smaller than the standard error in the thrust measurement and hence the fluctuations in the thrust measurement are not considered substantial with respect to the mean thrust level.

Since the thrust force, chamber pressure, and upstream fuel pressure were acquires simultaneously the spectral components of the chamber and fuel pressure were analyzed to determine if propellant delivery is the cause of the instability shown in Figure

4.49. Figure 4.50 shows the FFT of the thrust, chamber pressure, and upstream fuel pressure for a methanol flow rate of .85mL/min and an equivalence ratio of 1.76.

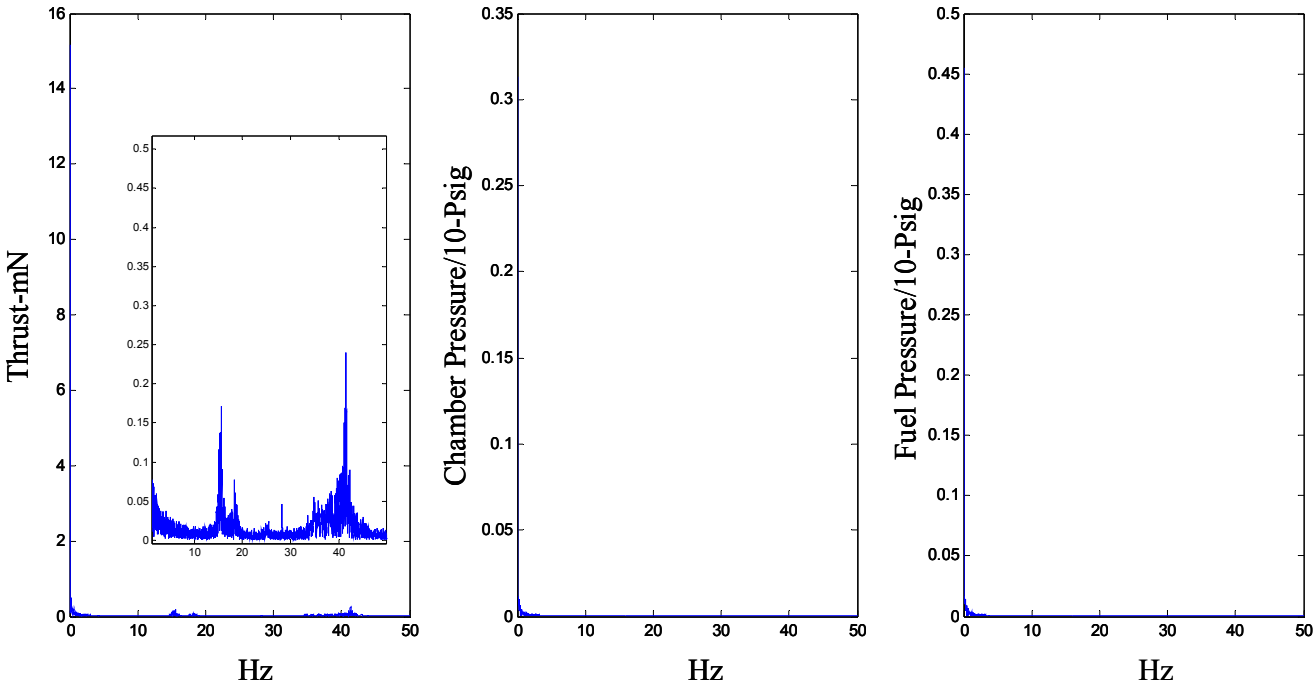

Figure 4.50. From left to right: FFT of thrust, chamber pressure, and fuel delivery pressure. The inset on the left most figure is a magnification or the thrust spectrum. The results suggest that fluctuations in the measurements of the chamber pressure and fuel delivery pressure are due to random signal noise and are not physical in nature.

Figure 4.50 shows the FFT results of the thrust, chamber pressure, and fuel delivery pressure. Note that the pressures given are raw data and are equivalent to one tenth of the actual pressure in psig. Figure 4.50 shows that the 40Hz fluctuation in the thrust force, through well below the mean thrust value, are entirely uncorrelated to fluctuations in the chamber pressure or fuel delivery pressure. Since the mass flow rates are electronically controlled the variation in thrust force is likely caused by fluctuations in the chamber temperature arising from a fluctuating heat release rate. Because the fluctuations were small relative to the mean thrust value the cause of the fluctuations was not investigated.

Figure 4.51, below shows the measured hot flow thrust for a methanol flow rate of 0.85mL/min and varying equivalence ratio, along with the values predicted from isentropic theory assuming that the gas properties in the combustor are the equilibrium gas properties at the measured chamber temperature and pressure (shown in blue). The values presented are mean values of the thrust measurement.

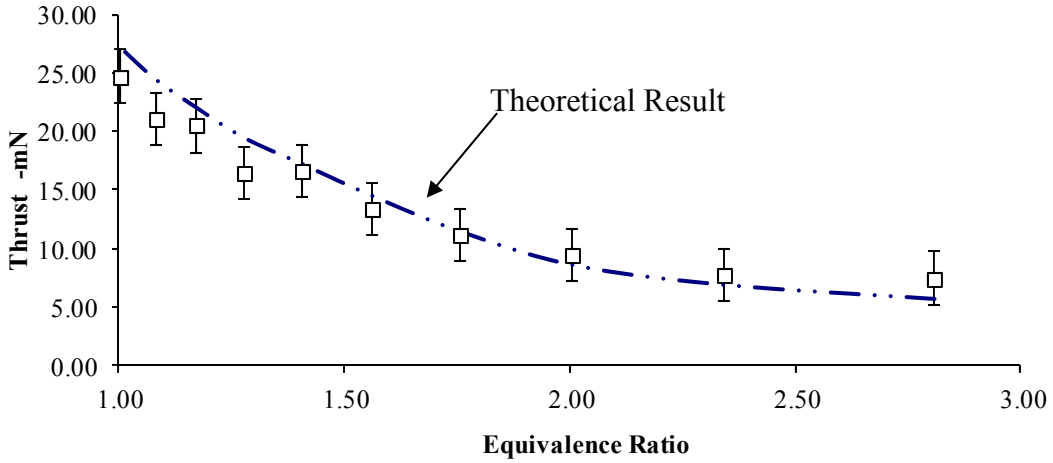

Figure 4.51. Thrust force versus equivalence ratio for methanol/steam/oxygen with a methanol flow rate of 0.85mL/min

In Figure 4.51 the maximum measured thrust is 24.71mN at an equivalence ratio of 1.0. The monotonous increase in thrust with decrease in equivalence ratio is expected since the combustor thermal performance increases monotonously as the mixture is made fuel lean, see Fig.4.43 and Ref. 2. At low thrust levels the measured thrust is higher than the theoretical result due to the calibration characteristics discussed previously. Since the theoretical result is calculated based on the measured chamber temperature, chamber pressure, and equilibrium gas properties it represents the thrust that would be produced through an ideal nozzle. The close agreement between the isentropic result and the experimental values indicates reasonable efficiency in the nozzles ability to convert the

stagnation enthalpy of the product gasses into thrust relative to the theoretical predictions even at moderate chamber pressures (maximum chamber pressure of 19.16psia with an average specific impulse efficiency of 91%).

The specific impulse efficiency, defined as the ratio of the delivered specific impulse to the specific impulse predicted based on equilibrium at the adiabatic flame temperature is shown in Figure 4.52, below. The thrust data is taken at a fuel flow rate of 0.85mL/min. Figure 4.52 also shows the specific impulse efficiency defined as the ratio of the specific impulse based on chemical equilibrium at the measured chamber temperature, and the specific impulse based on equilibrium at the adiabatic flame temperature.

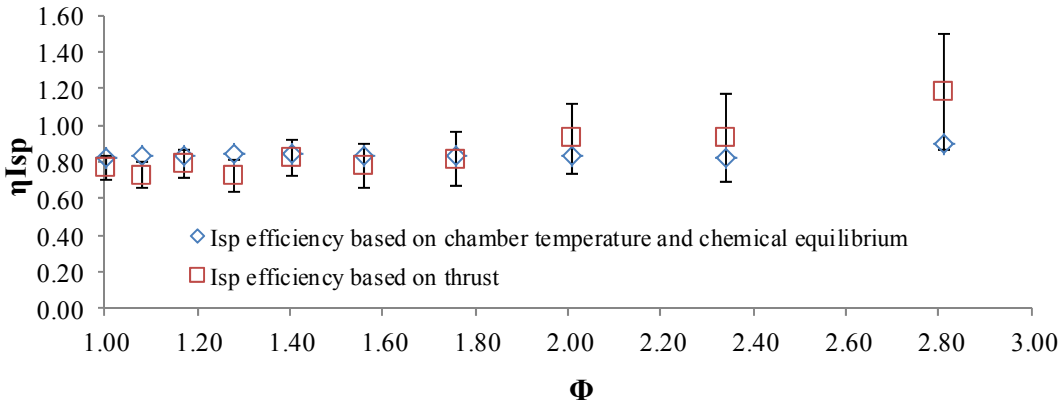

Figure 4.52. Specific impulse efficiency based on both delivered thrust and chamber thermodynamics

Figure 4.52 shows the specific impulse efficiency for a fuel flow rate of 0.85mL/min and varying equivalence ratio (Φ). The agreement between the Isp predictions based on the measured chamber temperature and equilibrium gas properties and the Isp based on the measured thrust is acceptable within the error margins of the thrust stand. The error being larger at higher equivalence ratios where the thrust output is

lower, see Fig. 3.31 and 3.34. The agreement suggests that the enthalpy of the combustion products is close to the enthalpy of the combustion products if they were at chemical equilibrium at the measured chamber temperature. This indicates that the combustion efficiency is high and the low chamber temperatures are due to wall heat losses and not incomplete combustion. Note also that the efficiency does not vary much with equivalence ratio, this is due to the unique thermal characteristics of the heat recirculating combustor where the chamber temperature increases monotonously from the rich extinction limit to the lean extinction limit; this provides for a situation where the thermal performance of the thruster is independent of equivalence ratio at constant fuel flow rate. [2]

Pulsed Performance

Pulsing measurements were taken with mixtures of methanol/oxygen. The mean and transient qualities of the thrust and chamber pressure were measured during the duration of the pulse and synchronized high speed video was taken to study the evolutionary nature of the flame during the pulse. Figure 4.53 shows a time trace of the one second pulse used in the experiments.

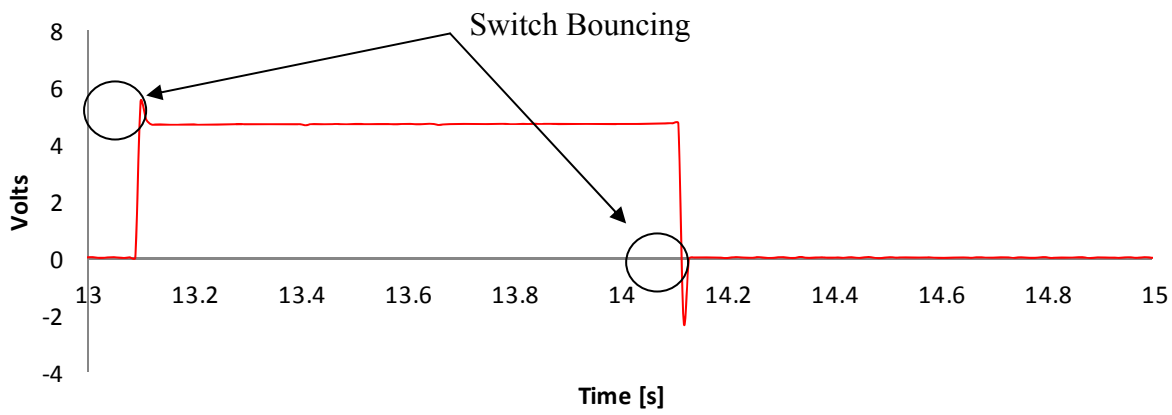

Figure 4.53.Trigger pulse used for the fuel and oxidizer solenoid valves.

Figure 4.53 shows the single square pulse used to trigger the solenoid valves, the pulse is high for one second while the beginning of the rising edge and the end of the trailing edge are separated by 1.08 seconds. The output power from the trigger is such that the valves are active only when the voltage is high.

Figure 4.54 shows the results from a single oxygen/methanol pulse with an oxidizer upstream pressure of 50psig and a fuel upstream pressure of 30psig. The upstream pressures were iteratively tuned so that the fuel and oxidizer enter the combustion chamber at approximately the same pressure.

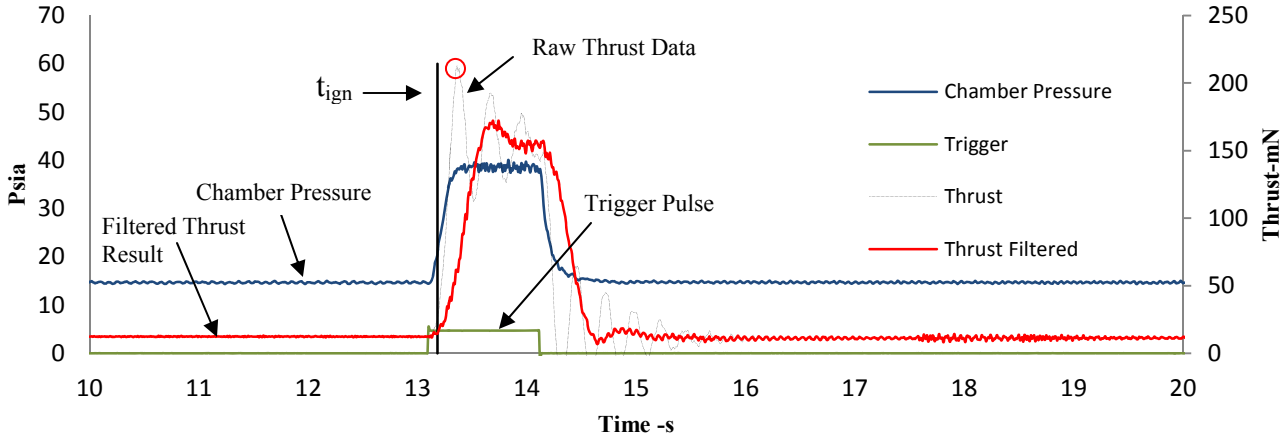

Figure 4.54. Characteristic methanol and oxygen thrust pulse, the difference between the rising edge of the pulse and the t_{ign} (the black line in the figure) is the ignition delay time

Figure 4.54 shows the trigger pulse, the raw thrust data, the filtered thrust data, the chamber pressure and the ignition delay time. The peak thrust, indicated by the red circle in the figure, occurs 250ms after ignition of the mixture and is 40% larger than the mean thrust. Because the peak thrust is larger than the mean thrust the thrust stand oscillates around the mean thrust at the thrust stand damped natural frequency. A digital stop-band filter was used to filter out the natural frequencies of the system (Fig. 3.45); the filtered result is shown in red. The result is a mean thrust of 147mN. Note that the chamber pressure fluctuates mildly for the duration of the thrust. As was done with the steady state results the flame dynamics were analyzed using a combination of high speed video and spectral analysis of both the thrust force and associated pressures. Utilizing the routine developed for tracking the approximate motion of the flame during FREI instability the flame was tracked for a 320mN pulse with chamber pressure ~70psia. Figure 4.55 along with the locations where the image intensity was tracked. In Figure 4.55 location 1 is the high speed video synchronization lamp, location 2 is the fuel injection head, location 3 is the exit to the combustion volume, location 4 is the entrance

to the exhaust channel, location 5 is the middle of the exhaust channel, and location 6 is the entrance to the nozzle.

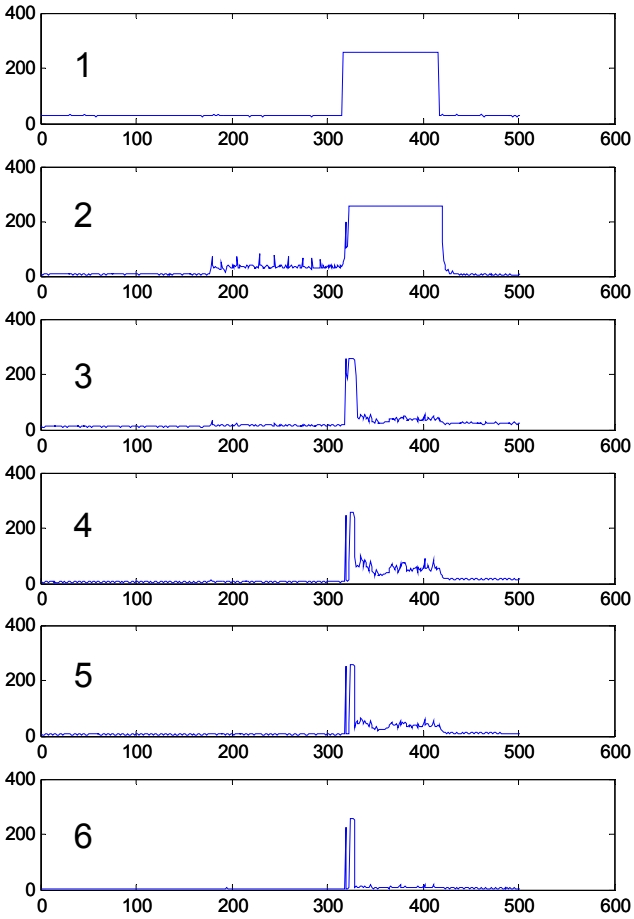

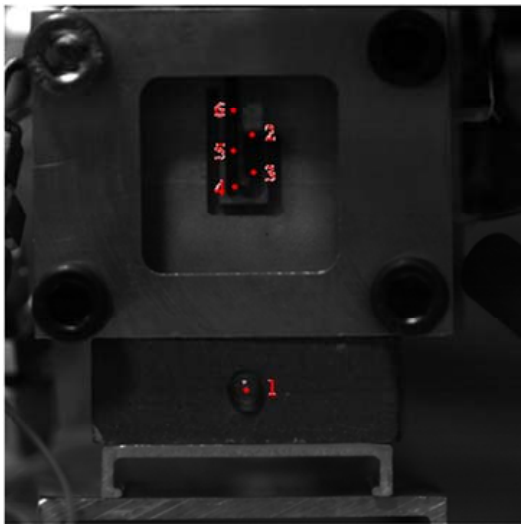

Figure 4.55. Time series of image intensities at various locations inside the combustor. Location 1 is the high speed video synchronization lamp, location 2 is the fuel injection head, location 3 is the exit to the combustion volume, location 4 is the entrance to the exhaust channel, location 5 is the middle of the exhaust channel, and location 6 is the entrance to the nozzle.

In Figure 4.55 the trigger is clearly shown in the top most image labeled '1'. The trigger duration is 1.0 sec. The image intensity at the injection head (labeled '2') saturates rapidly with a time delay of approximately equal to the ignition delay time, discussed later. The fluctuating intensity prior to triggering the pulse is due to the ignition spark. The bottom four plots, labeled 3-6 highlight the nature of the flame during the pulse. The spike in intensity following the initiation of the trigger pulse is due to hard start and the

delay time prior to stabilization of the flame occurs approximately 150ms after initiation of the pulse. The stabilization process is highly dynamic with the flame size oscillating between locations 2 through 4, 2 through 5, and 2 through 6. FFT of the six plots shown in Figure 4.55 along with the thrust force and chamber pressure show no correlation and only minor harmonic fluctuations other than those induced by the thrust stand natural frequency. Figure 4.56 shows the FFT of the thrust force.

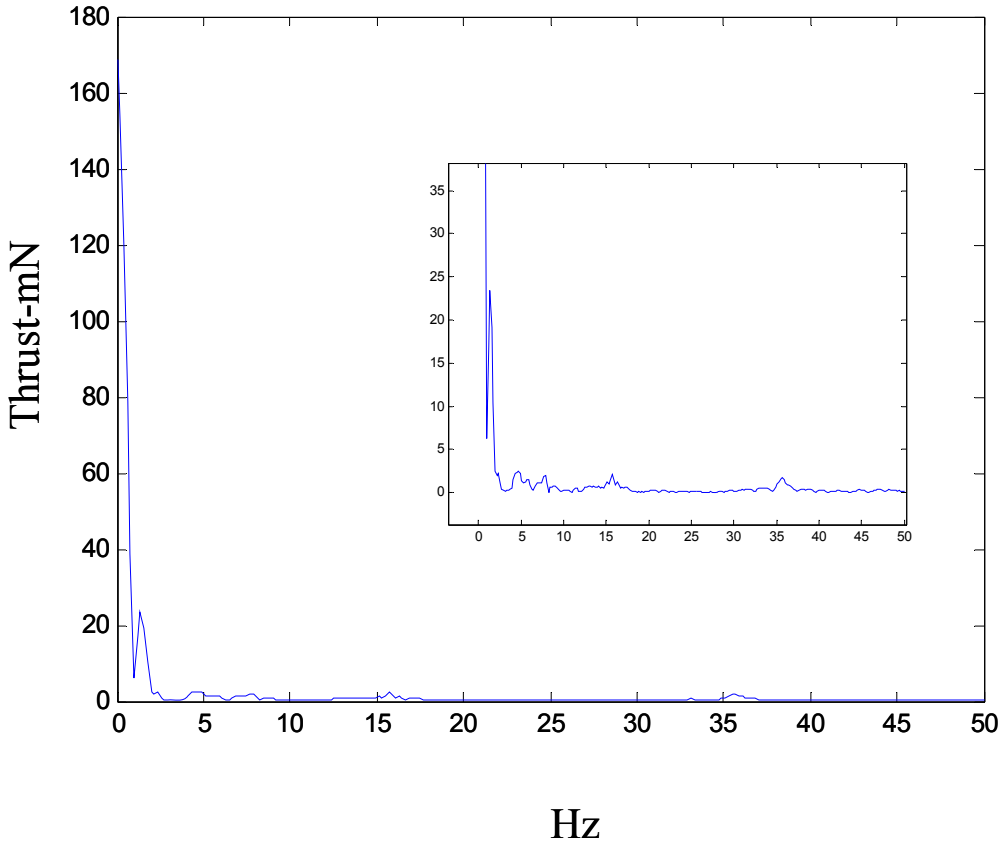

Figure 4.56. FFT of the thrust force issued from the thruster at a mean chamber pressure of 70psia and a mean thrust force of 320mN

Figure 4.56 shows the spectral characteristics of the thrust force issued from the combustor at a mean chamber pressure of 70psia and a mean thrust force of 320mN. Note that minor fluctuations occur at ~5 and ~15Hz these correspond to the natural frequencies

of the thrust stand. A small peak at ~35Hz is also apparent however the amplitude is <5mN which is less than 2% of the mean thrust level (see inset).

Note that the thrust overshoots the falling edge of the trigger pulse by ~170ms. This value is relatively constant for all tested conditions and possibly represents the amount of time required to burn down the fuel and oxidizer that remain in the lines between the valve and combustor after the valve is closed. The ignition delay time was determined through high speed cinematography of the flame during the pulse. The high speed images of the ignition sequence are shown in Figure 4.57. The high speed video frame rate is set to 100 Hz in order to synchronize the high speed video with the data acquisition module. In the figure, the emissions from the combustor at t=0.00 and t=0.02 are due to the ignition spark.

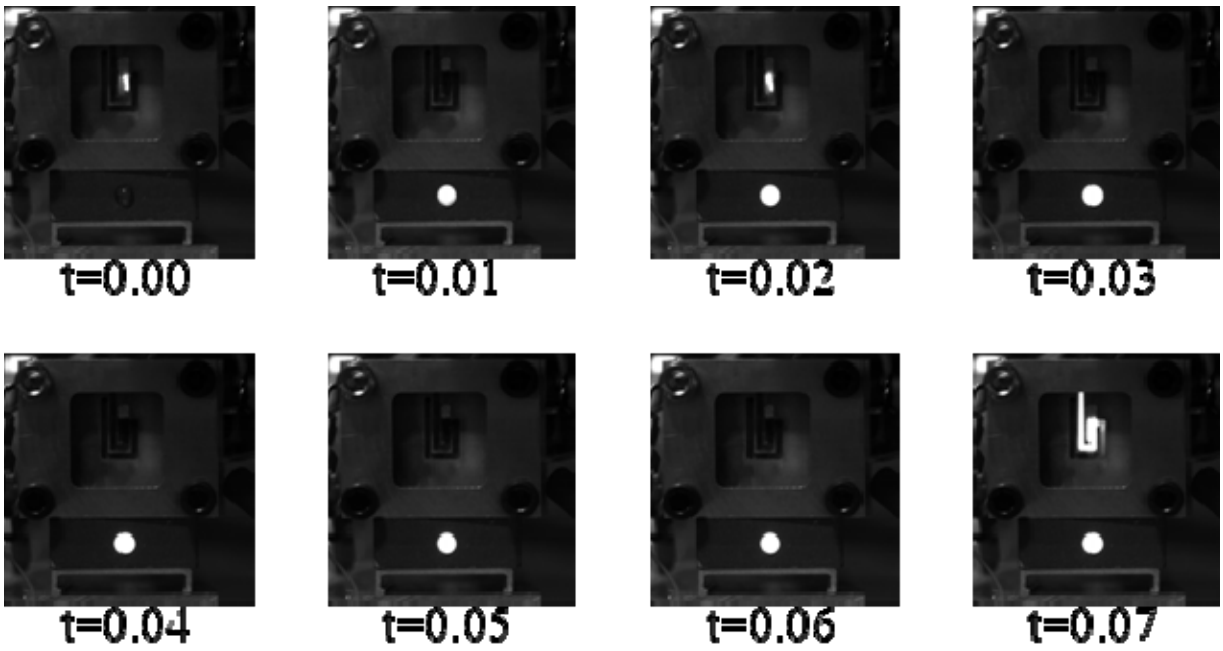

Figure 4.57. Ignition sequence, the white lamp below the combustor is the high speed synchronization lamp

Figure 4.57 shows the ignition sequence for the data set shown in Figure 4.54. The ignition delay time (t_{ign} in the figure) is 70ms. The bottom rightmost image shows the

ignition of the flame, note that the combustion is occurring in the combustion chamber, in the exhaust channel, and slightly upstream of the combustion chamber as well. This suggests fuel build up in the combustor leading to the explosive ignition and over pressurization of the chamber. This hard start is responsible for the high peak in thrust shown in Figure 4.54 prior to stabilization of the combustor at the mean thrust level. Figure 4.58 shows the ignition sequence for the same condition taken at 1000Hz. In image (A) the ignition kernel originates at the exit plane of the heat recuperator and ignites accumulated mixture in the exhaust channel (image C). Burn-down of the accumulated mixture occurs for ~.01 seconds prior to the flame stabilizing in the combustion chamber (not shown in the Figure).

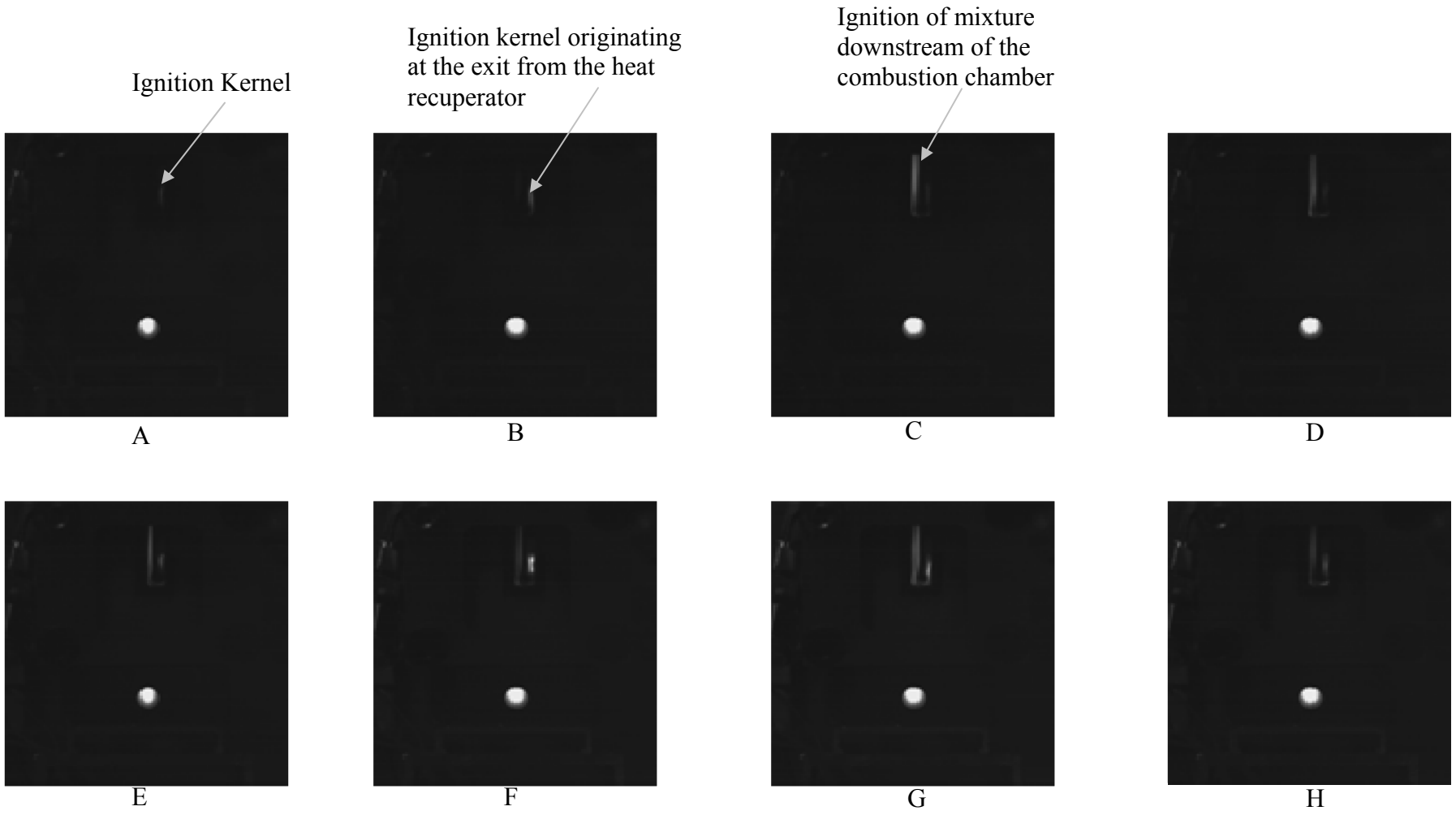

Figure 4.58. Ignition sequence taken at 1000HZ the ignition kernel originates at the heat recuperator and ignites the accumulated mixture downstream of the combustion chamber

Pulse data was collected for a number of conditions. The results for those conditions in terms of max thrust, mean thrust, response time, and overshoot times as a function of pressure ratio ($P_{chamber}/P_{exhaust}$) are shown in Figure 4.59. Note that the response time is the time difference between the peak trigger voltage and the peak thrust, and the overshoot time is the time difference between the falling edge of the trigger and the zero thrust level. In all cases the mean mixture ratio is near stoichiometric.

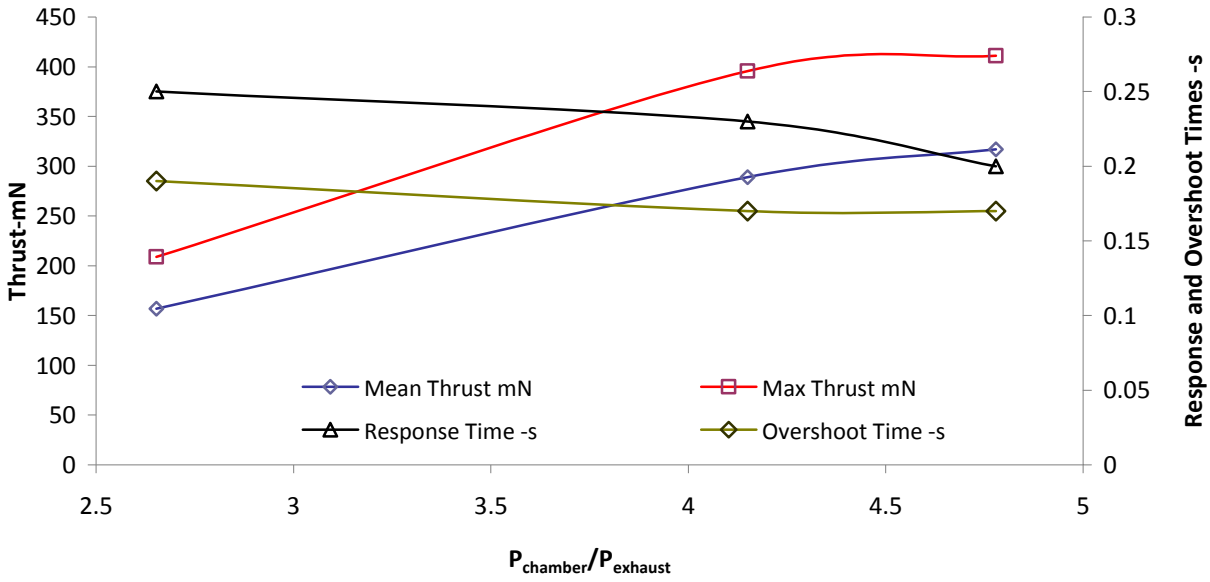

Figure 4.59. Mean and max thrust versus pressure ratio for the three tested conditions

Figure 4.59 shows that the max and mean thrust increase with pressure ratio with a maximum of 317mN mean thrust and 411mN max thrust as a pressure ratio of 4.77. The difference between the max thrust and mean thrust increase with pressure ratio, this is likely because the ignition delay time is relatively invariant with pressure ratio (as determined from the high speed videos). This means that at high pressure ratios a larger amount of fuel is discharged into the combustor prior to ignition, resulting in larger spikes in thrust due to hard start. Overshoot times are relatively constant with pressure ratio because the volume of fuel trapped in the lines after the

valve is closed does not depend on the pressure ratio of the combustor. Figure 4.60 shows the specific impulse, specific impulse efficiency, and the discharge coefficient for the three pressure ratios shown in Figure 4.59.

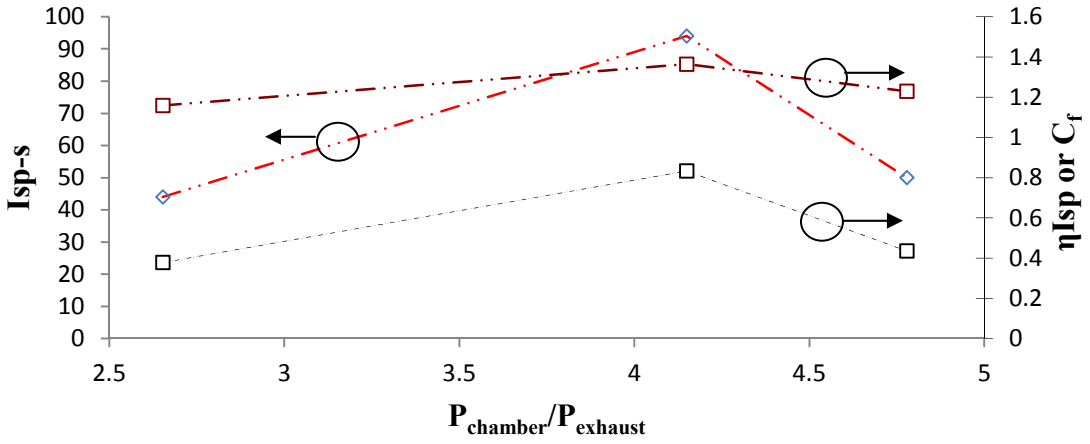

Figure 4.60. Specific impulse, specific impulse efficiency, and thrust coefficient for methanol/oxygen at varying pressure ratio.

In Figures 4.59 and 4.60 the thrust, specific impulse, specific impulse efficiency, and thrust coefficient peak at pressure ratio of 4.1 and decay in either direction. With regards to calculating the specific impulse efficiency the adiabatic-equilibrium specific impulse is determined based on the ratio of the measured specific impulse to the sonic velocity at the throat calculated from the adiabatic flame temperature and the equilibrium gas products. The maximum measured Isp efficiency is 83% at a pressure ratio of 4.1. This value is consistent with the low pressure, low thrust, steady state data presented in Fig. 4.52 However, the trend is inconsistent with ideal rocket theory which suggests a direct relationship between chamber pressure and thrust at constant mixture ratio. Likely performance losses could be attributed to incomplete vaporization or low combustion efficiency at certain conditions. High speed images

of the flames at 100% methanol concentration for each pressure ratio are shown below in Figure 4.61 along with their associated experimental conditions.

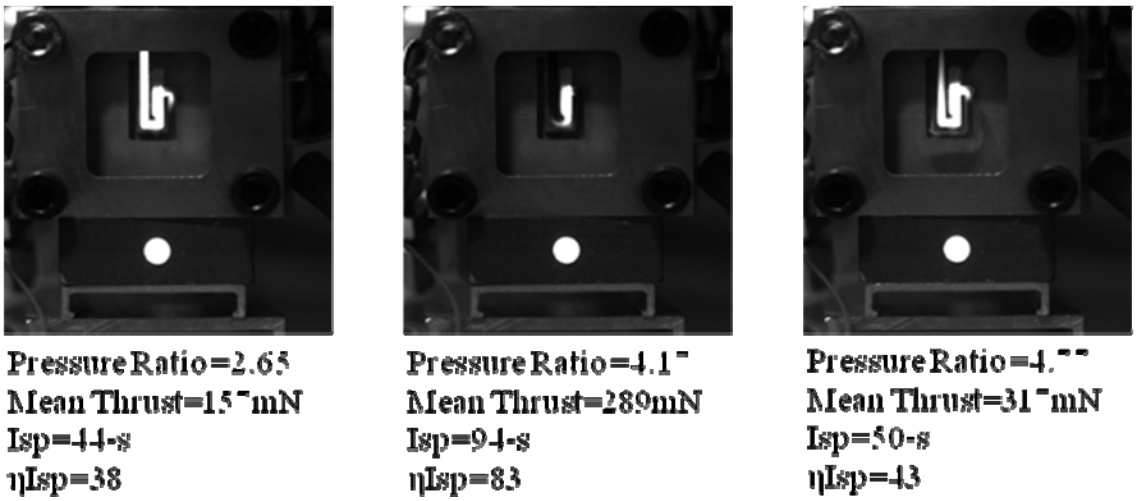

Figure 4.61. Characteristic images of the methanol/oxygen flame taken with high speed cinematography (100Hz) at three pressure ratios

The flame images show the variation in the volume occupied by the visible flame with variation in pressure ratio. At low and high pressure ratios the flame occupies the combustion chamber, exhaust channel, and a portion of the inlet channel with the largest flame at the lowers pressure ratio. This large flame volume suggests that the combustion is incomplete, i.e insufficient chamber characteristic length (L*). L* is related to the length of combustor required to vaporize, mix, and burn the fuel and oxidizer. Hence the volume occupied by the flame and the L* should be related. The minimum L* occurs at a pressure ratio of 4.1 concurrent with the maximum in performance with regards to thrust, specific impulse, and both specific impulse efficiency and thrust coefficient. The L* at this condition, which is calculated as ratio of the volume of the combustor occupied by the flame (including the volume of the heat recuperator) and the throat area, is 0.1170m.

Additional measurements were taken at lower heat loads by diluting the methanol fuel with water. Thrust data for methanol water mixtures of 90% methanol/10% water and 80% methanol/20% water were taken at varying pressure ratio. The methanol-water mixtures were used to approximate the global stoichiometry of superheated steam/oxygen/methanol since a high pressure on-demand steam oxygen generator was not available. Additionally, the dilution of the fuel with water results in a mixture that is less volatile, and consequently more difficult to vaporize.

Figure 4.62 shows the thrust delivered versus pressure ratio for the 100% methanol, 90% methanol, and 80% methanol conditions.

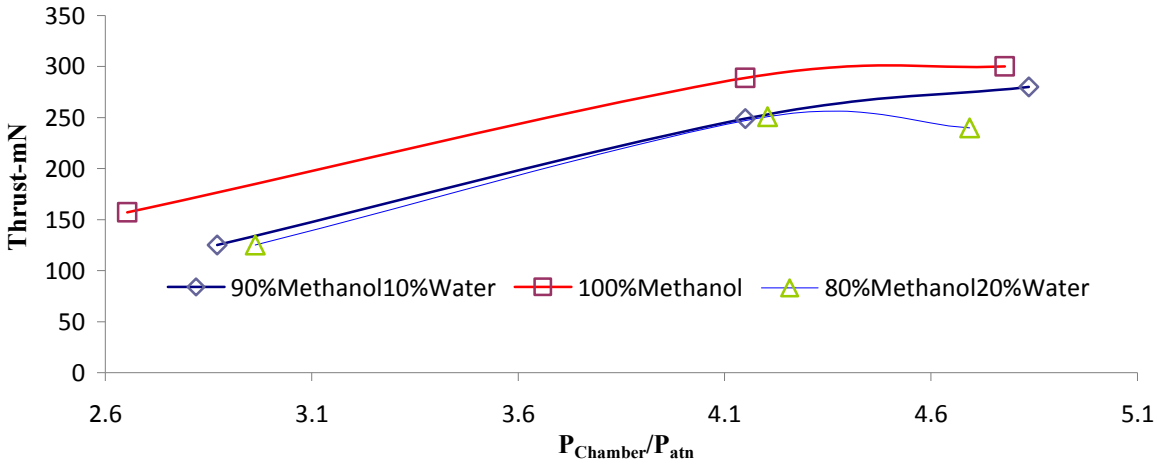

Figure 4.62. Measured thrust levels versus chamber pressure for the three tested fuel/water blends.

Figure 4.62 shows the measured thrust levels for three different fuel water blends. For both the 100% methanol and 90% methanol blends the thrust increases until the point of minimum L*, as discussed above, however in the 80% methanol case the decrease in the thrust with increase in pressure ratio above the condition of minimum L* is more substantial. It was determined during the course of the

experiments that the sharp decrease in performance is due to two phase losses that occur because heat feedback from the flame is insufficient to pre-vaporize the fuel that passes through the heat recuperator. Additionally, once the fuel leaves the recuperator the residence time in the chamber is insufficient for vaporization and combustion of the fuel. The liquid being ejected from the combustor can be seen in the high speed images along with the diamond shock structure in the exhaust plume. The presence of liquid was also seen on the underside of the thrust stand where the stand impinges with the jet.

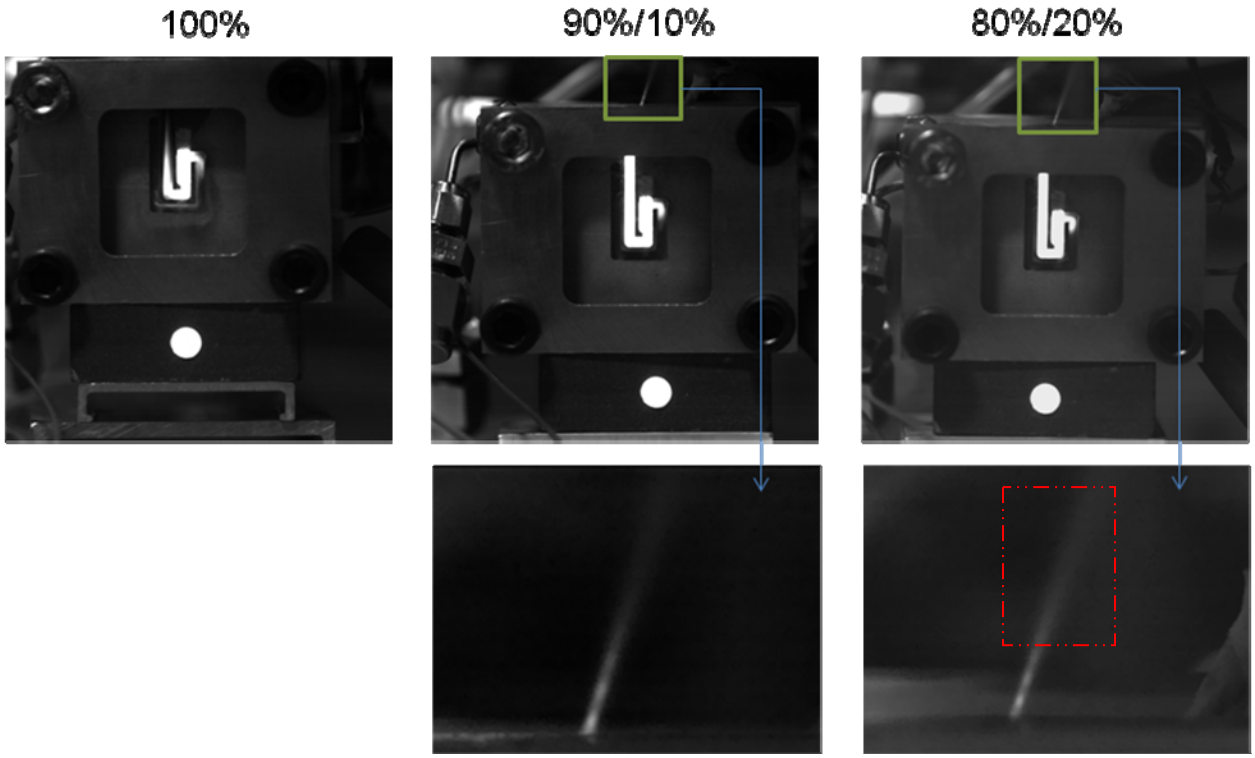

Figure 4.63. High speed (100Hz) flame images at Methanol volume fractions of 1.0,0.9,and 0.8. Note the presence of liquid in the exhaust jet (highlighted by the red square, and the presence of the exhaust plume shock structure. In the image the percentages are Methanol/Water vol/vol.

In Figure 4.63 the exhaust plume shock structure is indicated by the light and dark regions of the plume in the bottom left and right insets. Additionally, the liquid

spray in the exhaust plume is highlighted by the red square in the bottom rightmost image. It is inconclusive whether or not the liquid spray is methanol, water, or both.

Section 6: Experiments with Hydrogen Peroxide

Hydrogen peroxide experiments were conducted with three primary objectives presented below arranged in descending order or importance:

- Validation of the steam/oxygen/methanol or kerosene data presented above via oxidizer inlet temperature matching, explained in more detail below
- Demonstration of combustion with hydrogen peroxide decomposition products with a hydrocarbon fuel (preferably methanol or kerosene)
- Thrust production, specific impulse, density impulse and combustion efficiency measurement with hydrogen peroxide and a hydrocarbon fuel

As mentioned above the principle objective of the hydrogen peroxide experiments is to validate the steam/oxygen/hydrocarbon experiments presented in earlier in this report. To recall, these experiments were conducted by producing a steam oxygen mixture upstream of the inlet channel to the combustor via a lean burning hydrogen-oxygen flame. It is readily apparent that the heat release from a hydrogen oxygen flame is much higher than the heat released by hydrogen peroxide decomposition, and that this difference may produce unreliable results. In order to validate these results it is necessary to match the inlet temperature to the combustion volume prior to ignition with the superheated steam generator, with the inlet temperature prior to combustion with hydrogen peroxide decomposition products. The rationale being that if the inlet oxidizer streams are equivalent in mass flow rate and composition and the inlet

temperature to the combustion chamber is equal, then the same performance should be expected between both the thrust chamber operating on steam and oxygen produced from the hydrogen oxygen flame and the thrust chamber operating on steam and oxygen produced from the decomposition of hydrogen peroxide.

Catalyst Placement

As mentioned in Section 1.0 the performance of a hydrogen peroxide catalyst bed at the small scale is limited by the heat lost from hydrogen peroxide decomposition to both the catalyst material and the liquid constituents of the inlet hydrogen peroxide. In order to overcome this limitation the hydrogen peroxide catalyst is integrated into the inlet channel of the combustor, the reason for this is three fold:

- First, the catalyst material will be insulated by the low thermal conductivity base material of the combustor
- Second, upon ignition the catalyst material will be heated by the product gasses from the flame, alleviating the issues associated with poor decomposition efficiency due to heat losses from the catalyst bed
- Third, integrating the catalyst bed into the combustor, as opposed to placing it upstream, reduces the potential for re-condensation of the steam upstream of the combustion volume

For the experiments that follow the catalyst bed is fabricated by compressing silver swarth produced from the surface milling of a (.999) fine silver ingot into the inlet

channel of the combustor. A porous surface harderened alumina/zirconia blanket is placed at the downstream end of the catalyst bed in order to prevent attrition of the catalyst material. Further, the catalyst bed is instrumented with thermocouples at the midpoint and at the exhaust. Additional thermocouples were placed at the preheat location (inlet to the combustion chamber), the combustion volume exhaust, and the combustion chamber exhaust.

As a note, hydrogen peroxide was produced in house at high concentrations (>90%) via vacuum distillation of hydrogen peroxide of a lesser concentration (35%). The distillation was performed in a rotary evaporation column. The hydrogen peroxide was concentrated from 35% to 70% with a water bath temperature of 80C at a pressure of 25inHg vacuum. The condensate recovered had 6% hydrogen peroxide by mass remaining. A second round of distillation raised the concentration from 70% to 96% and was conducted at a water bath temperature of 80C and a pressure of 29inHg vacuum. The condensate recovered was 50% hydrogen peroxide by mass. Reducing the vacuum level to below 25inHg is crucial in the second round of distillation in order to keep the hydrogen peroxide vapor below the detonation limits and promote boiling of the water in solution below 90C, the temperature at which the hydrogen peroxide liquid will auto-decompose. The concentrations were measured by determining the refractive index using a handheld refractometer and relating the refractive index (in percent Brix) to the density.

The hydrogen peroxide was fed into the catalyst bed through a passivated Teflon syringe, stainless steel lines, and syringe pumps.

Immediate problems were encountered upon introduction of the hydrogen peroxide into the catalytic reactor. Starting from a cold start the heat released by the decomposition of the hydrogen peroxide was not capable of boiling off the constituents of the initial solution of hydrogen peroxide and water, and the water that is evolved as a consequence of decomposition. As mentioned in the background section of this report the volatilization of the liquids present in the catalytic reactor is key to achieving high product gas temperatures. Fig. 4.64, below shows the quasi-steady state temperatures measured at the locations discussed above.

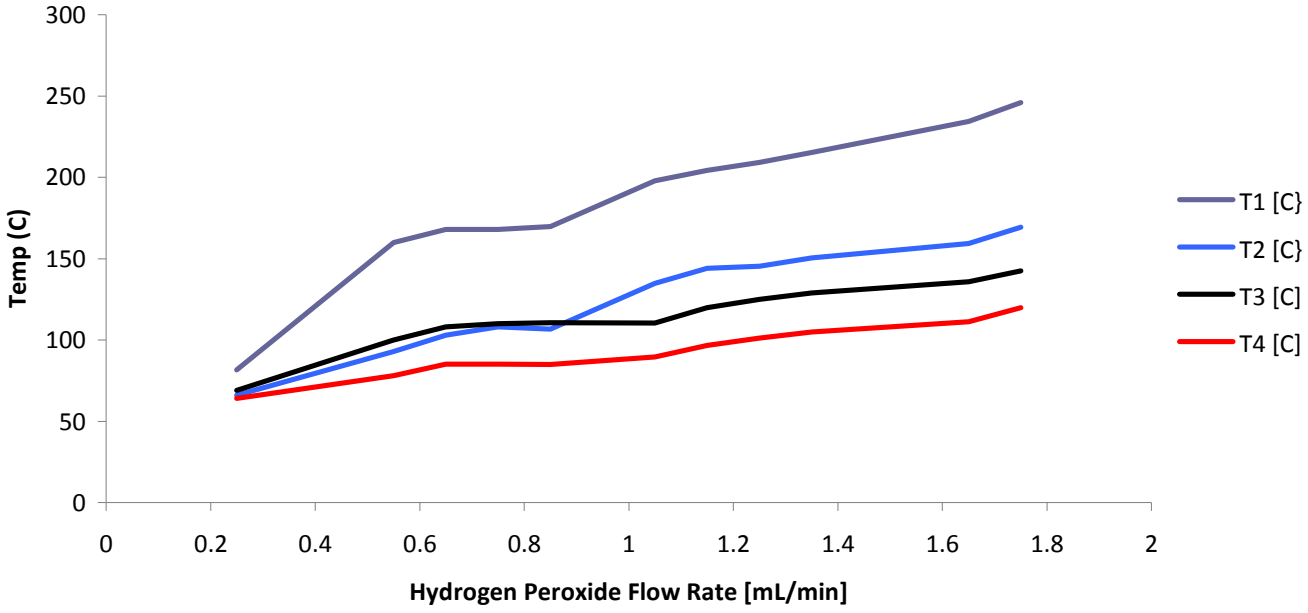

Figure 4.64. Thermocouple temperatures at various locations across the combustor versus hydrogen peroxide flow rate

The temperatures shown in Fig. 4.64 reveal some interesting qualities about the evolutionary process of steam and oxygen in the combustor. Note that T1 is the temperature in the center of the catalyst bed, T2 is the temperature at the exhaust of the catalyst bed, T3 is the temperature at the inlet to the combustor (the preheat

temperature), and T4 is the temperature at the middle of the exhaust channel. Steady state temperatures in the catalyst bed are greater then the boiling point of water for the majority of the tested conditions. At the other locations substantially higher rates of heat release were required to achieve gas phase steam in the inlet channel. It is important to note that in the initial start up process a substantial amount of liquid is absorbed by the porous alumina silicate combustor material. As the combustor heats up the temperature increase is inhibited by the latent heat of vaporization of the stored liquid. This is shown in the Figure by the regions on the plot where the temperature does not increase with increase in the flow rate of hydrogen peroxide, despite there being gas phase decomposition products in the inlet channel This is because any extra heat liberated by the decomposition of more hydrogen peroxide is being used to vaporize more stored water, instead of increasing the temperature of the gas. Additionally, gas phase decomposition products at the combustion volume inlet (T3) are not present until hydrogen peroxide flow rate of .55mL/min or higher, an immediate consequence being that the stability regimes for methanol and kerosene shown in previous sections can be truncated based on this value, since ignition from a cold start would not be possible below .55mL/min of hydrogen peroxide.

Additionally, temperature increase in the combustion chamber is stable and essentially linear once all the temperatures in the combustion chamber are larger than the boiling point of water (above 1.0mL/min hydrogen peroxide). Note that the experiment has to be prematurely terminated because the syringe volume was only 5.0mL, not enough to experience a steady state temperature at the highest flow rate.

In order to overcome this limitation the combustor was heated with a oxygen methane flame prior to the introduction of hydrogen peroxide. Upon introduction of the hydrogen peroxide the oxygen supply was shut off and the combustor was allowed to cool to the steady state decomposition temperature of the hydrogen peroxide. An attempt was made to stabilize the hydrogen peroxide methane flame, but the hydrogen peroxide was delivered from the syringe in pulses preventing stabilization of the flame. On this note delivering a stable flow of hydrogen peroxide would require a pressure fed system. However, even slightly pressurizing the hydrogen peroxide vessel would place the vapor present in the vessel well in the detonation limits for hydrogen peroxide, whereby even slight catalysis (for example contamination present in the pressure vessel) could lead to an explosion of the hydrogen peroxide vapor. The detonation limits for hydrogen peroxide are shown in Ref. 10.

Because the flame could not be stabilized with the syringe pump, and a pressure fed system would require substantial safety consideration, combustion experiments with hydrogen peroxide were not conducted.

Steady state decomposition temperatures for hydrogen peroxide decomposition obtained via the method described above are shown in Fig. 4.65, below.

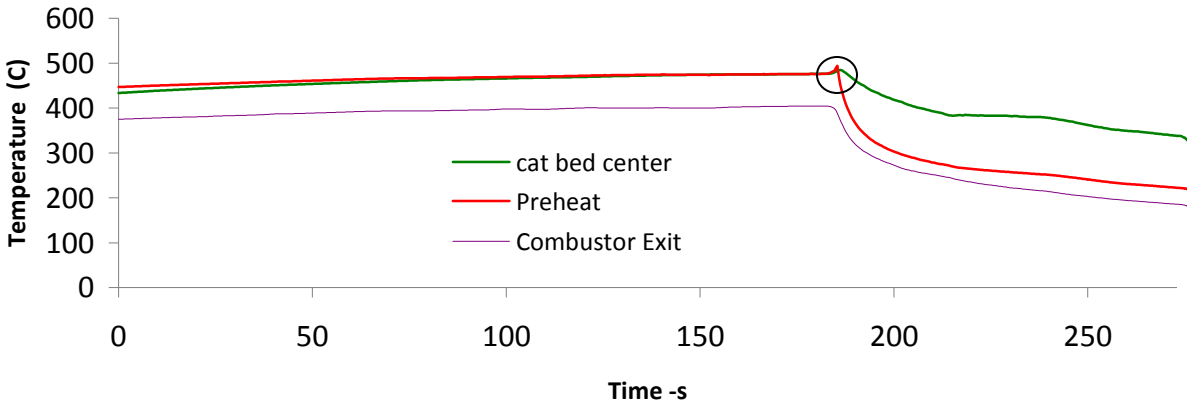

Figure 4.65. Steady state temperature obtained by preheating the combustor and allowing it to cool with hydrogen peroxide flowing, the circle marks the point where the fuel and oxygen are shut off.

In Fig. 4.65 the circle marks the location where the fuel and oxygen are shut off and the hydrogen peroxide decomposes as the combustor cools. Prior to removing the methane and oxygen the temperature in the catalyst bed and the preheat temperature are higher than the temperature at which hydrogen peroxide thermally decomposes, suggesting complete decomposition of the hydrogen peroxide, and further indicating that when the flame is present, heat transfer to the catalyst bed is high enough to promote efficient decomposition. Fig. 4.66 shows an image of the combustor after the methane and oxygen have been removed and the decomposition

temperature is approaching steady state. Note the orange glow in the catalyst bed due to the heat release from the hydrogen peroxide decomposition.

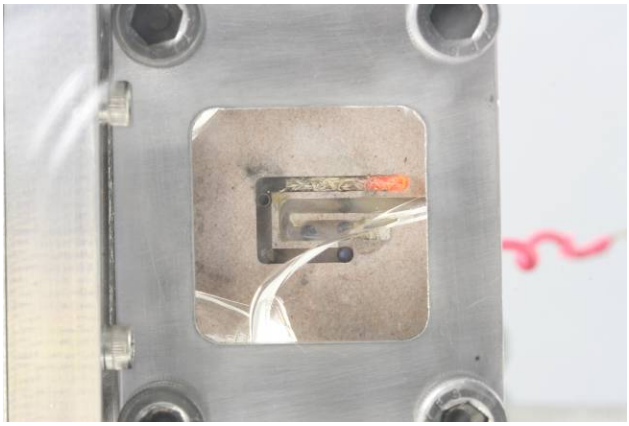

Figure 4.66. Combustor showing the decomposition of hydrogen peroxide after the methane and oxygen flame is removed. Note the orange glow in the catalyst bed due to the heat release from the hydrogen peroxide decomposition.

It is important to note that the temperature at the inlet to the combustion volume, labeled "preheat" temperature in Fig. 4.66, is ~200 C (approaching steady state at close to 225 C), again the experiment was stopped when the 5.0mL syringe was empty. This temperature is close to the temperature measured at the inlet to the combustion volume when the steam and oxygen is produced by the lean burning hydrogen oxygen flame presented earlier. The inlet temperatures versus the combined flow rate of hydrogen and oxygen is shown in Fig. 4.67, below.

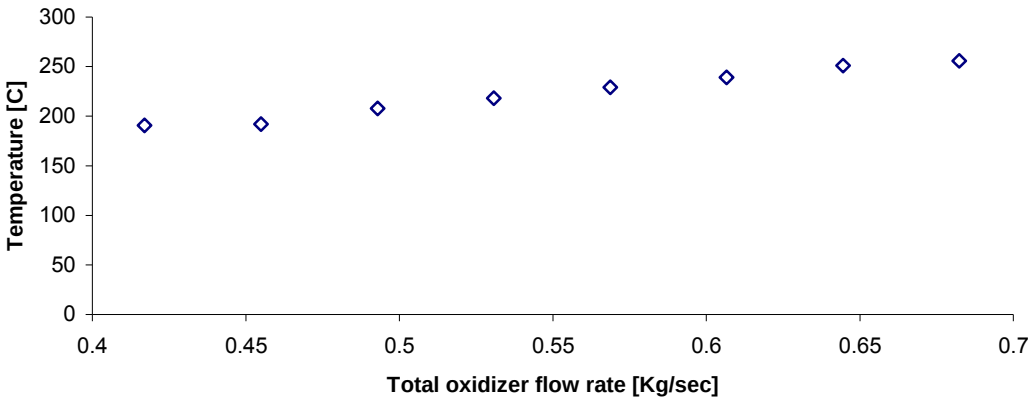

Figure 4.67. Temperatures to the inlet of the combustion volume versus total oxidizer flow rate

Section 6 References

[1] Ronney, P.D., "Analysis of Non-adiabatic Heat-recirculating Combustors," Combustion and Flame, Vol. 135, 2003, pp. 421-239

[2] Vijayan, V. and Gupta, A.K., "Combustion and Heat Transfer at Meso Scale with Thermal Energy Recirculation," *47 AIAA Aerospace Sciences Meeting, January 5-8, 2009*.

[3] Vijayan, V., and Gupta, A.K., "Effect of Channel Length on a Meso-Scale Spiral Combustor Performance" *46th AIAA/ASME/SAE/ASEE Joint Propulsion Conference and Exhibit*. Nashville, TN. July. 25-28, 2010, Paper AIAA 2010-7065.

[4] Oh, H., Huh, H., Ahn, J. and Ronney, Paul. "Effect of Scale on the Performance of Heat-Recirculating Reactors". *4th International Energy Conversion Engineering Conference and Exhibit*. San Diego, CA. June. 28-29, 2006.

[5] http://www.princeton.edu/~combust/database/other.html

[6] Liao, S.Y., Jiang, D.M., Huang, Z.H., Shen, W.D., and Yuan, Q, Chen., "Laminar Burning Velocities for Mixtures of Methanol and Air at Elevated Temperatures," *Energy Conversion and Management,* Vol. 48, Issue 3, March 2007, pp.857-863

[7] Saeed, Khizer., and Stone, C.R.,"Measurements of the Laminar Burning Velocity for Mixtures of Methanol and Air from a Constant Volume Vessel Using a Multi Zone Model," *Combustion and Flame,* Vol. 139, Issue 1-2,Oct. 2004, pp.152-166.

[8] Turns, Stephen. *An Introduction to Combustion*. 2nd ed., Boston, McGraw Hill, 2006.

[9] Barnett, H.C., and Hibbard, R.R., "Basic Considerations in the Combustion of Hydrocarbon Fuels," NACA Report 1300, 1959.

[10] Lewis, B. and Von Elbe, G. *Combustion Flames and Explosions in Gases*, Academic Press, 1987.

[11] Davu, D., Franco, R., Choudhuri, A., and Lewis, R., ***Investigation on Flashback Propensity of Syngas Premixed Flames,*** 41st AIAA/ASME/SAE/ASEE Joint Propulsion Conference and Exhibit, Tucson, Arizona, Paper No. AIAA-2005-3585.

[12] Vijayan V, Gupta AK. Flame dynamics of a meso-scale heat recirculating combustor. Appl Energy 2010;87:3718–28.

[13] Ahn, J., Eastwood, C., Sitzki, L., and Ronney, P.D., "Gas Phase and Catalytic Combustion in Heat Recirculating Burners," *Proceedings of the Combustion Institute*, Vol. 29, Issue 7, 2002, pp.957-963.

[14] http://webbook.nist.gov/chemistry/

[15] Vijayan, Vineeth., "Combustion and Heat Transfer in Meso-Scale Heat Recirculating Combustors,". PhD Dissertation, University of Maryland at College Park. 2010

[16] Osiander, Robert., Darrin, Garrison M. Ann., and Champion, John., *MEMS and Microstructures in Aerospace Applications*,1st ed., CRC Press: Taylor and Francis Group, New York, 2006.

[17] http://www.grc.nasa.gov/WWW/CEAWeb/

[18] Rothe, D.E. "Electron Beam Studies of Viscous Flow in Supersonic Nozzles." *AIAA Journal*. 9.5 (1971): 804-811.

[19] Massier, P, L Back, M Noel, and F Saheli. "Viscous Effects on Flow Coefficient for a Supersonic Nozzle." *AIAA Journal*. 8.5 (1970): 605-607

[2] Kuluva, G.A, and N.M Hosack. "Supersonic Nozzle Discharge Coeffiicients at Low Reynolds Number." *AIAA Journal*. 9.9 (1971): 1876-1877.

[21] Bayt, R, and K Bruer. "Systems Design and Performance of Hot and Cold Supersonic Microjets." *39th AIAA Aerospace Sciences Meeting and Exhibit. 8-11 January, 2001. Reno, Nevada*.

[22] Sutton, G. *Rocket Propulsion Elements*. 7. New York: John Wiley and Sons, 2001.

[23] Shirsat, V., Gupta, A.K. "Performance characteristics of methanol fuelled meso-scale heat-recirculating combustors." *Applied Energy*, Vol. 88, Issue 12, pp.5069-5082.

[24] Louisos, W., Hitt, D. "Viscous Effects in Performance of Two-Dimensional Supersonic Linear Micronozzles." *Journal of Spacecraft and Rockets*, Vol. 45, Issue 4, 2008, pp. 706-15.

Chapter 5: Contributions and Recommendations for Future Work

The work presented in this thesis is a continuation of fundamental research performed by *Vijayan and Gupta*, between 2006-2010. Their work was focused on developing a fundamental understanding of the effects of basic combustor characteristics on the combustor performance. These include: material thermal conductivity, heat exchanger length, and the effect of inlet conditions (inlet Re and Φ). This work focuses on the application of those fundamental insights towards the development of a meso-scale bi-propellant thruster. These include the departure from premixed gas phase combustion to partially-premixed and non-premixed combustion of liquid fuels. The use of porous heat recuperation for the pre-vaporization of liquid fuels. The development and analysis of a thrust stand with an accuracy of better than 1mN. An understanding of the characteristics of micro-nozzle flow at high temperatures, and both the steady state and pulsing performance of the combustor.

Section 1 Mixing

Partially-premixed combustion

Partially premixed combustion was studied with mixtures of methanol/superheated steam/oxygen. The steam oxygen mixture served as the oxidizer and was tailored to act as a surrogate to fully decomposed hydrogen peroxide. The effect of channel geometry on the performance of the combustor was

also studied in this phase. Conclusions from the partially premixed study can be summarized as follows, note that many open ended questions remain with regards to partially-premixed combustion, solutions to these questions were not pursued because the flashback characteristics make the configuration non-viable from a practical standpoint and the extinction regime of the non-premixed configuration is broader.

The extinction regimes are limited by blow-off at the lean combustion limit and flashback at the rich combustion limit for mixtures with inlet steam/oxygen ratios of 2:1 vol/vol. If the ratio of steam to oxygen is increased, representing the use of hydrogen peroxide of less concentration, the stability limits are effected only slightly. However, the nature of the rich extinction changes from flashback to blow-off. This is because the flame velocity of the global mixture decreases substantially with any increase in the steam volume fraction. The flame velocities and quenching distances for mixtures of methanol/steam/oxygen have been predicted numerically using Chemkin, calculations of the Damkholer number lend credence to the simulations, however, the flame velocity and quenching distance calculations are not validated with experiments.

Decreasing the channel aspect ratio allows for the stabilization of flames at lower total mass flow rates and richer equivalence ratios due to suppression of flashback at those conditions. The flashback likely occurs because of incomplete mixing in the upstream channel allowing for nearly stoichiometric mixture in regions of low channel velocity. Flashback may be suppressed a narrower channel widths due to a number of reasons. First: the channel aspect ratio was decreased while maintaining the inlet Reynolds number constant between combustor for the same inlet

conditions meaning that the channels were made both narrower and deeper. Increasing the depth increases the area of the channel wall exposed to the ambient increasing the heat-loss, decreasing the inlet temperature and leading to lower flame velocities in the channel. Second: the narrower channel may suppress flashback by quenching the flame.

All of the preheating occurs upstream of the fuel injection point, downstream of which the temperature variation is minimal, this is due to the increase in heat capacity rate downstream of the fuel injection point. If the mixing section of the inlet channel were longer then the preheat temperature may increase due to larger amounts of heat transfer from the products; however as discussed by *Vijayan and Gupta*, this would come at the expense of lower exhaust enthalpy and is undesirable for propulsion applications.

Non-Premixed Combustion

The non-premixed configuration was tested with both methanol/steam/oxygen and kerosene/steam/oxygen. Extinction limits in the non-premixed configuration burning methanol were limited by FREI instability and combustor failure at the lean limit and insufficient inlet oxidizer enthalpy at the rich limit. It was found that rich extinction could be predicted by estimating the amount of inlet enthalpy required for auto-ignition of the fuel, an extinction criteria was formulated to predict rich extinction based on this observation. FREI instability was observed in the globally lean regime, this instability was eliminated by replacing the Kanthal wire igniters with flush mounted silicon carbide igniters suggesting that the cause of the initial extinction is hydrodynamic in nature.

Kerosene combustion was achieved in the non-premixed configuration with excessive soot production observed at the rich limit and combustor failure at the lean limit.

Thermal Performance

The thermal performance of both the partially-premixed and non-premixed combustors was used to estimate the thruster performance and evaluate tradeoffs in the combustor design. For combustion with methanol/steam/oxygen in both the partially-premixed and non-premixed configuration the exhaust temperature increases with decrease in the global equivalence ratio with increase in temperature with increase in the heat input associated with the fuel. This occurs because the experiment is conducted by decreasing the global equivalence ratio at constant fuel flow rate, which comes with substantial increases in the mass throughput of the combustor. Although the measured flame temperature decreases as the mixture is made globally fuel lean the larger mass of product gasses contain more total enthalpy and are unable to loose that heat as they exit through the exhaust channel. This leads to a monotonic increase in the exhaust temperature with decrease in equivalence ratio. Additionally, because the oxidizer is created via exothermic chemical reaction it contributes to the heat released into the system. This means that the heat input to the combustor increases as the mixture is made fuel lean, lowering the thermal efficiency in the lean regime and resulting in a combustor whose efficiency is insensitive to changes in the equivalence ratio.

Other Notable Characteristics

From a design standpoint achieving ignition in meso-combustors is a challenging task. Traditionally, studies of minimum ignition energy are conducted in an essentially infinite medium and heat losses to the combustor wall are not a concern. However in the case of meso and micro-combustors a larger ignition energy is required to successfully ignite the mixture. Additionally, because preheat is *required* to stabilize the flame the ignition source must be of continuous operation and high frequency to achieve successful ignition. During the course of the experimentation the spark electrodes were also changed from Kanthal wires protruding into the combustion chamber to silicon carbide ignition electrodes flush mounted with the bottom of the combustion chamber. This had a notable effect on the dynamics of the flame including the suppression of FREI instability and quieter combustor operation. It was also observed that at certain conditions the flame seems to stabilize on the wire igniters, this is not the case with the silicon carbide ignition hardware.

Qualitatively operation in the partially-premixed mode resulted in a localized hot spot in the combustion chamber which led to cracking of the combustor wall at the lean extinction limit. This localization was eliminated by operating in the non-premixed combustion mode where the combustion appears much more diffuse with no visible flame or localized heating of the combustor material.

Section 3 Nozzle Discharge Characteristics

The effect of nozzle Reynolds number on discharge characteristics was evaluated for nozzles of rectangular cross section in both cold and hot flow conditions. A correlation is presented between discharge characteristics and Reynolds number that includes new experimental data and historical data taken from the literature. It was found that the variation in discharge coefficient with Reynolds number is dependent on the gas temperature. With high temperature flows showing a more rapid decrease in the discharge coefficient with decrease in the Reynolds number.

Section 4 Thrust Measurement

A mN level thrust stand was developed for the measurement of low thrust levels indirectly, without allowing the thruster to translate. The impulse balance used a deflecting cantilever beam to measure the thrust force. The characteristics of this measurement technique were evaluated and the potential sources of error discussed in detail. The thrust balance was used to measure thrust in both the steady state and pulsed modes.

Section 5 Thruster Performance

In the steady state the thruster demonstrated performance at low chamber pressures and thrust levels between ~7mN and ~25mN. The thrust output is very well matched with the theoretical predictions based on the measured chamber temperature, chamber pressure, and equilibrium assumption for the same conditions. The instability in the thrust measurement were filtered out from the natural frequencies of

the thrust stand and are shown to be minimal relative to the mean thrust level >4% and are not correlated to fluctuations in the chamber pressure and fuel delivery pressure. The specific impulse efficiency was determined both based on the measured chamber conditions and assumption of chemical equilibrium and based on the measured thrust and total weight flow rate. For the tested conditions the ratio of the ideal to measured specific impulse efficiency is very high, which suggests that the combustor efficiency is a consequence of wall heat losses and not incomplete combustion. Additionally, the insensitivity of the thrust chamber performance with equivalence ratio, which was predicted from the thermal performance, results is materialized in the thrust measurements. The implication for propulsion system design is that the flow control hardware used upstream of the thrust chamber does not need to be as accurate since the thrust chamber can tolerate variations in equivalence ratio without performance loss.

Section 6 Recommendations for Future Work

Upstream and Cold Flow and Nozzle Discharge Analysis

The work presented in this thesis has covered only the qualitative and quantitative characteristics of combustion and thrust production in a meso-scale thrust chamber. In order to determine if the results can be practically applied to a space system, it is necessary to consider the losses upstream of the combustion chamber and determine the performance gain that is provided by combustion, as compared to a cold gas discharged at similar chamber pressure.

Because the combustion products are at high temperature the energy

dissipated by viscous losses in both the combustor and the nozzle amount to an effective loss in stagnation pressure in the thrust chamber; for this reason the thrust produced via combustion should be compared to a baseline value. A baseline value may be established via the thrust produced by a cold flow thruster, the stagnation pressure of which is equal to the inlet pressures/forces to the combustor arising from both the injection of fuel and oxidizer. This would provide an assessment of the benefit provided by bi-propellant combustion as compared to cold-gas for the same thrust level and chamber pressure.

Furthermore, Figure 4.46 shows that at high temperatures the discharge coefficient through the nozzle decreases faster with decrease in Reynolds number compared to cold flow. The motivation behind bi-propellant combustion is to increase the stagnation temperature of the exhaust products and hence increase the combustor performance. However, increasing the stagnation temperature results in a decrease in the discharge coefficient due to viscous losses across the throat, therefore, there is a competition between increasing the enthalpy of the combustion products via an increase in the stagnation temperature, and decreasing the performance of the nozzle via an increase in the gas viscosity. This competition suggests that there is an optimum temperature which thrust chamber should operate in order to maximize the performance gain due to combustion for a particular throat Reynolds number. This optimum might be found by determining by determining the relationship between discharge coefficient and throat Reynolds numbers for fixed stagnation temperature over a wide range of temperatures.

Fuel Injection

Successful combustion has been demonstrated at both high and low pressure ratios via injection of fuel through a porous heat recuperator. The fuel is pressure fed into the heat recuperator via a syringe pump at low pressure (<2atm. absolute) and a blow-down tank at higher pressures (>2atm. absolute). Delivering low thrust at high pressures is hampered by the fact that the fuel delivery would require an inlet nozzle of unreasonably small diameter. Alternative fuel injection schemes such as electrospray should be investigated as a means or fuel delivery at flow rates necessary for low thrust levels <10mN.

Multi-Material Combustor

Targeted thermal control of micro-combustion and micro-power generation systems is necessary to optimize fuel efficiency at the small scale. This applies to both propulsion and micro-turbine systems, where the goal is to maximize the exhaust enthalpy, and to Thermo-Photo voltaic (TPV) and Thermo-Electric (TE) power generation systems, where designed in heat-losses direct the thermal energy away from the gas and towards the TPV or TE material.

Currently, the highest energy densities delivered by meso-scale liquid fueled combustors has been achieved by utilizing spiral countercurrent heat exchangers which are wrapped around the combustor in order to preheat reactants through structural conduction. Combating the adverse effects of heat loss from the combustion zone. These first generation of combustors utilized monolithic low thermal conductivity ceramic bodies, which while preventing heat loss from the reaction zone,

were not optimized to maximize the heat transfer to the reactants. A schematic and cross section of these combustors is shown in Figure 5.1.

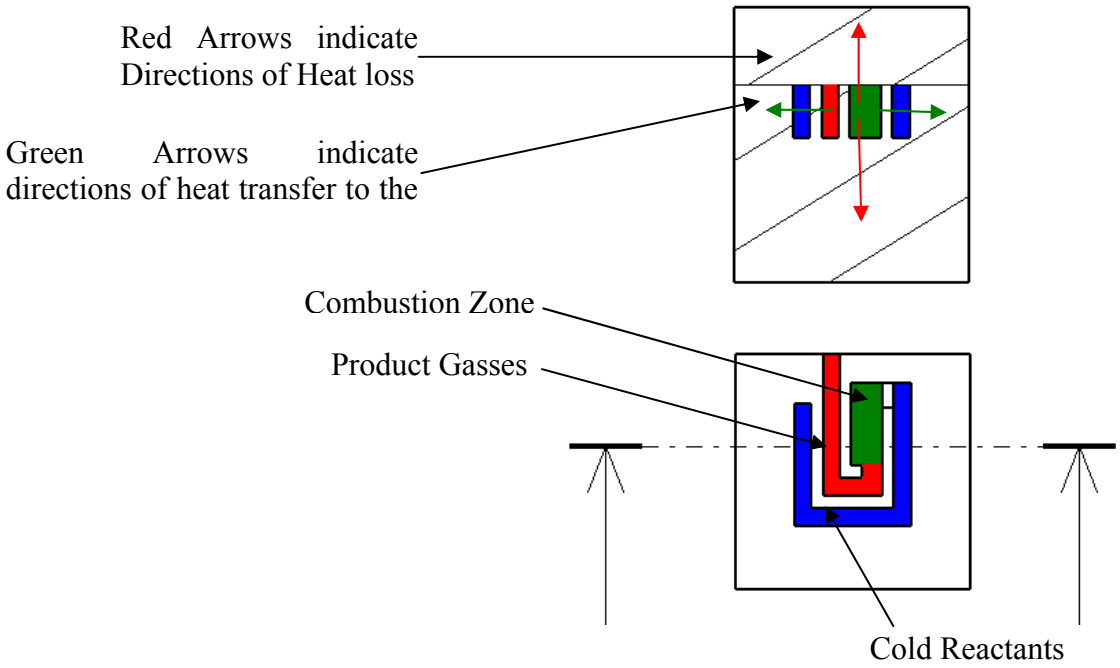

Figure 5.1. Traditional Swiss-Roll combustor

Detailed computational studies have shown that utilizing low thermal conductivity materials for the walls surrounding the combustion volume (those in thermal contact with the flame) is necessary to stabilize the flame is sub-quenching geometries. However if the same material is used for the entire combustor, as shown in the figure above, two competing thermal pathways are established. The first is across the channel, yielding productive heat transfer between the products and reactants, and the second is perpendicular to the channel, yielding heat loss. The next generation of spiral countercurrent meso-scale combustor should tilt the balance towards productive heat transfer across the channel by using a mixture of both high and low thermal conductivity materials. The proposed combustor is shown in Figure 5.2.

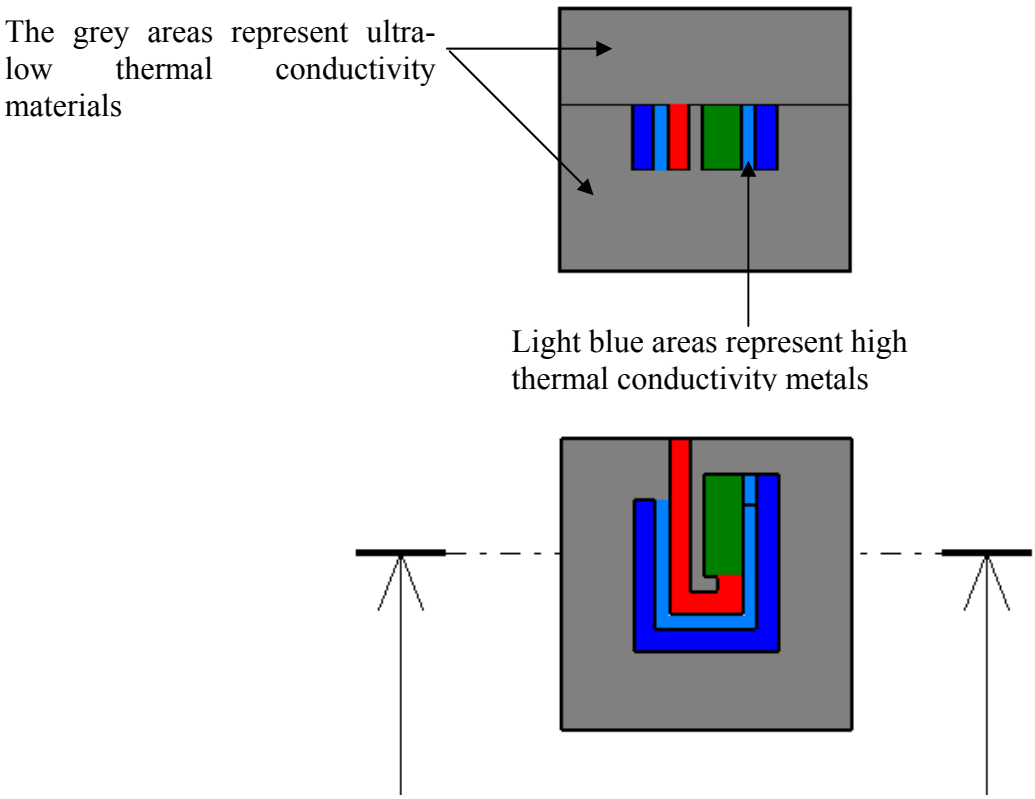

Figure 5.2. Mixed material combustor

Through using a mixture of high thermal conductivity channel walls and low thermal conductivity materials around the combustion zone and cold flow the proposed configuration will maximize heat transfer to the reactants while minimizing heat loss to the ambient. Using a mixture of materials enables a wide variety of configurations that can be tailored to a specific need. For example, tailoring high thermal conductivity walls to enable high preheat temperatures allows for ultra-lean combustion and high mass throughputs which could be utilized in a micro-gas turbine or propulsion, while the ultra low thermal conductivity material could simultaneously keep surface temperatures within the range of compatibility with TE materials (on the order of 300°C).

Integration of the Combustor with a Hydrogen Peroxide Catalyst Bed

In-order for the steam/oxygen/hydrocarbon combustors to become a viable propulsion device they must be adapted for use with hydrogen peroxide. As mentioned in Section 1.0 the performance of a hydrogen peroxide catalyst bed at the small scale is limited by the heat lost from hydrogen peroxide decomposition to both the catalyst material and the liquid constituents of the inlet hydrogen peroxide. It is suggested that the hydrogen peroxide catalyst bed be integrated into the inlet channel of the combustor, the reason for this is three fold:

- First, the catalyst material will be insulated by the low thermal conductivity base material of the combustor
- Second, upon ignition the catalyst material will be heated by the product gasses from the flame, alleviating the issues associated with poor decomposition efficiency due to heat losses from the catalyst bed
- Third, integrating the catalyst bed into the combustor, as opposed to placing it upstream, reduces the potential for re-condensation of the steam upstream of the combustion volume

An image of the proposed combustor with integrated catalyst bed is shown in Figure 5.3.

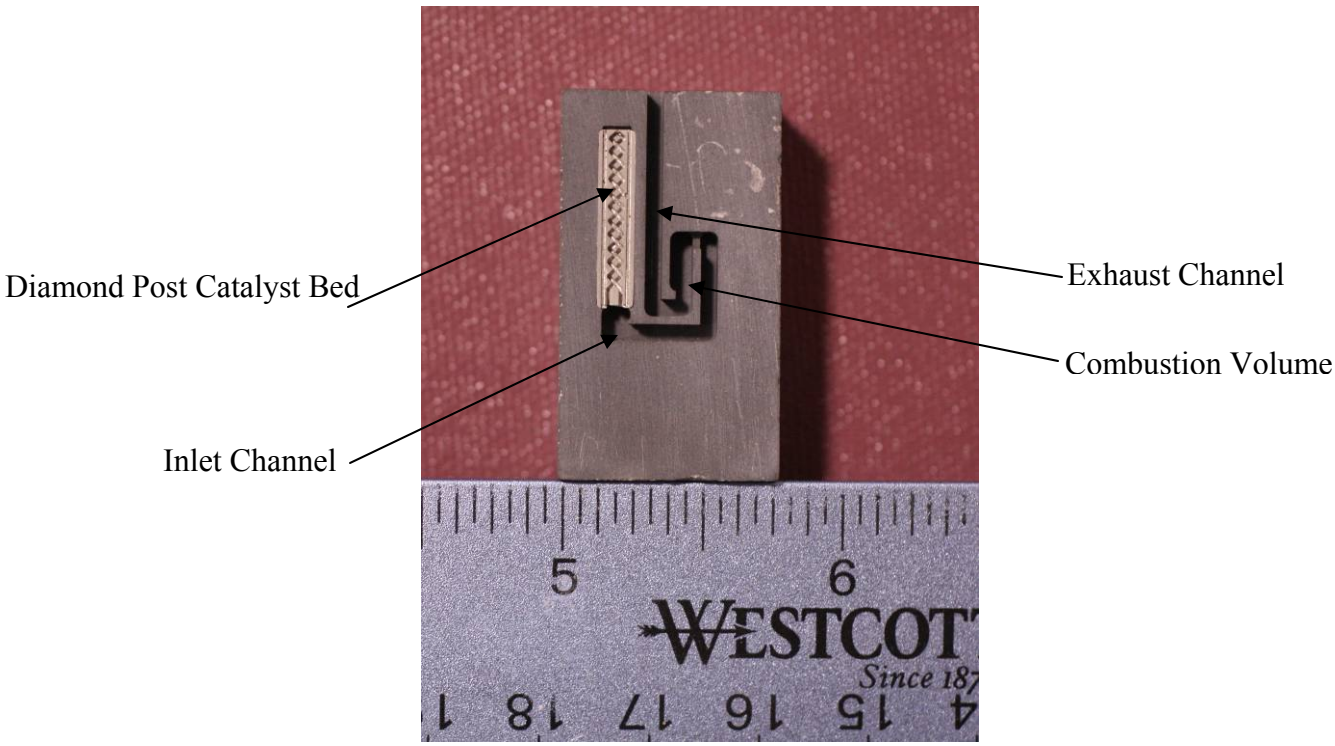

Figure 5.3. Integrated hydrogen peroxide catalyst bed Swiss Roll combustor concept. The catalyst bed is integrated into the inlet channel of the combustor. Note that the top dimensions are in inches.

Further improvements must also be made into reducing the large heat up period required prior to obtaining a hydrogen peroxide decomposition product gas temperature suitable for combustion with a fuel in the heat recirculating combustor. This may include mixing the hydrogen peroxide with a fuel, such as methanol, and injecting it over the catalyst bed or employing homogenous catalysis.

Investigation into Alternative Oxidizers and Propellant Handling Systems

In large scale propulsion systems the propellant accounts for a large fraction of the total propulsion system mass ~90%. However, in small scale systems the fraction of the total mass associated with the propellant may be as low as ~30%. This means that improving the thruster performance (I_{sp} or ρI_{sp}) may not lead to substantial

overall mass savings if the system static mass is not minimized as well. In this regard using two liquid at room temperature propellants, such as hydrogen peroxide and kerosene, would require two pumps, pump and valve control systems, valves, and all the associated hardware in order to deliver the propellants at the required pressures and flow rates. The large mass of all the ancillary equipment may outweigh the benefits of using high I_{sp} liquid bi-propellant systems. As an alternative, oxidizers such as nitrous oxide which are readily liquefied and have a very high vapor pressure at ambient conditions may be an attractive alternative. Novel design of the propellant handling system may be employed to minimize the mass of the required hardware. For example the high vapor pressure of the nitrous oxide may be used as both oxidizer and fuel pressurant integrated into a single positive displacement tank.

Appendix A:

Nomenclature

d	Quenching distance	mm
α	Thermal diffusivity	m^2/s
T_{exp}	Experimental temperature	°C
T_{ad}	Adiabatic flame temperature	°C
C	Heat capacity rate	kJ/K-s
T_{flame}	Flame temperature	°C
$T_{exhaust}$	Exhaust temperature	°C
$\dot{Q}$	Heat transfer rate	Watts
$\dot{Q}_{loss}$	Heat loss rate	Watts
Δv	Velocity Change	m/s
C*	Characteristic Velocity	m/s
Φ	Equivalence Ratio	Unit less
AR	Aspect Ratio	Unit less
V_y	'y' Velocity	m/s
S_L	Laminar Flame Speed	m/s
ηC^*	C* Efficiency	Unit less
Isp	Specific Impulse	s
ηIsp	Isp Efficiency	Unit less
T_{exp}	Experimental Temperature	°C
T_{ad}	Adiabatic Flame Temperature	°C

C_p	Constant Pressure Specific Heat	KJ/KgK
ρ	Density	Kg/m^3
C*	Characteristic Velocity	m/s
S_L	Laminar Flame Speed	m/s
Φ	Equivalence Ratio	Unit less
E_{crit}	Extinction Criteria	Unit less
$\dot{m}_{ox}$	Oxidizer Mass Flow Rate	kg/sec
$\dot{m}_f$	Fuel Mass Flow Rate	kg/sec
$C_{p,ox}$	Oxidizer Heat Capacity	kJ/kgK
$C_{p,fuel}$	Fuel Heat Capacity	kJ/kgK
T_p	Preheat Temperature	°C
T_{AI}	Auto-ignition Temperature	°C
C_d	Discharge Coefficient	Unit less
P	Ambient Pressure	Pa
P_0	Stagnation Pressure	Pa
k	Specific Heat Ratio	Unit less
M	Mach Number	Unit less
T_0	Stagnation Temperature	°C
R	Specific Gas Constant	J/kgK
$\dot{m}$	Total Mass Flow Rate	kg/sec
μ	Viscosity	Pa-s
Re	Reynolds Number	Unit less
ηC^*	C* Efficiency	Unit less

C^*_{th}	C* Thermodynamic	m/s
C^*_{exp}	C* Experimental	m/s
A_t	Throat Area	m^2
v_{eff}	Effective Exhaust Velocity	m/s
LHV	Lower Heating Value	J/kg

Appendix B: Publications

Shirsat, V., Gupta, A.K. "Theoretical Performance and Efficiency of a Meso-Scale Thrust Chamber". 50th AIAA Aerospace Sciences Meeting including the New Horizons Forum and Aerospace Exposition, Nashville, TN.

Shirsat, V., Gupta, A.K."Extinction, Discharge, and Thrust Characteristics of Methanol fueled Meso-Scale Thrust Chamber" Accepted for Publication in *Applied Energy*.

Shirsat, V., Gupta, A.K."A Review of Progress in Heat Recirculating Combustors" Review Article *Applied Energy*, *Volume 88, Issue 12*, *December 2011*, *Pages 4294-4309*

Shirsat, V., Gupta, A.K. "Performance characteristics of methanol fuelled meso-scale heat-recirculating combustors." *Applied Energy*, Vol. 88, Issue 12, pp.5069-5082.

Bibliography

[1]Wertz, J. *Reducing Space Mission Cost*. Boston: Kluwer Academic Publishers, 1996.

[2]Bonafacio, S. “Analysis and Design of a Multi-phase Catalytic Reactor for the Decomposition of Hydrogen Peroxide in Space Propulsive Systems”. PhD Dissertation, Universita degli Studi di Napoli “Federico II”..Web. 2006

[3]Baker, A., Curiel, A., Schaffner, J., and Sweeting, M.""You can get there from here”: Advanced Low Cost Propulsion Concepts for Small Satellites beyond LEO." *ACTA ASTRONAUTICA*. 57. (2005): 288-301.

[4]Stokes, P.R. "Hydrogen Peroxide for Propulsion and Power." Science Museum of London. London, Jan 14, 1998. Address.

[5].Scharlemann. C., Schiebel., M, Marhold, K., Tajmar, M., Miotti, P., Kappenstain, C., Batonneau, Y., Brahmi, R., “Development and Test of a Miniature Hydrogen Peroxide Monopropellant Thruster”

[6]. Musker, A. Roberts, G., Ford, S., Reakes, E., Westbury, T. “Auto-Ignition of Fuels Using Highly Stabilized Hydrogen Peroxide.”

[7.] Ventura, M.C. "Advancements in High Concentration Hydrogen Peroxide Catalyst Beds."

[8.] An, S., Lim, H. and Kwon, S., "Hydrogen Peroxide Thruster Module for Microsatellites with Platinum Supported by Alumina as Catalyst".

9. Zhou, X. Hitt, D.L. "One Dimensional Modeling of Catalyzed H2O2 Decomposition in Micro-Channel Flows".

[10]. Schumb, Walter. "Hydrogen Peroxide"Reinhold Publishing Company New York, New York. 1955

[11]. Fernandez-Pello, A.C, "Micro-Power Generation using Combustion: issues and approaches" 29th Int. Symposium on Combustion, The Combustion Institute, Pittsburgh, PA, 2002, pp. 1–45

[12] Wu, M., Wang, Y., Yang, V., and Yetter, R.A., "Combustion in Meso-Scale Vortex Chambers," *Proceedings of the Combustion Institute,* Vol. 31, Issue 2, Jan. 2007, pp.3235-3242.

[13] Ahn, J., Eastwood, C., Sitzki, L., and Ronney, P.D., "Gas Phase and Catalytic Combustion in Heat Recirculating Burners," *Proceedings of the Combustion Institute,* Vol. 29, Issue 7, 2002, pp.957-963.

[14] Sher, I., Levinson-Sher, D., and Sher, E., "Miniaturization Limitations of HCCI Internal Combustion Engines," *Applied Thermal Engineering*, Vol. 29, Issues 2-3, Feb. 2009, pp. 400-411.

[15] Vijayan, V. and Gupta, A.K., "Combustion and Heat Transfer at Meso Scale with Thermal Energy Recirculation," *47 AIAA Aerospace Sciences Meeting, January 5-8, 2009*.

[16] Kim, N., Aizumi, S., Yokomari, T., Kato., S., Fujimori, T. and Maruta, K., "Development and Scale Effects of Small Swiss Roll Combustors," *Proceedings of the Combustion Institute*, Vol. 31, 2007, pp. 3243-3250.

[17] Jones, A.R., Lloyd, S.A., and Weinberg, F.J., "Combustion in Heat Exchangers," *Proceedings of the Royal Society of London. Series A, Mathematical and Physical Sciences,* Vol. 60, 1978, pp.97-115.

Chapter 2

[1]Jacobson, S., and Epstien A. "An Informal Survey of Power MEMS." *International Symposium on Micro-Mechanical Engineering*. Tsuchiura and Tsukuba, Japan, December 1-3, 2003.

[2] Ahmed, Mahabub., "Flame Dynamics of a Mesoscale Combustor,". PhD Dissertation, University of Texas at El Paso. 2008.

[3] Wu, M-H., Wang, Y., Yang, V., and Yetter, R. A., "Combustion in Meso-Scale Vortex Chambers," *Proceedings of the Combustion Institute,* Vol. 31, Issue 2, Jan. 2007, pp.3235-3242.

[4] Sitzki, L.,Borer, K., Schuster, E. and Ronney, P. "Combustion in Microscale Heat-Recirculating Burners" *Third Asia Pacific Conference on Combustion*. Seoul, Korea, June 24-27, 2001.

[5] Sher, I., Levinson-Sher, D., and Sher, E., "Miniaturization limitations of HCCI Internal Combustion Engines," *Applied Thermal Engineering*, Vol. 29, Issues 2-3, Feb. 2009, pp. 400-411.

[6] Jones, A.R., Lloyd, S.A., and Weinberg, F.J., "Combustion in Heat Exchangers," *Proceedings of the Royal Society of London. Series A, Mathematical and Physical Sciences,* Vol. 60, 1978, pp.97-115.

[7]Vijayan, V., Gupta, A.K., "Combustion and Heat Transfer at Meso-scale with Thermal Energy Recirculation" *6th International Energy Conversion Engineering Conference (IECEC)*. Cleveland, OH. July. 28-30, 2008.

[8] Cho, J-H., Chien, S. L., Richards, C., D., Richards, R. F., Ahn, J., and Ronney, P, D., "Demonstration of an External Combustion Micro-Heat Engine," *Proceedings of the Combustion Institute,* Vol. 32, 2009, pp.3099-3105.

[9] Turns, S., *An Introduction to Combustion*. 2nd ed., McGraw Hill, Boston, 2006.

[10] Vijayan, V., Gupta, A.K., "Experimental Investigation of a High Power Density Ceramic Meso-scale Combustor " *47th AIAA Aerospace Sciences Meeting including The New Horizons Forum and Aerospace Exhibition*. Orlando, FL. Jan. 5-8, 2009.

[11] Vijayan, V. and Gupta, A.K., "Experimental Investigation of a Meso-scale Liquid Fueled Combustor " *45th AIAA/ASME/SAE/ASEE Joint Propulsion Conference and Exhibit*. Denver, CO. Aug. 2-5, 2009.

[12] Oh, H., Huh, H., Ahn, J. and Ronney, Paul. "Effect of Scale on the Performance of Heat-Recirculating Reactors". *4th International Energy Conversion Engineering Conference and Exhibit*. San Diego, CA. June. 28-29, 2006.

[13] Lee, M., Cho, S., Choi, B. and Kim N. "Scale and Material Effects on Flame Characteristics in Small Heat Recirculation Combustors of a Counter-Current Channel Type" *Applied Thermal Engineering,* Vol. 30, 2010, pp. 2227-2235.

[14] Lee, M. and Kim N. "Experiment on the Effect of Pt-Catalyst on the Characteristics of a Small Heat-Regenerative CH_4-air Premixed Combustor" *Applied Energy,* Vol. 87, 2010, pp. 3409-3416.

[15] Vijayan, V. and Gupta, A.K., "Effect of Channel Length on a Meso-Scale Spiral Combustor Performance" *46th AIAA/ASME/SAE/ASEE Joint Propulsion Conference and Exhibit*. Nashville, TN. July. 25-28, 2010, Paper No. AIAA-2010-7065.

[16] Kim, N., Kato, S., Kataoka, T., Yokomori, T., Maruyama, S., Fujimori, T., and Maruta, K. "Flame Stabilization and Emission of Small Swiss-roll Combustors as Heaters" *Combustion and Flame,* Vol. 141, 2005, pp.229-240.

[17] Spadaccini, C.M., Zhang, X., Cadou, C. P., Miki, N., and Waitz, I. A. "Development of a Catalytic Silicon Micro-Combustor for Hydrocarbon-Fueled Power MEMS", MEMS 2001, Las Vegas NV, Jan 2002

[18] Vijayan, V., and Gupta, A.K., "Flame Dynamics of a Meso-scale Heat Recirculating Combustor" *7th International Energy Conversion Engineering Conference*. Denver, CO. Aug. 2-5, 2009, Paper No. AIAA 2009-4604.

[19]Ahn, J., Eastwood, C., Sitzki, L., and Ronney, P. D., "Gas Phase and Catalytic Combustion in Heat Recirculating Burners," *Proceedings of the Combustion Institute,* Vol. 29, Issue 7, 2002, pp.957-963.

[20]Vijayan, V., and Gupta, A.K., "Thermal Performance of a Meso-scale Heat Regenerating Combustor" *7th International Energy Conversion Engineering Conference*. Denver, CO. Aug. 2-5, 2009.

[21] Vijayan, V., and Gupta, A.K. "Thermal Performance of a Meso-scale Liquid Fueled Combustor" *Applied Energy,* 2011.

[22] Vijayan, V., and Gupta, A.K. "Flame Dynamics of a Meso-scale Heat Recirculating Combustor" *Applied Energy,* Vol. 87, 2010, pp.3718-3728.

[23] Jejurkar, S., and Mishra, D. "A Review of Recent Patents on Micro-Combustion and Applications" *Recent Patents in Engineering,* Vol. 3, 2009, pp.194-209.

[24] Epstein, A.H., Senturia, S.D., Waitz, I.A., Lang, J.H., Jaconson, S.A., Ehrich, F.F., Schmidt, M.A., Ananthasuresh, G.K., Spearing M.S., Breuer, K.S., Nagle, S.F.: US Patent US20026392313B1, 2002.

[25] Mehra, A., and Waitz, I. A, "Development of a Hydrogen Combustor for a Microfabricated Gas Turbine Engine", Solid *State Sensor and Actuator Workshop*, Hilton Head, GA, 1998.

[26] Vijayan, V., "Combustion and Heat Transfer in Meso-Scale Heat Recirculating Combustors,". PhD Dissertation, University of Maryland at College Park, 2010.

[27] Youngner, D. W.: US patent US20026378292B1 (2002).

[28]Lewis, David., Janson, Siegfried., Cohen, Ronald., Antonsson, Erik. "Digital MicroPropulsion" *Sensors and Actuators A,* Vol. 80, 2000, pp.143-154.

[29] Masel, R.I., and Shannon, M.A.: US patent US20016193501B1, 2001.

[30] London, A.P., Ayon, A.A, Epstien, A.H., Spearing, S.M., Harrison, T., Peles, Y., and Kerrebrock, J.L.. "Microfabrication of a High Pressure Bipropellant Rocket Engine" *Sensors and Actuators A,* Vol. 92, 2001, pp. 351-357.

[31] Yetter, R.A, Yang, V., Aksay, I.A and Dryer, F.L. *Meso and Micro Scale Propulsion Concepts for Small Spacecraft*. Arlington VA. AFOSR. 2004. AFRL-SR-AR-TR-05-0016,FA9260-01-1-0376.

[32] Herrault, F., Crittenden, T., Yorish, S., Birdsell, E., Glezer, A., and Allen, M. G. "A self-resonant MEMS-fabricated, Air-breathing engine" *Solid-State Sensors, Actuators, and Microsystems Workshop*, Hilton Head Island, South Carolina, June 1-5 2008.

[33] Fu, K., A.J. Knobloch, F.C. Martinez, D.C. Walter, C. Fernandez-Pello, A.P. Pisano, D. Liepmann, K. Miyasaka, and K. Maruta. "Design and Experimental Results of Small-scale Rotary Engines." *Proceedings of 2001 ASME International Mechanical Engineering Congress and Exposition*. New York, NY, ASME, 41, pp. 295-302.

[34]Aichlmayr, H. T., Kittelson, D. B. and Zachariah, M. R. "Miniature Free-piston Homogeneous Charge Compression Ignition Engine-compressor Concept- Part I: Performance Estimation and Design Considerations Unique to Small Dimensions",*Chemical Engineering Science*, vol. 57, 2002, pp. 4161-4171.

[35] Dahm, W. J. A., Ni, J., Mijit, K., Mayor, J. R., Qiao, G., Dyer, S. W., Benjamin, A. G. , Gu, Y., Lei, Y., and Papke, M.L., "Micro Internal Combustion Swing Engine (MICSE) for Portable Power Generation Systems". AIAA Paper 2002-0722, AIAA, Reno, NV. 2002.

[36] Federici, J. A., Norton, D. G., Bruggemann, T., Voit, K. W., Wetzel, E. D., and Vlachos, D. G. "Catalytic Microcombustors With Integrated Thermoelectric Elements for Portable Power Production" *Journal of Power Sources* ,Vol.161, 2006, pp.1469–1478.

[37] Cohen, A L., Ronney, P., Frodis, U., Sitzki, L.; Meiburg, E., and Wussow S.: US patent 6,613,972 B2, 2003.

[38]Guazzoni, "High Temperature Spectral Emittance of Oxides of Erbium, Samarium, Neodynium, and Ytterbium", *Applied Spectroscopy*, Vol. 26, 1972, pp. 60-65.

[39]Xue, H., Yang, W. M., Chou, S. K., Shu, C. and Li, Z. W. "Microthermophotovoltaics power system for portable mems devices", *Microscale Thermophysical Engineering*, 9 2005, pp.85-97

[40] Lee, K. H., and Kwon, O. C. "Studies on a Heat-recirculating Microemitter for a Micro thermophotovoltaic System". *Combustion & Flame*, 153, 2008, pp. 161-172

[41]Nelson, R.: US patent 4,584,426, 1986.

Chapter 3

[1] Vijayan, V., "Combustion and Heat Transfer in Meso-Scale Heat Recirculating Combustors,". PhD Dissertation, University of Maryland at College Park, 2010.

[2] Wu, C.K.,Wang, H.X., Meng, X., Chen, X. Pan, W.X. "Aerodynamics of indirect thrust measurement by the impulse method", *Acta Mechanica Sinica,* Vol.27, 2011, pp. 152-163.

[3] Lun, J. "Development of a vacuum arc thruster for nanosatellite propulsion". Masters Thesis. Stellenbosch University.2008

Chapter 4

[1] Ronney, P.D., "Analysis of Non-adiabatic Heat-recirculating Combustors," Combustion and Flame, Vol. 135, 2003, pp. 421-239

[2] Vijayan, V. and Gupta, A.K., "Combustion and Heat Transfer at Meso Scale with Thermal Energy Recirculation," *47 AIAA Aerospace Sciences Meeting, January 5-8, 2009*.

[3] Vijayan, V., and Gupta, A.K., "Effect of Channel Length on a Meso-Scale Spiral Combustor Performance" *46th AIAA/ASME/SAE/ASEE Joint Propulsion Conference and Exhibit*. Nashville, TN. July. 25-28, 2010, Paper AIAA 2010-7065.

[4.] Oh, H., Huh, H., Ahn, J. and Ronney, Paul. "Effect of Scale on the Performance of Heat-Recirculating Reactors". *4th International Energy Conversion Engineering Conference and Exhibit*. San Diego, CA. June. 28-29, 2006.

[5] http://www.princeton.edu/~combust/database/other.html

[6] Liao, S.Y., Jiang, D.M., Huang, Z.H., Shen, W.D., and Yuan, Q, Chen., "Laminar Burning Velocities for Mixtures of Methanol and Air at Elevated Temperatures," *Energy Conversion and Management,* Vol. 48, Issue 3, March 2007, pp.857-863

[7] Saeed, Khizer., and Stone, C.R.,"Measurements of the Laminar Burning Velocity for Mixtures of Methanol and Air from a Constant Volume Vessel Using a Multi Zone Model," *Combustion and Flame,* Vol. 139, Issue 1-2,Oct. 2004, pp.152-166.

[8] Turns, Stephen. *An Introduction to Combustion*. 2nd ed., Boston, McGraw Hill, 2006.

[9] Barnett, H.C., and Hibbard, R.R., "Basic Considerations in the Combustion of Hydrocarbon Fuels," NACA Report 1300, 1959.

[10] Lewis, B. and Von Elbe, G. *Combustion Flames and Explosions in Gases*, Academic Press, 1987.

[11.] Davu, D., Franco, R., Choudhuri, A., and Lewis, R., ***Investigation on Flashback Propensity of Syngas Premixed Flames,*** 41st AIAA/ASME/SAE/ASEE Joint Propulsion Conference and Exhibit, Tucson, Arizona, Paper No. AIAA-2005-3585.(

[12.] Vijayan V, Gupta AK. Flame dynamics of a meso-scale heat recirculating combustor. Appl Energy 2010;87:3718–28.

[13] Ahn, J., Eastwood, C., Sitzki, L., and Ronney, P.D., "Gas Phase and Catalytic Combustion in Heat Recirculating Burners," *Proceedings of the Combustion Institute*, Vol. 29, Issue 7, 2002, pp.957-963.

[14] http://webbook.nist.gov/chemistry/

[15] Vijayan, Vineeth., "Combustion and Heat Transfer in Meso-Scale Heat Recirculating Combustors,". PhD Dissertation, University of Maryland at College Park. 2010

[16] Osiander, Robert., Darrin, Garrison M. Ann., and Champion, John., *MEMS and Microstructures in Aerospace Applications*,1st ed., CRC Press: Taylor and Francis Group, New York, 2006.

[17] http://www.grc.nasa.gov/WWW/CEAWeb/

[18] Rothe, D.E. "Electron Beam Studies of Viscous Flow in Supersonic Nozzles." *AIAA Journal*. 9.5 (1971): 804-811.

[19] Massier, P, L Back, M Noel, and F Saheli. "Viscous Effects on Flow Coefficient for a Supersonic Nozzle." *AIAA Journal*. 8.5 (1970): 605-607

[2] Kuluva, G.A, and N.M Hosack. "Supersonic Nozzle Discharge Coeffiicients at Low Reynolds Number." *AIAA Journal*. 9.9 (1971): 1876-1877.

[21] Bayt, R, and K Bruer. "Systems Design and Performance of Hot and Cold Supersonic Microjets." *39th AIAA Aerospace Sciences Meeting and Exhibit. 8-11 January, 2001. Reno, Nevada*.

[22] Sutton, G. *Rocket Propulsion Elements*. 7. New York: John Wiley and Sons, 2001.

[23] Shirsat, V., Gupta, A.K. “Performance characteristics of methanol fuelled meso-scale heat-recirculating combustors.” *Applied Energy*, Vol. 88, Issue 12, pp.5069-5082.

[24] Louisos, W., Hitt, D. "Viscous Effects in Performance of Two-Dimensional Supersonic Linear Micronozzles." *Journal of Spacecraft and Rockets*, Vol. 45, Issue 4, 2008, pp. 706-15.